SAPIENZA
UNIVERSITÀ DI ROMA

Search for New Physics in mono-jet final states

in pp collisions at $\sqrt{s} = 13$ TeV
with the ATLAS experiment at the LHC

Scuola di dottorato Vito Volterra

Dottorato di Ricerca in Fisica – XXIX Ciclo

Candidate

Giuliano Gustavino
ID number 1488078

Thesis Advisors

Prof. Stefano Giagu
Dr. Valerio Ippolito

Co-Advisors

Prof. Luca Malgeri
Prof. Giacomo Polesello

A thesis submitted in partial fulfillment of the requirements
for the degree of Doctor of Philosophy in Physics

October 2016

Thesis defended on January 25$^{\text{th}}$, 2017
in front of a Board of Examiners composed by:

Prof. Vittorio Lubicz (chairman)
Prof. Daniele Del Re
Prof. Fiorella Burgio
Prof. Fabio Bellini

Search for New Physics in mono-jet final states
in pp collisions at $\sqrt{s} = 13$ TeV with the ATLAS experiment at the LHC

Ph.D. thesis. Sapienza – University of Rome

Version: January 25$^{\text{th}}$, 2017

Author's email: giuliano.gustavino@cern.ch

A zia Maria,
al suo sorriso
ed al suo esempio
di una vita vissuta sempre
con gioia ed allegria.

Abstract

Many cosmological observations indicate that the matter predicted and described by the Standard Model constitutes only a small fraction of the entire known Universe. These astrophysics measurements infer the existence of Dark Matter which is constituted by beyond the Standard Model particles. Among the possible different approaches to search this kind of particles, in this thesis a detailed description of the mono-jet analysis is addressed in which final states with high transverse momentum and an energetic hadronic jet needed to tag the events are considered.

The results presented are based the full dataset recorded in 2015 in the ATLAS experiment at the centre of mass energy of colliding protons of 13 TeV at LHC. The level of agreement observed between data and Standard Model predictions are interpreted as limits in different theoretical contexts such as compressed supersymmetric models, theories which foresee extra-spatial dimensions and in the Dark Matter scenario. In the latter the limits are then compared with the ones obtained by other ATLAS analyses and by experiments based on completely different experimental techniques.

Finally, a set of possible analysis improvements is introduced in order to reduce the main uncertainties which affect the signal region and to increase the discovery potential by exploiting further the information of the final state.

Acknowledgments

I would probably need another complete section to thank the people that, with their support, patience, and love, have allowed the successful completion of this thesis and my PhD.

A special thanks is addressed to Valerio Ippolito for making me into a physicist, for believing in in me, and being a friend. When I was deciding on a thesis project, I chose the mono-jet analysis for the possibility to work with you again and if I could go back in time I would make definitely the same decision.

Thanks to Stefano Giagu for being my supervisor and for giving me the possibility and responsibility of choosing my way and cultivating my own interests in physics. Thank you for teaching to be clever, pushing me to do better, and encouraging me to think outside the box. I will remember these lessons for the rest of my career and life.

Thanks to Carlo Dionisi for supporting me and simply for being an inspirational example of a physicist.

Thanks to Francesco, Francesco, Elvira, and Marco for your stimulating suggestions and company during these past three years. It was a pleasure to share this experience with you, always combining duty with a dash of mirth.

Thanks to Emma, Cristiano, and Veronica for your cheerfulness and pleasantness. Our collaboration, teamwork, and friendship have been essential for my scientific training and my PhD. I hope to work again with you in the future.

Grazie a Gizza e Peter, al nostro speciale e fraterno rapporto. Grazie non solo per il sostegno fondamentale per la riuscita e la stesura di questa tesi, ma per essere stati due pilastri su cui potermi sempre appoggiare nei momenti di bisogno e veri amici con cui poter condividere le gioie ed i successi.

Grazie a Giulia e alla sua gioia di vivere che è stata sempre una spinta ed una carica nei momenti più felici come in quelli più bui e incerti.

Grazie ad Arianna, Daniele, Mastro, Gianluca, Silvia e tutti i compagni di avventure di quest'ultimo anno a Ginevra. La vostra amicizia e buon umore hanno reso speciale ed indimenticabile questa esperienza in una città ricca di opportunità per gente che vuole 'vivere la vita da vivere la vita da protagonista'. I baccanali passano ma gli amici restano!!

Grazie a Francesca per aver creduto sempre in me, anche più di quanto abbia creduto io in me stesso.

Grazie a Daniele, Frakkia, Mol, Mattizza, Nello, Yak e gli altri amici di L'Aquila sui quali ho potuto sempre contare anche dopo lunghi periodi di assenza e che quando li rincontro sembra mi siano stati sempre accanto.

Grazie alla mia famiglia ed in particolare a mia madre, mio padre e mio fratello, che sono i miei più grandi fan e che mi hanno permesso di diventare quello che sono.

Finalmente gracias a Cris que por mí fue todo y con quien pasé tres años maravillosos. Gracias para creer en mi, para comprenderme, para ser paciente, para apoyarme y simplemente gracias por como eres. Te quiero.

Supervisor's foreword

Astronomical and cosmological observations support the existence of invisible matter that can only be detected through its gravitational effects, thus making it very difficult to study. This mysterious matter known as “Dark Matter” makes up about 27% of the known Universe. As a matter of fact, one of the main goals of the physics program of the experiments at the Large Hadron Collider (LHC) of the CERN laboratory, is the search for new particles that can explain the Dark Matter.

In this context, Giuliano Gustavino's thesis documents his original work performed in searching for Dark Matter effects in the data collected by the ATLAS experiment at LHC at the highest centre of mass energy, 13 TeV, ever reached at a particle collider. The results of Giuliano's work provide an outstanding picture of Dark Matter limits at low Dark Matter masses from new physics models. These limits are complementary to the ones obtained with direct detection experiments. Moreover, they expand our knowledge of one of the most important and challenging questions facing physicists today.

Rome, March 2017

Prof. Stefano Giagu

Contents

Chapter 1

Introduction

The Standard Model is a quantum field theory which describes with extreme accuracy the physical processes of subatomic particles through the strong, weak and electromagnetic interactions. The discovery of the Higgs boson in 2012 at the Large Hadron Collider (LHC) represented the last and most compelling proof of its validity. Nevertheless this theory can explain the phenomenology only up to the electroweak energy scale since it does not describe the gravitational interactions. If the SM is an effective theory, the stability of the Higgs mass under radiative corrections requires a fine tuning of the parameters of the theory which is considered unnatural. To solve this problem it is necessary to introduce extensions to the model.

Moreover the Standard Model cannot provide a valid candidate to explain many astrophysical and cosmological measurements which indicate that the visible particles constitute only a small fraction of the matter that composes the Universe. The existence of Dark Matter is well-established because of these observations and its nature still remains one of the greatest unsolved puzzles of fundamental physics. Several theories beyond the Standard Model postulate the existence of new particles that are stable (or at least long-lived) and neutral, thus fulfilling two important requirements for being the Dark Matter in the universe. One class of candidates of interest for searches at the LHC are the weakly interacting massive particles (WIMPs). These are expected to couple to the known particles through a generic weak interaction, which could be either the Standard Model weak interaction or a new type. WIMPs existence can be probed through three different approaches: direct detection looks at the scattering between the WIMPs and the target material of the experiment; indirect searches instead focus on the detection of the relic products coming from the WIMPs annihilations; experiments at colliders search for processes in which WIMPs are pair produced in particle collisions. These latter lead to signatures with missing momentum in the final state from DM particles which escape undetected from the experimental apparatus. In order to access the production of invisible particles, the most promising route is the mono-jet final state, defined by the presence of a high-transverse momentum jet radiated by the incoming partons, accompanied by a large momentum imbalance in the plane transverse to the beam.

The mono-jet final state is defined by a high transverse momentum jet from the initial state radiation in order to tag the events in addition to the presence of high missing momentum in the transverse plane to the beams. This kind of processes constitutes the most sensitive channel for many of the Dark Matter scenarios which can be investigated at LHC. The mono-jet channel is also sensitive to theories beyond the Standard Model that foresee the existence of extra-spatial-dimensions to solve the hierarchy problem and furnish a possible explanation of the weakness of gravity relative to the other forces. It also can constrain supersymmetric models which constitute an elegant extension of the Standard Model able to provide a natural explanation to the Higgs mass value, Dark Matter candidates and predict the gauge coupling unification at an energy scale of about 10^{16} GeV.

An overview of the Standard Model is introduced in Chapter 2 and the crucial role of the Higgs boson in the mass generation mechanism.

Two possible extensions that allow to solve some of the anomalies and the limitations of the theory are briefly addressed in Chapter 3: the Minimal Supersymmetric Standard Model which predicts scenarios in which the supersymmetric particles, invisible in the detectors, are produced in association to an initial state radiated jet and the Large Extra-Dimensions (ADD) model that foresees the existence of final states with the presence of a quark or gluon and a graviton that escapes the detection.

In Chapter 4 the Dark Matter paradigm is addressed, introducing the most popular cosmological model. The three different approaches used to search for WIMPs are introduced and the results obtained by the different experiments are discussed. The models used for the Dark Matter interpretation in the mono-jet analysis based on the data collected at LHC between 2010 and 2012 are finally illustrated.

The main characteristics and the constituents of the LHC accelerator and the ATLAS detector are shown in Chapter 5.

In Chapter 6 the identification and reconstruction performance of the several physics objects used in the analysis are outlined describing the kinematic and quality requirements applied.

The description of the mono-jet selection, the evaluation of the backgrounds, the fitting strategy and the improvements implemented with respect to the previous analysis are described in detail in Chapter 7. The results interpretation in the Dark Matter and Supersymmetric scenarios and the ADD model are also shown providing the first results of the exploration of the mono-jet channel at the new centre-of-mass energy of 13 TeV.

The comparison between the Dark Matter interpretations of the mono-jet analysis and the results obtained by other searches performed at LHC and by the direct detection experiments is introduced in Chapter 8, pointing out the role of this analysis in the context of the Dark Matter search.

Finally in Chapter 9 future prospectives of the analysis are addressed with emphasis on the improvements on the background estimation and on the fitting strategy in order to increase the discrimination power between signals and background.

Chapter 2

The Standard Model

The Standard Model is the theory that has been able to explain most of the phenomenology of the microscopic world and to identify its elementary constituents. Experimental evidences of its validity come from experiments of High Energy Physics of the twentieth and twenty-first centuries. This chapter briefly describes the Standard Model and the role of the Higgs boson in the theory.

2.1 Fundamental Particles and Forces

The Standard Model (SM) is a relativistic quantum field theory, based on the *gauge* symmetry $SU(3)_C \otimes SU(2)_L \otimes U(1)_Y$ that describes three of the four fundamental interactions:

- $SU(3)_C$ is the color symmetry group, related to the strong interactions;
- $SU(2)_L$ is the weak symmetry group of isospin related to the weak interactions;
- $U(1)_Y$ is the weak symmetry group of hypercharge related to the electromagnetic interactions.

Nevertheless the SM does not describe the gravitational interaction which can be considered negligible at the collider energy scale.

The existing ordinary matter can be sorted in two main categories of fundamental building blocks according with their properties: interacting particles (fermions) and mediators of the forces (bosons) which control their interactions:

fermions fermions half-integer spin particle, obey the Pauli exclusion principle and governed by Fermi-Dirac statistics;

bosons integer spin particles that follow the Bose-Einstein statistics.

The fundamental fields which describe all the particles predicted by the SM are fermionic *matter* fields. They interact with each other through bosonic *gauge* fields. The first category can be defined by means of the chirality operator, $P_{L,R} = \frac{1}{2}(1 \mp \gamma_5)$, and their left-handed component will transform as a $SU(2)_L$ doublet while their right-handed part will transform as $SU(2)_R$ singlet.

The *matter* fields are composed by:

quarks which exist in six different flavours and are grouped in three families. For each family there is a *up* component with isospin $I = +1/2$ and a electric charge $Q = 2/3e$ and a *down* component with $I = -1/2$ and $Q = -1/3e$, where e is the module of the electron charge;

leptons which are also six and grouped in three families of different flavour. Each family consists of one charged lepton and of one neutral charged weakly interacting particle: the neutrino. In the SM the neutrinos are treated as massless particles but the observations of neutrino oscillations prove that they have a non-vanishing value of the mass.

As just mentioned, the interactions between quarks and leptons are mediated by the exchange of gauge bosons:

gluons are the eight color charged mediators of the strong interaction, one for each generator of $SU(3)_C$. They are massless and electrically neutral;

photon is the mediator of the electromagnetic interaction, it is massless and carries no electrical charge;

$W^{\pm}$ **and** Z are the three gauge bosons responsible for the weak interaction. They get mass through spontaneous symmetry breaking (see Section 2.5).

The main properties (particle type, generation), the masses and the quantum number of leptons, quarks and gauge bosons are summarized in Figure 2.1.

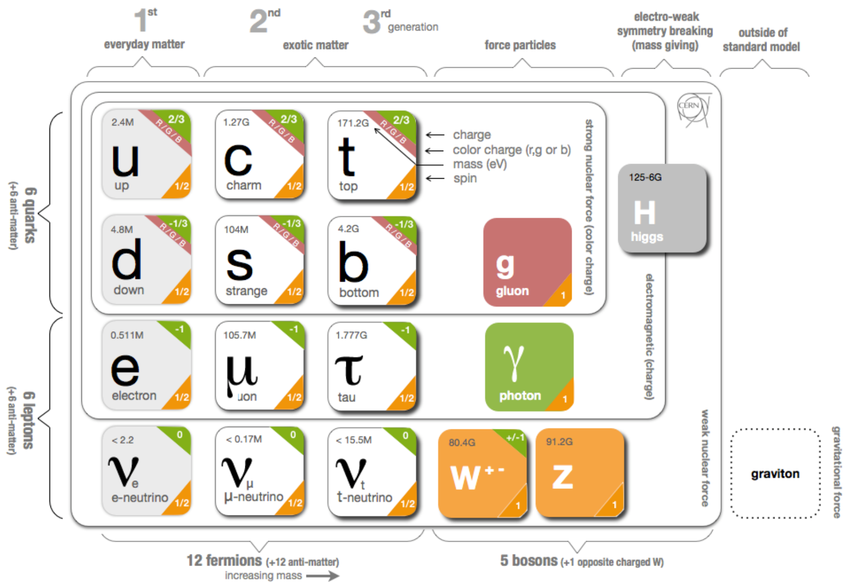

Figure 2.1. An overview of the Standard Model with the main particles and interaction mediators proprieties [1].

The SM is a local gauge theory based on the $SU(3)_C$ symmetry group that describes quantum cromodynamics and on $SU(2)_L \otimes U(1)_Y$ which defines the electroweak sector. In the next sections an explanation of the SM lagrangian from a quantum field point of view will be given.

2.2 Quantum ElectroDynamics

The first relativistic quantum field theory historically developed is Quantum Electro-Dynamics (QED) [2, 3]. It is proposed to describe the electromagnetic interactions of particles.
Starting from the Dirac equation that determines the free massive fermions lagrangian

$$\mathscr{L}_{Dirac} = \bar{\psi}(i\gamma^\mu \partial_\mu - m)\psi \,, \tag{2.1}$$

in which γ_μ are the Dirac matrices and m the mass of the fermionic field ψ, the invariance under the local transformation of the unitarian abelian group $U(1)$ is required

$$\psi(x) \to \psi' = e^{if(x)}\psi(x) \,, \tag{2.2}$$

where $f(x)$ is the function that defines the transformation in each point of the space. Here the fermionic field $\psi(x)$ conserves this symmetry with the introduction of the electromagnetic field $A_\mu(x)$, invariant as well under the same local phase transformation,

$$A_\mu(x) \to A'_\mu(x) = A_\mu(x) + \partial_\mu f(x) \,. \tag{2.3}$$

The interaction terms between the ψ and A_μ fields ensure gauge invariance and the electrodynamic lagrangian can be obtained adding the electromagnetic kinetic term:

$$\mathscr{L}_{QED} = \bar{\psi}[i\gamma^\mu(\partial_\mu - ieA_\mu) - m]\psi - \frac{1}{4}F_{\mu\nu}F^{\mu\nu} \,, \tag{2.4}$$

in which the tensor field is defined as $F_{\mu\nu} = \partial_\mu A_\nu - \partial_\nu A_\mu$.

The mass term of the gauge field A_μ is not allowed by the local transformation invariance getting the massless photon as observed in Nature. This theory is one of the greatest achievements of particle physics. Its predictions have been verified by high precision experiments such as the measurements of the anomalous electron magnetic moment [4].

2.3 Quantum ChromoDynamics

Quantum ChromoDynamics (QCD) [5, 6] describes the strong interactions between quarks (carrying a color or anti-color charge) and gluons (carrying a color and an anti-color charge). It is a non-abelian-Yang-Mills theory that, using the $SU(3)_C$ symmetry group, requires the gauge fields $G^a_{\mu\nu}$ to be massless. Each of the eight generators of the non-abelian theory, T_a with $a = 1, ..., 8$ (respecting the commutation rules $[T_a, T_b] = if_{abc}T^c$ where f_{abc} are the structure constant of the particular gauge group), introduces a mediator: the gluon.

As done in the QED case, the starting point is the Dirac lagrangian where the invariance under local transformations of the quark and gluon fields is imposed:

$$\begin{aligned} q(x) \quad &\to \quad q'(x) = e^{i\alpha(x)_a T_a} q(x), && (2.5) \\ G^a_\mu(x) \quad &\to \quad G^{a'}_\mu(x) = G^a_\mu(x) - \frac{1}{g}\partial_\mu \alpha(x)_a - f^{abc}\alpha_c G^c_\mu(x) \,. && (2.6) \end{aligned}$$

In the formulas above g represents the coupling constant of the strong interactions and $\alpha(x)_a$ with $a = 1, 2, ..., 8$ defines the local transformation.
The QCD lagrangian can be then formulated as

$$\mathscr{L}_{QCD} = \bar{q}(i\gamma^\mu\partial_\mu + igT^a G^a_\mu - m)q - \frac{1}{4}G^a_{\mu\nu}G^{\mu\nu}_a \,, \tag{2.7}$$

where $G^a_{\mu\nu} = \partial_\mu G^a_\nu - \partial_\nu G^a_\mu - gf^{abc}G^b_\mu G^c_\nu$ is not a purely kinetic term but includes also the possibility of interactions between the gluons, since the gluons themselves bring a color charge. This is one of the main differences with respect to QED and it is proper of the non-abelian groups. Finally, the local gauge invariance requires the gluons to be massless. Other important differences between QCD and QED are:

- color confinement: since the potential energy of the quarks, has an additional linear term with respect the electromagnetic one $V = \frac{a}{r} + br$, quarks cannot exist isolated therefore they cannot be directly observed;

- asymptotic freedom: the interaction between the particles becomes weaker and weaker with the increasing of the energy scale; this allows, in contrast with QED, to perform perturbative calculations only at high energy since the coupling constant α_S decreases with increasing energy.

2.4 Electroweak Interactions

The first theory of weak interactions was introduced by Fermi [7]: it gave an explanation to the β-decay under the hypothesis of the existence of a contact interaction, the associated interaction lagrangian is:

$$\mathscr{L}_{Fermi} = -\frac{G_F}{\sqrt{2}}\bar{\psi}_u\gamma^\mu(1-\gamma_5)\psi_d\bar{\psi}_\nu\gamma_\mu(1-\gamma_5)\psi_e \,. \tag{2.8}$$

Nevertheless, this theory violates unitarity and is not renormalizable, being an effective field theory that describes weak processes at low energy.

The electroweak theory proposed by Weinberg [8] and Salam [9] was born with the purpose of proving that QED and weak interactions are different manifestations of the same interaction.

The $SU(2)_L \otimes U(1)_Y$ symmetry group, whose generators are the weak isospin $\vec{\tau} = \frac{1}{2}\vec{\sigma}$ (where $\vec{\sigma}$ are Pauli matrices) and Y the hypercharge operator, defines a chiral theory. The fermions' *left-handed* and *right-handed* components are transformed in different ways under local gauge transformations,

$$\psi(x)_L \quad \rightarrow \quad \chi'(x)_L = e^{i\vec{\alpha}(x)\vec{\tau}+i\beta(x)Y}\psi(x)_L \,, \tag{2.9}$$
$$\psi(x)_R \quad \rightarrow \quad \psi'(x)_R = e^{i\beta(x)Y}\psi(x)_R \,. \tag{2.10}$$

Here $\alpha(x)$ and $\beta(x)$ represent the phases of the local gauge transformation, χ_L the weak isospin doublet (for instance $\binom{\nu_e}{e}$) and describes the *left-handed* fermions, while ψ_R is the isospin singlet which depicts the *right-handed* fermions. The *gauge* invariance of this theory, under the transformations in Eq. (2.9) and (2.10) brings to the electroweak Lagrangian:

$$\begin{aligned}\mathscr{L}_{EWK} &= \sum_{\ell=e,\mu,\tau} \bar{\psi}^{\ell}_{L}\gamma^{\mu}[i\partial_{\mu} + ig\vec{\tau}\cdot\vec{W}_{\mu} - \frac{g'}{2}B_{\mu}]\psi^{\ell}_{L} + \\ &+ \bar{\psi}^{\ell}_{R}\gamma^{\mu}[i\partial_{\mu} + g'B_{\mu}]\psi^{\ell}_{R} + \\ &-\frac{1}{4}\vec{W}_{\mu\nu}\cdot\vec{W}^{\mu\nu} - \frac{1}{4}B_{\mu\nu}\cdot B^{\mu\nu}\,,\end{aligned} \tag{2.11}$$

with $\vec{W}_{\mu\nu} = \partial_{\nu}\vec{W}_{\mu} - \partial_{\mu}\vec{W}_{\nu}$ (same as $B_{\mu\nu}$), where the fields $\vec{W}_{\mu}$ and B_{μ} are introduced for the $SU(2)_L$ and $U(1)_Y$ symmetry group respectively, and the coupling constants g and g' are added for the respective interactions.

In order to re-obtain the photon field it is possible to apply a transformation of these fields:

$$A_{\mu} = W^3_{\mu}\sin\theta_W + B_{\mu}\cos\theta_W\,, \tag{2.12}$$

$$Z_{\mu} = W^3_{\mu}\cos\theta_W - B_{\mu}\sin\theta_W\,, \tag{2.13}$$

$$W^{\pm}_{\mu} = \frac{1}{\sqrt{2}}(W^1_{\mu} \mp W^2_{\mu})\,, \tag{2.14}$$

where θ_W is the Weinberg angle defined in terms of the coupling constants g and g' through:

$$\sin\theta_W = \frac{g'}{\sqrt{g^2+g'^2}}\,, \tag{2.15}$$

$$\cos\theta_W = \frac{g}{\sqrt{g^2+g'^2}}\,. \tag{2.16}$$

The electric charge can hence be written as a function of g and θ_W:

$$e = g\sin\theta_W = g'\cos\theta_W\,. \tag{2.17}$$

However this theory is not complete because the gauge invariance does not allow massive terms for the W and Z bosons ($m^2W_{\mu}W^{\mu}$ and $m^2B_{\mu}B^{\mu}$) and the fermions ($m^2f\bar{f}$). This contradicts the experimental results that prove only the photon as massless gauge boson.

2.5 The Higgs-Brout-Englert Mechanism

In 1964, Higgs , Brout and Englert provided a model, today known as Higgs-Brout-Englert mechanism, to solve the mass problem for fermions and boson preserving the gauge invariance. This model introduces a new scalar boson through a mechanism of spontaneous symmetry breaking: the Higgs boson. The symmetry breaking can occur when the lagrangian of the system shows a symmetry in its ground state, which is degenerate. In such case, there is actually no clear choice to describe the state of minimum energy therefore the symmetry is broken by choosing one of the degenerate eigenstates.

In the electroweak theory the $SU(2)_L \otimes U(1)_Y$ symmetry group is spontaneously broken in $U(1)_{em}$ (charged related group), which has to be conserved. For the Goldstone theorem, three massless Goldstone bosons appear, then absorbed by three of the four gauge bosons, giving mass to the vector bosons and keeping the photon massless. The easiest way to break the symmetry under the transformation of the $SU(2) \otimes U(1)$ group consists of introducing a complex scalar field in form of a isospin doublet:

$$\Phi = \begin{pmatrix} \phi^+ \\ \phi^0 \end{pmatrix} = \frac{1}{\sqrt{2}} \begin{pmatrix} \phi_1 + i\phi_2 \\ \phi_3 + i\phi_4 \end{pmatrix} , \tag{2.18}$$

where ϕ_i are real fields.
The easiest scalar Higgs lagrangian can be written in terms of a kinematic and a potential term:

$$\mathscr{L}_{Higgs} = (D^\mu \Phi)^\dagger D^\mu \Phi - V_{Higgs} \, , \tag{2.19}$$

where

$$D^\mu = \partial^\mu + \frac{i}{2} g \sigma_j W_j^\mu + i g' Y B^\mu \, , \tag{2.20}$$

$$V_{Higgs} = \mu^2 \Phi \Phi^\dagger + \lambda (\Phi \Phi^\dagger)^2 \, , \tag{2.21}$$

with μ and λ which are free parameters.

In order to have a stable theory, the potential has to be inferiorly bounded which corresponds to impose $\lambda > 0$; nevertheless the sign of μ^2 is not determined hence for $\mu^2 < 0$ the minimum is degenerate and it does not coincide with the origin. It indeed belongs to a circumference as shown in Figure 2.2. Among the

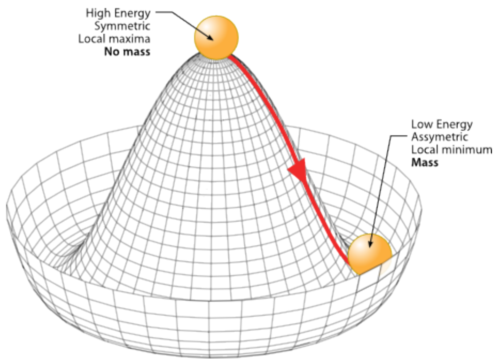

Figure 2.2. Higgs potential $V_{Higgs} = \mu^2 \Phi \Phi^\dagger + \lambda (\Phi \Phi^\dagger)^2$ in the $(\Re(\Phi), \Im(\Phi))$ plane.

various minimum states on the surface of a four-dimensional hypersphere, choosing a particular vacuum expectation value with $\phi_1 = \phi_2 = \phi_4 = 0$ and $\phi_3 = v$:

$$\Phi_0 = \frac{1}{\sqrt{2}} \begin{pmatrix} 0 \\ v \end{pmatrix} \qquad \text{with} \qquad v = \sqrt{\frac{-\mu}{\lambda}} \, , \tag{2.22}$$

the electroweak symmetry breaking, with the consequent generation of massive vector bosons and the symmetry invariance of $U(1)_{em}$, is ensured.

Applying a perturbative expansion around the vacuum state, four scalar fields θ_1, θ_2, $\theta_3, h(x)$ are introduced and the $\Phi(x)$ field can be defined as:

$$\Phi(x) = e^{\frac{i\vec{\tau}\cdot\theta(x)}{v}} \begin{pmatrix} 0 \\ \frac{v+h(x)}{\sqrt{2}} \end{pmatrix} \approx \frac{1}{\sqrt{2}} \begin{pmatrix} \theta_2 + i\theta_1 \\ v + h - i\theta_3 \end{pmatrix}. \tag{2.23}$$

The four fields are independent and parametrize correctly the fluctuations around the origin $\Phi(0)$. θ_1, θ_2 e θ_3 are the massless Goldstone bosons generated by the spontaneous symmetry breaking of the electroweak group. The lagrangian is still locally gauge invariant for $SU(2)$ and the Goldstone bosons can be deleted by exploiting the gauge freedom. The resulting field can be finally written as:

$$\Phi(x) = \frac{1}{\sqrt{2}} \begin{pmatrix} 0 \\ v + h(x) \end{pmatrix}, \tag{2.24}$$

where $h(x)$ is the Higgs scalar field.

Replacing Eq. (2.24) in Eq. (2.19) and writing W^3_μ and B_μ in terms of Z_μ and A_μ, the gauge boson masses can be expressed as a function of the coupling and of the vacuum expectation value:

$$M_W = \frac{1}{2} vg, \; M_Z = \frac{1}{2} v\sqrt{g^2 + g'^2}\,. \tag{2.25}$$

A direct relationship between the vector boson masses and Weinberg angle can be also found:

$$\frac{M_W}{M_Z} = \cos\theta_W\,. \tag{2.26}$$

Three of the four degrees of freedom introduced in the theory are thus absorbed in the $W^\pm$ and Z fields giving them mass and leaving the photon massless.

Furthermore the value of v can be determined using the empirical value of the Fermi constant G_F evaluated from the muon decay:

$$\frac{G_F}{\sqrt{2}} = \frac{g^2}{8M_W^2} \tag{2.27}$$

and, using Eq. (2.25), the vacuum expectation value is

$$v = \sqrt{\frac{1}{\sqrt{2}G_F}} \sim 246 \text{ GeV}\,. \tag{2.28}$$

Applying this formalism in the mass term V_{Higgs} in Eq. (2.21), a direct relationship between the Higgs boson mass and the vacuum expectation value can be obtained as

$$m_h = \sqrt{2v^2\lambda}\,. \tag{2.29}$$

Nevertheless, the Higgs boson mass m_h is not predicted by the theory because λ is a free parameter.

In the SM, the Higgs boson doublet can be used also to generate the quark and lepton masses. It can be achieved by adding to $\mathscr{L}_{EWK}$ in Eq. 2.12 a term that is invariant under $SU(2)_L \otimes U(1)_Y$:

$$\mathscr{L}_{leptons} = -\lambda_l \left[(\bar{\nu}, \bar{l})_L \begin{pmatrix} \phi^+ \\ \phi^0 \end{pmatrix} l_R + \text{h.c.} \right], \tag{2.30}$$

where λ_l is the Yukawa coupling, which defines the coupling of the interaction between the Higgs and fermion fields. Substituting the Higgs field formulated in Eq. (2.24), the lepton mass term and the interaction between the lepton l and the Higgs field can be obtained:

$$\mathscr{L}_{leptons} = -m_l \bar{l} l - \frac{m_l}{v} \bar{l} l h \, . \tag{2.31}$$

This procedure can be also used in the case of quarks but, since both the components of the doublet are massive, in order to build the upper component in the doublet the following parametrization is used:

$$\Phi_C = -i\sigma_2 \Phi^* = \begin{pmatrix} -\bar{\phi}^0 \\ \phi^- \end{pmatrix} \to \sqrt{\frac{1}{2}} \begin{pmatrix} v+h \\ 0 \end{pmatrix} . \tag{2.32}$$

The resulting gauge invariant lagrangian is

$$\mathscr{L}_{quark} = -\lambda_d^{ij} (\bar{u}_i, \bar{d}'_i)_L \begin{pmatrix} \phi^+ \\ \phi^0 \end{pmatrix} d_{jR} - \lambda_u^{ij} (\bar{u}_i, \bar{d}'_i)_L \begin{pmatrix} -\bar{\phi}^0 \\ \phi^- \end{pmatrix} u_{jR} + \text{h.c.} \, , \tag{2.33}$$

with $i, j, n = 1, 2, 3$ and $d'_i = \sum_{n=1}^{3} V_{in} d_n$, where V_{in} is the Cabibbo-Kobayashi-Maskawa (CKM) matrix and d_n are the d, s and b quarks. Finally the lagrangian can be also expressed in diagonal form:

$$\mathscr{L}_{quark} = -m_d^i \bar{d}_i d_i \Big(1 + \frac{h}{v}\Big) - m_u^i \bar{u}_i u_i \Big(1 + \frac{h}{v}\Big) \, . \tag{2.34}$$

The choice of the Higgs field is hence sufficient to generate the masses of the gauge boson and of the fermions, but the fermions masses remain free parameters of the theory which not predicted by the SM.

Chapter 3

Beyond the Standard Model

The Standard Model is not believed to be the fundamental and complete theory to describe Nature for several unsolved and still unexplained limitations. In this chapter a few observed anomalies will be outlined and an overview of the supersymmetric and the extra-spatial dimensions theories will be given which provide solutions to these deficiencies.

3.1 Few Standard Model limitations

The announcement of the Higgs boson discovery in July 2012 states once again the success of the SM in particle physics: the missing piece of the puzzle was found. The SM is further consolidated by precision measurements performed by the experiments located at CERN in the following years until today. However, although the SM is believed to be theoretically self-consistent, it is not able to give a complete explanation of several observed phenomena of particle physics.

One of the most debated issues of the SM is called “hierarchy problem”. It is the question that asks the reason of the huge discrepancy between the weak force and gravity. It is related to the finite and relatively small mass of the Higgs boson. Indeed there is no mechanism to prevent to the scalar particles to acquire large masses through radiative corrections, thus the Higgs mass would receive huge quantum corrections (related to interactions with virtual particles) from every particle which couples to the Higgs field. Defining the bare mass of the Higgs boson as m_h^0 and the radiative corrections to the Higgs mass as Δm_h, the resulting mass is

$$m_h = \sqrt{(m_h^0)^2 + (\Delta m_h)^2}\,. \tag{3.1}$$

The $\Delta {m_h}^2$ contribution can be written as

$$\Delta {m_h}^2 = -\frac{\lambda_f^2}{16\pi^2}\left(2\Lambda^2 + \mathcal{O}\left[m_f^2 \ln\frac{\Lambda}{m_f}\right]\right)\,, \tag{3.2}$$

where λ_f and m_f are the Yukawa couplings and the masses of the fermions respectively and Λ is an energy cutoff which is interpreted as the energy scale up to which SM is still valid. However, if the SM alone is the only existing theory which can describe Nature until the Planck scale[1], the quantum correction $\Delta {m_h}^2$ would be much larger than ${m_h}^2$ and a large cancellation, called "fine tuning", would be needed.

As just mentioned in Chapter 2, the SM does not describe the gravitational interactions, for which a quantization of the general relativity is needed. Hence the SM can be defined as an effective theory valid at the electroweak scale and a new theory, that include it, will be required at the Planck scale.

An important SM drawback comes from the lack of an explanation of the Dark Matter existence in Nature, whose existence can be inferred by several cosmological observations. A more detailed discussion on the Dark Matter paradigm will be given in Chapter 4.

These and other fundamental problems motivate the idea that the SM is not a definitive and complete theory. In the following sections and in the next chapter, a review of several scenarios beyond the SM that aim to explain the problems mentioned so far, will be presented. These models are of particular interest in this thesis, because they predict new observable phenomena that would appear with an hadronic jets plus missing transverse momentum signature in the final state.

3.2 Supersymmetry

Supersymmetry (SUSY) [12, 13, 14, 15] is a theory born in the 1970s that provides an elegant solution to the hierarchy problem. It lays the grounds to obtain a Grand Unified Theory that permits to merge the three forces predicted by the SM into one single force and furnishes also Dark Matter candidates. This symmetry posits a relationship between the fermions and bosons and causes an effective doubling of the number of fundamental particles, predicting a boson superpartner for each fermion and viceversa. If the symmetry was exact, these superpartners, or sparticles, would have the same mass as their SM counterparts. However, since no such superpartners are found to exist, it is theorized that the symmetry must be broken, leading to large mass differences between the SM particles and SUSY particles. Typically, it is assumed that a spontaneous symmetry breaking is induced by a hidden sector, and it is due to "soft breaking" terms added to the Lagrangian:

$$\mathscr{L} = \mathscr{L}_{SUSY} + \mathscr{L}_{soft} \,. \tag{3.3}$$

The latter term solves the mass degeneracy between SM and SUSY particles by making the superparticles heavier. It is "soft" because it should give high masses to the superpartners not to reintroduce any unwanted quadratic divergences like those seen in the SM. Fermi statistics implies an opposite sign of the correction term in Eq. (3.2) for each boson with respect to the fermion. Therefore all the fermion terms have a counter term that naturally cancels the quadratic divergence introduced, the remaining terms in the Higgs mass correction are:

$$\Delta {m_h}^2 = \frac{\lambda_f^2}{16\pi^2} |m_S^2 - m_f^2| \,, \tag{3.4}$$

[1] $\Lambda_{\mathrm{P}} = 1.22 \cdot 10^{19}$ GeV, the energy scale where quantum effects of gravity are expected to dominate.

where m_S denotes the mass of the fermion superpartner. In order to avoid too much fine tuning, these corrections must not be much greater than m_h,

$$|m_S^2 - m_f^2| \lesssim 1\text{TeV}^2\,, \tag{3.5}$$

which sets the scale of validity of the SM to be of the order of the TeV. At higher scales, new particles would be produced and thus the SM should be substituted by its supersymmetric extension, which would be valid up to the Planck scale.

The supersymmetry breaking effects are transmitted from a hidden to the visible sector through known interactions involving an additional "messenger sector". The most known possible mechanisms for SUSY breaking are mediated by gravity that leads to the Minimal Supergravity (mSUGRA) [16, 17] or by means of the electroweak and QCD gauge interactions described by the Gauge Mediated SUSY Breaking (GMSB) [18, 19].

The Minimal Supersymmetric Standard Model (MSSM) constitutes the minimal supersymmetric extension of the SM. It has more than 120 free input parameters to be tuned, which manifest the ignorance about how SUSY is broken. It is defined by requiring the minimal gauge group as in the SM and minimal particle content: the three generations of fermions (without right-handed neutrinos), the gauge bosons of the SM and two Higgs doublets (corresponding to five physics Higgs states) and their superpartners are necessary to give masses to both up and down-type quarks.

The baryon and lepton numbers are no longer conserved by all of the renormalizable couplings in the theory. Since their conservation has been tested very precisely, a new $\mathbb{Z}_2$ symmetry, called R-parity is needed. This symmetry acts on the MSSM fields and forbids these couplings. It can be defined as:

$$R = (-1)^{3(B-L)+2s} \tag{3.6}$$

where B and L refer to the baryon and lepton quantum numbers respectively and s is the spin of the particle.

The chiral and gauge supermultiplets of the MSSM are listed in Table 3.1. The superpartners of the Higgs bosons, the *higgsinos*, *wino* and *bino*, mix with each other resulting in six mass eigenstates:

4 neutralinos $\tilde{\chi}_0^{1,2,3,4}$: electrically neutral fermions, the lightest of which is typically stable. In the models that conserve the R-parity, the lightest neutralino is stable and all supersymmetric cascade decays end up with it.

2 charginos $\chi_{1,2}^{\pm}$: electrically charged fermions. The heavier chargino can decay through Z_0 to the lighter chargino. Both can decay through a $W^{\pm}$ to neutralino.

3.2.1 Compressed Scenarios

In order to probe the phenomena predicted by the MSSM, a variety of simplified models based on a single decay chain are often considered to avoid to explore the entire parameter space foreseen by the complete theory. Of particular relevance for the mono-jet signature are the "compressed" models, i.e. models spectra with very small mass difference Δm between the lightest SUSY particle (LSP) and the next-to-lightest SUSY particle (NLSP) which in turn are decoupled from the rest

Standard Model particles and fields		Supersymmetric partners			
		Interaction eigenstates		Mass eigenstates	
Symbol	Name	Symbol	Name	Symbol	Name
$q = d, c, b, u, s, t$	quark	$\tilde{q}_L$, $\tilde{q}_R$	squark	$\tilde{q}_1$, $\tilde{q}_2$	squark
$l = e, \mu, \tau$	lepton	$\tilde{l}_L$, $\tilde{l}_R$	slepton	$\tilde{l}_1$, $\tilde{l}_2$	slepton
$\nu = \nu_e, \nu_\mu, \nu_\tau$	neutrino	$\tilde{\nu}$	sneutrino	$\tilde{\nu}$	sneutrino
g	gluon	$\tilde{g}$	gluino	$\tilde{g}$	gluino
$W^\pm$	W-boson	$\tilde{W}^\pm$	wino	$\tilde{\chi}^\pm_{1,2}$	chargino
H^-	Higgs boson	$\tilde{H}^-_1$	higgsino		
H^+	Higgs boson	$\tilde{H}^+_2$	higgsino		
B	B-field	$\tilde{B}$	bino	$\tilde{\chi}^0_{1,2,3,4}$	neutralino
W^3	W^3-field	$\tilde{W}^3$	wino		
H^0_1	Higgs boson	$\tilde{H}^0_1$	higgsino		
H^0_2	Higgs boson	$\tilde{H}^0_2$	higgsino		
H^0_3	Higgs boson				

Table 3.1. Standard Model particles and fields and their associated superpartners in the MSSM in the mass and interaction eigenstate formalism [20]

of the supersymmetric spectrum. In scenarios where the R-parity is assumed to be conserved, sparticles are produced in pairs and the LSP is stable and identified as the lightest neutralino $\tilde{\chi}_0$.

Different compressed scenarios which involve the production of squarks are considered in this thesis:

- Stop pair production with $\tilde{t} \to c + \tilde{\chi}_0$;
- Sbottom pair production with $\tilde{b} \to b + \tilde{\chi}_0$;
- Squark pair production with $\tilde{q} \to q + \tilde{\chi}_0$.

Indeed if only light flavour squark-antisquark production is allowed and this process is not sensitive to the flavour, the masses can be considered degenerate [21]; on the other hand if this is not the case then a more specific study of stop and sbottom pair production is doable [22].

For relatively small mass difference Δm between the stop, sbottom or squarks and the neutralino, both the transverse momenta of the jets and the missing transverse momentum in the final state can be low, making difficult the separation between the signal and the multi-jet background. For this reason the presence of initial state radiation jets plus large $E_{\mathrm{T}}^{\mathrm{miss}}$, given by the boosted squark-pair system, is required to identify the signal events (see Figure 3.1).

3.3 Extra Spatial Dimensions

The hierarchy problem can be solved with the introduction of new extra spatial dimensions, which could also explain the weakness of gravity relative to the other forces.

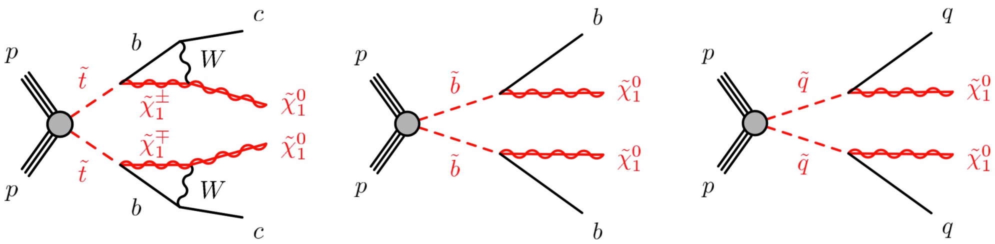

Figure 3.1. Feynman diagrams for the direct stop, sbottom, squark production processes studied. Left: stop pair production, with the stops decaying each into a charm quark and a neutralino. Center: sbottom pair production, each decaying to a bottom quark and a neutralino. Right: inclusive squark pair production, with the squarks decaying each to a quark and a neutralino.

The first 5-dimensional spacetime based model was proposed by Theodor Kaluza in 1921 [23] in which the two known forces at the time, gravity and electromagnetism, were unified:

$$g_{ab} = \begin{pmatrix} g_{\mu\nu} + \phi^2 A_\mu A_\nu & \phi^2 A_\mu \\ \phi^2 A_\nu & \phi^2 \end{pmatrix} \tag{3.7}$$

with $g^{\mu\nu}$ the four-dimensional spacetime metric, A^μ the electromagnetic vector potential and ϕ a new scalar field.

An important assumption, on which the theory is based in order to explain why the fifth dimension is not visible, is that the first derivative of all physics quantities with respect to the fifth dimension is zero,

$$\frac{\partial f(x)}{\partial x_5} = 0\,. \tag{3.8}$$

The purely classical vision of Kaluza's theory was then interpreted few years later, in 1926, by Oscar Klein [24] in the quantum mechanics model. From Eq. (3.8) he interpreted the new dimension as compactified on a cylindrical space with a size of $\lambda_5 \sim 10^{-30}$ cm. Therefore the fifth dimension can be understood to be the circle group $U(1)$ closed and periodic, $x_5 = x_5 + 2\pi R$, where R is the radius of the fifth dimension.

From this, it is relatively straightforward replacing $U(1)$ with a general Lie group and hence enlarging the number of dimensions to a generic integer n. This kind of theory was implemented into the string theories, developed in the later half of the previous century, an example is the 11-dimensional M-theory [25].

Arkani-Hamed, Dimopolous and Dvali proposed in 1998 a theory (ADD theory) based on extra-dimensions that could yield measurable effects on the TeV scale [26]. The model starts from the 3+1 known dimensions adding n spatial extra-dimensions compactified to a radius R. This model assumes also that gravity can propagate in the higher-dimensional space, denoted as *bulk*, while SM particles are confined to the known four dimensions, the *branes*. The Newton's gravitation potential of two masses m_1 and m_2 placed at distance $r \ll R$ becomes:

$$V(r) \sim \frac{m_1 m_2}{M_D^{n+2}} \frac{1}{r^{n+1}}\,, \tag{3.9}$$

where M_D^{n+2} is the scale of gravity in the $4+n$ dimensions. If the masses are placed at distances $r \gg R$, their gravitational flux lines cannot continue to penetrate in the extra-dimensions, and the known $1/r$ potential is obtained:

$$V(r) \sim \frac{m_1 m_2}{M_D^{n+2}} \frac{1}{R^n r} \,. \tag{3.10}$$

Therefore the gravity scale M_D is related with the Planck mass M_P through the relation:

$$M_P^2 \sim M_D^{n+2} R^n \,. \tag{3.11}$$

This theory is particularly interesting when R is small enough to yield M_D close to the electroweak scale m_{EW}. In fact it would solve naturally the hierarchy problem and it would be also possible to probe experimentally the physics of quantum-gravity at collider experiments [27]. Indeed setting $M_D \sim m_{EW}$ the typical Radius R is:

$$R \sim 10^{\frac{30}{n}-17} \left(\frac{1 \text{ TeV}}{m_{EW}}\right)^{1+\frac{2}{n}} \text{cm} \,. \tag{3.12}$$

The possibility of $n = 1$ which results to $R \sim 10^{13}$ cm is already excluded by experimental cosmological evidences, it would cause deviations of the gravity in the range of the solar system distances. The $n > 1$ hypothesis instead, which corresponds to $R < 1$ mm, cannot be excluded by astrophysic observations or by measurements of the gravitational interactions at small distances or by the collider experiments.

In a low-energy effective field theory below the fundamental scale M_D, the ADD model is able to describe the infrared behavior of the gravitational interaction with SM particles only through a spin-two object which acts as mediator of the gravitational interactions and respects the Einstein equation in $4+n$ dimensions: the "graviton". The solutions of the free field equations in compactified extra-dimensions are massive graviton modes, each with its own mass m_k, the so called Kaluza-Klein (KK) *towers.*

The Einstein equation in $4+n$ dimensions establishes the Lagrangian of the free graviton field $G_{\mu\nu}^{(k)}$, and its interaction term is defined as:

$$\mathscr{L}_{grav} = -\frac{\sqrt{8\pi}}{M_P} G_{\mu\nu}^{(k)} T^{\mu\nu} \tag{3.13}$$

where $T^{\mu\nu}$ is the energy-momentum tensor of the SM fields.

The decay rate of the graviton is suppressed by a factor M_P^2, leading to a stable or very long lived particle. Therefore the graviton searches at a collider experiment are focused on final states with missing transverse momentum probing the graviton as a non-interacting particle and tagging the events with a SM object produced in association with it. In Figure 3.2 Feynman diagrams at LO for graviton production in association with a quark or gluon emission are shown.

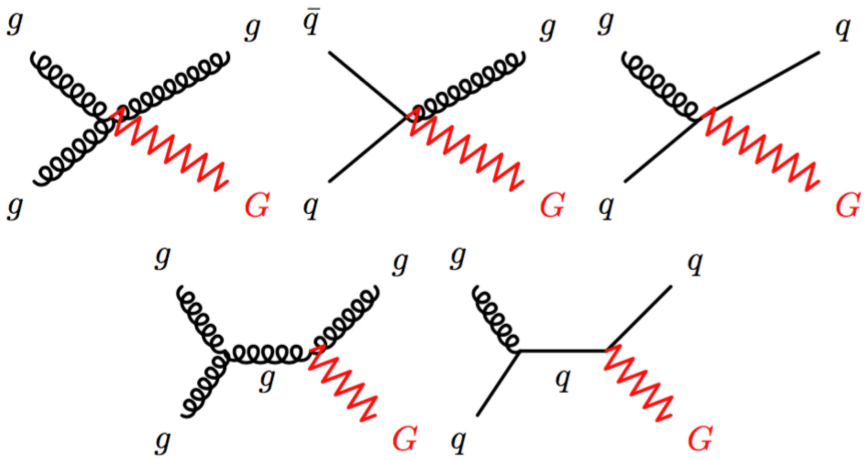

Figure 3.2. Some of the LO Feynman diagrams at LO for graviton production in association with a quark or a gluon.

Chapter 4

The Dark Matter Paradigm

Although the existence of Dark Matter (DM) is well-established to explain a range of astrophysical and cosmological measurements, its nature and particle properties still remain one of the greatest unsolved puzzles of particle and astroparticle physics [28].

In this chapter a brief overview of the simplest and most popular cosmological model, the Lambda Cold Dark Matter (ΛCDM) model in which a category of non-interactive particles is requested to explain the cosmological observations, will be done. Then the wide spectrum of DM searches will be described, showing also the mono-jet analysis results based on the data collected in *pp* collisions at $\sqrt{s} = 8$ TeV. Finally the several theoretical interpretation frameworks, on which the search of DM at ATLAS is based, are overviewed.

4.1 The ΛCDM model

The most successful theory of the universe that collected most consensus between the cosmologists and astrophysics is based on the Big Bang model, according to which the universe expanded from a very high-density and high-temperature state dated roughly $1.4 \cdot 10^{10}$ years. Many observed phenomena confirmed and led the development of this model, whose first stone was probably established by the discovery of Hubble's law [29, 30].

The model is based on three assumptions. The first is the Einstein equation of general relativity, it connects the matter and energy content of the universe to its geometry:

$$R_{\mu\nu} - \frac{1}{2} g_{\mu\nu} R = \frac{-8\pi G_N}{c^4} T_{\mu\nu} + \Lambda g_{\mu\nu}. \tag{4.1}$$

Here the left-hand side of the equation contains the information on the geometry: $R_{\mu\nu}$ is the Ricci tensor and R its contraction that represents the degree of difference in the geometry and in volume between a given Riemannian metric and the metric of flat Euclidean space; $g_{\mu\nu}$ is the metric tensor. The right-hand side describes the energy content of the universe: G_N is the Newton constant, c is the speed of light, $T_{\mu\nu}$ is the energy-momentum tensor and Λ is the so-called *cosmological constant*.

Einstein introduced Λ to obtain a stationary solution for the universe but once the expansion of the universe was discovered he abandoned this concept. However, this term later proved to be useful in explaining observed phenomena, such as Type-Ia

supernovae and parameter estimates from the Cosmic Microwave Background (CMB) yielding indications for the existence of the Dark Energy. It is an unknown form of energy which is hypothesized to permeate all of space and it is responsible of the acceleration and expansion of the universe. With this Λ-term, a quantity of energy remains even in absence of energy or momentum associated with the matter content of the universe $T_{\mu\nu} = 0$. This is the so-called "vacuum energy", which generates a gravitational field even in the absence of any matter.

The second ingredient of the model is the definition of the universe's symmetry which allows to solve Eq. (4.1). The hypothesis of a statistical isotropic and homogeneous universe hugely simplifies the solutions, and is justified also by the structure of the CMB map and by galaxy surveys on scales larger than ~ 100 Mpc. This symmetry implies a specific form of the metric that can be written as:

$$ds^2 = -c^2 dt^2 + a(t)^2 \left(\frac{dr^2}{1 - kr^2} + r^2 d\Omega^2 \right) . \tag{4.2}$$

The dimensionless variable $a(t)$ is called *scale factor* and it is taken to be 1 at the present time. k is a constant which describes the spatial curvature and can take the values $+1, 0$ or -1, according to the case of a closed 3-sphere, the usual flat Euclidean space or a open 3-hyperboloid respectively. With the metric defined in this way the $\mu\nu = 00$ component of the Einstein's field equation, Eq. (4.1), is the first Friedmann equation:

$$\frac{\dot{a}^2 + kc^2}{a^2} = \frac{8\pi G_N \rho + \Lambda c^2}{3} = \frac{8\pi G_N}{3} \rho_{tot} . \tag{4.3}$$

Here ρ_{tot} is the total average energy density of the universe that includes the matter and radiation contributions ρ as well as the cosmological constant Λ, $H \equiv \dot{a}^2/a^2$ is the *Hubble parameter*, known also as Hubble constant H_0, measured by the Planck experiment to be $H_0 = 67.8 \pm 0.9$ km s^{-1}Mpc^{-1} [32]. From Eq. (4.3) the universe results to be flat for the critical density

$$\rho_c = \frac{3H^2}{8\pi G_N}. \tag{4.4}$$

A standard cosmological convention is to use the densities normalized to the critical one, Ω_i, and to express the total density of the universe Ω as the sum over the several components:

$$\Omega \equiv \sum_i \frac{\rho_i}{\rho_c} \Omega = \sum_i \Omega_i . \tag{4.5}$$

The first Friedmann equation (4.3) can be expressed in terms of the new definition of densities:

$$1 - \Omega = -\frac{k}{H^2 a^2} \equiv \Omega_k , \tag{4.6}$$

where the role of the k value stands out: the universe is *flat* if $\Omega = 1$, *opened* if $\Omega < 1$ and *closed* if $\Omega > 1$.

The first observation that proved the expansion of the universe was the Lemaitre and Hubble detection of a cosmological redshift of the light emitted by distant galaxies [29, 30]. The redshift consists of the wavelenght increase of electromagnetic radiation coming from an astronomical object. Given an emitted wavelength λ_e and an observed wavelength λ_o the redshift parameter z is defined by

$$1 + z \equiv \frac{\lambda_o}{\lambda_e}. \tag{4.7}$$

Eq. 4.7 can be written in the cosmological context in terms of the scale factor

$$1 + z \equiv \frac{a(t_0)}{a(t_e)}, \tag{4.8}$$

where t_0 defines the time of observation and t_e the time of emission of the radiation [33].

The evolution of the several components of the cosmological densities can be expressed in terms of the redshift. Their dependencies derive from their equations of state that rule the components themselves and consist of the third fundamental concept of the cosmological model.

The continuity equation can be obtained starting from the second Friedmann equation which is derivable from the first one in Eq. (4.3) after some mathematical manipulations

$$\frac{\ddot{a}}{a} = -\frac{4\pi G_N}{3}(\rho + 3p)\,. \tag{4.9}$$

Considering the ideal gas law as a good approximation of the expanding universe to describe the equation of state of the cosmological component X, for which the pressure p and density ρ are related by $p_X = \omega_X \rho_X$, the continuity equation can be formulated as

$$\frac{\mathrm{d}\rho}{\rho} = -3(1+\omega)\frac{\mathrm{d}a}{a}\,. \tag{4.10}$$

Now, simply exploiting the relationship between the redshift z and the scale factor a, Ω_X can be expressed in terms of the redshift and of the ω_X parameter:

$$\Omega_X = \Omega_X^0 (1+z)^{3(1+\omega)}\,. \tag{4.11}$$

The matter density Ω_M is diluted as the universe expands changing its volume and it scales as $(1+z)^3$, while the cosmological constant is simply constant. Radiation, that includes also the ultra-relativistic matter as the neutrinos, indeed scales as $(1+z)^4$ and its contribution is negligible in today's universe ($\Omega_R \sim\ 10^{-5}$), it was important instead in the first phase of the universe at redshifts higher than 10^3. Contrariwise the cosmological constant was insignificant at early times, but constitutes the main contribution in the total density today.

This leads to the following expression for the expansion rate as a function of the redshift z:

$$\frac{H^2(z)}{H_0^2} = \left(\Omega_X(1+z)^{3(1+\omega_X)} + \Omega_K(1+z)^2 + \Omega_M(1+z)^3 + \Omega_R(1+z)^4\right)\,. \tag{4.12}$$

By measuring the abundance of each of the different forms of densities, this equation allows us to project back in time, approaching the Big Bang itself.

A brief history of the universe is illustrated in the following (see also Fig. 4.1) to define the instant of the DM *freeze- out* that is the epoch at which the thermodynamic equilibrium is broken below the expansion rate of the universe and the DM particles were decoupled from the others (more details will be introduced in the next section).

- $T \sim 10^{16}$ GeV: the Planck epoch, when the quantum gravitational interactions either dominated. At the end of this epoch, the gravitational force loses relevance, and the universe starts to be described by the SM gauge group.

- $T \sim 10^{2}$ GeV: electroweak symmetry breaking era, could be the origin of baryogenesis. The epoch ended with the SM gauge symmetry breaking into $SU(3) \times U(1)$.

- $T \sim 10^{1} \div 10^{3}$ GeV: DM *freeze-out* epoch, when the weakly interacting DM candidates with masses between the GeV and the TeV scale are decoupled from the SM particles.

- $T \sim 0.3$ GeV: QCD phase transition, in which the quarks and gluons started the hadronization forming the first hadrons, including protons and neutrons.

- $T \sim 1$ MeV: neutrino *freeze-out* occured producing the cosmic neutrino background.

- $T \sim 100$ keV: Big Bang nucleosynthesis (BBN), in which the first light elements (D^3, He^4, He, Li) began to form.

- $T \sim 1$ eV: the matter density became equal to the radiation density, allowing for the formation of structure to begin.

- $T \sim 0.4$ eV: photon *freeze-out* produced the Cosmic Microwave Background radiation, observed today (see Section 4.3).

- $T \sim 10^{-4}$ eV: today.

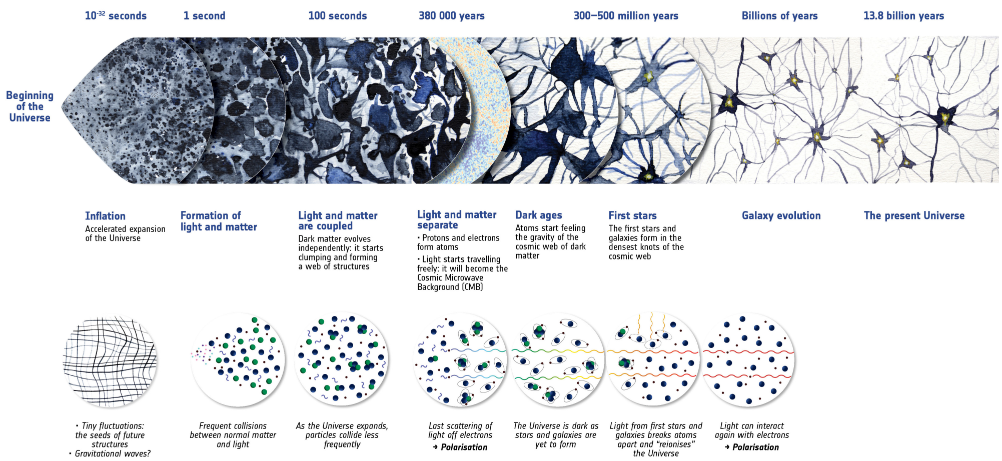

Figure 4.1. Schematic illustration of the history of the universe from the Big Bang to the present [34].

4.2 Relic Density

The hypothesis of a cold (non-relativistic) DM candidate, on which the ΛCDM model is based, is strongly supported by the cosmological observations. Indeed, the matter density observed today, $\Omega_M = 0.308 \pm 0.012$, is largely greater than the expected one, obtained by calculations based of the element abundances in the stars.

The starting point to evaluate the amount of relic DM abundance in the universe is the DM *freeze-out* moment. As mentioned before, the annihilation of the existing particles is balanced by the creation of particles from the energy of the system, keeping the abundance of the particle in a state of equilibrium. With the universe expansion and the resulting temperature decrease, the energy of the system reaches a point in which it is no more able to produce DM particles and the density of the DM particles is too low to generate interactions and collisions. In this way, a decoupling between the DM candidates with the rest of the SM particles is reached. From this moment the DM abundance is kept fixed and is diluted in the space-time because of the expansion of the universe.

The relic density of a non-relativistic particle species can be calculated starting from the Boltzmann equation used to determine the particle number density of a given kind of particles:

$$\frac{\mathrm{d}n}{\mathrm{d}t} + 3H_0 n = -\langle\sigma v\rangle(n^2 - n_{eq}^2)\,, \tag{4.13}$$

In the formula the natural units ($\hbar = c = 1$) are assumed. Here n denotes the particle number density, n_{eq} the one for thermal equilibrium and $\langle\sigma v\rangle$ the thermal average of the total annihilation cross-section times the particle velocity (the annihilation rate). The latter can be expanded in powers of v^2 in a non-relativistic scenario:

$$\langle\sigma v\rangle = a + b\langle v^2\rangle + (\langle v^4\rangle) \approx a + 6b/x\,, \tag{4.14}$$

with $x = m/T$. The particle number density in the thermal equilibrium can be described by the Maxwell-Boltzmann distributions of a species of mass m (heavy enough to make the particles non-relativistic) at some temperature T,

$$n_{eq} = g\left(\frac{mT}{2\pi}\right)^{\frac{3}{2}} e^{-\frac{m}{T}}\,, \tag{4.15}$$

where g is the number of degrees of freedom.

Solving Eq. (4.13) in the long before and long after the *freeze-out* regimes, i.e. $x \ll x_F$ and $x \gg x_F$, with $x_F = m/T_F$ defined by the *freeze-out* temperature T_F, for a generic particle χ the relic density can be expressed as:

$$\Omega_\chi h^2 = \frac{1.07\cdot 10^9\ \mathrm{GeV}^{-1}}{M_P}\frac{x_F}{\sqrt{g_F^*}}\frac{1}{a + 3b/x_F}\,. \tag{4.16}$$

Here h is the scaled Hubble parameter defined by $h = H_0/100\ \mathrm{kms}^{-1}\mathrm{Mpc}^{-1}$, g_F^* is the number of relativistic degrees of freedom at *freeze-out*. Evaluating the parameters a and b, which depend on the particle mass, and calculating the annihilation cross-sections in all of the possible channels, an estimation of the relic density can be obtained. This is useful to perform an order-of-magnitude estimation using an approximate version of Eq. (4.16):

$$\Omega_\chi h^2 \sim \frac{3 \cdot 10^{-27}\mathrm{cm}^3\mathrm{s}^{-1}}{\langle \sigma v \rangle} \, . \tag{4.17}$$

This approximation makes clear that the relic density is inversely proportional to the annihilation rate at *freeze-out*; in fact, for larger annihilation cross-section, the relic density is smaller, as a larger fraction of χ could annihilate. This dependency is shown in Figure 4.2 where the density decreases exponentially while the ratio of the mass to temperature increases. Once the interaction rate becomes too small and the *freeze-out* is reached, the comoving (moving with respect to the expansion of the universe) particle number density begins to remain constant, since at low values of the annihilation rate the *freeze-out* occurs sooner, and thus the relic density is larger. This phenomenon in which the weaker is the annihilation rate, the higher is the final relic density, is often referred to as the *survival of the weak*.

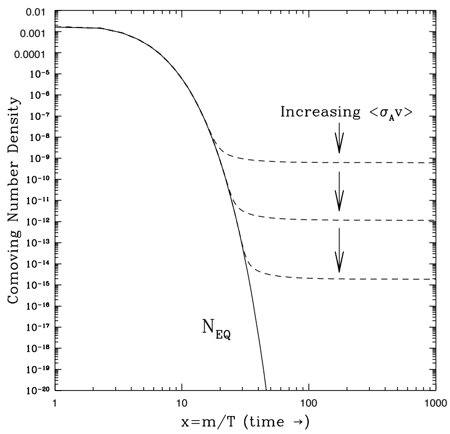

Figure 4.2. Evolution of the comoving particle number density as a function of the DM mass divided by the temperature [35].

It is important to note that these equations are all formulated assuming a series of simplifications and the results can change drastically in more complex or more specific scenarios (see for example the references [36, 37, 38]).

4.3 Cosmological Observations

Many and different cosmological observations argue that the SM particles, *baryonic matter* in cosmology, cannot fully explain the structure and dynamics of the universe. A new ingredient is needed to complete the puzzle.

The first to introduce the idea of the DM existence was the astrophysicist Fritz Zwicky in 1933 [39]. Applying the virial theorem he measured the velocity distribution of galaxies in the Coma Cluster via their Doppler-shifted spectra. It seemed to be 400 times higher than the calculation based on their luminosity, in which the galaxy masses were added to get the total cluster one. Zwicky concluded that some other type of non-luminous matter existed and although his estimates were off by more than an order of magnitude with respect to today's calculations (mainly due to an obsolete value of the Hubble constant). Nevertheless he correctly inferred that most of the matter was "dark".

Afterwards, a strong evidence for the existence of DM came from the observation in the 1970s of the rotation curves of galaxies, that is the circular velocity of stars and gases as a function of their distance from the galactic centre [40]. The expected Newtonian dynamics is well known and the rotation velocity, $v(r)$, is:

$$v(r) = \sqrt{\frac{G_N M(r)}{r}}, \quad \text{with} \quad M(r) = 4\pi \int \rho(r) r^2 \mathrm{d}r, \tag{4.18}$$

where $\rho(r)$ is the visible matter density at a distance r from the galactic center. The velocity should decrease as $1/\sqrt{r}$ moving beyond the centre of the galaxy, where most of visible galactic mass is concentrated. This behavior is well reproduced only in some cases and frequently the observations of galaxies are not in agreement with this expectation. Two of the most popular and evident examples are shown in Figure 4.3 that illustrates the expected and observed radial velocity of the galaxies NGC 2903 and NGC 3198. The rotation velocity appears to be constant with respect to the distance to the galactic centre, and this implies the existence of a missing invisible mass has to be taken in account with a density $\rho_\chi \propto r^2$. This clearly supports the presence of spherical DM halos within the galaxies.

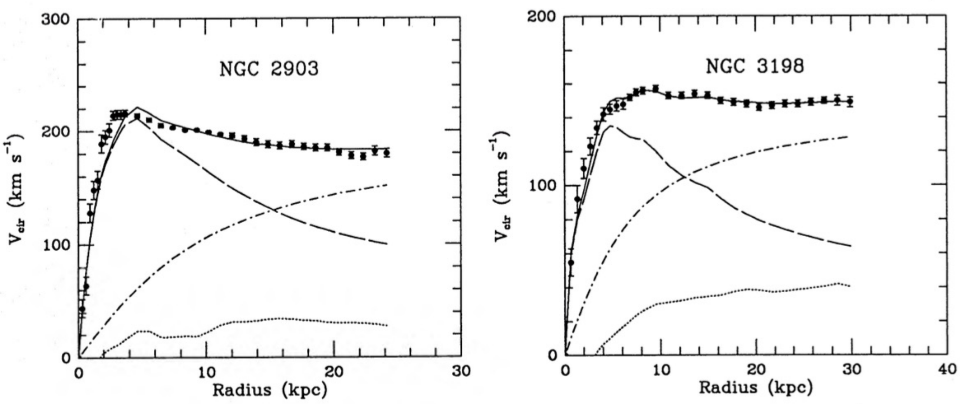

Figure 4.3. Rotation curve of galaxies NGC 2903 and NGC 3198. The circular velocity is shown as a function of the distance from the galactic centre, with the gas content (dotted lines), matter content (dashed lines), and measured values (black circles). The dash-dotted line shows the fitted difference between data and expectation given by the addition the DM contribution in the halo [40].

Gravitational lensing is an effect predicted by Einstein's theory of general relativity for which light rays from a luminous source are deflected when there is a large amount of matter between the source and the observer because of the deformation of the space-time curvature. This phenomenon can be used to measure cluster masses without relying on observations of dynamics. Generally, this method proves the impossibility to explain the gravitational effects due to lensing with the only presence of the baryonic matter, and gives an important input to the DM existence.

Maybe the most famed example of this phenomenon is observed in the galaxy cluster Abell-1689, that has the largest system of gravitational arcs ever found [41].

Another spectacular DM evidence comes from the Bullet Cluster (1E 0657-558), which consists of a collision between two galaxy clusters. The NASA Chandra X-ray Observatory studied the Bullet Cluster in detail, determining the mass distribution of the underlying galaxies through weak gravitational lensing and the X-ray emission from the hot gas. Figure 4.4 shows an image of the Bullet Cluster where the compositeness of baryonic matter is highlighted, in pink in the left picture and in red and yellow in the right one. Due to the large distance scales in question, during the collision the stellar matter was only moderately affected and the stars from each galaxy simply passed through the other galaxy without any inelastic interactions, the only visible effect was a reduction of the velocity due to gravitational effects. On the other hand, the halo constituted of gaseous component was much more spread out because of the electromagnetic interactions. The centre of mass of the cluster provided by the gravitational lensing technique is highlighted with green contours that remain mostly spherical in shape. The effects of the collision demonstrate that the luminous matter is not sufficient to explain the observations, an invisible component of matter is needed, the blue halo in the left pictures. Moreover, it shows as the DM particles did not interact in any significant way beyond gravity, but rather the two DM structures passed through each other.

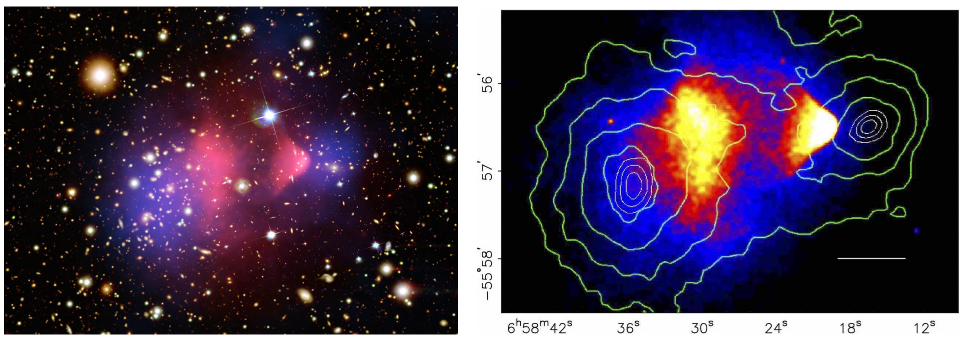

Figure 4.4. Pictures of the Bullet Cluster (1E 0657-558). On the left, the pink regions correspond to the visible mass distribution of the cluster as inferred from X- ray emission and in blue the inferred mass distribution due to the presence of DM [42]. On the right, gravitational lensing contours (green lines) are superimposed on the Bullet Cluster picture highlighting the offset with respect to the visible (colored) matter center of mass [43].

Although the listed and other astrophysical observations provide a compelling proof of the existence of DM, they do not provide any means to estimate the total amount of DM in the universe. This information can be extracted from the analysis of the CMB spectrum. As mentioned in Section 4.1, it was produced by the *freeze-out* of the photons that decoupling from the rest of the primordial bath, when photons started to travel freely through the spacetime leaving a snapshot of the universe of only 380,000 years of life. It is one of the milestones of today's cosmology from which it is possible to evaluate the main ΛCDM model parameters. Today, photons reached in the present universe the microwave frequencies and CMB has been measured to appear as a black body spectrum with a temperature of 2.7255 ± 0.0006 K [31] with anisotropic fluctuations on the level of 10^{-5} K, as shown in Figure 4.5. These

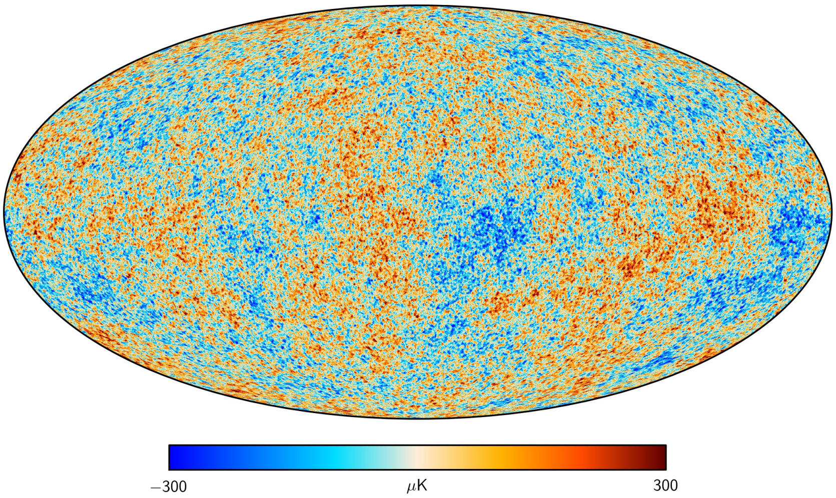

Figure 4.5. The full sky map of the CMB after foreground subtraction as derived from the joint baseline analysis of Planck, WMAP, and 408 MHz observations. The colour scheme varies from -300μK (blue) to 300μK (red) [32]

fluctuations are fundamental to constrain the cosmological parameters. They are parameterized as an expansion of spherical harmonics $Y_{lm}(\theta, \phi)$:

$$\frac{\delta T}{T}(\theta, \phi) = \sum_{\ell=2}^{\infty} \sum_{m=-\ell}^{m=\ell} a_{\ell m} Y_{\ell m}(\theta, \phi)\,, \tag{4.19}$$

where $\ell = 1, 2, ...\infty$, $m = -\ell, ..., \ell$ and $a_{\ell m}$ indicates the multipole coefficients.

Fitting a N-dimensional model to this spectrum, the N cosmological parameters can be obtained and constrained extracting their best-fit values [44]. The latest temperature power spectrum provided by Planck is shown in Figure 4.6 as a function of the multipole moment ℓ, which is related to the angular scale $\phi \sim \pi/\ell$. The best-fit of the ΛCDM theoretical spectrum is performed on the data and represented by the red line; the residues on the bottom part of the figure are also shown with the relative uncertainty of $\pm 1\sigma$.

The effects given by the pressure of the photons lead to erase the temperature anisotropies while the non-relativistic baryons tend to form clusters of matter. This leave an imprint in the form of harmonic peaks in the multipole expansion. The position, shape and relative height of the peaks retain important information coming from the instant relative to the photon decoupling. The position of the first peak is sensitive to the curvature of the universe Ω_K and to a small extent also to the amount of Dark Energy. The second and third peaks are related to the amount of DM and Dark Energy in the universe, while in general the shape of the spectrum is determined by the baryons and Dark Matter densities, which are estimated to be:

$$\Omega_b h^2 = 0.02226 \pm 0.00023\,, \quad \Omega_c h^2 = 0.1186 \pm 0.0020\,, \tag{4.20}$$

where $\Omega_b h^2$ is the baryon density and $\Omega_c h^2$ is the cold-DM density. Moreover, the CMB measurements support the *flat* universe condition, being the total energy

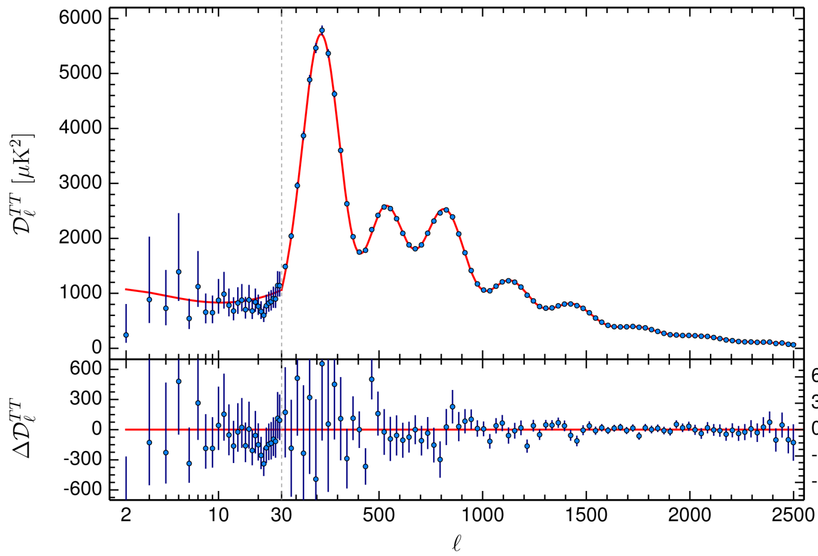

Figure 4.6. The Planck temperature power spectrum. The best-fit based on the ΛCDM theoretical likelihood is shown with the data [32]. More details in the text.

density close to the critical one. This confirms the need of a sizable Dark Energy contribution which is evaluated to be $\Omega_\Lambda = 0.692 \pm 0.012$ by the last Planck results.

On the base of the ΛCDM model, the best fit values from the Planck data yield an amount of Dark Energy in the universe of about 69%, 26% of DM and only 5% of baryonic matter.

An heterogeneous spectrum of cosmological observations seems to confirm the ΛCDM theoretical model pointing to the existence of new particle candidates as responsible of gravitational effects which are not explained by the SM. Other models do not introduce new matter in the universe but assert that the variation of the gravity laws at large scale are able to explain several of the phenomena listed above, but do not gather all the observations together in a consistent way. DM so far remains the only solution able to account for all observed phenomena. However, no particle candidate that suits the required properties to constitute the relic abundance of DM was still detected.

4.4 Dark Matter Candidates

In order to give an explanation to the cosmological observations outlined in the previous section, the DM candidates have to fulfill the following requirements:

- to be stable or at least long-lived, since they survived without decaying from the *freeze-out* era until now;
- to not interact via electromagnetic and strong forces, hence the name 'dark';
- to have the right mass and abundance to yield the observed relic density.

Among the fundamental particles of the SM, **neutrino** is the only candidate that could have the characteristics to be a DM candidate, complying some of the necessary requirements. However it is ruled out being a relativistic particle and its abundance in the universe is not large enough to account for the amount of DM estimated by the CMB spectrum. Indeed the upper bound of the neutrino density would be $\Omega_\nu h^2 = 0.0062$ at 95% CL [31].

The **sterile neutrino** is a theoretically well-motivated particle which may be added to the SM. It could be defined allowing the existence of right-handed neutrinos which get mass through a similar process as the charged leptons and quarks [47]. It would interact only gravitationally with the SM particles and would be very difficult to detect. Furthermore it could provide an elegant explanation to the observed active neutrino masses in a natural way via the See-Saw mechanism [48, 49]. The mass range available of the sterile neutrino is still wide and it could also sufficient to explain the relic density observed.

In order to give a solution to the *strong CP problem*[1], Peccei and Quinn postulated the existence of a new global symmetry $U(1)_{PQ}$ spontaneously broken at the scale f_a [50]. Through this mechanism a new particle with properties close to a DM candidate is generated: the **axion** [51, 52]. The value of the scale f_a sets the cosmological instant in which the axions would have been produced in the universe and they would come out from thermal and non-thermal processes, producing light particles, that can be interpreted to be good candidates of hot or cold DM.

The **Weak Interactive Massive Particles** (**WIMPs**) are the most common and studied DM candidates, as they are found in many particle physics theories, naturally have the correct relic density, and may be detected in several ways. They fulfill all the request listed at the beginning of the section. The mass range between few GeV to TeV is allowed and the cross-sections of interaction between SM and DM particles are of the same order of the weak processes. If these particles are assumed to be produced thermally in the early universe, their relic density after the *freeze-out* can be calculated as done in Section 4.2. Given a WIMP candidate with a mass in the permitted range, under the hypothesis that it weakly couples to the SM, then it naturally matches the observed relic density measured by CMB [46]. This is often referred as the *WIMP miracle* and is the reason why WIMPs constitute one of the most favoured DM candidates.

Many theoretical models for physics beyond the SM contain new particles that can be identified as WIMP. Probably the most popular are the SUSY ones, in which the LSP particles can be the perfect candidates, thanks to their long-lived and non interacting properties. In the MSSM outlined in the subsection 3.2, the WIMP candidates can be identified in gravitinos or neutralinos according to the scenarios and on the mechanisms for SUSY breaking. Also in the large-extra-dimensions scenarios, see subsection 3.3, the lightest KK particle (LKP) is a possible WIMP candidate due to its stability and non interacting features.

The models briefly summarized in this section are only a subset of the valid existing theories which introduce a particle with requirements listed above. In the following sections and in the mono-jet analysis a generic WIMP candidate will be considered in the DM searches trying to probe the wide range of its properties (spin,

[1] In QCD there could be a violation of CP symmetry in the strong interactions not observed in nature. As there is no known reason for it to be conserved in QCD specifically, this is a “fine tuning” problem known as the *strong CP problem*.

couplings, mass), without restricting the interpretation to one specific model and giving an explanation of its nature and origin.

4.5 WIMP Searches

There are three typologies of search experiments to detect the WIMPs based on very different techniques and detection systems: the direct detection experiments that search for elastic scattering between the DM particles and the nuclei of the active material, the indirect searches that look at the annihilation products coming from WIMP pairs collisions, and the collider searches, where the production of WIMPs are probed as a signal of missing transverse momentum in the final state. A scheme of the different approaches is illustrated in Figure 4.7. The general techniques for direct and indirect searches and an overview of recent results are given below as well as a brief summary of the Run-1 mono-jet results at ATLAS.

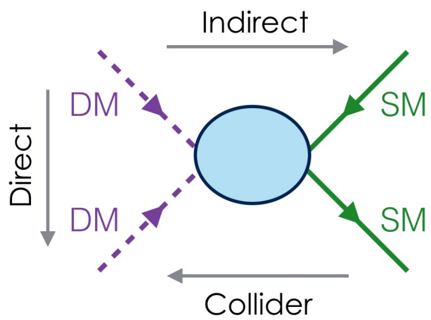

Figure 4.7. Scheme of the DM interaction with the SM particles seen in the different directions probed by the several search approaches.

4.5.1 Direct Detection

The idea of the direct detection experiments is based on the possibility to detect the nuclear recoils originated by scattering of the WIMPs with the nuclei that compose the active material of the detectors. It is made possible because the ration of the Milky Way galaxy, that crosses the DM halo, generates a wind of WIMP which flows in the opposite direction with respect to the solar system motion seen in the Earth rest frame. Assuming a local density of the DM halo of the order of $\rho_\chi \sim 0.3$ GeV/cm^3, a candidate WIMP with $m_\chi \sim 100$ GeV, and a speed of the Earth through the DM halo of $\langle v/c \rangle \sim 10^{-3}$, then the local WIMP flux is about $\Phi \sim 10^5 \mathrm{cm}^{-2}\mathrm{s}^{-1}$ [33]. The rate can be approximately written as:

$$R \sim N \frac{\rho_\chi}{m_\chi} \sigma_{\chi N} \langle v \rangle \tag{4.21}$$

where N is the number of the nuclei in the target and $\sigma_{\chi N}$ the cross-section for WIMP-nucleus elastic scattering. The recoil energies depends on the WIMP mass and typically are in a range between 1 and 100 keV for masses $m_\chi = 10$ GeV $\div$ 10 TeV. Since the WIMPs can interact only weakly and gravitationally, the cross-section of the collisions is very small therefore the events coming from this kind of processes are extremely rare. For this reason the direct detection experiments must reduce the background as much as possible, reaching the so-called "zero-background?? conditions, in order to achieve very high sensitivity to the DM signal. Detectors are usually placed deep underground to suppress the cosmic radiation background and shielded against residual radiation due to muons or radioactivity from the rocks, very low intrinsic radioactive material are exploited. Moreover, large volumes of active material have to be used, in order to collect a large number of interesting events coming from the recoils of the nucleus targets, which are given by the ratio of the detector mass, M_{Det}, to the atomic mass of the nucleus m_A, $N = M_{Det}/m_A$.

Two kinds of interactions are commonly classified according to the type of the WIMP-nucleus coupling:

spin independent (SI) with scalar or vector coupling, where the WIMP couples to the nucleus as a whole ($\propto A^2$, where A is the number of nucleons in the nucleus); for this purpose, target composed by Ge and Xe are usually preferred;

spin dependent (SD) with pseudo-scalar or axial-vector coupling, sensitive to the spin content J of the nucleon such that the cross-section is proportional to $J(J+1)$ and rather independent on the mass of the nucleus.

Different techniques for the detection of the nuclear recoils are used. They are based on the detection of scintillation light, ionization charge or phonons depending on the technology installed and on the range of DM mass which they try to probe. Figure 4.8 shows a scheme of the different detection techniques in relation with the different active materials employed.

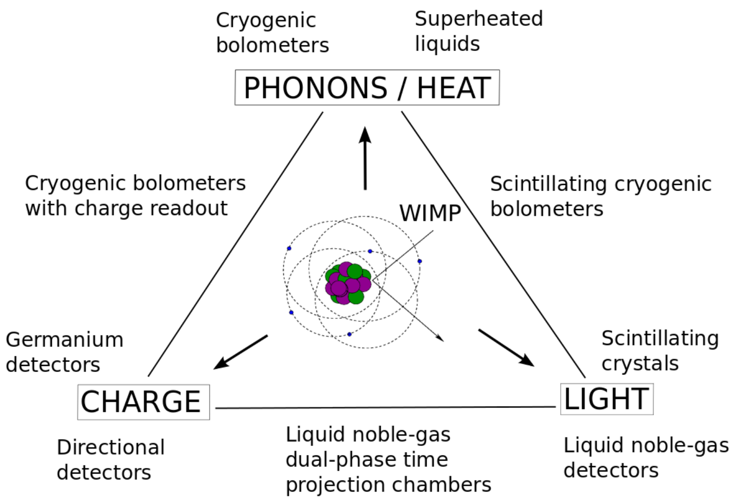

Figure 4.8. Scheme of the possible signals that can be measured in direct detection experiments depending on the technology they use [53].

Many of the experiments make use of the pulse shape information or of the combination of two techniques at the same time, exploiting the different energy

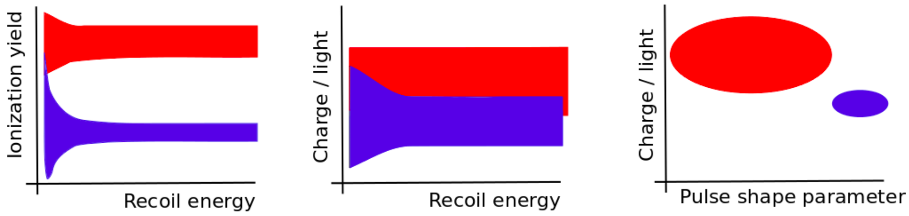

Figure 4.9. Schematic representation of signal (blue) and background (red) regions for a bolometer like a germanium detector (left), a liquid xenon TPC (middle) and a liquid argon time projection chambers (right) [53].

release between the nuclear recoil and the background coming from the electron recoil. This is illustrated schematically in Figure 4.9.

The sensitivity of the direct detection experiments depends on the value of the WIMP mass: when m_χ is close to the nucleus mass this kind of approach reaches the best performance, while for m_χ below or of the order of few GeV, this approach loses completely its sensitivity, because the WIMP-nucleus scattering would not cause any detectable recoil. Then, since the WIMP flux is inversely proportional to m_χ for fixed energy density, the sensitivity also decreases at high DM masses.

Because of the rotation of the Earth around its axis and around the Sun, the direction of the DM wind with respect to an observer on the Earth changes its intensity during the day and during the year. The first effect can be only observed with gaseous detectors or anisotropic response scintillators. The second subdominant effect instead can only be detected by experiments with a heavy target material.

The most important results of the many direct detection experiments based on different techniques are shown in Figure 4.10, where the WIMP-nucleon cross-section versus the WIMP mass is plotted in the SI scenario in two complementary ranges of m_χ. In Figure 4.11 the SD scenario is assumed in the hypothesis of interactions between WIMPs and protons or WIMPs and neutrons. Among the results shown, DAMA and DAMA-LIBRA [54], consisting of NaI(Tl) active material corresponding to a cumulated exposure of 1.17 t·y, observed a annual modulation of the event rate at 8.9 σ level. Despite the fact that the DAMA collaboration and other experiments (like CoGeNT [55], CDMS-Si [56]) claimed a WIMP-like signal in different regions of the SI plot, their results contradict the ones of many other experiments that exclude a large area of the phase space. Relevant results come from the LUX [62], XENON [58] experiments, that use double-phase techniques based on both the scintillation and ionization information, providing the strongest limits on the WIMP-nucleon scattering cross-section in both the SD and SI scenarios in the region $m_\chi \gtrsim 10$ GeV. Finally the PICO [59, 60] experiment based on a bubble detector with superheated liquid of C_3F_8 suspended in a gel matrix is able to set the most stringent limits in the SD scenario.

4.5.2 Indirect Detection

Indirect DM searches are based on the detection of the annihilation products of the DM particles, like gamma rays, neutrinos, positrons, anti-protons or anti-nuclei, looking for excesses or anomalies that could be interpreted as a DM signal.

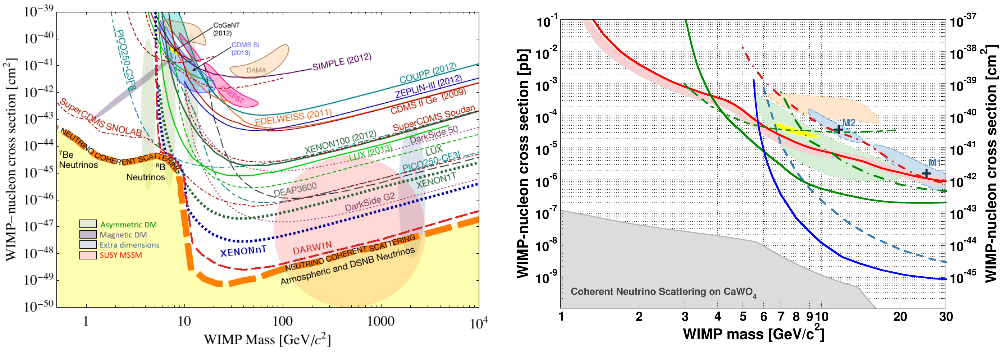

Figure 4.10. On the left: collection of spin-independent WIMP-nucleon cross-section limits versus WIMP mass coming from different existing or projected experiments . On the right: Expanded plot showing spin-independent WIMP-nucleon cross-section limits in the WIMP mass region up to 30 GeV [61].

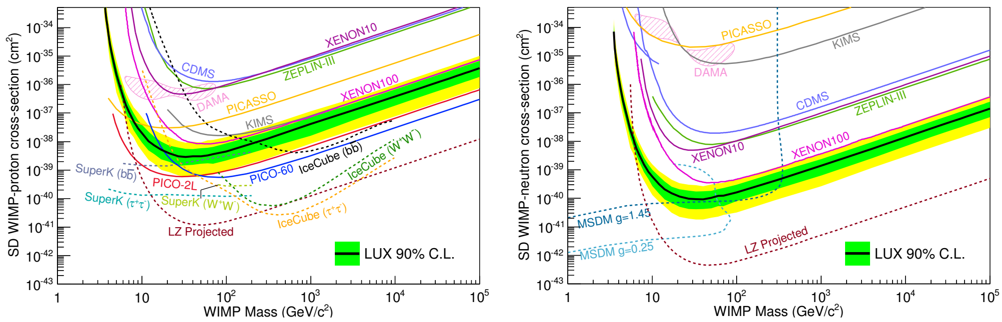

Figure 4.11. Spin-dependent WIMP-nucleon cross-section limits versus WIMP mass coming from different experiments. On the left is shown the case of a scattering between WIMPs and protons and on the right between WIMPs and neutrons [62].

Assuming that WIMPs are gravitationally captured in heavy objects like the Earth, the Sun or the galactic center, the high density reached in these objects could make possible their annihilation.

Neutrinos are particularly interesting because, while most of the possible DM annihilation products are immediately absorbed, they can cross also large amount of matter without leaving their energy.

Some of the resulting neutrinos then travel and can be detected in neutrino telescopes such as IceCube [63] and Super-Kamiokande [64] for example through the detection of upward going muons coming from the interactions of muon neutrinos in the Earth. Under the assumption that the neutrino detected comes from WIMPs annihilating to $b\bar{b}$ or W^+W^-, the results are usually interpreted in limits of the velocity-averaged self-annihilation cross-section $\langle\sigma v\rangle$ and can also be translated in terms of the WIMP-nucleon scattering cross-section and compared with the direct detection ones.

Although the $\gamma\gamma$ production in the WIMPs annihilations are loop-suppressed, the final states are very clear and mono-energetic photon signals can be detected by satellite experiments (Fermi-LAT [65, 66]), to avoid interaction between these objects with the Earth's atmosphere, and Cherenkov telescopes (like HESS [67, 68]). An interesting input comes from the Fermi-LAT data where a feature has been found in using a predetermined search region around the galactic center (see Figure 4.12 on the left). Moreover *dwarf spheroidal galaxies*, faint sort of galaxies which are assumed to be satellites of the Milky Way, are observed to count a large mass-to-light ratio of the order of 100. If this is due to DM accumulated in them, they are promising targets for the observation of gamma rays.

Antiparticles arise as additional WIMP annihilation products in the halo where the best measurements of the positron flux comes from PAMELA [69] and AMS-02 [70], which observe an excess in the positron fraction in charged cosmic rays in agreement with other experiment results (see Figure 4.12 on the right). All these inputs can give a complementary point of view in the WIMPs searches but more data are needed to confirm the observed excesses that could be explained by cosmological phenomena.

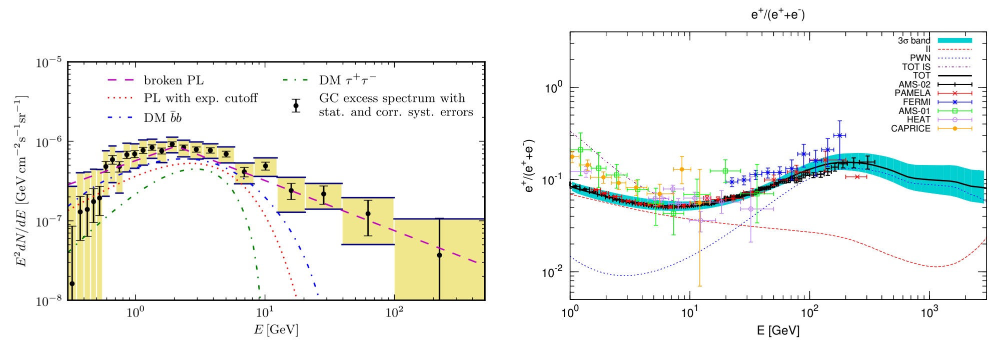

Figure 4.12. On the left: The Fermi GeV γ-ray excess in the residual γ-ray spectrum after subtraction of astrophysical γ-ray emissions and best-fit model spectra of two dark-matter annihilation channels [66]. On the right: Collection of data on the GeV "excess" of galactic positrons in the positron fraction spectrum and best fit expectations for interstellar production and speculations of the AMS-02 collaboration [70]. More info in [61].

4.5.3 Run-1 Mono-jet Results

LHC [80] is able to generate very rare processes through proton-proton collisions, emulating the conditions of the first instant after the Big Bang. From these collisions it could be possible to produce a pair of WIMPs that crosses the detector without interacting leading to an imbalance of the total momentum in the transverse plane. To tag this kind of events a visible SM object is usually required in the final state that could be radiated from the initial state partons. There is a wide spectrum of possible signatures tagged via the detection of an initial state radiation and, for statistic reasons, the most sensitive for a large range of WIMPs production scenarios is the mono-jet final state. The selection is based on the request of large missing transverse momentum in the detector and a high transverse momentum jet , with no presence of additional charged leptons. More details of the selection and the analysis of this channel will be given in Chapter 7.

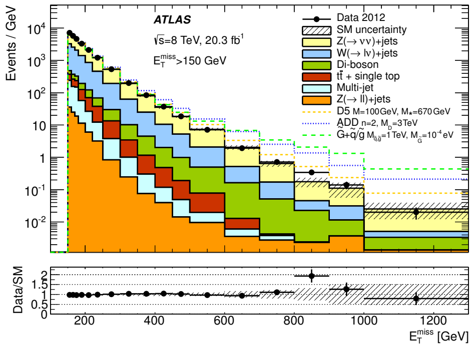

Figure 4.13. Data/MC comparison in the signal region after the fit performed in the Run-1 analysis using the entire data sample of 20.3 fb^{-1} at $\sqrt{s} = 8$ TeV. The error bands in the ratios include the statistical and experimental uncertainties on the background expectations. Signal hypotheses in the DM, SUSY and LED scenarios are also plotted [71].

The philosophy of the DM search at the ATLAS experiment [83] is based on making as few assumptions as possible to perform an agnostic search for WIMPs. Two different theoretical approaches opening in many different scenarios were carried forward during the data collection between 2010 and 2012 (Run-1). This was done in order to provide a scan of the full WIMP parameters space as broad as possible, and to have the possibility to understand and measure the properties of WIMPs in case of a discovery.

The theoretical approaches are based on the Effective Field Theory (EFT) and in the so-called simplified models which will be discussed in more detail in Sections 4.6 and 4.7. In the EFT context the processes are studied in a contact interaction scenario where the DM production processes are mediated by a single new heavy particle with mass beyond the TeV scale. The role of the mediator can be described with a operator which defines the interaction kind (vectorial, axial-vectorial, scalar, pseudo-scalar, tensorial etc.). Since no deviation from the SM prediction was observed in the mono-jet channel using the data collected during the Run-1 corresponding to 20.3 fb^{-1} at $\sqrt{s} = 8$ TeV as shown in Figure 4.13, it was possible to set the limits in the WIMP-nucleon scattering cross-sections versus m_χ. Results are compared with the ones from direct and indirect detection experiment. Figure 4.14 proves that the detection of DM candidates in a collider can give complementary results with respect to the other detection approaches and in particular in the low DM mass region where these detectors lose their sensitivity.

Besides the EFT operators, in the collider experiments the pair production of WIMPs was also investigated within simplified models, where a pair of WIMPs couples to a pair of quarks explicitly via a new mediator particle (for example a Z'). The free parameters to constrain in this context are the mass and spin property of the mediator and of the DM particles, the width of the mediator and the vertex couplings between mediator-partons (g_q), and mediator-WIMPs (g_χ).

Figure 4.15 shows how, for a given mediator mass M_{med} (in this specific case a Z' like mediator) and two values of its width Γ, the real value of the mass suppression scale would compare to the suppression scale $M_* = M_{\rm med}/\sqrt{g_q\, g_\chi}$ derived assuming a contact interaction (shown as dashed lines). In this case the contact interaction

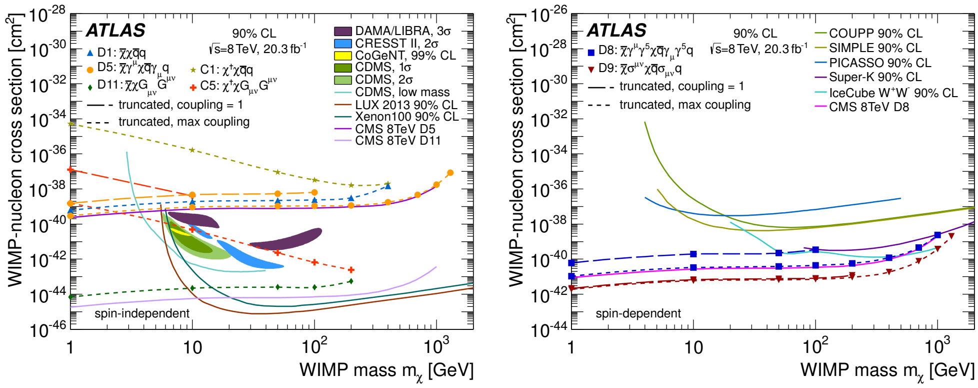

Figure 4.14. Inferred 90% CL limits on the spin-independent (left) and spin-dependent (right) WIMP-nucleon scattering cross-section as a function of DM mass m_χ for different operators. Results from direct-detection experiments for the spin-independent cross-section, and the CMS (untruncated) are shown for comparison [71].

regime is reached for M_{med} values larger than 5 TeV. In the intermediate range the contact interaction approach would not be the proper choice. In fact, in the case of $m_\chi = 400$ GeV, the bounds would be underestimated in the middle region 700 GeV $< M_{\text{med}} <$ 5 TeV with respect to the actual values because the mediator is produced resonantly and the actual M_* value is higher than in the contact interaction regime. Instead, in the small mediator mass regime below 700 GeV, the M_* limits are optimistic and overestimated because the WIMP is heavier than the mediator, and the WIMP pair production via this mediator is kinematically suppressed.

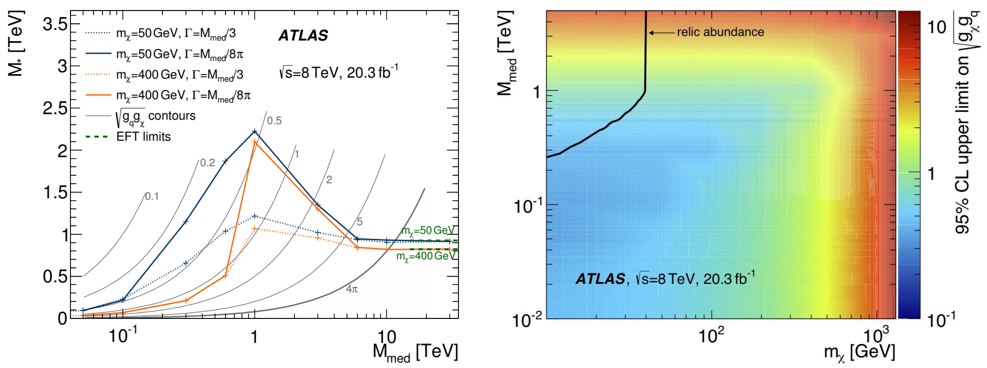

Figure 4.15. Left: comparison between the limits in the plane (M_{med}, M_*) in the EFT and simplified model approach choosing two m_χ and Γ hypotheses. Right: upper limit on the couplings $\sqrt{g_q\, g_\chi}$ in the plane (M_{med}, m_χ). In both figures a Z' like mediator model is used [71]. More information in the text.

It is also possible to constrain the couplings $\sqrt{g_q\, g_\chi}$ of the simplified model vertices in the plane of mediator and WIMP mass (M_{med} versus m_χ) as shown in the right plot in Figure 4.15. Within this model, the regions above the relic density line (as measured by the WMAP satellite, assuming annihilation in the early universe in the absence of any interaction other than the one considered) lead to values of the relic density larger than measured and therefore are excluded.

4.6 Effective Field Theory

In the EFT approach, as mentioned in the previous section, the processes that describe DM production by proton-proton collisions are parameterized by a set of effective (non-renormalizable) operators, introduced after integrating out the mediator. This approximation remains valid only when the energy scale, or suppression scale M_*, of the process is much lower than the scale of the interaction process. An illustration of the contact interaction diagram is shown in Figure 4.16.

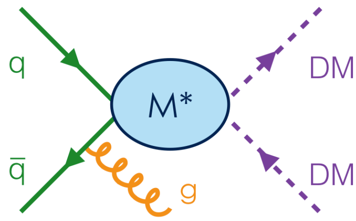

Figure 4.16. Contact interaction diagram in the mono-jet final state with an emission of a gluon radiated from the initial state.

Effective models are mainly used to compare the collider results with the ones coming from direct and indirect searches, in which the EFT approach is always valid, translating limits on the suppression scale into limits on the WIMP-nucleon scattering cross-section. The following conditions are required to carry out a search for contact interaction production of DM at the LHC:

- DM is either a fermionic (Dirac or Majorana) or scalar (complex or real) WIMP;
- WIMPs couple to the SM through a mediator from which it is kinematically possible to pair-produce them;
- the process by which the SM couples to DM can be represented as a *s*-channel production of a mediator of spin 0, 1, or 2, and which couples to either a quark-antiquark pair or a pair of gluons;
- the mediator is too heavy to be produced on-shell at the LHC, therefore the interaction can be treated as a contact interaction.

In direct searches, the momentum transfer of the WIMP-nucleus interaction is of the order of keV and, in indirect searches, the energies involved in the annihilation processes are of the order of the WIMP mass. At colliders like LHC, instead, since collisions happen at very high energy, these processes can occur at an energy beyond the validity of the EFT. The main problem hence is to understand the validity regime of the EFT approach in this kind of events [72, 73, 74, 75].

Considering for example a process $pp \to \chi\chi + jet + X$ at the energy scale M_* where the WIMP is a fermion and the mediator is a heavy scalar boson S, at energies much smaller than the mediator mass M_{med}, the mediator can be integrated out and an effective operator can be used to describe the interaction. The lowest-dimensional possible operator has dimension six and can be written as

$$\mathcal{O}_{D1'} = \frac{1}{M_*^2}(\bar{\chi}\chi)(\bar{q}q). \tag{4.22}$$

A list of all possible effective operators is reported in Tables 4.1 and 4.2 where the WIMP particle is treated as fermionic or scalar particle respectively.

Name	Operator	Name	Operator
D1	$\frac{m_q}{(M_*)^3}\bar{\chi}\chi\bar{q}q$	D1’	$\frac{1}{(M_*)^2}\bar{\chi}\chi\bar{q}q$
D2	$\frac{im_q}{(M_*)^3}\bar{\chi}\gamma^5\chi\bar{q}q$	D2’	$\frac{i}{(M_*)^2}\bar{\chi}\gamma^5\chi\bar{q}q$
D3	$\frac{im_q}{(M_*)^3}\bar{\chi}\chi\bar{q}\gamma^5 q$	D3’	$\frac{i}{(M_*)^2}\bar{\chi}\chi\bar{q}\gamma^5 q$
D4	$\frac{m_q}{(M_*)^3}\bar{\chi}\gamma^5\chi\bar{q}\gamma^5 q$	D4’	$\frac{1}{(M_*)^2}\bar{\chi}\gamma^5\chi\bar{q}\gamma^5 q$
D5	$\frac{1}{(M_*)^2}\bar{\chi}\gamma^\mu\chi\bar{q}\gamma_\mu q$	D6	$\frac{1}{(M_*)^2}\bar{\chi}\gamma^\mu\gamma^5\chi\bar{q}\gamma_\mu q$
D7	$\frac{1}{(M_*)^2}\bar{\chi}\gamma^\mu\chi\bar{q}\gamma_\mu\gamma^5 q$	D8	$\frac{1}{(M_*)^2}\bar{\chi}\gamma^\mu\gamma^5\chi\bar{q}\gamma_\mu\gamma^5 q$
D9	$\frac{1}{(M_*)^2}\bar{\chi}\sigma^{\mu\nu}\chi\bar{q}\sigma_{\mu\nu}q$	D10	$\frac{i}{(M_*)^2}\epsilon_{\mu\nu}{}^{\alpha\beta}\bar{\chi}\sigma^{\mu\nu}\chi\bar{q}\sigma_{\alpha\beta}q$
D11	$\frac{\alpha_s}{4(M_*)^3}\bar{\chi}\chi G_{\mu\nu}G^{\mu\nu}$	D12	$\frac{i\alpha_s}{4(M_*)^3}\bar{\chi}\gamma^5\chi G_{\mu\nu}G^{\mu\nu}$
D13	$\frac{i\alpha_s}{4(M_*)^3}\bar{\chi}\chi G_{\mu\nu}\tilde{G}^{\mu\nu}$	D14	$\frac{\alpha_s}{4(M_*)^3}\bar{\chi}\gamma^5\chi G_{\mu\nu}\tilde{G}^{\mu\nu}$

Table 4.1. EFT operators that describe the interaction between the SM partons and Dirac fermion WIMP. Couplings to Majorana fermion WIMP can be obtained by a simple scaling of the cross-section. α_s is the strong interaction coupling and $G_{\mu\nu}$ is the quantum field which describes the strong interaction mediators. All operators are discussed in more detail in Reference [73, 74]

For processes with a momentum transfer Q_{tr} much lower than the energy scale of the process ($Q_{tr} \ll M_*$), the operator can be expanded in powers of Q_{tr}^2 and, in this case, the propagator of a particle of mass M can be expressed as:

$$\frac{1}{Q_{\mathrm{tr}}^2 - M_{med}^2} = -\frac{1}{M_{med}^2}\left(1 + \frac{Q_{\mathrm{tr}}^2}{M_{med}^2} + \mathcal{O}\left(\frac{Q_{\mathrm{tr}}^4}{M_{med}^4}\right)\right), \tag{4.23}$$

Clearly retaining only the lowest-dimensional operator is a good approximation as long as $Q_{tr}^2 \ll M_{med}^2 \sim M_*^2$. Keeping the leading and relevant term $1/M_{med}^2$, the suppression scale can be expressed as:

$$\frac{1}{M_*^2} = \frac{g_\chi g_q}{M_{med}^2}. \tag{4.24}$$

Perturbative conditions impose an upper limit on the couplings $g_q, g_\chi < 4\pi$. Now, in the reasonable assumption in which $M_{med} > m_\chi$, in a s-channel process ($Q_{tr} > 2m_\chi$)

Name	Operator	Name	Operator
C1	$\frac{m_q}{(M_*)^2}\chi^\dagger\chi\bar{q}q$	C2	$\frac{im_q}{(M_*)^2}\chi^\dagger\chi\bar{q}\gamma^5 q$
C3	$\frac{1}{(M_*)^2}\chi^\dagger\partial_\mu\chi\bar{q}\gamma^\mu q$	C4	$\frac{i}{(M_*)^2}\chi^\dagger\partial_\mu\chi\bar{q}\gamma^\mu\gamma^5 q$
C5	$\frac{\alpha_s}{4(M_*)^2}\chi^\dagger\chi G_{\mu\nu}G^{\mu\nu}$	C6	$\frac{i\alpha_s}{4(M_*)^2}\chi^\dagger\chi G_{\mu\nu}\tilde{G}^{\mu\nu}$

Table 4.2. EFT operators that describe the interaction between the SM partons and complex scalar WIMP. Couplings to real scalar WIMP can be obtained by a simple scaling of the cross-section. α_s is the strong interaction coupling and $G_{\mu\nu}$ is the quantum field which describes the strong interaction mediators. All operators are discussed in more detail in Reference [73]

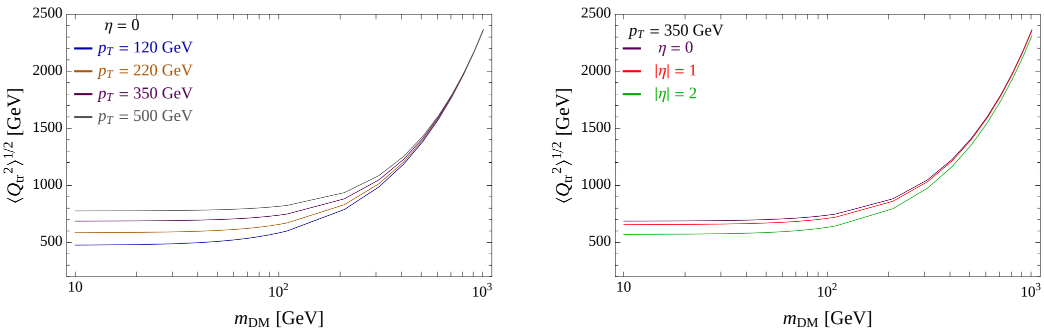

Figure 4.17. The momentum transfer weighted with PDFs in the s-channel as a function of WIMP mass for fixed values of p_T and η of the radiated jet at $\sqrt{s} = 8$ TeV [73].

the condition on the energy scale in terms of m_χ can be obtained:

$$M_* > \frac{Q_\mathrm{tr}}{\sqrt{g_q g_\chi}} > \frac{Q_\mathrm{tr}}{4\pi} > \frac{m_\chi}{2\pi}. \tag{4.25}$$

In order to evaluate what is the value of the energy above which the EFT approach is no longer valid, a correct estimation of the momentum transfer is needed. To have a first raw idea about the validity of the EFT as a function of m_χ, the value of Q_{tr} in Eq. (4.23) can be evaluated as the square root of the averaged squared momentum transfer in the s-channel

$$\langle Q^2_\mathrm{tr}\rangle = \frac{\sum_q \int \mathrm{d}x_1\mathrm{d}x_2\,[f_q(x_1)f_{\bar{q}}(x_2) + f_q(x_2)f_{\bar{q}}(x_1)]\,\theta(Q_\mathrm{tr} - 2m_\mathrm{DM})Q^2_\mathrm{tr}}{\sum_q \int \mathrm{d}x_1\mathrm{d}x_2\,[f_q(x_1)f_{\bar{q}}(x_2) + f_q(x_2)f_{\bar{q}}(x_1)]\,\theta(Q_\mathrm{tr} - 2m_\mathrm{DM})}, \tag{4.26}$$

where the θ-function restricts the calculation to the kinematically allowed region $Q_{tr} > 2m_\chi$, $f_{q,\bar{q}}$ are the parton density functions and $x_{1,2}$ are the fractions of momentum carried by the two partons.

In Figure 4.17, the behavior of $\langle Q^2_\mathrm{tr}\rangle$ as a function of the DM mass (labelled as m_DM) is shown for fixed values of η and p_T of the radiated jet for pp collisions at $\sqrt{s} = 8$ TeV. It proves that the lower (higher) is the jet p_T (η), the lower is the momentum transfer, and therefore the better is the validity of the EFT. In order to test this latter some degrees of arbitrariness are required and the study of its accuracy is not trivial (more details on its evaluation can be found in Reference [74]).

With the increase of the centre of mass energy of the *pp* collision in the data collection started in 2015 at LHC (Run-2), final states with higher jet p_{T} coming from the initial state radiation are probed and the phase space, in which the contact interaction approximation is valid, is further reduced. Therefore, although the EFT interpretation is a simple model to describe the DM processes based on few free parameters, a complete theory approach to base the DM interpretations is desirable.

4.7 Simplified Models

One of the main advantages of DM searches at LHC, with respect to the other types of DM detection approaches, derives by the possibility to study the properties of the WIMPs if an excess is found in the collected data.

During Run-2 an approach based on a set of DM models able to describe a wide spectrum of possible scenarios is followed. It permits to cover a large range of the parameter space proper of the high energy collider searches in which the mediators of the DM-SM interactions are produced resonantly [76, 77]. These models are called simplified models because of the limited number of free parameters they require, in order not to lose much in generality and to yield an easier investigation and coverage of many possible scenarios.

Each simplified model predicts the pair production of a stable DM candidate in proton-proton collisions through the exchange of a mediator. The several scenarios foreseen are not a state of a particular complete theory (e.g. SUSY) but the result of additional terms summed to the SM lagrangian and each of these terms has to be renormalizable and consistent with Lorentz invariance. Furthermore the leptonic and baryonic number conservation and minimal flavor violation are assumed.

The models consider mediators with minimal decay width, so only decays in SM particles and in WIMPs are kinematically allowed. Only Dirac DM particles are chosen because the choice of Majorana fermions or scalars produce changes in the kinematic distributions of the visible particle.

The free parameters of the simplified models are:

$$\{m_\chi, M_{med}, g_\chi, g_q\} \tag{4.27}$$

that are respectively the DM and mediator masses and the couplings between mediator-WIMPs and mediator-quarks. The parameter scan performed in the several analyses searching for DM has been studied taking into account the corresponding changes in kinematic distributions in the final state.

The simplified models considered in the DM interpretations based on the first data collected at $\sqrt{s} = 13$ TeV are the *s*-channel processes in which the propagator is written in a Breit-Wigner form:

$$\frac{1}{Q_{tr}^2 - M_{med}^2 + iM_{med}\Gamma}, \tag{4.28}$$

where Γ is the intrinsic width of the mediator particle. Three cases can be distinguished:

off-shell mediator: if $Q^2_{tr} \gg M^2_{med}$. The cross-sections are suppressed and the width contribution is minor or negligible, hence they are proportional only to the coupling $\sigma \propto g^2_\chi g^2_q$;

on-shell mediator: if $Q^2_{tr} \sim M^2_{med}$. This is the most promising scenario for collider searches, as cross-sections are enhanced. The width here is relevant in the cross-section calculation and in the narrow width approximation (NWA), $\Gamma \ll M_{med}$, the cross-section scales[2] as $\sigma \propto g^2_\chi g^2_q/\Gamma$. Furthermore, in the NWA the cross-section of the mono-jet processes can be factorized in the mediator production times the branching ratio of the mediator decay in the WIMPs: $\sigma(pp \to j\chi\chi + X) \sim \sigma(pp \to jA + X)BR(A \to \chi\bar{\chi})$;

EFT : if $Q^2_{tr} \ll M^2_{med}$, as seen in the previous section. This demonstrates that the simplified models can reproduce also the EFT scenarios. In fact the cross-sections are suppressed by a factor $1/M^4_{med}$ and if the mediator is too heavy to be produced in the pp collisions, it can also prove the contact interaction approach.

The nature of the mediator, like spin and CP properties, can change the kinematic distributions of the final states. In the following, different scenarios are discussed.

4.7.1 Vector and Axial-Vector Mediators

The spin-1 mediators are considered as possible candidates in the first searches of the Run-2 as also done in the Run-1, using a simplified model with the addition of a $U(1)$ gauge symmetry to the SM. The DM candidate is assumed to interact with the SM only through this vector or axial-vector mediator, depending on the spin considered. The diagram of the process is illustrated in Figure 4.25.

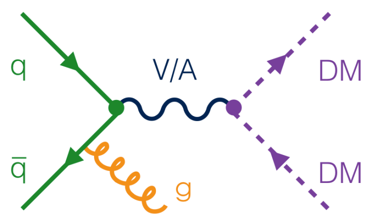

Figure 4.18. Mono-jet diagram of the simplified model in which the DM particles are produced in pair through the exchange of a spin-1 mediator.

In general the Lagrangian of the process in the case of a leptophobic vector and axial-vector mediator[3] [78, 79] is

$$\mathcal{L}_{A/V} = \sum_{q=u,d,s,c,b,t} V_\mu \bar{q}\gamma^\mu(g^V_q - g^A_q\gamma^5)q + g_\chi V_\mu \bar{\chi}\gamma^\mu(g^V_\chi - g^A_\chi\gamma^5)\chi. \tag{4.29}$$

[2]In NWA the integral of the square propagator $\int \frac{ds}{(s-M^2_{med})^2+M_{med}\Gamma^2} = \frac{\pi}{M_{med}\Gamma}$ is non-zero only for a small region of s, where the PDFs can be taken as constant.

[3]The mediator is assumed to not couple with the leptons to avoid the tight limits set by the dilepton searches.

In the case of vector interactions, the axial-vector couplings g_q^A vanish and vice-versa for axial-vector interactions where the vector couplings g_q^V vanish.

In the simplified models the couplings g_q^V, g_q^A are assumed to be universal to all quarks and only pure vector or axial-vector mediator are considered. The minimal widths in the two scenarios are:

$$\Gamma^{\mathrm{V}}_{\mathrm{min}} = \frac{g_\chi^2 M_{med}}{12\pi}\left(1+\frac{2m_\chi^2}{M_{med}^2}\right)\beta_{DM}\theta(M_{med}-2m_\chi) + \sum_q \frac{3g_q^2 M_{med}}{12\pi}\left(1+\frac{2m_q^2}{M_{med}^2}\right)\beta_q\theta(M_{med}-2m_q), \tag{4.30}$$

$$\Gamma^{\mathrm{A}}_{\mathrm{min}} = \frac{g_\chi^2 M_{med}}{12\pi}\beta_{DM}^3\theta(M_{med}-2m_\chi) + \sum_q \frac{3g_q^2 M_{med}}{12\pi}\beta_q^3\theta(M_{med}-2m_q)\ . \tag{4.31}$$

where $\beta_f = \sqrt{1-\frac{4m_f^2}{M_{med}^2}}$ is the velocity of the fermion f with mass m_f in the mediator rest frame.

A scan over the couplings, illustrated in Figure 4.19, shows that the shape of the missing transverse momentum ($E_{\mathrm{T}}^{\mathrm{miss}}$) distributions do not depend on these parameters (and consequently the width) in the ranges considered. In addition a similar behavior is observed also in the off-shell regime. In these case only the production cross-sections change. In the EFT scenario, the comparison between a pure EFT sample and simplified models with a heavy mediator and different values of the couplings demonstrates the reproducibility of the contact interaction scenario with this approach (see Figure 4.20).

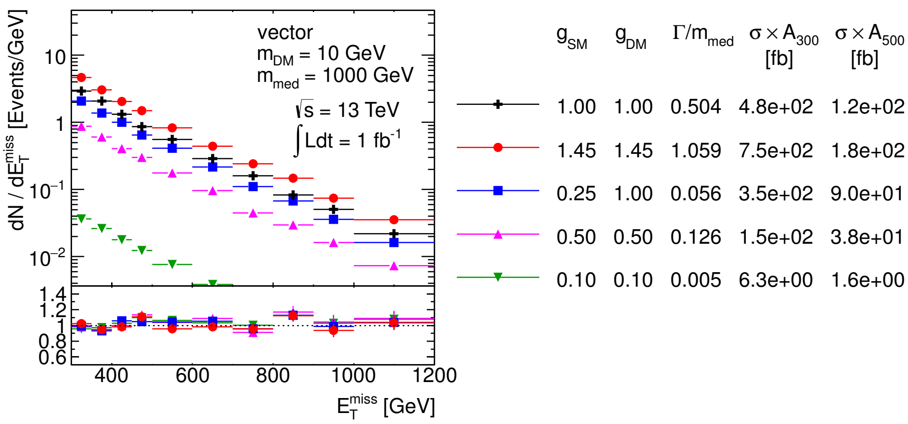

Figure 4.19. Comparison of $E_{\mathrm{T}}^{\mathrm{miss}}$ distributions between vector simplified models with $M_{med} = 1$ TeV, $m_\chi = 10$ GeV and various widths. The ratios of the normalized distributions with respect to the first one are shown. A_{300} and A_{500} denote the acceptance of a $E_{\mathrm{T}}^{\mathrm{miss}} > 300$ GeV and $E_{\mathrm{T}}^{\mathrm{miss}} > 500$ GeV cut, respectively [77].

Fixing the couplings and the mediator mass, the effects of a scan over the DM masses m_χ change the kinematic distributions and the three different mass regimes

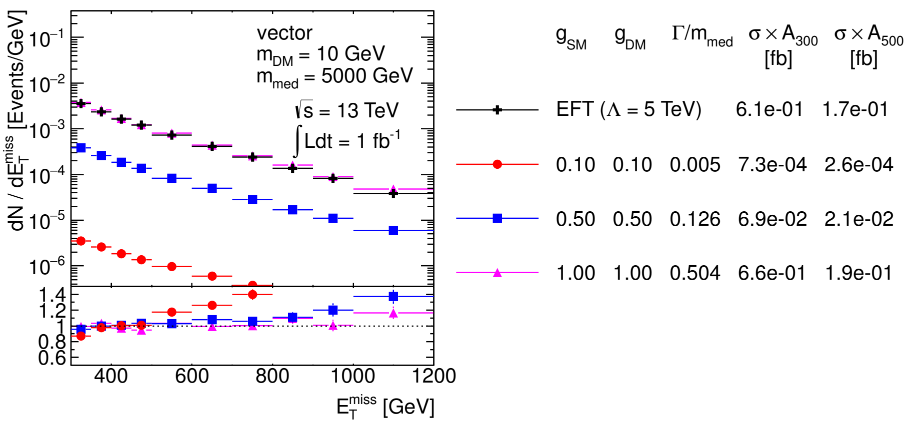

Figure 4.20. Comparison of E_T^{miss} distributions between the D5 EFT sample and the vector simplified models with $M_{med} = 5$ TeV, $m_\chi = 10$ GeV and various widths. The ratios of the normalized distributions with respect to the EFT one are shown. A_{300} and A_{500} denote the acceptance of a $E_T^{miss} > 300$ GeV and $E_T^{miss} > 500$ GeV cut, respectively [77].

can be explored. For $M_{med} \gg 2m_\chi$ the kinematic distributions are independent on the variation of m_χ, while approaching to the resonance region and off-shell regions ($M_{med} \gtrsim 2m_\chi$), a fine scan is needed to catch the shape variations as demonstrated in Figure 4.21.

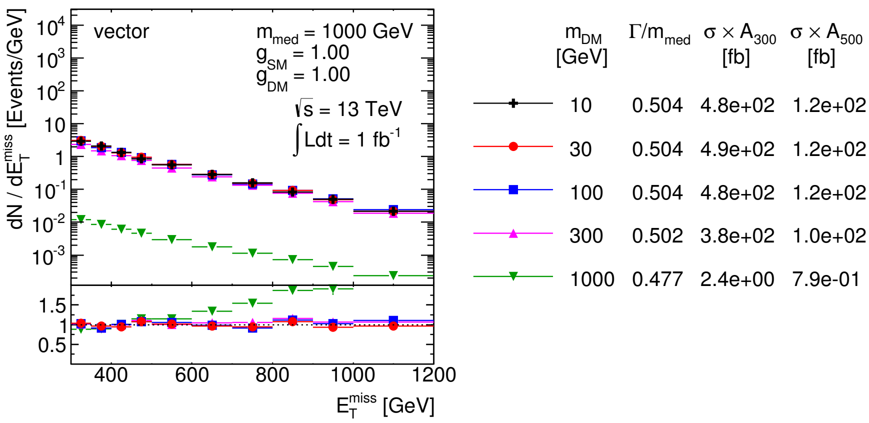

Figure 4.21. Comparison of E_T^{miss} distributions between vector simplified models with $M_{med} = 1$ TeV, couplings $g_q = g_\chi = 1$ and various DM masses. The ratios of the normalized distributions with respect to the first one are shown. A_{300} and A_{500} denote the acceptance of a $E_T^{miss} > 300$ GeV and $E_T^{miss} > 500$ GeV cut, respectively [77].

Changing the mediator mass, keeping fixed the other parameters, yields to different E_T^{miss} spectra in the on-shell regime where the higher is M_{med} the harder will be the distributions (Figure 4.22) while in the off-shell case the kinematical distributions are similar (Figure 4.23).

Finally, comparing samples with different spin structure of the couplings (vector and axial-vector) no significant differences are observed in the E_T^{miss} shape between

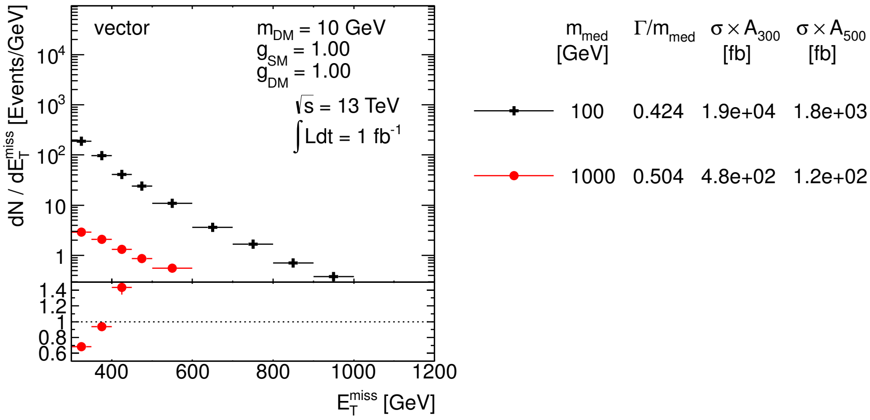

Figure 4.22. Comparison of $E_{\mathrm{T}}^{\mathrm{miss}}$ distributions between vector simplified models with $m_\chi = 10$ GeV, couplings $g_q = g_\chi = 1$ and two different mediator masses. The ratios of the normalized distributions are also shown. A_{300} and A_{500} denote the acceptance of a $E_{\mathrm{T}}^{\mathrm{miss}} > 300$ GeV and $E_{\mathrm{T}}^{\mathrm{miss}} > 500$ GeV cut, respectively [77].

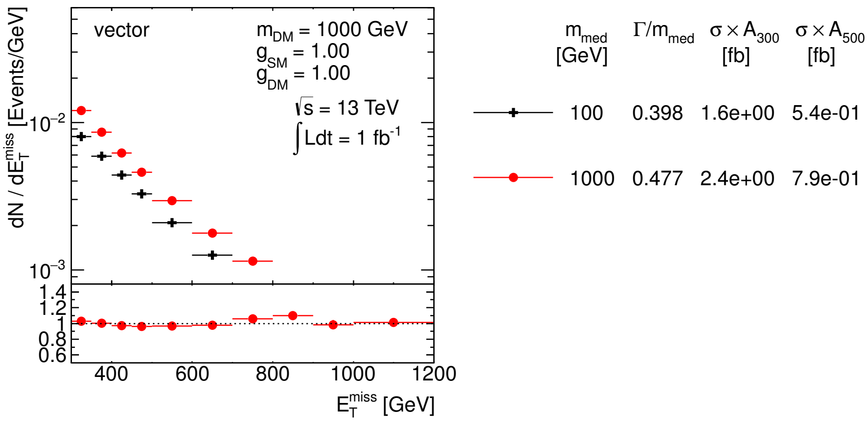

Figure 4.23. Comparison of $E_{\mathrm{T}}^{\mathrm{miss}}$ distributions between vector simplified models with $m_\chi = 1$ TeV, couplings $g_q = g_\chi = 1$ and two different mediator masses. The ratios of the normalized distributions are also shown. A_{300} and A_{500} denote the acceptance of a $E_{\mathrm{T}}^{\mathrm{miss}} > 300$ GeV and $E_{\mathrm{T}}^{\mathrm{miss}} > 500$ GeV cut, respectively [77].

the samples with the same mass parameters and values of the coupling, Figure 4.24. Concerning the cross-sections, in the on-shell region the values are close in the two spin hypotheses while in the other regimes sizable differences are observed.

In conclusion, a scan over the DM and mediator masses is performed in the Run-2 mono-jet analysis with a choice of the axial-vector mediator with coupling $g_\chi = 1$ and $g_q = 0.25$. This particular choice of the couplings allows to cover a wide part of the plane (m_χ, M_{med}). Complementary sensitivity from searches in final states with one jet and missing transverse momentum and in final states with two jets will be shown in Chapter 8. Moreover, it is important to mention that for this particular choice of the couplings NWA is still valid, as $\Gamma/M_{med} \lesssim 0.06$.

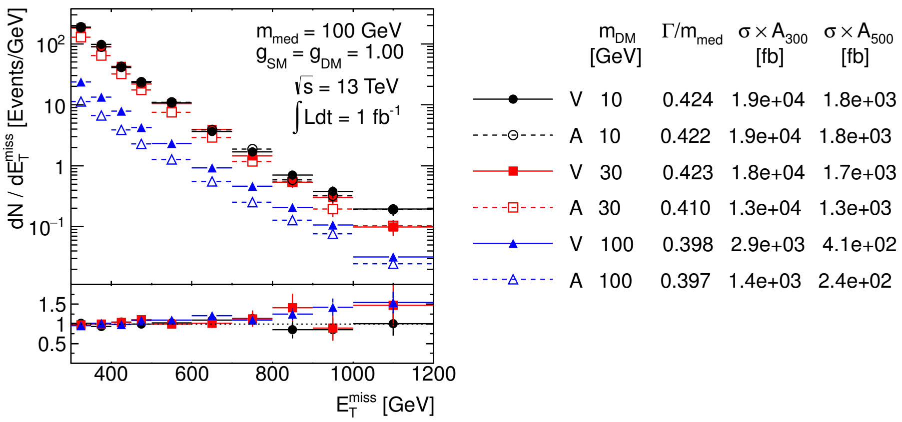

Figure 4.24. Comparison of $E_{\mathrm{T}}^{\mathrm{miss}}$ distributions between simplified models with vector (V) and axial-vector (A) mediator with mass $M_{med} = 100$ GeV, couplings $g_q = g_\chi = 1$ and different values of the DM masses. The ratios of the normalized distributions relative to the same mass points are also shown. A_{300} and A_{500} denote the acceptance of a $E_{\mathrm{T}}^{\mathrm{miss}} > 300$ GeV and $E_{\mathrm{T}}^{\mathrm{miss}} > 500$ GeV cut, respectively [77].

4.7.2 Scalar and Pseudo-Scalar Mediators

Similarly to the spin-1 mediator case, the search for a scalar ϕ or pseudo-scalar a mediator is also considered in Run-2. Considering for simplicity that the SM can be extended with the inclusion of the mediator without taking into account any mixing with the SM Higgs boson, the processes that derives from the proton-proton collisions are loop-suppressed as it can be seen from the Feynman diagrams in Figure 4.25.

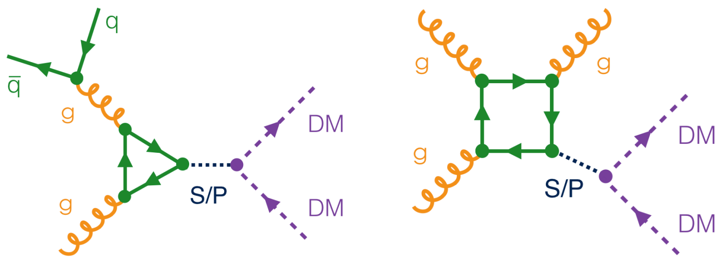

Figure 4.25. Mono-jet diagrams of the simplified model in which the DM particles are produced in pair through the s-channel exchange of a spin-zero particle.

The tree-level Lagrangians that derive from this kind of processes are:

$$\mathcal{L}_\phi = g_\chi \phi \bar{\chi}\chi + \frac{\phi}{\sqrt{2}} g_q \sum_i \left(y_i^u \bar{u}_i u_i + y_i^d \bar{d}_i d_i + y_i^\ell \bar{\ell}_i \ell_i \right) , \tag{4.32}$$

$$\mathcal{L}_a = i g_\chi a \bar{\chi}\gamma_5 \chi + \frac{ia}{\sqrt{2}} g_q \sum_i \left(y_i^u \bar{u}_i \gamma_5 u_i + y_i^d \bar{d}_i \gamma_5 d_i + y_i^\ell \bar{\ell}_i \gamma_5 \ell_i \right) , \tag{4.33}$$

where also in this case the coupling g_q si considered to be the same for all the SM particles for simplicity and the Yukawa couplings y_i^f are normalized to the Higgs vacuum expectation value as $y_i^f = \sqrt{2} m_i^f / v$.

The minimal mediator width (neglecting the contributions from quarks other than top in the loop) is given by:

$$\begin{aligned}\Gamma_{\phi,a} = &\sum_f N_c \frac{y_f^2 g_q^2 m_{\phi,a}}{16\pi}\left(1-\frac{4m_f^2}{m_{\phi,a}^2}\right)^{x/2} + \frac{g_\chi^2 m_{\phi,a}}{8\pi}\left(1-\frac{4m_\chi^2}{m_{\phi,a}^2}\right)^{x/2} \\ &+ \frac{\alpha_s^2 y_t^2 g_q^2 m_{\phi,a}^3}{32\pi^3 v^2}\left|f_{\phi,a}\left(\frac{4m_t^2}{m_{\phi,a}^2}\right)\right|^2\end{aligned} \tag{4.34}$$

where $x = 3$ for scalars and $x = 1$ for pseudo-scalars. The loop integrals, with f as complex functions, are

$$f_\phi(\tau) = \tau\left[1+(1-\tau)\arctan^2\left(\frac{1}{\sqrt{\tau-1}}\right)\right], \tag{4.35}$$

$$f_a(\tau) = \tau\arctan^2\left(\frac{1}{\sqrt{\tau-1}}\right) \tag{4.36}$$

where $\tau = 4m_t^2/m_{\phi,a}^2$.

As performed for the spin-1 case a scan on the free parameters, see plots in Figure 4.26-4.28, proves that the same conclusions can be applied also for this spin hypothesis.

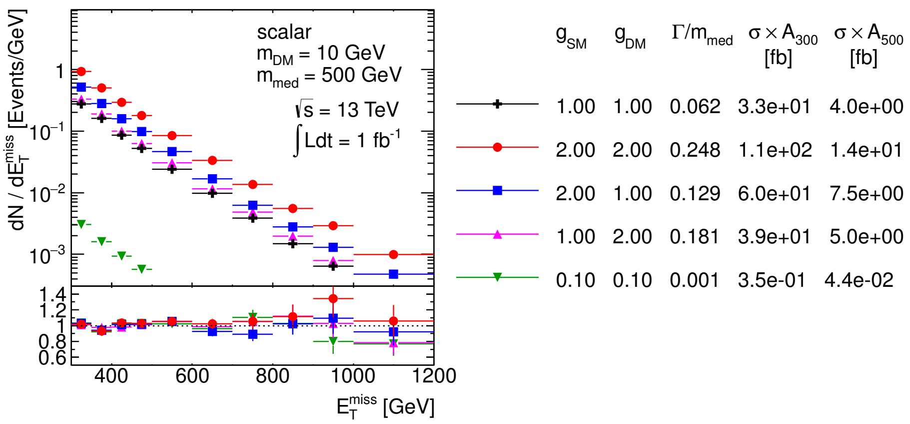

Figure 4.26. Comparison of $E_{\mathrm{T}}^{\mathrm{miss}}$ distributions between scalar simplified models with $M_{med} = 500$ GeV, $m_\chi = 10$ GeV and various widths. The ratios of the normalized distributions with respect to the first one are shown. A_{300} and A_{500} denote the acceptance of a $E_{\mathrm{T}}^{\mathrm{miss}} > 300$ GeV and $E_{\mathrm{T}}^{\mathrm{miss}} > 500$ GeV cut, respectively [77].

As it is shown in Figure 4.29 no relevant differences in the shapes are observed between the scalar and pseudo-scalar coupling choices, while the cross-sections for the pseudo-scalar samples setting the same parameters are higher than the scalar models. The cross-sections of the DM simplified models used in this thesis are listed in Appendix A in Tables A.5–A.8.

In conclusion the search for this kind of processes in the mono-jet final state is particularly interesting since the dijet searches are strongly disfavored for this kind of scenarios, being the processes double-loop-suppressed. A similar scan done for the spin-1 case is performed in Run-2 in the (m_χ, M_{med}) plane with the coupling $g_q = g_\chi$ guaranteeing NWA with $\Gamma/M_{med} \lesssim 0.1$.

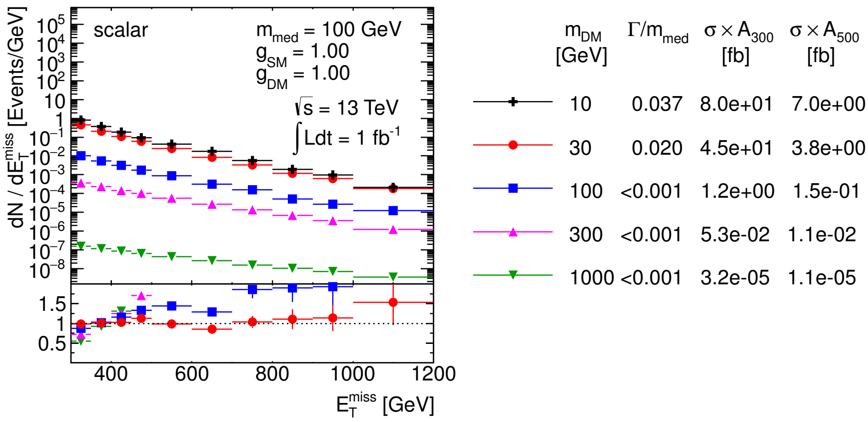

Figure 4.27. Comparison of $E_{\mathrm{T}}^{\mathrm{miss}}$ distributions between scalar simplified models with $M_{med} = 100$ GeV, couplings $g_q = g_\chi = 1$ and various DM masses. The ratios of the normalized distributions with respect to the first one are shown. A_{300} and A_{500} denote the acceptance of a $E_{\mathrm{T}}^{\mathrm{miss}} > 300$ GeV and $E_{\mathrm{T}}^{\mathrm{miss}} > 500$ GeV cut, respectively [77].

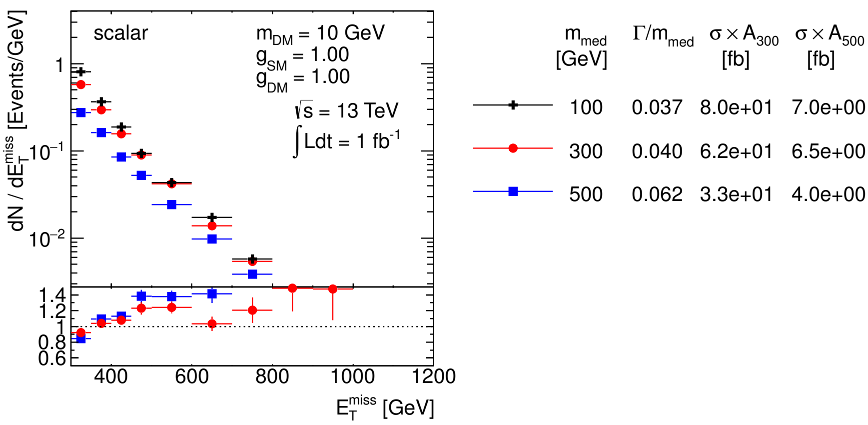

Figure 4.28. Comparison of $E_{\mathrm{T}}^{\mathrm{miss}}$ distributions between scalar simplified models with $m_\chi = 10$ GeV, couplings $g_q = g_\chi = 1$ and two different mediator masses. The ratios of the normalized distributions are also shown. A_{300} and A_{500} denote the acceptance of a $E_{\mathrm{T}}^{\mathrm{miss}} > 300$ GeV and $E_{\mathrm{T}}^{\mathrm{miss}} > 500$ GeV cut, respectively [77].

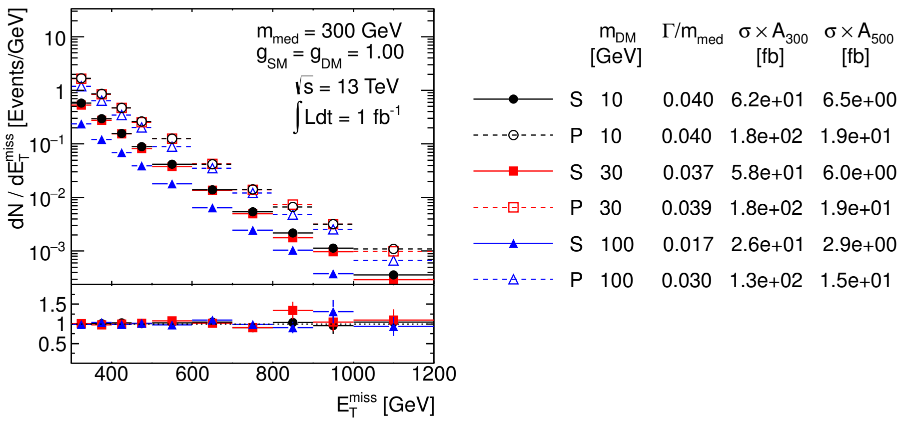

Figure 4.29. Comparison of $E_{\mathrm{T}}^{\mathrm{miss}}$ distributions between simplified models with scalar (S) and pseudo-scalar (P) mediator with mass $M_{med} = 300$ GeV, couplings $g_q = g_\chi = 1$ and different values of the DM masses. The ratios of the normalized distributions relative to the same mass points are also shown. A_{300} and A_{500} denote the acceptance of a $E_{\mathrm{T}}^{\mathrm{miss}} > 300$ GeV and $E_{\mathrm{T}}^{\mathrm{miss}} > 500$ GeV cut, respectively [77].

Chapter 5

Experimental Facilities

In this section the main features of the Large Hadron Collider, built at the European Organization for Nuclear Research (CERN, *Conseil Européen pour la Recherche Nucléaire*) and the ATLAS detector's structure and functionalities are described.

5.1 The Large Hadron Collider

The Large Hadron Collider (LHC) [80] is the current largest and most powerful particle accelerator in the world. It has a circumference of 27 km, situated underground on the border between Switzerland and France, close to Geneva, Switzerland. It is a two-ring-superconducting-hadron accelerator and collider installed in the existing tunnel that was constructed for the Large Electron Positron (LEP) machine at CERN. LHC is able to produce proton-proton, proton-lead and lead-lead collisions with unprecedented high energy and luminosity. The operating center-of-mass energies in proton-proton collisions have so far been 7 TeV in 2010-2011, 8 TeV in 2012 and 13 TeV in 2015 and currently in 2016. The 7 and 8 TeV periods together constitute the LHC Run-1, while the 13 TeV period consists in the LHC Run-2.

5.1.1 Accelerator Complex

LHC is the last step of a multi-stage accelerator system [81] that is schematized in Figure 5.1. The starting point is an injector chain consisting in a linear accelerator (LINAC2) that brings the proton to the energy of 50 MeV. Then the proton beam passes through a 157 m circumference, the Proton Synchrotron Booster (SPB), in which it reaches an energy of 1.4 GeV. Next it is injected into the Proton Synchrotron (PS), a 628 m circumference accelerator which brings the protons to the energy of 25 GeV. Later in the 7 km circumference of the Super Proton Synchrotron (SPS) the protons are accelerated to 450 GeV to then be injected into LHC, which provides the final acceleration to the protons using the radio frequency cavities in order to reach the nominal energy. The beam composed by lead ions follows the same route, with the exception of starting from a different linear accelerator, and traveling into the Low Energy Ion Ring (LEIR) of 78 m of length instead of PSB.

The LHC ring layout is sectored in octants, numbered in clockwise order as shown in Figure 5.2 where two separate beams run in opposite directions and are

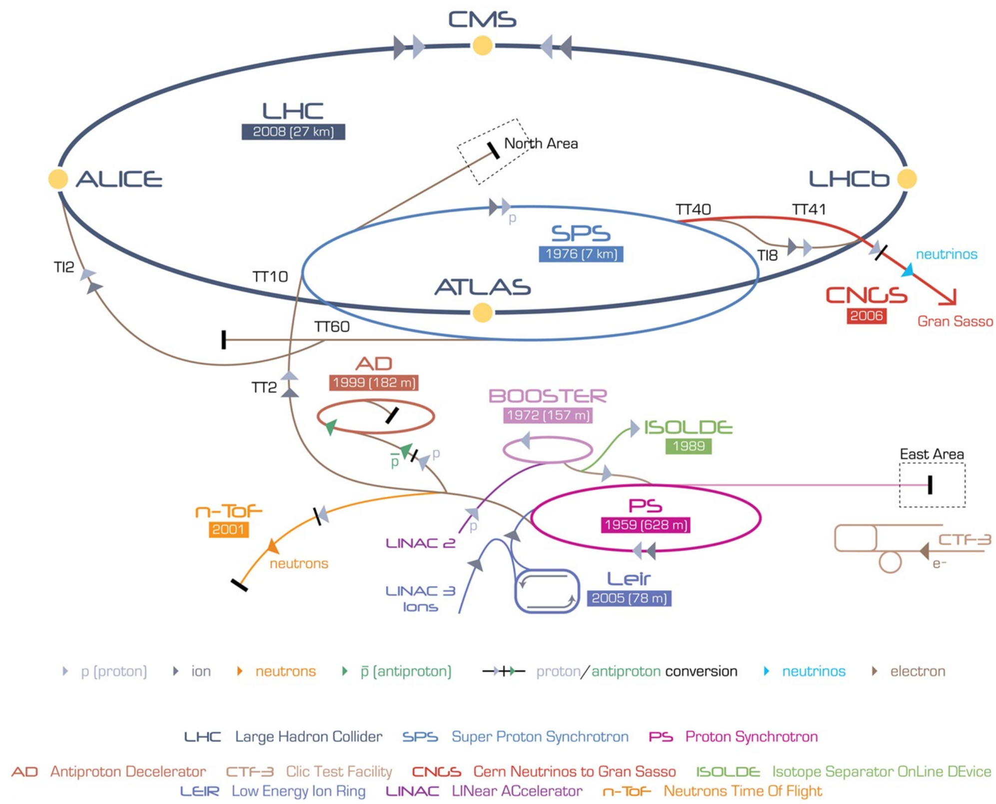

Figure 5.1. Scheme of the LHC injection system and a subset of the many experiments supported by these accelerators [82].

diverted in the collision points with quadrupole magnets. Each of the eight octants has a specific purpose with four collisions points where the experiments are located and four sites in which a determined function related to the LHC beam is perfomed:

1. ATLAS (A Toroidal LHC ApparatuS) experiment [83], interaction point with proton-proton, lead-proton and lead-lead collisions;
2. ALICE (A Large Ion Collider Experiment) experiment [84], interaction point with lead-proton and lead-lead collisions;
3. beam cleaning;
4. radio frequencies cavities for the acceleration of the LHC beams;
5. CMS (Compact Muon Solenoid) experiment [85], interaction point with proton-proton, lead-proton and lead-lead collisions;
6. beam dumping;
7. beam cleaning;
8. LHCb (LHC beauty) experiment [86], interaction point with proton-proton collisions;

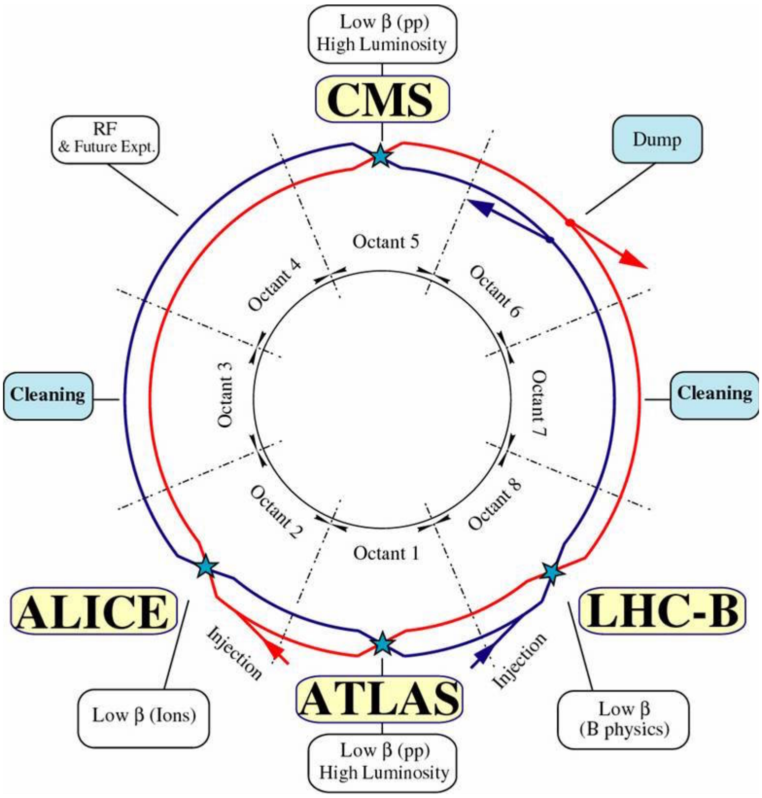

Figure 5.2. Schematic layout of LHC with the two beams running in opposite directions [80].

5.1.2 LHC Performance

At LHC, the collisions take place between the interaction of so-called 'proton-bunches', which reached a frequency of 20 MHz in 2010-2012 and the beginning of 2015, and of 40 MHz from 2015 until today. In order to collect the most amount of data and increase the rate of interesting physics interactions, reaching a very high frequency collisions is one of the main aims of LHC. In a particle collider the instantaneous luminosity $\mathscr{L}$ is the quantity that relates the events rate to the cross-section of a desired process:

$$\frac{dN_{events}}{dt} = \mathscr{L}\sigma. \tag{5.1}$$

Luminosity can be defined using a set of beam parameters:

$$\mathscr{L} = \frac{N_p^2 n_b f \gamma}{4\pi\epsilon\beta^*} F, \tag{5.2}$$

where N_p is the number of particles per bunch, n_b the number of bunches in a single beam, f the beam revolution frequency and γ the relativistic γ-factor. In the denominator ε is the normalized transverse beam emittance, which is a measure of the average spread in the position-momentum phase space of the beam, and β^* the beta function at the collision point, related to the spread of the bunch in the transverse plane to the beam direction. The numerator is related to the rate of interactions, while the denominator describes the intersection area of the two beam profiles. Finally the factor F is a geometrical correction that takes in account the crossing angle with which the beams are made to collide. In equation (5.2), the beams are assumed to run in circles and to have the same parameters.

For physics analyses, the interesting quantity that is actually often used is the total integrated luminosity L, obtained by integrating the delivered instantaneous luminosity $\mathscr{L}$ over the time periods in which the detector is able to record data with nominal detection conditions. In Figure 5.3 the integrated luminosity delivered by LHC and recorded by the ATLAS experiment are shown.

The high number of particles per package increases the number of interesting events, but also those of pile-up. This kind of events are generated by the superposition of interactions of particles from previous or subsequent bunch-crossing, said out-of-time, or by different interactions obtained in the same bunch-crossing, in-time. The interesting events are characterized by particles with high transferred momentum in the interaction, large diffusion angles and high transverse momentum and have to be distinguished from the so-called "minimum bias" events that generally are featured by the presence of high longitudinal and low transverse momentum particle jets. Typically the amount of pileup activity is expressed and described

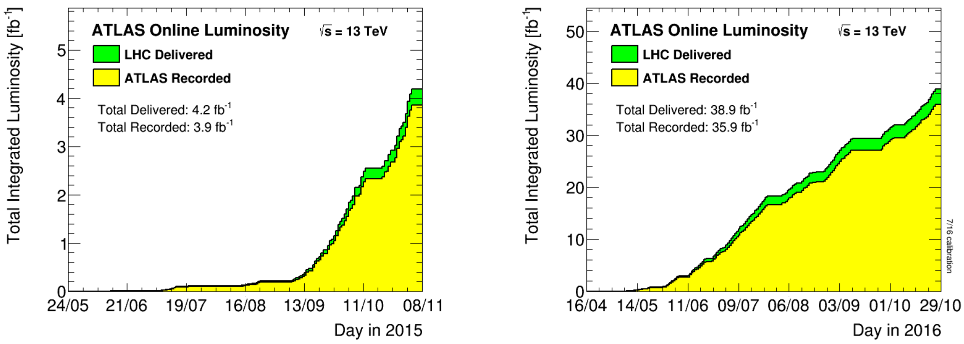

Figure 5.3. Cumulative luminosity versus time delivered to (green) and recorded by ATLAS (yellow) during stable beams for pp collisions at 13 TeV centre-of-mass energy in 2015 (left) and 2016 (right) [87].

from two variables: the reconstructed primary vertices N_{PV} for in-time interactions and the average number of interactions per bunch-crossing $\langle\mu\rangle$.

During Run-2, the LHC machine performance are progressively improved reaching in 2015 and 2016 the parameters listed in Table 5.1. In Figure 5.4 the maximum number of inelastic collisions per bunch crossing and the instantaneous luminosity peaks during stable beams are shown.

5.2 The ATLAS Detector

ATLAS is a multipurpose experiment which extends for a length equal to 44 meters while the diameter reaches 25 meters, for a total mass of about 7000 tons. The scheme of its structure is shown in Figure 5.5. It is designed to study an extensive physics landscape, which ranges from improving the accuracy of the measurements

Variable	2015	2016
$\sqrt{s}$ [TeV]	13	13
Integrated luminosity recorded [fb^{-1}]	3.86	35.98
Peak luminosity [$\mathrm{cm}^{-2}\mathrm{s}^{-1}$]	$5.02 \cdot 10^{33}$	$1.37 \cdot 10^{34}$
$\langle\mu\rangle$ (int/crossing)	13.6	24.9
Peak events / bunch-crossing	40.5	51.1
Bunch spacing ($1/f$) [ns]	25	25

Table 5.1. List of the main characteristics of the LHC accelerator reached during Run-2 in 2015 and 2016.

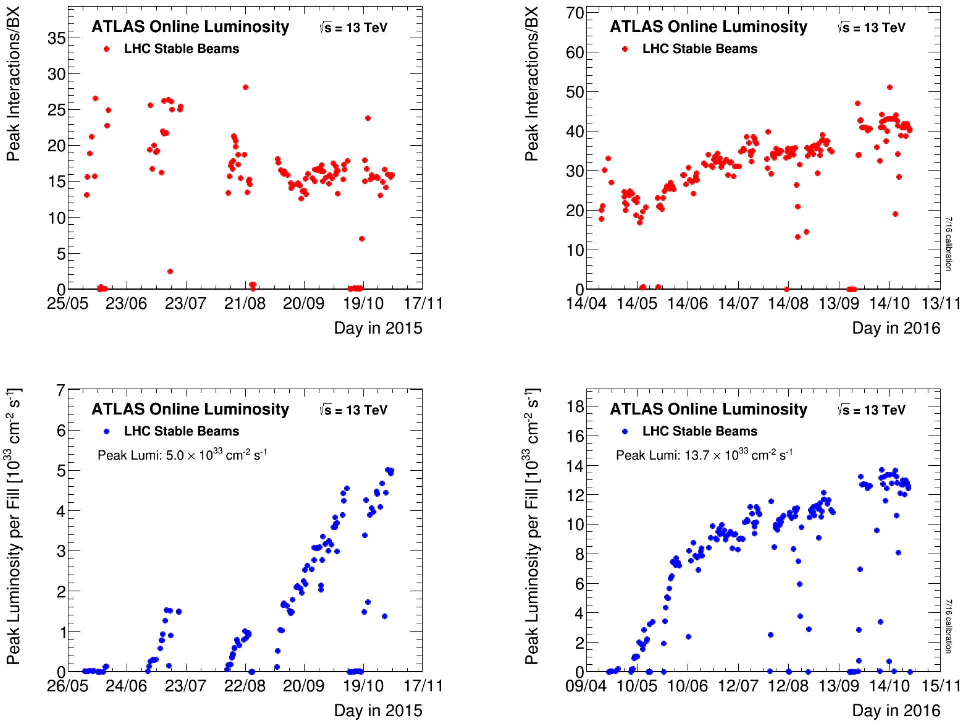

Figure 5.4. The peak instantaneous luminosity delivered to ATLAS (top) and the maximum number of inelastic collisions per beam crossing (bottom) during stable beams for pp collisions at 13 TeV centre-of-mass energy is shown for each LHC fill as a function of time in 2015 (left) and 2016 (right) [87].

of the SM parameters to the search for the Higgs boson discovered in 2012 and to the search of New Physics phenomena up to the TeV energy scale.

Among the peculiarities of the ATLAS experiment stand out:

- the fast electronics and detectors resistant to high doses of radiation and with a high granularity to avoid the overlap of more events, due to the high frequency collisions and the high number of particles produced in each interaction;
- the internal detector capable of tracking the trajectory of a large number of particles, that allows an optimal identification of τ leptons and jets coming from b-quarks and permits to recognize a large amount of vertices of interaction;

- the electromagnetic calorimeter with high performance in the identification of electromagnetic showers and in the measurement of their direction;
- the hadron calorimeter with an excellent hermeticity to perform an accurate measure of the energy of the jets and missing transverse momentum;
- the spectrometer able to achieve a high efficiency of identification and reconstruction of muons and their momentum.

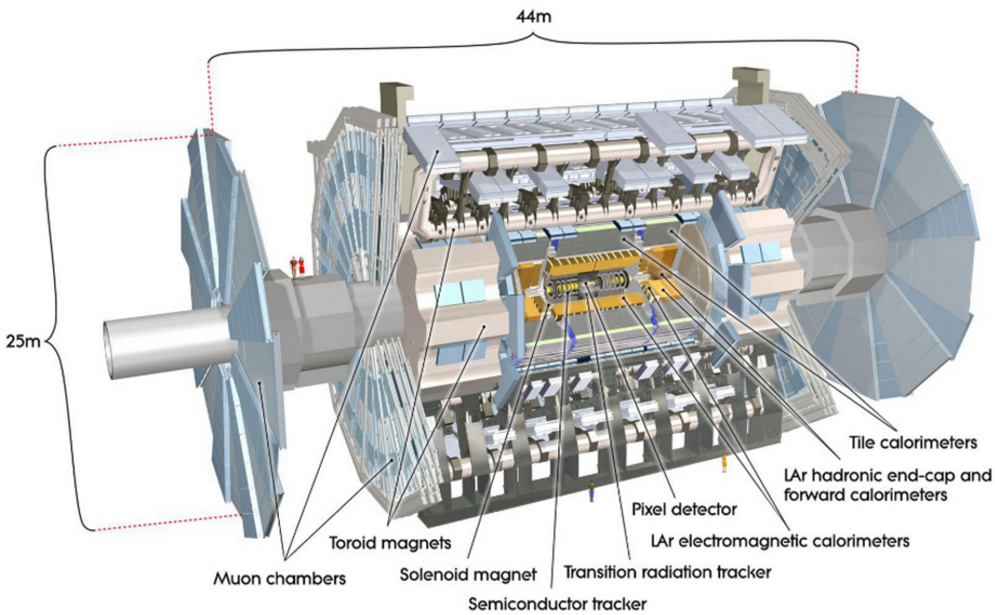

Figure 5.5. Scheme of the ATLAS detector [83].

5.2.1 Coordinate System

ATLAS is designed with cylindrical symmetry around the axis of the beam collision. The point of the nominal interaction of the beams defines the origin of the reference system: the positive x-semi-axis points towards the center of the ring from the interaction point, while the y-axis has a positive direction towards the sky. Therefore the (x, y) plane constituted is perpendicular to z-axis oriented along the direction of the beams (Figure 5.6).

In ATLAS the cylindrical coordinates ϕ, which denotes the azimuthal angle, and y which identifies the rapidity variable defined as

$$y = \frac{1}{2} \log \big(\frac{E + p_z}{E - p_z} \big), \tag{5.3}$$

are used in the case of massive particles. If the mass of the particles can be neglected the pseudo-rapidity η is commonly used. It is determined by:

$$\eta = -\log \big(\tan \frac{\theta}{2} \big), \tag{5.4}$$

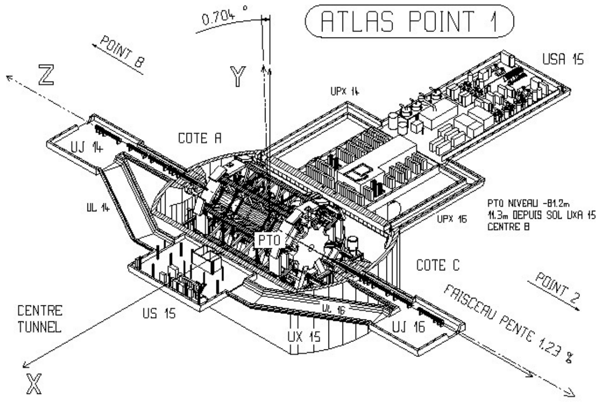

Figure 5.6. Scheme of the reference system of ATLAS.

where θ is the polar angle.

In a hadron collider the momentum along the z-axis of the initial system may not be known (given that collisions occur at parton level) and quantities that do not depend on the Lorentz boost along the longitudinal axis are needed. For this reason pseudo-rapidity is generally used to identify the various sections of the experimental apparatus: the central area of the detector ($|\eta| < X$, where X depends on the specific part of the detector) is called "barrel", while those external ($|\eta| > X$) are called "end-caps".
Since also the angle ϕ is invariant under Lorentz transformations, in order to indicate the distance between the particles, the variable ΔR is introduced and defined as:

$$\Delta R = \sqrt{\Delta\eta^2 + \Delta\phi^2}. \tag{5.5}$$

Other important quantities used in ATLAS are the transverse momentum p_{T} and the transverse energy E_{T} defined in the (x, y) plane (the only plan in which the laws of conservation of energy and momentum can be applied).

5.2.2 Magnets

The magnetic field is crucial for the momentum measurement of all the charged particles produced in the interaction. The ATLAS magnetic system [88] consists of three different types of superconducting magnets schematized in Figure 5.7.

Central Solenoid: it provides a magnetic field of about 2 T parallel to the beam for the internal tracking system. Its scope is to make possible the reconstruction of the transverse momenta of the charged particles from the primary vertex.

Barrel Toroid: it is a cylindrical symmetrical toroid designed to generate a magnetic field of 0.5 T in the central zone of the muon spectrometer, along the tangential direction of the circumference centered on the z-axis.

End-Caps Toroids: they are two smaller toroids designed to provide a 1.0 T field in the forward areas of the muon spectrometer.

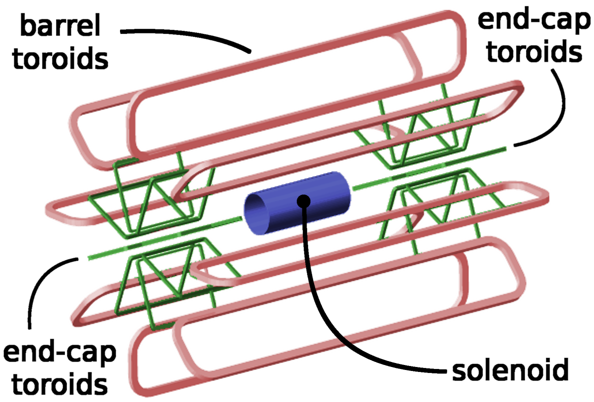

Figure 5.7. Schematic design of the ATLAS experiment magnets: in red are visible the toroidal magnets, in blue is shown the solenoid at the center of the detector and in green the toroidal magnets located in the end-caps.

5.2.3 Tracking System

The Inner Detector (ID) [89, 90] is the closest ATLAS apparatus element to the interaction point. It was designed for the tracking of the charged particles produced in the proton-proton collisions. It was built to be able to recognize the tracks of many charged particles (of the order of thousand) for each collision. For each track the momentum, direction, impact parameter[1] and charge of the particle are measured. It is also able to reconstruct the primary vertices and the possible secondary vertices from the decay of long-lived particle. The entire ID is immersed in the solenoidal magnetic field of 2 T.

The ID can be divided into three regions: a central area and two end-caps that cover the rest of the cylindrical cavity. It is composed by the combination of detectors able to achieve high-granularity tracking, in the region close to the collision point, and by detectors with a lower spatial resolution in the outer region. It consists of three independent and complementary parts illustrated in Figure 5.8 and schematized in Figure 5.9 and it is designed to reach an excellent resolution of the charged particles momentum:

$$\frac{\sigma_{p_\mathrm{T}}}{p_\mathrm{T}} = 0.05\%\, p_\mathrm{T} \oplus 1\% \tag{5.6}$$

where p_T has to be expressed in GeV.

Silicon Pixel Detector

The silicon detectors extends in the region with $|\eta| < 2.5$ and are arranged on concentric cylinder around the beams axis in the barrel at the radial distances of 50.5, 88.5 and 122.5 mm, and on disks perpendicular to the beams in the end-caps at the longitudinal distances of 49.5, 58.0 and 65.0 mm. All pixels are identical, segmented in the R-ϕ direction and z, with a native resolution of 10 μm in the R-ϕ

[1]The impact parameter is defined as the minimum distance between the track and the vertex.

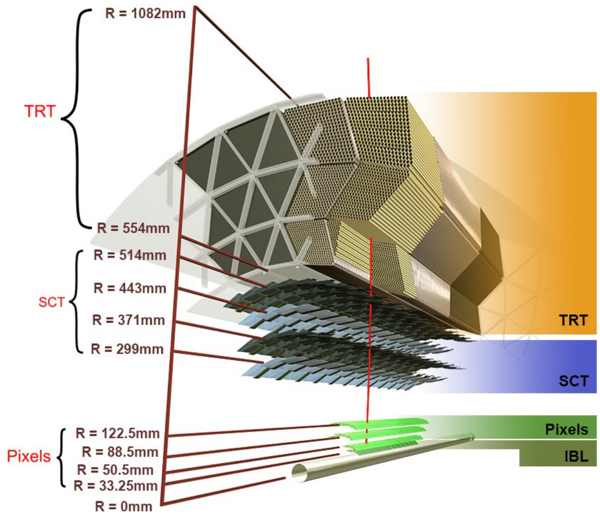

Figure 5.8. A 3D visualization of the structure of the barrel of the ID. The beam-pipe, the IBL, the three Pixel layers, the four cylindrical layers of the SCT and the 72 straw layers of the TRT are shown [92].

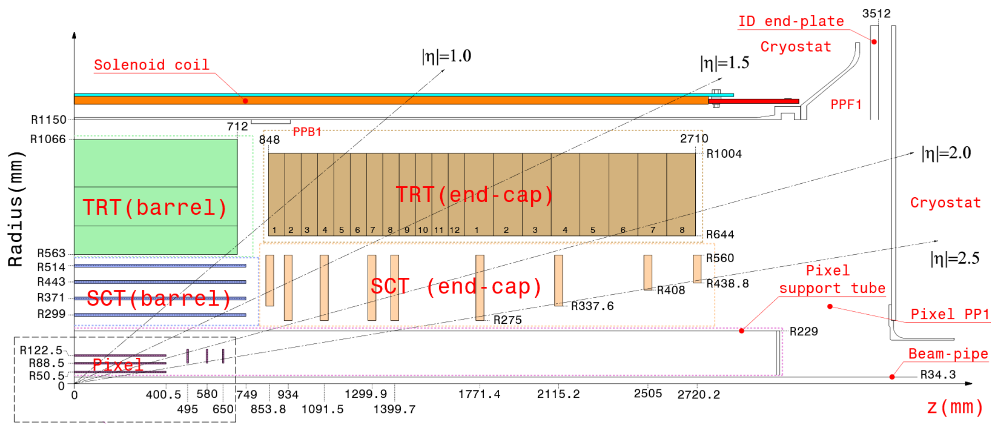

Figure 5.9. A quarter-sectional view of the ATLAS inner detector, showing each of the sub-detectors and the geometrical space that they cover [83].

direction and 115 μm in the $R(z)$ one of the barrel (end-caps). In total, in 2012 there were 1744 sensors each containing 46080 read-out pixels, with a total amount of about 80 million read-out channels. During the LHC long shutdown between Run-1 and Run-2, a new tracking layer, known as the Insertable B-Layer (IBL) [91], was added at a radius of 33.3 mm adding other 12 million pixel read-out channels to the system. High precision in measuring the position of the *hits* allows to reconstruct the tracks of a very short-lived particles, which is crucial for the identification of jets from b-quarks as well as the measurements of impact parameters of tracks.

Semi-Conductor Tracker (SCT)

The SCT detector is constituted of strips axially placed with respect to the beam-pipe and located in the barrel, in four concentric forms. The strips have a step 80 μm and only provide a one-dimensional measurement. Other identical silicon-strip sensors are glued back-to-back with the first creating between them an angle of 40 mrad and make possible the measurement of the second coordinate. A resulting spatial resolution of 17 μm for the first coordinate and of 580 μm for the second one is achieved. For what concern the end-caps region, the SCT detector is divided into 9 disks for each side. Each disk consists of modules mounted concentrically and is formed by silicon stripes pointing radially the beam-pipe. The entire SCT, including the barrel region and end-caps, is mapped to more than 6 million channels.

Transition Radiation Tracker (TRT)

A large number of *hits* (an average of about 30 per track) is produced in the TRT detector, which occupies the most external part of the ATLAS tracker system. It provides a crucial contribution in the reconstruction of the tracks and in the improvement of the momentum resolution in the region $|\eta| < 2.0$ with a radially extension between 56 and 107 cm from the beam-pipe. Furthermore, this detector allows the identification of the electrons in a large energy range, providing a complementary information to the calorimeter.
TRT is a detector consisting of tubes filled with a gaseous mixture of 70% Xe, 20% CO_2 e 10% CF_4. The charge generated by a crossing particle is collected by a thin wire of tungsten (anode), placed at the center of the tube and connected with the read-out electronics consisting of 351000 channels. TRT measures only the coordinate R-ϕ in the barrel and z-ϕ in the end-caps with a nominal resolution of 130 μm for tube.

5.2.4 Calorimeter System

The calorimeter system [93] is used to identify and measure the energy of photons, electrons, isolated hadrons, jets and the missing transverse momentum in the range of $|\eta| < 4.9$.

A view of the entire ATLAS calorimeter is shown in Figure 5.10. The system is composed of electromagnetic and hadronic calorimeters. Both types use a sampling technique where the active material layers alternate with layers of passive material. The passive part, also called absorber, causes an avalanche of particles (shower) while the active portion detects the resulting particles. Over the η-region matched to the inner detector, the fine granularity of the electromagnetic calorimeter is ideally suited for precision measurements of electrons and photons energy. The less dense granularity of the rest of the calorimeter is sufficient to satisfy the physics requirements for jet reconstruction and missing transverse momentum measurements. The calorimeter surrounding the internal ID, extends up to a radius of 4.25 m and along z up to 6.7 m from the collision point of the beams.

Another function performed by calorimeters is to limit the particle flow that can reach the muon spectrometer. The total depth of the electromagnetic calorimeter exceeds 22 radiation lengths $(X_0)^2$ in the barrel and 24 in the end-caps, while the hadron calorimeter has a depth of 9.7 interaction lengths $(\lambda)^3$ in the barrel and 10 in end-caps.

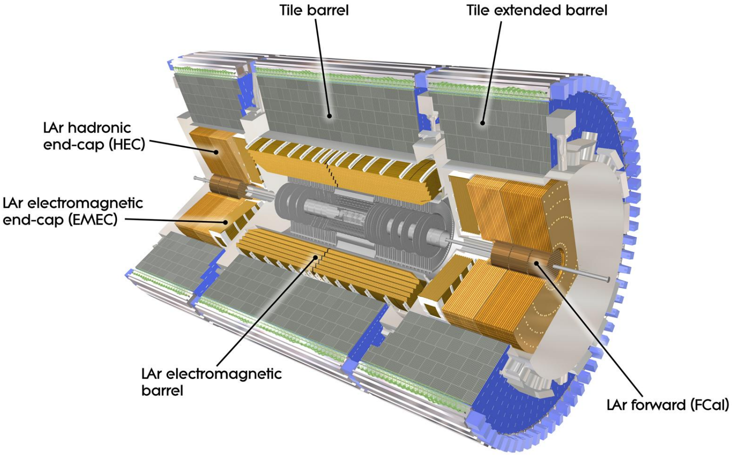

Figure 5.10. Schematic view of the ATLAS calorimeter system [83].

Electromagnetic Calorimeters

The electromagnetic (EM) calorimeter [94] is the subdetector responsible of the electromagnetic showers reconstruction. It is divided into two parts, one consisting of two half-barrel calorimeters in the region $|\eta| < 1.47$ defined as *ElectroMagnetic Barrel* (EMB) and the other consisting of two coaxial wheel calorimeters, one for each side of the forward areas, called *ElectroMagnetic End-Caps* (EMEC) covering the region $1.37 < |\eta| < 3.2$. In the region $|\eta| < 1.8$ an additional calorimeter layer finely segmented of Liquid Argon (LAr) and lead is located in the innest position to the beam-pipe.

As mentioned before, lead is used as absorbent material and LAr acts as active material. This technology was chosen because it demonstrated to be resistant to radiation preserving high performance. It needs very low temperature to work and for this reason the calorimeter is placed inside three independent cryostats to maintain the temperature of 89 K. The electrodes, which collect the charge yielded in the calorimeter, are parallel to the incident particles and folded forming an accordion geometry, as visible in Figure 5.11, to prevent that a particle impinges only on the active or passive material. This particular design avoids the presence of dead-zones allowing to achieve optimal tightness and minimizes the electronic dead-time.

[2] The radiation length is defined as $\frac{1}{X_0} = \frac{1}{A} 4\alpha N_A Z(Z+1) r_e \log 183 Z^{-1/3}$, where α is the electroweak coupling constant $\alpha = \frac{1}{137}$, $N_A = 6.022 \cdot 10^{23}/$ mole is Avogadro's number, Z and A are respectively the number and the atomic weight of the material crossed, $r_e = 2.818 \cdot 10^{-13}$ cm is the classical electron radius.

[3] $\lambda = \frac{a}{N_A \sigma_{\text{tot}}}$ where a is the atomic weight of the material crossed, N_A Avogadro's number, and σ_{tot} the total cross section.

The energy resolution of this calorimeter is:

$$\frac{\Delta E}{E} = \frac{10\%}{\sqrt{E}} \oplus 0.3\%, \tag{5.7}$$

$$\sigma_\eta = \frac{40\text{mrad}}{\sqrt{E}}, \tag{5.8}$$

where E must be used in GeV.

In the barrel region, which is the one also covered by the tracking system and dedicated to precision measurements, the EM calorimeter has three longitudinal layers:

1st sampling It is 4.3 X_0 thick and constituted of small strips cells of $\Delta\eta \times \Delta\phi = 0.0031 \times 0.098$. It is mainly useful to distinguish photons from $\pi_0 \to \gamma\gamma$, as well as electrons from $\pi^\pm$ and to improve the measurement in the η-direction.

2nd sampling It is segmented into square towers $\Delta\eta \times \Delta\phi = 0.025 \times 0.025$ and provides $\sim 16\ X_0$, so that most of the energy is deposited in this layer.

3rd sampling It is specifically dedicated to high energy electrons and photons ($E_\mathrm{T} > 50$ GeV) which produce wide clusters and thus the size of the towers in η was doubled with respect to the second layer without having loss in resolution.

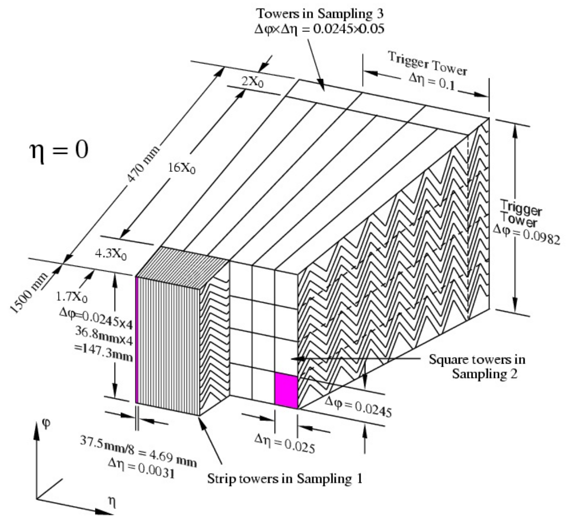

Figure 5.11. Structure of the EM calorimeter in the barrel [83].

EMEC consists of wheels form calorimeters that cover the η-range between 1.375 and 3.2. The general structure is the same of EMB, but it is geometrically rotated into the radial rather than axial direction as well as the accordion geometry orientation. The region between EMB and EMEC, within $1.375 < |\eta| < 1.52$, is referred as *crack* region and contains a large amount of material needed for ID. For this reason it is often source of energy loss reducing the total calorimeter performance and the analyses which require high precision photons and electrons use to remove this region from the analysis selection.

Hadronic Calorimeter

This calorimeter is designed to measure the energy and direction of the hadronic jets produced by the hadronization of quarks and gluons. The hadronic showers are wider and longer than the electromagnetic ones thus it is located just outside the EM calorimeter. The energy resolution for $|\eta| < 3.1$ is:

$$\frac{\Delta E}{E} = \frac{50\%}{\sqrt{E}} \oplus 3\%, \tag{5.9}$$

while in the regions $3.1 < |\eta| < 4.9$ is:

$$\frac{\Delta E}{E} = \frac{100\%}{\sqrt{E}} \oplus 10\%, \tag{5.10}$$

where the energy is always expressed in GeV.
The entire system is composed of three parts:

Hadronic Tile Calorimeter This section of the calorimeter [102] consists of a region in the barrel, which covers the region $|\eta| < 1.0$, and other two extensions covering $0.8 < |\eta| < 1.7$. It is constituted by steel, as absorber material, and by tiles of scintillating material as active medium. These latter are positioned in such a way that the shower impinges on them in order to improve e/h (the ratio of the calorimeter response to an electron and a hadron) which is about 1.3.

Hadronic LAr end-caps Calorimeter (HEC) It is still a sampling calorimeter using LAr as scintillating material and copper plates as absorbers since the amount of radiation in the end-caps is greater than in the barrel. It is constituted by two independent wheels of outer radius of 2.03 m and covers the η-range from 1.5 and 3.2. The first wheel consists of copper plates 25 mm thick, while the second uses plates of 50 mm.

LAr Forward Calorimeter (FCal) It is located in the end-caps cryostats with EMEC and HEC. FCal covers the outer regions of $3.1 < |\eta| < 4.9$, where the particles energy and density are extremely high. It is composed of three layers in which the one closest to the interaction point is a Cu/LAr calorimeter designed for electromagnetic calorimetry and the other two are hadronic W/LAr calorimeters. Finally behind FCal there is a passive layer of brass which absorbs the remaining hadron shower.

5.2.5 Muon Spectrometers

Muons pass through matter losing along the way only a small fraction of their initial energy. Their detection is thus relatively easy since the other particles generally cannot cross the calorimeters. In ATLAS, as in all the experiments designed to measure a broad spectrum of physics processes, the spectrometer is located in the outer part of the detector [96]. It consists of separate trigger and high-precision tracking chambers in the toroidal magnetic field. The muon chambers are arranged in the barrel ($|\eta| < 1.05$) in three cylindrical layers around the beam axis that often are called “stations”, while in the end-caps region ($1.05 < |\eta| < 2.7$) they are placed in three wheels. In Figures 5.12 and 5.13 the layout of the muon chambers in the x-y and R-z plane is illustrated. The overall momentum resolution of the muon spectrometer (MS) is $\sigma_{p_\mathrm{T}}/p_\mathrm{T} \sim$ 2-3% over most of the kinematic range, while for high-momentum muons of the order of $p_\mathrm{T} \sim$ TeV it reaches about 10%.

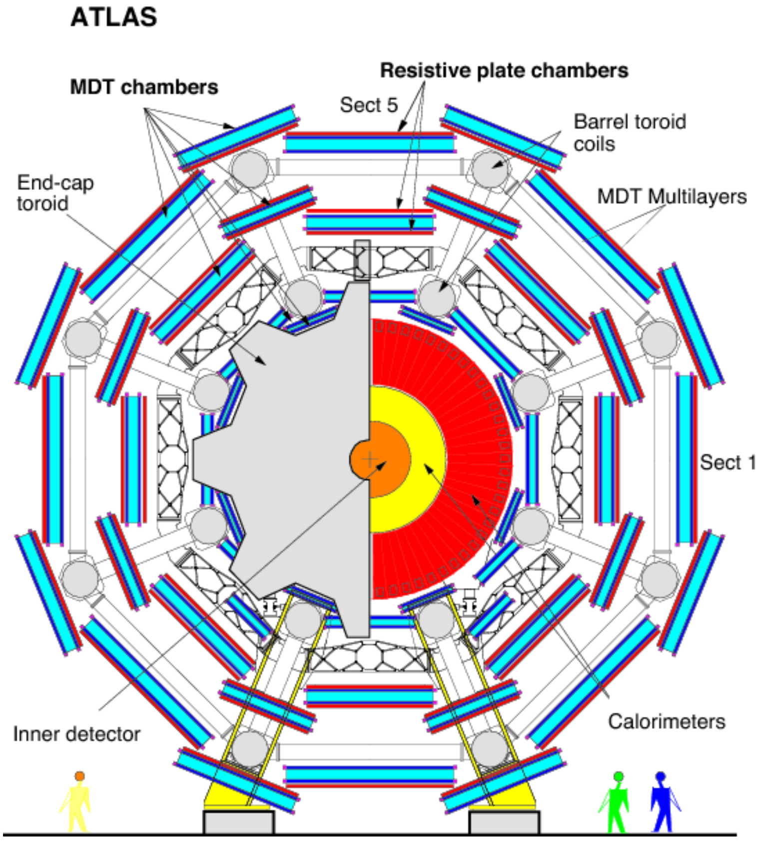

Figure 5.12. Schematic view of the transversal projection of the muon spectrometer [97].

The MS is composed of four sub-detectors that make use of different technologies:

Monitored drift-tube chambers (MDTs) They are high precision chambers located in the barrel and in the end-caps and consist of aluminum tubes of 30 mm in diameter and 400 μm of thickness. In the middle of each tube there is a Tungsten-Rhenium wire of 50μm in diameter and the tubes are filled with a mixture of Ar and CO_2 providing an excellent resistance against ageing. On both sides of each chamber, the tubes are installed in two multi-layers and each of them is formed by three (for the central and external stations) or four (for internal stations) layers of tubes. The resolution achieved by a single tube is about 80μ m, while the total chamber resolution is about 35μm.

Chatode Strip Chambers (CSCs) They consist of multi-wire proportional chambers with cathodes segmented into orthogonal strips. They replace the MDTs that worsen their performance at rates grater than 150 Hz/cm^2 covering the η-region from 2.0 to 2.7. The strips in the transverse plane and parallel to the

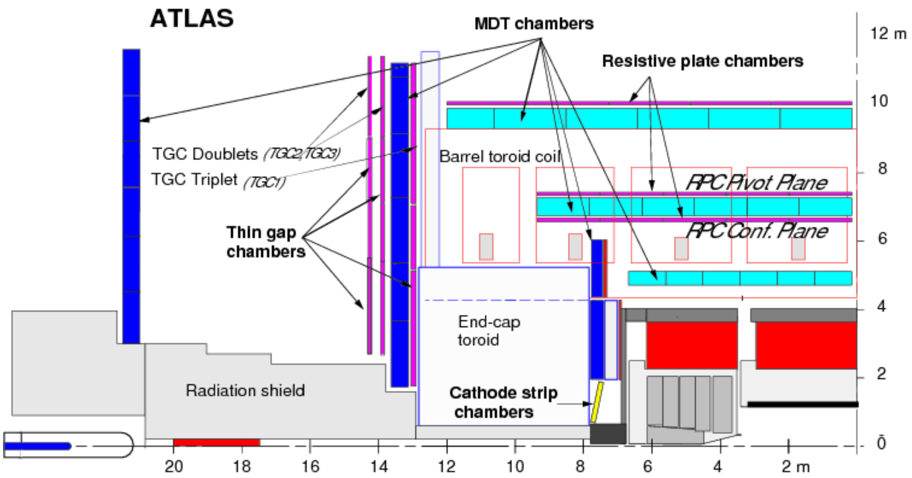

Figure 5.13. Schematic view of the longitudinal projection of the muon spectrometer [97].

wires measure the coordinate η and ϕ, respectively. The drift time achieved is less than 40 ns and the precision with which is measured is 7 ns. The spatial resolution reached by CSC is 40 μm in the radial direction and 5 mm in the second coordinate ϕ.

Resistive plate chambers (RPCs) These chambers are used for trigger measurements at Level 1 (see next Section) and provide a measure of the second coordinate in the barrel ($|\eta| < 1.05$). A RPC chamber is a detector in which the gas, a mixture of $C_2H_2F_4$ and a small fraction of resistive component SF_6, is contained between two bakelite plates, maintained at 2 mm distance. The primary ionization generated by the passage of a charged particle is amplified in the gas by the high electric field of about 4.5 kV/mm between the bakelite plates and identified as a signal induced by metallic reading strips placed in the outer sides of the bakelite plates. Each chamber is formed by two detector layers in which the strips are placed orthogonally to permit the reading of the two coordinates. Two layers of chambers are installed in the middle station, and provide the trigger for the low-p_T threshold. A third layer of RPC is installed on the outer chamber station, and it is used, together with the other planes, for the high-p_T thresholds.

Thin gap chambers (TGC) Every chamber of TGC is a proportional wire chamber filled with a mixture of CO_2 and n-pentane (n-C_5H_{12}). TGCs provide a measure of the second coordinate in the end-caps ($1.05 < |\eta| < 2.4$).

During the shutdown between Run-1 and Run-2, the last missing chambers included in the initial MS design were added in the transition region between the barrel and the end-caps ($1.0 < |\eta| < 1.4$). Four MDT chambers equipped with RPCs were also installed inside two elevator shafts to improve the efficiency in that region with respect to Run-1. Some of the new MDT chambers are composed of tubes with a smaller radius compared to the others used in the rest of MS, allowing to endure higher rates.

5.2.6 Trigger System

In Run-2 the LHC bunch-crossing rate reaches the impressive frequency of 40 MHz. The ATLAS detector cannot read out and record the events at this frequency, thus a trigger system implementation was needed to select only the most interesting events. The relevant variables to discriminate the events to store are the transverse momentum or transverse energy of objects in the event and their multiplicity. The rate of the events depends strongly by the choice of a threshold of the discriminating variables and in many cases the rate of events selected is too high to be stored. In order to mitigate, this problem, a prescale system is used. It consists in a technique of storage based on saving a random number of events that passes the threshold of a determined trigger. This is governed by the prescale factor f_{ps}, where $f_{ps} = 10$ means that only 1 of the 10 interesting events is recorded. Most of the analyses are interested to events characterized by objects in the final states with very high p_{T} and make use of unprescaled triggers hence simply using all the events selected by the trigger ($f_{ps} = 1$).

The ATLAS trigger and data-acquisition system for Run-2 [98] consists of two levels of online event selection (replacing the old Run-1 three-levels trigger) that permit to reduce the event rate through a hardware Level-1 (L1) and a software-based high-level trigger (HLT) schematized in Figure 5.14.

L1 determines the regions of interest (RoIs) in the calorimeters and MS using fast and dedicated hardwares, and reducing the rate from 40 MHz to $\sim$ 100 kHz with about 2.5 μs of total latency.

HLT born from the merging of the L2 and Event Filter levels used during Run-1. It consists of fast algorithms accessing to data from a RoI or using the full-event information. This trigger level reduce the rate of events of two order of magnitude reaching an average of $\sim$ 1 kHz with a latency of 0.2 μs

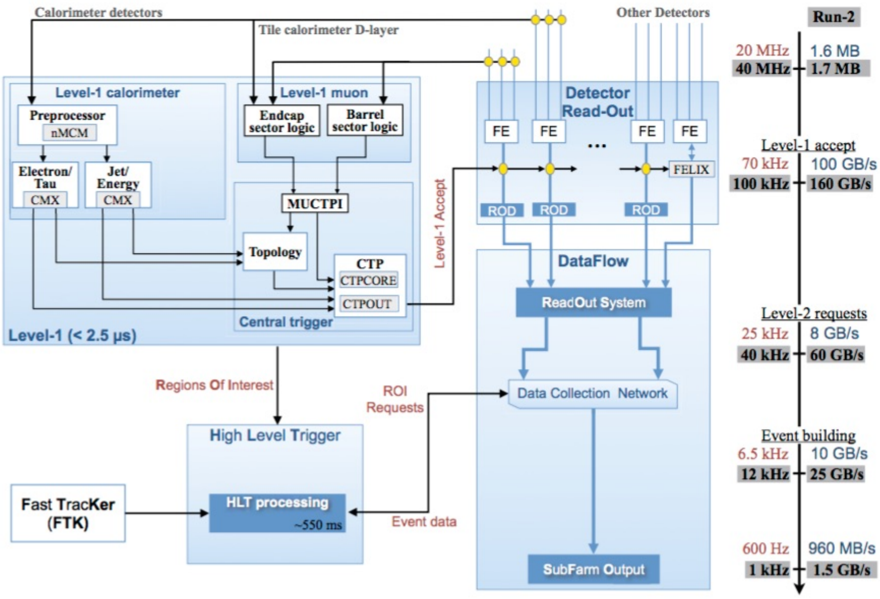

Figure 5.14. Schematic view of the ATLAS trigger system [99].

Chapter 6

Physics Objects

The identification and reconstruction of all the physics objects of a final state is the first crucial step of every analysis at ATLAS. In this chapter the identification and reconstruction techniques are outlined as well as the isolation requirements that are used in the mono-jet analysis. Two working points for each object are considered in this thesis: *baseline*, used for the preselection, overlap removal and veto, and *good* used in the analysis selection to define the different regions.

6.1 Electrons

In the mono-jet analysis only the electrons reconstructed in the central region ($|\eta| < 2.47$) of the ATLAS detector are considered. The reconstruction is based on the combination of the energy deposits (clusters) in the EM calorimeter and the tracks in ID.

The reconstructed electron candidates are distinguished from the background objects such as hadronic jets or converted photons, by algorithms of electron identification. These algorithms use variables related to the electron clusters and tracks including variables that combine both the information. In Run-2, with the installation of IBL, the discrimination between electrons and converted photons is further improved by measuring the number of *hits* in this innermost pixel layer.

The identification algorithm used during Run-2 is the likelihood-based (LH) method. It is a multivariate analysis (MVA) technique that evaluates several properties of the electron candidates to make a selection decision.

Three levels of identification are provided for the electrons and, in order of electron purity, they are labelled as *loose*, *medium* and *tight*. These working points are defined by a LH discriminant based on the same variables on which a different selection is applied so that the electrons selected by *tight* are all selected by *medium*, which in turn are all selected by *loose*.

The cut applied on the likelihood discriminator depends on the electron pseudorapidity η and transverse energy E_{T} and, since some shower shape distributions depend on the pileup, the cut on the LH discriminant is chosen also as a function of the number of primary vertices. For high energetic electrons that tend to deposit a smaller fraction of their energy in the early layers of the EM calorimeter and more in the later layers or in the hadronic calorimeter, the distributions of the variable on which the method is based can be different and change the efficiency of the cuts. The *loose* and *medium* operating points are robust against these effects while for the *tight* one, in order to maintain the same performance, the candidates with $E_{\mathrm{T}} > 125$ GeV are requested to fulfill the same criteria of *medium* with some additional rectangular cuts on electron discriminating variables (further details can be found in Ref. [100]).

The electron efficiency profiles as a function of E_{T}, η and the number of vertices are shown in the plots in Figure 6.1 in which $Z \to ee$ events are selected using 8.8 fb^{-1} of data recorded at $\sqrt{s} = 13$ TeV and MC simulations.

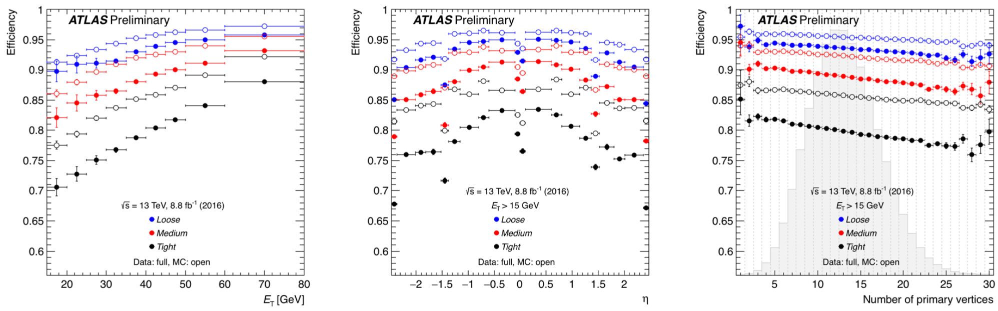

Figure 6.1. Electron identification efficiencies in $Z \to ee$ events as a function of the transverse energy, pseudo-rapidity and number of reconstructed primary vertices using 8.8 fb^{-1} of data recorded at $\sqrt{s} = 13$ TeV and MC simulations. The lower efficiency in data than in MC comes from known mismodelling on the TRT conditions and calorimeter shower shapes in the GEANT4 detector simulation taken into account in the likelihood discriminant. In the right plot, the distribution of the number of reconstructed primary vertices is overlaid in grey [101].

The uncertainties for the three different levels of identifications on the combined electron reconstruction and identification efficiencies as a function of the electron E_{T} and η are shown in Figure 6.2.

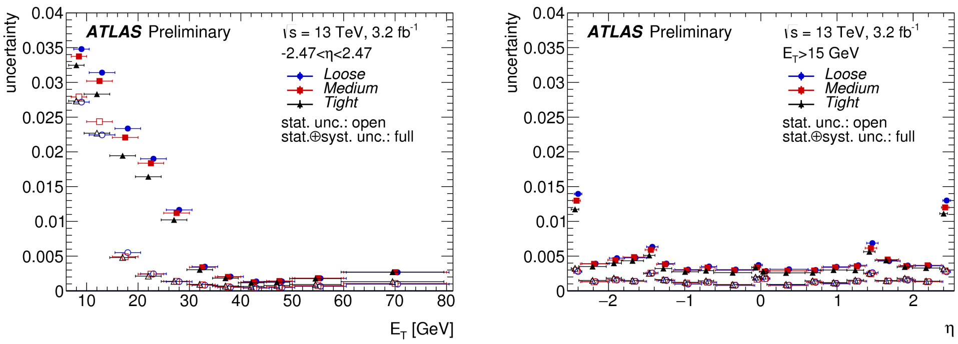

Figure 6.2. Absolute uncertainty on the combined electron reconstruction and identification efficiencies in $Z \to ee$ events as a function of the transverse energy (left) and the pseudo-rapidity (right) using 3.2 fb^{-1} of data recorded at $\sqrt{s} = 13$ TeV and MC simulations [100].

The isolation discriminants are based on calorimeter and/or track information evaluated in a cone ideally built around the electron candidate. They allow to discriminate prompt electrons (coming from heavy resonance decays, such as $W \to e\nu$,

$Z \to ee$) from non-isolated electron candidates such as electrons originating from converted photons or from heavy flavor hadron decays and light hadrons misidentified as electrons. The variable used to define the discriminant are:

- the calorimetric isolation energy, *topo*-E_{T}^{cone20}, defined as the sum of transverse energies of topological clusters [102] within a cone of $\Delta R = \sqrt{(\Delta\phi)^2 + (\Delta\eta)^2} = 0.2$ around the cluster of the electron candidate;

- the track isolation, $p_{\mathrm{T}}^{varcone20}$, defined as the sum of transverse momenta of all the tracks within a variable-cone size of $\Delta R = \min(0.2, 10\ \mathrm{GeV}/E_{\mathrm{T}})$ around the track associated to the electron candidate and originating from the reconstructed primary vertex of the hard collision.

topo-$E_{\mathrm{T}}^{cone20}/p_{\mathrm{T}}$ and $p_{\mathrm{T}}^{varcone20}/p_{\mathrm{T}}$ variables are used to define the different working points listed in Table 6.1.

	Efficiency		
Operating point	Calorimeter isolation	Track isolation	Total efficiency
LooseTrackOnly	-	99%	99%
Loose	99%	99%	$\sim 98\%$
Tight	96%	99%	$\sim 95\%$
Gradient	$0.1143\%E_{\mathrm{T}} + 92.14\%$	$0.1143\%E_{\mathrm{T}} + 92.14\%$	90/99 at 25/60 GeV
GradientLoose	$0.057\%E_{\mathrm{T}} + 95.57\%$	$0.057\%E_{\mathrm{T}} + 95.57\%$	95/99 at 25/60 GeV

Table 6.1. Electron isolation working points with the relative efficiencies information.

Baseline electrons are required to have the transverse energy $E_{\mathrm{T}} > 20$ GeV and $|\eta| < 2.47$. In addition, the baseline electrons satisfy the *loose* electron likelihood identification criteria. The baseline electron definition also requires that the calorimeter cluster fulfills certain quality criteria to prevent the presence of issues in the subdetectors. Finally the baseline electrons are required to pass the overlap removal selection described in Section 6.5.

Good electrons are a subset of baseline electrons required to fulfill the *tight* likelihood criteria. The impact parameter variables d_0/σ_{d_0} and $|z_0|\sin\theta$[1] are required to be smaller than 5 mm and 0.5 mm, respectively. In order to avoid a drop in the identification efficiencies for high E_{T} values, electrons with $E_{\mathrm{T}} > 300$ GeV are only required to pass the *medium* criteria of the likelihood.

6.2 Photons

The photon information are not included to obtain the first mono-jet results of Run-2, but their use in the veto and in the definition of a new control region is discussed in Chapter 9.

Similarly to the electron case, the photon reconstruction is based on the EM calorimeter energy deposits, requiring small or no energy deposit in the hadronic

[1] d_0 and z_0 are the transverse and longitudinal impact parameters. d_0 is the distance of the closest approach of the track to the measured beam-line, while z_0 is the distance along the beam-line between the point where d_0 is measured and the beam-spot position. θ is the polar angle of the track. σ_{d_0} indicates the standard deviation of d_0.

calorimeter [103]. If the ECAL cluster has not associated any track, it is considered as an "unconverted photon", while if the cluster is matched to a pair of oppositely-charged tracks, collinear to the production vertex and compatible with electrons in TRT, the cluster is considered as a "converted photon". The track-pairs reconstruction becomes inefficient at large conversion radius, thus also a cluster matched to one track can be considered as converted photon if no *hits* in the innermost layer of the pixel detector are measured to distinguish it from the electron candidates.

The isolation requirement and the information based on the properties of the shape and the electromagnetic showers help to discriminate prompt photons from background photons. These latter are usually poor isolated because surrounded by hadronic activity and the transverse energy flow in a cone with angular distance ΔR around the direction of the photon candidate can be used to suppress this kind of events.

The transverse energy flow can be evaluated through *topo*-E_{T}^{coneX}, already defined for the electrons, and p_{T}^{coneX} consisting in the sum of the transverse momenta of the tracks (with $p_{\mathrm{T}} > 1$ GeV and coming from the primary vertex) in a cone with $\Delta R = X/100$ excluding the tracks associated to photon conversions. The several working points with the relative cuts defined in ATLAS are summarized in Table 6.2.

Working point	Calo isolation	Track isolation
FixedCutTightCaloOnly	*topo*-$E_{\mathrm{T}}^{cone40} < 0.022\, p_{\mathrm{T}} + 2.45$ [GeV]	-
FixedCutTight	*topo*-$E_{\mathrm{T}}^{cone40} < 0.022\, p_{\mathrm{T}} + 2.45$ [GeV]	$p_{\mathrm{T}}^{cone20}/p_{\mathrm{T}} < 0.05$
FixedCutLoose	*topo*-$E_{\mathrm{T}}^{cone20} < 0.065\, p_{\mathrm{T}}$	$p_{\mathrm{T}}^{cone20}/p_{\mathrm{T}} < 0.05$

Table 6.2. Photon isolation working points and the relative requirements applied.

Since the hadrons reconstructed as photons leak a portion of energy in HCAL and produce a broader transverse energy deposit in ECAL, the photon identification discriminants are based on the shower shape in ECAL and on the fraction of energy deposited in HCAL. There are two identification levels: *loose* exploits the information only in HCAL and in ECAL second sampling layer, providing a highly efficient selection; *tight* exploits the full granularity of ECAL, including the fine segmentation of the first sampling layer, and applies tighter requirements also on the discriminant variables used by *loose*. In both cases, the identification discriminants are tuned separately for unconverted and converted photons, in several pseudo-rapidity regions.

Photon reconstruction and identification are performed in the η-range where the ECAL depth is enough to contain the whole photon shower and the segmentation of the ECAL strips is fine enough to allow the rejection of neutral hadrons: $|\eta| < 1.37$ in the ECAL barrel and $1.52 < |\eta| < 2.37$ in the ECAL end-caps. In Figure 6.3 the photon tight identification efficiency is shown in $Z \to \ell\ell\gamma$ events using 11.6 fb^{-1} of data recorded at $\sqrt{s} = 13$ TeV in the cases of converted and unconverted photons.

Baseline photon are required to have the transverse energy $E_{\mathrm{T}} > 20$ GeV, $|\eta| < 2.37$, the *tight* identification criteria. As in the baseline electron definition, they also requires that any issue in the calorimeter is present and they have to pass the overlap removal selection.

Good photons have to pass the baseline photon criteria with some additional

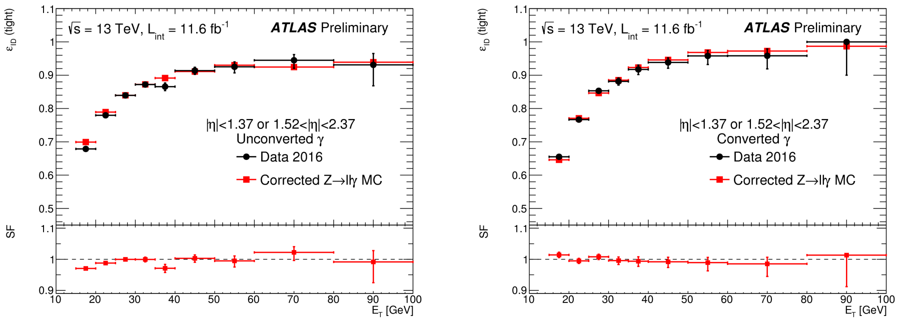

Figure 6.3. Photon *tight* identification efficiency of unconverted and converted photons to the $Z \to \ell\ell\gamma$ events as a function of the transverse energy using 11.6 fb^{-1} of data recorded at $\sqrt{s} = 13$ TeV and MC simulations [104].

shower shape requirements and the *FixedCutTight* isolation is also applied.

6.3 Muons

In ATLAS the muon reconstruction [105] is based on the information provided by ID, MS, and calorimeter sub-detectors. Four different muon types are defined:

Combined (CB) muons, by using the combination of the MS track with an ID track (they consist in the majority of the muon candidates and have the best purity and momentum resolution);

Segment-Tagged (ST) muons, reconstructed by the combination of tracks in ID and the track segments in the MDT or CSC chambers;

Extrapolated (ME) muons, if the reconstruction occurs only in MS with a loose requirement on compatibility with originating from the interaction point;

Calorimeter-Tagged (CT) muons are matched using a combination of the tracks information in ID and the energy deposits in the calorimeter.

Muon identification is performed to suppress the contribution of fake muons coming from pion and kaon decays and to select muon candidates with robust momentum measurement. They are based on a set of quality requirements that exploit specific features of each of the muon types. The identification working points defined in ATLAS are *loose*, *medium*, *tight*, and *high-*p_{T}.

In the mono-jet analysis only *medium* muons are handled. This selection minimizes the systematic uncertainties associated with muon reconstruction and calibration. Only CB and ME tracks are used and a set of requirements on the number of *hits* in the different MDT and CSC layers and a selection on the compatibility between ID and MS momentum measurements are applied. In Figure 6.4 the muon *medium* identification efficiency is shown as a function of p_{T} and η obtained by $Z \to \mu\mu$ and $J/\Psi \to \mu\mu$ events using 3.2 fb^{-1} at $\sqrt{s} = 13$ TeV.

The several contributions to the total uncertainty in the efficiency scale factor (SF), defined as the ratio between the efficiency evaluated from data events and from

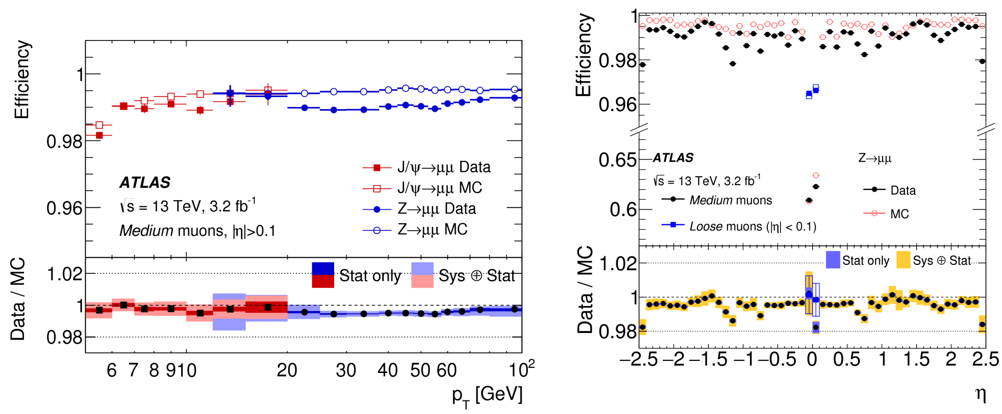

Figure 6.4. *Medium* identification efficiency of muons coming from $Z \to \mu\mu$ and $J/\Psi \to \mu\mu$ events using 3.2 fb^{-1} at $\sqrt{s} = 13$ TeV and from MC simulations as a function of the muon p_{T} and η. On the right, the efficiency of the *loose* selection (squares) in the region $|\eta| < 0.1$ that is the region where the two identification criteria differ significantly is also shown [105].

MC simulations is shown in Figure 6.5 as a function of p_{T} and η. The combined uncertainty is also plotted as the sum in quadrature of the individual contributions. Since no significant dependence of the SFs with p_{T} is observed in the momentum range considered in the $Z \to \mu\mu$ events, an upper limit on the SF variation for high muon momenta is extracted from simulation, leading to an additional uncertainty of 2-3% per TeV for muons with $p_{\mathrm{T}} > 200$ GeV.

In this thesis muons coming from cosmic showers are additionally removed applying a cut on the impact parameters $z_0 < 1$ and $d_0 < 0.2$.

The isolation working points defined for the muons are the same of the electrons listed in Table 6.1 obtained requiring the same electron efficiencies but based on the track and calo-based variables $p_{\mathrm{T}}^{varcone30}/p_{\mathrm{T}}$ and *topo*-$E_{\mathrm{T}}^{cone20}/p_{\mathrm{T}}$. In the analysis the isolation requirements are not applied to muons because the impact of these in all the regions defined is negligible.

Baseline muons are defined as muons with $p_{\mathrm{T}} > 10$ GeV and $|\eta| < 2.5$ which pass the overlap removal selection and are used in the $E_{\mathrm{T}}^{\mathrm{miss}}$ calculation (see Section 6.6).

Good muons have the same definition of the baseline ones but a cut on the impact parameters variables requiring $d_0/\sigma_{d0} < 3$ and $|z_0 sin\theta| < 0.5$ mm is also applied.

6.4 Jets

Hadronic jets are one of the main components of the mono-jet final states. They are cones of hadrons produced by the fragmentation of the quarks and gluons. This kind of objects deposits energy in the calorimeters and in particular in HCAL and are generally characterized by a high multiplicity of tracks in ID.

In the mono-jet analysis the jets are reconstructed using the anti-k_t clustering

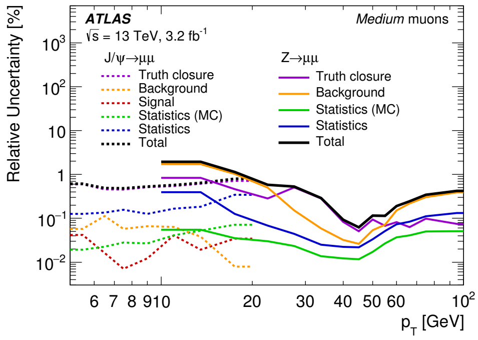

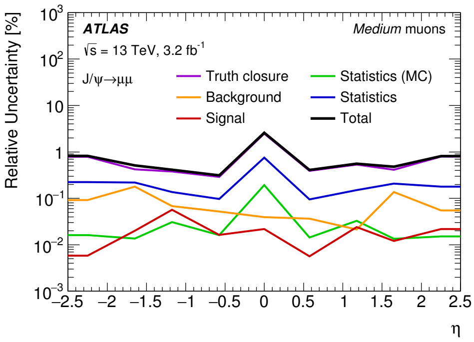

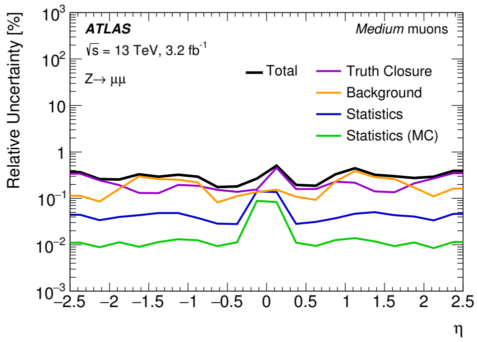

Figure 6.5. Total uncertainty in the efficiency scale factor for *Medium* muons as a function of p_{T} (top) and η (bottom) extracted from $J/\Psi \to \mu\mu$ and $Z \to \mu\mu$ events using 3.2 fb^{-1} at $\sqrt{s} = 13$ TeV and MC simulations. For more information about the several contributions which compose the total uncertainty, see Ref. [105].

algorithm, with topological calorimeter clusters as jet constituents [106], with a distance parameter $R = 0.4$. This algorithm is based on the definition of the distance d_{ij} between the constituents i and j and of the distance between the i-th constituent and the beam d_{iB}:

$$d_{ij} = \min(k_{ti}^{2p}, k_{tj}^{2p}) \frac{\Delta_{ij}^2}{R^2}\,, \tag{6.1}$$

$$d_{iB} = k_{ti}^{2p}\,, \tag{6.2}$$

where $\Delta_{ij}^2 = (y_i - y_j)^2 + (\phi_i - \phi_j)^2$ and k_{ti}, y_i and ϕ_i are respectively the transverse momentum, rapidity and azimuthal angle of the i-th particle. The p parameter governs the relative power of the energy versus the geometrical scales (Δ_{ij}). In the anti-k_t algorithm it is set to $p = -1$.

The clustering starts by identifying the smallest distances: if the smallest one is d_{ij}, the i-th and j-th entities are recombined (the four-momenta are summed), while if it is d_{iB} the entity i is considered as a jet and removed from the list of entities. The clustering in the anti-k_t algorithm proceeds from the hardest to the softest constituents and the results are conical hard jets. If two jets are reconstructed close to each other, the harder one is conical while the softer one misses the overlap region. In general the most realistic situation is $k_{t1} \sim k_{t2}$ and in this case both the cones are clipped, with the boundary b between them defined by $\Delta_{1b}/k_{t1} = \Delta_{2b}/k_{t2}$. The algorithm, as well as the k_t one defined setting $p = 1$ which instead sums before the softest constituents and then the harder ones, is infrared and collinear robust. It means that if a very soft parton is added or a parton splits into collinear pair of constituents, the final set of jets reconstructed does not change.

The measured jet transverse momentum is then corrected for detector effects, weighting the energy deposits arising from electromagnetic and hadronic showers differently, to cure the non-compensation of the calorimeters and finally additional corrections due to pileup are also applied.

The jet-vertex tagging technique, JVT, is further adopted for the pileup jets suppression [107]. This technique uses a multivariate combination of two variables:

- Jet Vertex Fraction (JVF), defined as the sum of the scalar transverse momenta of the tracks which are associated with the jet and originate from the hard-scatter vertex, divided by the scalar sum of the p_{T} of all the tracks, corrected with a factor that takes into account the average scalar sum of pileup tracks associated with a jet;

- $R_{p_{\mathrm{T}}}$, defined as the scalar sum of the p_{T} of the tracks that are associated with a jet and originate from the hard-scatter vertex divided by the fully calibrated jet p_{T}, which includes pileup subtraction.

The combination of these variables provides a strong discrimination against the pileup as can be observed in Figure 6.6 where the two-dimensional plot of (JVF, $R_{p_{\mathrm{T}}}$) is shown for jets coming from the hard scattering processes (left) and from pileup events (right). Pileup jets are expected to populate the region relative to low values of $R_{p_{\mathrm{T}}}$ and JVF, while hard-scatter jets are expected to have large values of $R_{p_{\mathrm{T}}}$ and JVF. On the left in Figure 6.7, the jet selection efficiency of a JVT > 0.59 cut on a jet balanced against a Z boson decaying in two muons as a function of the jet p_{T} is shown. An overall efficiency $> 90\%$ is observed from the plots based on 13.3 fb^{-1} of data collected at $\sqrt{s} = 13$ TeV. On the right, the average number of jets with $p_{\mathrm{T}} > 20$ GeV as a function of the number of interactions per bunch crossing is plotted before and after applying the JVT cut proving the robustness of the selection with the increase of the pileup.

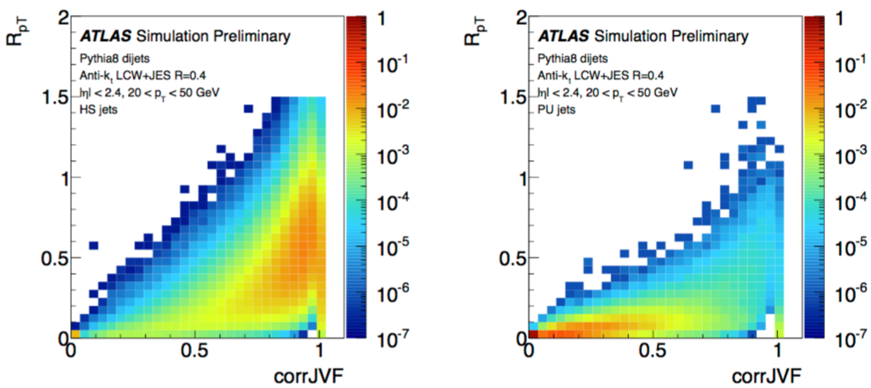

Figure 6.6. Correlation plot of JVF versus $R_{p_{\mathrm{T}}}$ for hard scatter (left) and pileup (right) jets [107].

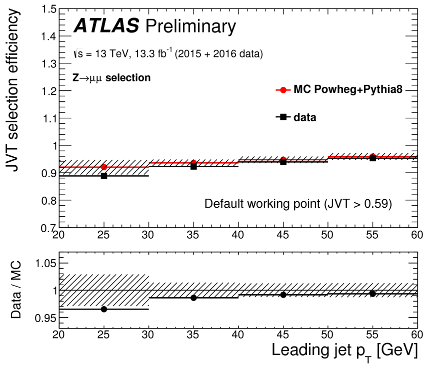

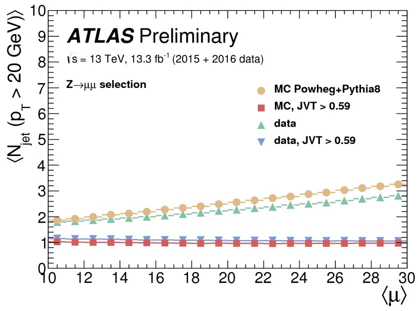

Figure 6.7. On the left: jet selection efficiency of a JVT > 0.59 cut as a function of the leading jet p_{T}. On the right: the average number of jets with $p_{\mathrm{T}} > 20$ GeV as a function of the number of interactions per bunch crossing. The events come from a selection of $Z \to \mu\mu$ events plus jets using 13.3 fb^{-1} of data collected at $\sqrt{s} = 13$ TeV. [108].

The hadronic showers contain a large variety of particles of which a large fraction is not observable in the detector such as the neutrinos coming from decays contained in the jets themselves. For this reason and for other effects like the calorimeter non-compensation already mentioned before, the presence of dead material in the detector or simply the particle reconstruction inefficiency, a loss of a significant fraction of the energy associated to the shower is expected. This means that the reconstructed jet momentum could not reproduce perfectly the true process and for this purpose a jet calibration is needed after the reconstruction. It is typically referred to the Jet Energy Scale (JES) and consists in several steps designed to account for different effects in part mentioned before and analyzed in detail in Ref. [109]. JES calibration provides the method used to correct jets to the hadronic scale by considering the mean of the jet response distribution (E_{reco}/E_{truth}) in bins of p_{T} and η. The corrections applied take into account effects given by the identification of the direction that points to the hard-scatter vertex, the pileup and the differences between the observed events and MC simulations. In Figure 6.8 the main contributions to the total jet energy scale uncertainties are plotted as a function of the jet p_{T} and η for jets in the central region of the detector. The total uncertainty varies from about 6% for soft jets with $p_{\mathrm{T}} \sim 20$ GeV, decreasing to 1% for jets with $p_{\mathrm{T}} = 200 - 1800$ GeV and increasing up to 3% for jets of higher p_{T}.

While the mean of the E_{reco}/E_{truth} distribution is cured by the JES corrections, the width quantifies the residual spread. The width of the Gaussian jet response distribution is known as the Jet Energy Resolution (JER). Deviations in jet response can originate from different factors such as the stochastic nature of hadronic showers, electronic noise of the calorimeter and pileup effects which not always can be reduced. The stochastic term is proportional to the inverse square root of energy while the noise term is proportional to the inverse of energy. Therefore, JER becomes less important with the increasing of the jet energy and typically JER as a function of p_{T} is measured in-situ in order to determine which portion of the resolution is irreducible and coming from physics processes, and which is given by detector and limitations of the reconstruction procedure. The total uncertainty on the jet energy

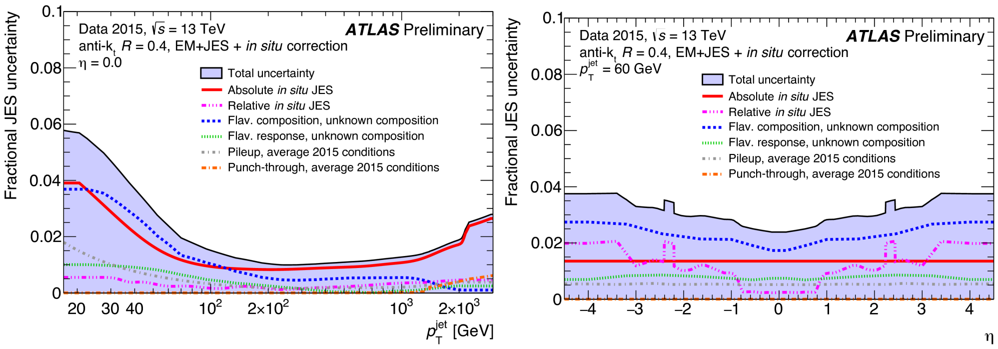

Figure 6.8. Jet energy scale uncertainties estimated for 2015 data as a function of jet $p_{\rm T}$ for central jets with $\eta = 0$ (right) and as a function of the pseudo-rapidity for jets with $p_{\rm T} = 60$ GeV [110].

resolution is shown in Figure 6.9 for jets in the central region of the detector as a function of the jet $p_{\rm T}$.

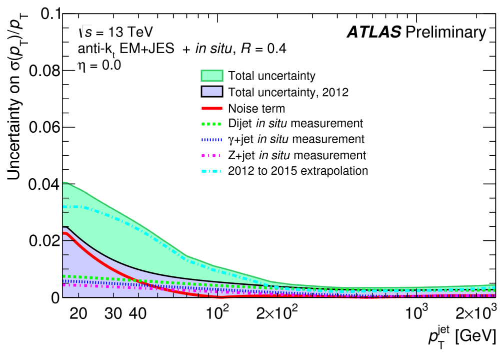

Figure 6.9. Jet energy resolution uncertainties estimated for 2015 data as a function of jet $p_{\rm T}$ for central jets with $\eta = 0$. Uncertainties are shown under the assumption of no knowledge of flavor. More information in Ref. [109].

The main backgrounds for jets, usually identified as *fake jets*, can be due to calorimeter noise or to collision events called non-collision backgrounds (NCB). These latter basically consist of beam-induced-background (BIB) due to proton losses upstream of the interaction point that induce secondary cascades leading to muons, or to cosmic-ray showers produced in the atmosphere which overlap with collision events. This kind of background in the mono-jet analysis will be addressed in the next chapter.

The jet selection criteria are based on variables that use:

- the characteristic ionization signal shape in the LAr calorimeters to suppress the coherent and sporadic noise in the calorimeter;

- the energy deposits information like the electromagnetic (f_{EM}) of hadronic (f_{HCAL}) fractions defined as the ratio of the energy deposited in the EM or hadronic calorimeter to the total energy of the jet and the maximum energy fraction in any single calorimeter layer, f_{max} (in fact BIB and calorimeter noise tend to be more localized longitudinally in the calorimeters than jets coming from *pp* collisions);

- the tracks information and in particular the charged fraction f_{ch}, defined as the ratio of the scalar sum of the p_{T} of the tracks coming from the primary vertex and the jet p_{T}.

The combination of these variables defines two jet cleaning criteria: *loose* and *tight*. The *loose* selection is designed to provide an efficiency $> 99.5\%$ for $p_{\mathrm{T}} > 20$ GeV, while the *tight* selection, that includes the *loose* one adding a harder cut on the f_{ch}/f_{max} variable moved from 0.01 to 0.1, is designed to further reject the NCB achieving an efficiency greater than 95% for $p_{\mathrm{T}} > 20$ GeV, that reaches about 99.5% for jets with $p_{\mathrm{T}} > 100$ GeV.

Baseline jets are selected for offline analysis. They have $|\eta| < 2.8$, $p_{\mathrm{T}} > 20$ GeV and pass the *loose* jet cleaning level and fulfill the following criteria:

- $20 < p_{\mathrm{T}} < 50$ GeV, $|\eta| < 2.4$ and pass a cut on the JVT;
- $20 < p_{\mathrm{T}} < 50$ GeV, $|\eta| > 2.4$;
- $p_{\mathrm{T}} > 50$ GeV.

Further rejection of NCB due to losses on the LHC collimators or beam-gas interactions are suppressed by imposing the *tight* jet cleaning criterion on the leading jet.

Good jets are defined as the baseline jets with increased p_{T} threshold of 30 GeV.

b-tagging

In the mono-jet analysis the *b*-tagging information is not used but, as will be shown in Chapter 9, it could be a very useful tool to reduce the background of the analysis coming from $t\bar{t}$ and single-top production processes.

Exploiting the long life of the *b*-quark (~ 1.5 ps, $c\tau \sim 450$ μm) the ATLAS strategy to identify the jet produced from these particles, called *b*-jets, is based on a Boosted Decisions Tree (BDT) discriminant built taking as inputs the outputs of three basic *b*-tagging algorithms [112, 113] that use different discriminant ingredients:

- the inclusive secondary vertex, in which the addition of IBL brought a crucial improvement in the reconstruction with respect to Run-1;
- the impact parameters, since the the *b*-hadron topology is characterized by at least one vertex displaced;
- the multi-vertex reconstruction, exploiting the topological structure of *b*- and *c*-hadron decays inside the jet.

The p_{T} and η distributions of the jets are also included in the BDT training to take into account the correlations with the other input variables. The training of the multivariate classifier MVc10 used in the mono-jet studies is performed on jets from $t\bar{t}$ events considering the *b*-jets as signal, and a mixture composed of 7% of *c*- and 93% of *light*-flavour jets as background.

The MV2c10 discriminant distribution is shown in Figure 6.10 and the choice of the cut value defines the different working points with different efficiencies and background rejection powers, which are listed in Table 6.3. The working point with an efficiency of 60% is used to tag the b-jets in the analysis selection.

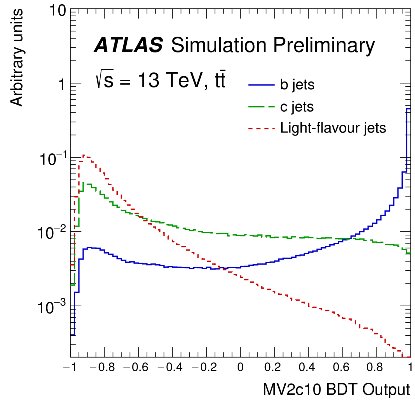

Figure 6.10. MV2c10 BDT output distribution for b- (solid blue), c- (dashed green) and *light*-flavour (dotted red) jets [112].

BDT cut value	b-jet efficiency [%]	c-jet rejection	light-jet rejection	τ rejection
0.9349	60	34	1538	184
0.8244	70	12	381	55
0.6459	77	6	134	22
0.1758	85	3.1	33	8.2

Table 6.3. Working points for the MV2c10 b-tagging algorithm, including efficiency and rejections rates for jets with $p_{\mathrm{T}} > 20$ GeV [112].

6.5 Overlap Removal

In order to solve ambiguities between leptons, photons and jets reconstructed event by event, an overlap removal is applied to the objects that satisfy the baseline definitions mentioned in the previous sections. The following removal criteria are applied:

- remove jet in case any pair of jet and electron satisfies $\Delta R(j, e) < 0.2$;
- remove electron in case any pair of jet and electron satisfies $0.2 < \Delta R(j, e) < 0.4$;
- remove muon in case any pair of muon and jet with at least three tracks satisfies $\Delta R(j, \mu) < 0.4$;
- remove jet if any pair of muon and jet with less than three tracks satisfies $\Delta R(j, \mu) < 0.4$.

With the introduction of the b-tag information and the photons in the studies performed in Section 9 additional requirement has to be fulfilled:

- keep the jet and remove the electron or muon if $\Delta R(j, e/\mu) < 0.2$ and the jet is b-tagged (since the jet is likely coming from a semi-leptonic b-decay);
- remove photon and keep the electron if $\Delta R(\gamma, e) < 0.4$;
- remove photon and keep the muon if $\Delta R(\gamma, \mu) < 0.4$;
- keep photon and remove the jet if $\Delta R(\gamma, j) < 0.4$.

6.6 Missing Transverse Momentum

Once that all the objects are defined and reconstructed in the event, the measure of the momentum imbalance in the transverse (η, ϕ) plane is possible. It permits to evaluate the missing transverse momentum that is the most important ingredient of the mono-jet final state. Its components $E^{\text{miss}}_{x(y)}$ can be formulated as the negative sum of the momenta, reconstructed in the transverse plane, associated to all the objects of the final state:

$$E^{\text{miss}}_{x(y)} = E^{\text{miss},e}_{x(y)} + E^{\text{miss},\gamma}_{x(y)} + E^{\text{miss},\tau}_{x(y)} + E^{\text{miss, jets}}_{x(y)} + E^{\text{miss},\mu}_{x(y)} + E^{\text{miss, soft}}_{x(y)}, \qquad (6.3)$$

where each term is given by the negative vectorial sum of the momenta of the respective calibrated objects. Its magnitude and azimuthal angle are:

$$E^{\text{miss}}_{\text{T}} = \sqrt{(E^{\text{miss}}_{x})^2 + \left(E^{\text{miss}}_{y}\right)^2}\,, \qquad (6.4)$$

$$\phi^{miss} = \arctan(E^{\text{miss}}_{y}/E^{\text{miss}}_{x})\,. \qquad (6.5)$$

$E^{\text{miss}}_{\text{T}}$ calculations is based on all the energy deposits in the calorimeter up to $|\eta| = 4.9$. Clusters associated with either electrons, photons or hadronic decays of tau leptons and those associated with jets are calibrated with the same JES. However, since the τ-leptons are not reconstructed in the analysis, the energy from τ-jets is included in the jet term.

The last term in Eq. (6.3) incorporates all the contributions detected in ID and in the calorimeter that are not associated to any specific object. It can be evaluated using the particle tracks resulting in the Track Soft Term (TST) or with the calorimetric deposits known as Calo Soft Term (CST).

Since the $E^{\text{miss}}_{\text{T}}$ is defined as the momentum imbalance in each events in which are present any number of different objects, the performance of its reconstruction and resolution can be studied in well known final states topologies where the systematic effects relative to the other objects can be kept under control and removed. The $Z(\mu\mu)$+jets and $Z(ee)$+jets processes in a selection around the the Z boson peak provides a very high purity sample of events where the truth $E^{\text{miss}}_{\text{T}}$ is zero. $W(\mu\nu)$+jets and $W(e\nu)$+jets processes instead provide regions where a source of "genuine?? $E^{\text{miss}}_{\text{T}}$ can be examined.

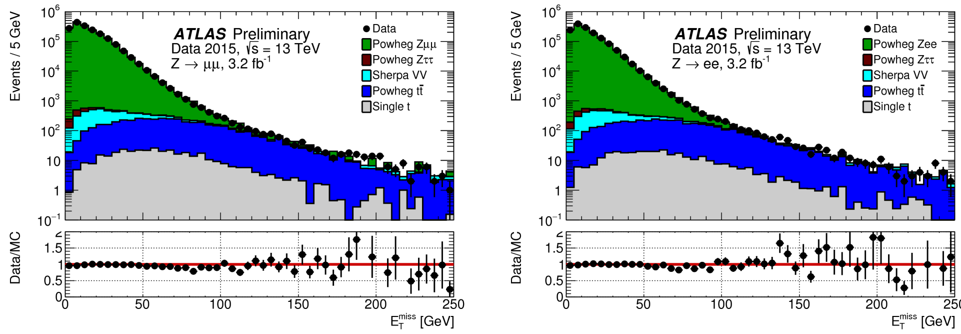

Figure 6.11. Left: Data-MC comparison of the $E_{\mathrm{T}}^{\mathrm{miss}}$ distribution in $Z(\mu\mu)$+jets events. Right: TST $E_{\mathrm{T}}^{\mathrm{miss}}$ soft term distribution for a selection of $Z(\mu\mu)$ events requiring no primary-vertex jet activity. Both the plots are based on 3.2 fb^{-1} collected during 2015 at $\sqrt{s} = 13$ TeV [114].

A good level of agreement between MC simulations and data collected during 2015 can be observed for the full $E_{\mathrm{T}}^{\mathrm{miss}}$ and the soft term in Figure 6.11 in which $Z(\mu\mu)$ events are selected.

In order to evaluate the $E_{\mathrm{T}}^{\mathrm{miss}}$ scale performance [115], the average value of the projections of the TST $E_{\mathrm{T}}^{\mathrm{miss}}$, CST $E_{\mathrm{T}}^{\mathrm{miss}}$ and Track $E_{\mathrm{T}}^{\mathrm{miss}}$ (completely based on the tracks information of the hard objects) on the Z boson axis in $Z(\mu\mu)$ events with zero and any number of jets are plotted in Figure 6.12. In the zero-jet case, a similar behavior is observed between the three $E_{\mathrm{T}}^{\mathrm{miss}}$ definitions. The track based methods show a greater underestimation of the soft recoil due to their insensitivity to soft neutral particles.

In the sample without the veto on the jets the Track $E_{\mathrm{T}}^{\mathrm{miss}}$ shows the same effect attributed to the loss of neutral particles from high-p_{T} jets recoiling. The difference between the TST and CST $E_{\mathrm{T}}^{\mathrm{miss}}$ definitions is given by the imperfect treatment of energy loss by the muons in the calorimeter-based soft term.

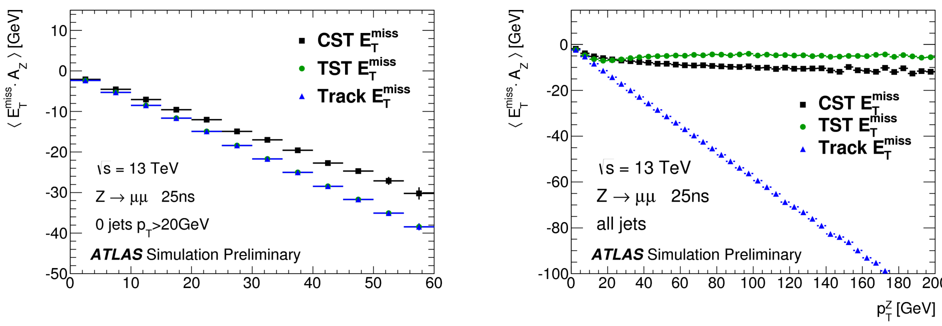

Figure 6.12. Comparison for TST $E_{\mathrm{T}}^{\mathrm{miss}}$, CST $E_{\mathrm{T}}^{\mathrm{miss}}$ and Track $E_{\mathrm{T}}^{\mathrm{miss}}$ of the mean projection of $E_{\mathrm{T}}^{\mathrm{miss}}$ along the direction of the $Z(\mu\mu)$ events applying and not applying the jet veto [115].

In order to evaluate the $E_{\mathrm{T}}^{\mathrm{miss}}$ scale in samples with non-zero $E_{\mathrm{T}}^{\mathrm{miss}}$ the linearity is defined as the difference between the truth and reconstructed $E_{\mathrm{T}}^{\mathrm{miss}}$ divided by the truth value. Its value is zero if the $E_{\mathrm{T}}^{\mathrm{miss}}$ is reconstructed to the right scale. The linearity in sample enriched with $W(\mu\nu)$ events is shown in Figure 6.13 as a function of the truth $E_{\mathrm{T}}^{\mathrm{miss}}$. The plots prove how $E_{\mathrm{T}}^{\mathrm{miss}}$ cuts of below 70 GeV are poorly modeled in the simulations. However the high $E_{\mathrm{T}}^{\mathrm{miss}}$ cut applied in the mono-jet selection guarantees the well description of the transverse momentum imbalance in each event.

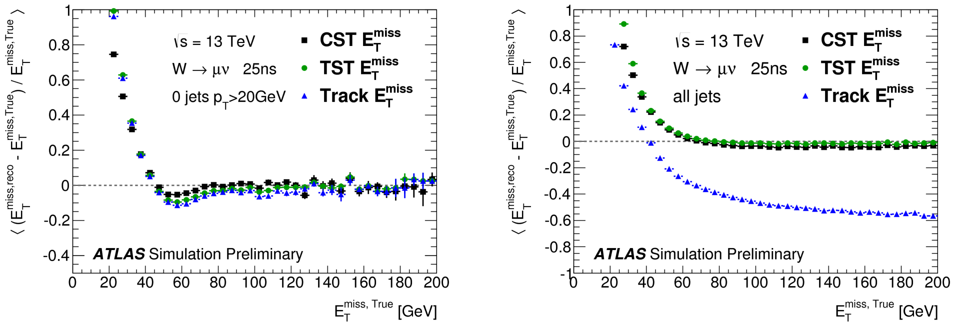

Figure 6.13. Comparison for TST $E_{\mathrm{T}}^{\mathrm{miss}}$, CST $E_{\mathrm{T}}^{\mathrm{miss}}$ and Track $E_{\mathrm{T}}^{\mathrm{miss}}$ of the mean projection of $E_{\mathrm{T}}^{\mathrm{miss}}$ along the direction of the $W(\mu\nu)$+jets events applying and not applying the jet veto [115].

In order to evaluate the $E_{\mathrm{T}}^{\mathrm{miss}}$ resolution the RMS of E_x^{miss}, E_y^{miss} of the distribution is used, in order to better accommodate the non-Gaussian tails observed in track-based $E_{\mathrm{T}}^{\mathrm{miss}}$ methods. In Figure 6.14 the distributions of RMS as a function of the scalar sum of transverse momenta of the objects $Z(\mu\mu)$+jets and $W(\mu\nu)$+jets events show as the CST and TST $E_{\mathrm{T}}^{\mathrm{miss}}$ definitions have similar behavior since the resolution is dominated by the jet term. It is instead evident as the Track $E_{\mathrm{T}}^{\mathrm{miss}}$ definition suffers of the missing reconstruction of neutral particles with the consequence of larger spread of the $E_{\mathrm{T}}^{\mathrm{miss}}$ distribution.

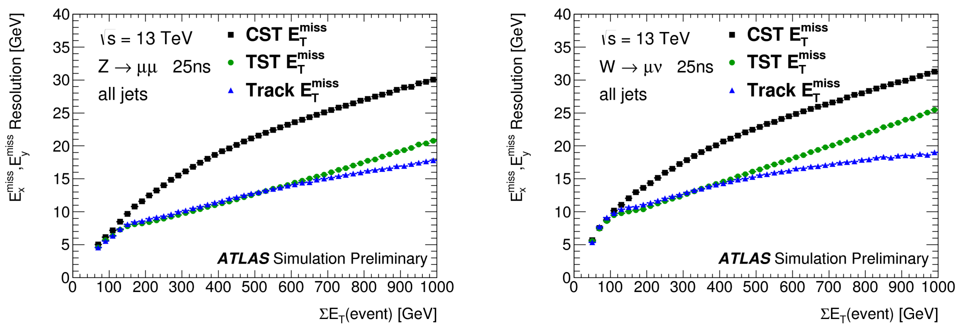

Figure 6.14. Comparison for TST $E_{\mathrm{T}}^{\mathrm{miss}}$, CST $E_{\mathrm{T}}^{\mathrm{miss}}$ and Track $E_{\mathrm{T}}^{\mathrm{miss}}$ of the $E_{\mathrm{T}}^{\mathrm{miss}}$ resolution in terms of RMS of E_x^{miss} and E_y^{miss} as a function of the CST $\sum E_{\mathrm{T}}$ in $Z(\mu\mu)$+jets and $W(\mu\nu)$+jets events. direction of the $W(\mu\nu)$+jets events applying and not applying the jet veto [115].

The total systematic uncertainty on $E_{\mathrm{T}}^{\mathrm{miss}}$ derives from the systematics which affect each of the terms of Eq. (6.3). The uncertainties provided for the hard objects are propagated into their respective $E_{\mathrm{T}}^{\mathrm{miss}}$ terms. Then the uncertainty contributions relative to the resolution and scale of the soft term is mostly based on the balance measurement between hard and soft contributions in $Z(\mu\mu)$ events (more information in Ref. [115]). The variation of the TST $E_{\mathrm{T}}^{\mathrm{miss}}$ coming from the combined TST systematic uncertainties is shown in Figure 6.15.

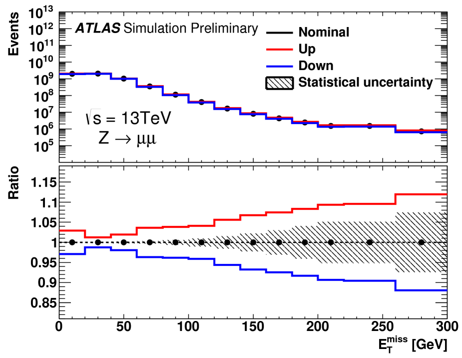

Figure 6.15. TST $E_{\mathrm{T}}^{\mathrm{miss}}$ in $Z(\mu\mu)$ events with the systematic variations up and down coming from the combined TST systematic uncertainties. The hatched band in the ration plot shows the statistical uncertainty [115].

In this analysis TST is used because of the better performance provided and its better stability against pileup with respect to CST. In Figure 6.16 the distribution of $E_{\mathrm{T}}^{\mathrm{miss}}$ divided by the square root of the scalar sum of transverse momenta of the objects used to calculate $E_{\mathrm{T}}^{\mathrm{miss}}$ itself, based on TST on the left, and CST on the right, as a function of the average of number of vertices is shown, proving the better performance of the track-based $E_{\mathrm{T}}^{\mathrm{miss}}$ with the pileup.

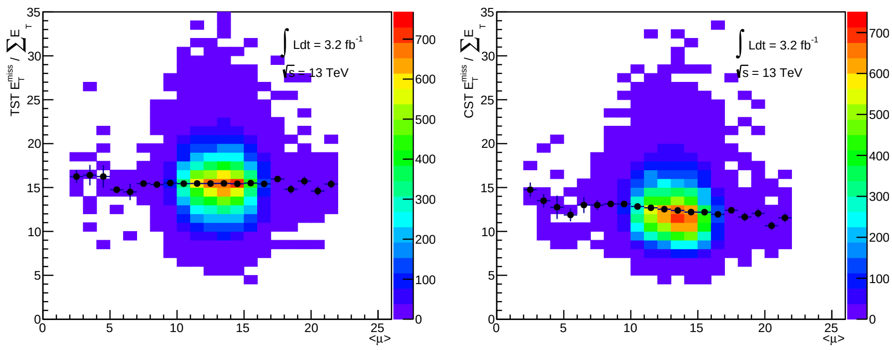

Figure 6.16. Correlation plots of the average of number of vertices $\langle\mu\rangle$ versus the TST-based (left) and the CST-based (right) $E_{\mathrm{T}}^{\mathrm{miss}}/\sqrt{\sum E_{\mathrm{T}}}$ variable in the mono-jet signal region using 3.2 fb^{-1} of data recorded at $\sqrt{s} = 13$ TeV. The profile of the soft term distribution is superimposed to make clearer the pileup dependence of the soft term evaluation using the two difference techniques.

Chapter 7

The Mono-jet Analysis

In this chapter a detailed overview of the first Run-2 mono-jet analysis based on data collected during the first year of ATLAS at $\sqrt{s} = 13$ TeV is provided (consult also Reference [116]). The selection criteria, the fitting strategy and the background estimations are addressed as well as the improvements and innovations introduced, which led to a significant improvement in sensitivity with respect to the Run-1 analysis. Finally the systematic uncertainties implemented in a global simultaneous fit are described and the results with the interpretations in the context of DM production, SUSY compressed scenarios and ADD model are presented.

7.1 Data & MC Samples

Before introducing the details of the analysis, in this section the data and MC simulation samples used in the analysis are outlined.

7.1.1 2015 Data Sample

The first mono-jet results of Run-2 are based on the data collected during 2015 in the proton-proton collision at a center of mass energy of $\sqrt{s} = 13$ TeV. The amount of data taken yields to a total integrated luminosity of 3.2 fb^{-1}, after the application of the Good-Run-List (GRL) requirement, that ensures that all the constituents of the ATLAS detector were fully operational. The events that compose this data sample were collected between August 4$^{\text{th}}$ and November 2$^{\text{nd}}$ which corresponds to the period in which the LHC worked at a bunch-crossing spacing of 25 ns with an instantaneous luminosity higher than $10^{33}\text{cm}^{-2}\text{s}^{-1}$ with a peak of $5 \cdot 10^{33}\text{cm}^{-2}\text{s}^{-1}$ and an average number of interactions per bunch-crossing $\langle\mu\rangle = 13.6$.

7.1.2 MC Simulations

All the MC samples used were generated in order to simulate the proton-proton collisions with a 25 ns of bunch spacing at the centre of mass energy of $\sqrt{s} = 13$ TeV. They are needed to compute the detector acceptance and the reconstruction efficiencies, evaluate the signal and background contributions, and estimate the systematic uncertainties in the final results.

All the MC simulations used in the analysis are generated by different multi-purpose event generators that make possible a high precision estimation of the contributions due to several physics processes. These are based on theoretical calculations of the hard processes based on the matrix element (ME), then effects due to the hadronizations, EWK and QCD radiations are added to the parton showering (PS) generator.

One of the most used generators is SHERPA [117] that is a multi-purpose framework able to handle both the ME and PS steps. Different and almost independent modules are implemented in the framework allowing to have more than one ME generator or PS in parallel that can be chosen and set in the generation.

The general framework called POWHEG-BOX [118] is able to implement the NLO calculations in shower MC programs according to the POWHEG method [119]. The POWHEG algorithm is a method which starts with the generation of the hardest radiation of the process and then adds to the event the other subsequent and softer radiations with the help of an additional shower generator. Thus POWHEG simply replaces the hardest emission with its own obtained by NLO calculations.

MC@NLO [120] is instead a generator based on a algorithm called *subtraction method* providing a proper matching between NLO calculations and PS through the application of event weights. It is used in this analysis interfaced to the MadGraph ME generator.

Background Processes

The main source of background in the mono-jet finals states comes from processes in which a Z boson is produced in association with jets and decays in two invisible neutrinos emulating perfectly a WIMP pair production, constituting the so-called irreducible background. The second background in order of importance is given by the W boson production in association with jets, with W that decays leptonically and in particular in a τ lepton, which subsequently decays hadronically, and a neutrino. Other sources of background are due to the misidentification and misreconstruction of the leptons which come from other leptonic decays of the vector bosons, diboson (WW, WZ, ZZ) production, $t\bar{t}$, single-top, multi-jet backgrounds. Due to the limited MC modeling of the multi-jet process and of non-collision background, the latter are evaluated directly from data.

The MC simulations of W+jets and Z+jets events are generated using the SHERPA-2.1.1 [117] generator with NLO PDF set `CT10` [121]. ME are calculated for 0, 1 and 2 jets at NLO and for 3 and 4 jets at LO, with boson p_{T} filters using the COMIX [122] and OPENLOOPS [123] matrix element generators. This allows to increase the statistics of the simulation in all the boson p_{T} spectrum and in particular in the tails at high boson p_{T}, which is the crucial region for this analysis. The samples are further produced separately in slices with b-veto, c-filter-b-veto and b-filter and then are summed to get an inclusive set of samples. The generated samples are merged with a dedicated PS developed by SHERPA [124] following the ME+PS@NLO prescription in Ref. [125] and thus including the contributions and the corrections given by the QCD radiations. In the $Z(\ell\ell)$ production processes, a cut on $m(\ell\ell) > 40$ GeV is applied and an additional set of samples with 10 GeV $< m(\ell\ell) <$ 40 GeV is also included to increase the MC statistics around the low dilepton mass resonances. The simulated samples are initially normalized to NNLO predictions, calculated using perturbative QCD (pQCD) according to DYNNLO [126, 127] using MSTW2008 90% CL NNLO PDF sets [128].

Simulated samples of top quark pairs ($t\bar{t}$) processes and single top-quarks in the Wt-channel and s-channel are produced with the POWHEG-BOX v2 [129] generator with the CT10 PDF sets in the ME calculations. Electroweak t-channel single top-quark events are instead generated using POWHEG-BOX. In the generation the four-flavor scheme has been used for the calculations of NLO matrix elements with the fixed four-flavor PDF set CT10. The parton shower, fragmentation, and underlying event are simulated using PYTHIA-6.428 [130] with the CTEQ6L1 [131] PDF sets and the corresponding Perugia 2012 set of tuned parameters [132]. The top-quark mass is set to 172.5 GeV and in order to model the bottom and charm hadron decays the EvtGen v1.2.0 program [133] is used.

Finally the diboson samples which describe the WW, WZ, and ZZ production processes are generated using SHERPA-2.1.1 with CT10 PDFs and normalized to NLO pQCD predictions [134]. The matrix elements contain all diagrams with four electroweak vertices and are calculated for up to 1 (4ℓ, $2\ell+2\nu$ channels) or 0 partons ($3\ell+1\nu$) at NLO and up to 3 partons at LO.

Signal Processes

The ADD samples (see Section 3.3) have been produced with PYTHIA-8.165 with the PDF set NNPDF23LO [135]. Different numbers of extra dimensions in the range $n = 2, ..., 6$ and M_D in the range $[2, 5]$ TeV are generated with a cut of $p_{\mathrm{T}} > 150$ GeV at matrix element, and requiring at least one jet with $p_{\mathrm{T}} > 100$ GeV at the truth level. Thus without taking into account the effects of the detector, in order to be fully efficient in the $E_{\mathrm{T}}^{\mathrm{miss}} > 250$ GeV region. For each number of extra dimensions n, only one value of the gravity scale M_D is generated since is not affecting the acceptance, while the cross-section depends on M_D as $\sigma_{ADD} = 1/M_D^{n+2}$. Therefore, different values of M_D can be explored by changing the normalization of the samples. The renormalization scale is set to the geometric mean of the transverse mass of the two produced particles, $\sqrt{(p_{\mathrm{T},G}^2 + m_G^2)(p_{\mathrm{T},p}^2 + m_p^2)}$, where m_G, $p_{\mathrm{T},G}$ and m_p, $p_{\mathrm{T},p}$ denote the mass and the transverse momentum of the graviton G and the parton p in the final state respectively. The factorization scale is set to the minimum transverse mass $\sqrt{m^2 + p_{\mathrm{T}}^2}$ of the graviton and the parton. The cross-sections of the ADD signal samples used in the analysis are listed in Appendix A in Tables A.1.

Signals for the SUSY compressed scenarios mentioned in Section 3.2.1 are generated with MG5_aMC@NLO v5.2.2.3 [120] interfaced to PYTHIA-8.186 with the ATLAS A14 [136] tune to reproduce the squark decay, with PS, hadronization, and underlying event. The ME calculation is performed at LO including the emission of up to two additional partons. The renormalization and factorization scales are set to the sum of transverse masses of all final state particles. The NNPDF23LO PDF set is used for the generation and the ME-PS matching is performed using the CKKW-L [137] prescription, with a matching scale[1] set to

[1] The ME matching scale is the scale used in the calculations which take into account the overlap between jets from ME and PS.

a quarter of the pair-produced squark mass considered in the process. The MC samples are produced with squark masses in the range between 250 and 700 GeV and $\Delta m = 5, ..., 25$ GeV. The cross-sections are calculated at NLO in the strong coupling constant, adding the resummation of soft gluon emission at NL-logarithmic (NLO+NLL) accuracy [22, 138, 139]. The values of the cross-sections of the SUSY samples used in the analysis are listed in Appendix A in Tables A.2–A.4. Its values and the relative uncertainty are taken from an envelope of cross-section predictions using different PDF sets and factorization and renormalization scales, as described in Ref. [140].

WIMP signals are generated with POWHEG-BOX v2 [119, 141, 142] using revision 3049 of the DMV and DMS_tloop model implementations of WIMP pair production with s-channel spin-1 and spin-0 mediator exchange respectively at NLO precision including PS, introduced in Ref. [143]. The $H_{\mathrm{T}}/2$ value is chosen to set the renormalization and factorization scales, where $H_{\mathrm{T}} = \sqrt{m_{\chi\chi}^2 + p_{\mathrm{T},j1}^2} + p_{\mathrm{T},j1}$ with $m_{\chi\chi}$ the invariant mass of the WIMP pair and $p_{\mathrm{T},j1}$ the transverse momentum of the leading jet (the jet with the highest p_{T}). Events are generated using the NNPDF30_nlo_as_0118 [144] parton distribution functions and interfaced to PYTHIA-8.205 with the ATLAS `A14` tune for PS. As mentioned in Section 4.7 the couplings are set to $g_\chi = 1$ and $g_q = 0.25$ for the spin-1 case and $g_\chi = g_q = 1$, in the spin-0 case. The mediators are implemented as a Breit-Wigner with Γ/m_A up to about 5% as explained in 4.7. The simulated samples are generated with WIMP masses m_χ ranging between 1 GeV and 1 TeV and mediator masses $m_{A/P}$ between 10 GeV and 2 TeV. In Figure 7.1 the different grid points used in the analysis are listed in the axial-vector and pseudo-scalar mediator case, respectively. For the axial-vector model, 7 additional samples are generated for $m_\chi = 150$ GeV and $m_A = 1$ TeV for coupling values of 0.1, 0.25, 0.5, 0.75, 1, 1.25 and 1.5. For the pseudo-scalar model, 6 additional samples are generated for $m_\chi = 50$ GeV and $m_P = 300$ GeV mediator for coupling values 0.1, 2, 3, 4, 5, 6. Finally the *bornktmin* and *bornsuppfact* parameters [141] are set to 150 GeV in order to impose cut on the minimal p_{T} of the Born-level process in the generation. The cross-sections of the DM simplified models used in the analysis are listed in Appendix A in Tables A.5–A.8.

In the MC samples, the 13 TeV pileup conditions as a function of the instantaneous luminosity are simulated taking into account also the overlap of the hard-scattering processes with the minimum-bias events generated with PYTHIA. The detector effects are described by MC simulations [145] based on the GEANT4 program [146].

MC Weights

Each event coming from MC simulations is corrected through a set of specific weights proper of the algorithm used in the generation of the simulated samples and the performance in the identification and reconstruction of the several objects. The total weight is defined as a product of several contributions as:

$$w_{\mathrm{tot}} = \prod_i w_i \,, \tag{7.1}$$

where the single weights w_i applied in the analysis are:

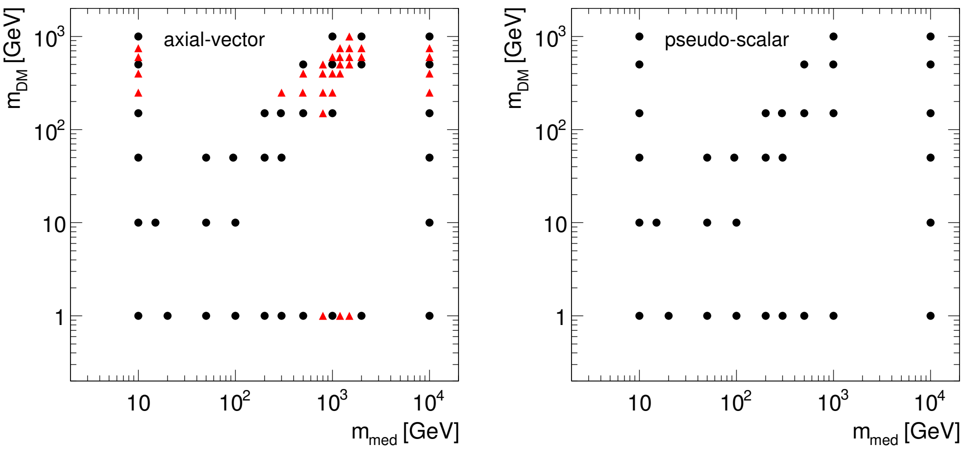

Figure 7.1. Mass grid of signal samples generated for the first mono-jet results with a axial (left) and pseudo-scalar (right) mediator decaying in a pair of Dirac DM fermions. The minimum width is considered for the couplings set to $g_q = 0.25$ and $g_\chi = 1$ in the axial mediator case and $g_q = g_\chi = 1$ in the pseudo-scalar one. The points in red have been added at a later stage with a limited MC statistics in order to obtain finer binning close to the sensitivity reached.

- MC weight: it is related to the MC algorithm and takes into account the subtraction terms deriving from the matching of the ME and PS generators and from the addition of radiated jets from the tree level process. They can typically assume positive and negative values and can also include the cross-section of the considered process;

- scale factor (SF): as mentioned in the previous chapter, it derives from the ratio of efficiencies calculated on data and MC: SF $= \varepsilon_{\text{data}}/\varepsilon_{\text{MC}}$. Hence to each events, in which the presence of a specific object is requested, will be associated a specific SF coming from reconstruction, identification, isolation and trigger efficiencies;

- anti-SF: as the reconstruction efficiency correction affects the events in which a object is tagged, the same occurs in the events in which a specific object veto is used. For this reason the anti-SF are introduced based on the fact that the sum of weighted MC events in which a object is selected, N_{sel}, and thus of vetoed N_{veto} events, has to be equal to the sum of total events:

$$N_{\text{veto}} + N_{\text{sel}} = N_{\text{tot}} \,. \tag{7.2}$$

  Hence applying the SF for each event, a SF average $\langle \text{SF} \rangle$ is calculated:

$$\langle \text{SF} \rangle \cdot N_{\text{sel}} + \text{anti-SF} \cdot N_{\text{veto}} = N_{\text{tot}} \,. \tag{7.3}$$

  Finally the anti-SF can be extracted:

$$\text{anti-SF} = 1 + (1 - \langle \text{SF} \rangle)(N_{\text{sel}}/N_{\text{veto}}) \,; \tag{7.4}$$

- cross-section: it consists of the cross-section value of the physics process multiplied by the eventual k-factor that takes into account the higher order contributions. If the MC samples are split in slices, as for example the SHERPA V+jets background introduced before, an additional efficiency filter weight is applied;
- events generated: it is used in the denominator and consists in the sum of all the MC weights (first item in the list) corresponding to specific physics processes. In addition to the weights listed, it allows to normalize the events to the integrated luminosity of 1 fb^{-1};
- luminosity: it scales the events to the total integrated luminosity relative to the data sample used in the analysis.

There is also an additional weight that takes into account the difference of the pileup distribution between data and MC. It is usually applied, however the effect of these pileup corrections have a negligible effect in the analysis and for this reason the relative weights are not applied to the MC events.

7.2 Event Selection

A first baseline selection is applied to all the data and MC simulation samples. Events are preselected requiring a logical OR of missing transverse momentum and single lepton triggers and at least one jet with a p_{T} greater than 100 GeV.

The data sample was selected using a trigger logic that selects events with $E_{\mathrm{T}}^{\mathrm{miss}} > 70$ GeV corresponding to the lowest unprescaled $E_{\mathrm{T}}^{\mathrm{miss}}$ trigger.

Each event is required to have a primary vertex of interaction with at least two associated ID tracks with $p_{\mathrm{T}} > 0.4$ GeV. If more than one primary vertex candidate is found, the one with the largest sum of p_{T}^2 of the associated tracks is chosen.

A lepton veto is applied for baseline muons and baseline electrons identified in the final states.

In order to suppress noise and NCB, only good jets as defined in Section 6.4 are considered in the analysis.

In order to suppress the multi-jet background, coming mainly from jet energy mismeasurements, up to four jets are permitted in each event and separation in the transverse plane of $\Delta\phi(\mathrm{jet}, p_{\mathrm{T}}^{\mathrm{miss}}) > 0.4$ between the missing transverse momentum direction and each jet is imposed.

The leading jet is required to have $p_{\mathrm{T}} > 250$ GeV, $|\eta| < 2.4$ and to pass the *tight* jet cleaning to suppress the energy deposits in the calorimeters due to muons of beam-induced or cosmic-ray origin (more details in Section 7.4.4).

Finally the missing transverse momentum in the event is required to be greater than 250 GeV.

The full signal region (SR) selection is summarized in Table 7.1.

7.3 Trigger

As mentioned in the previous section, the lowest unprescaled trigger available during the data collection corresponding of 3.2 fb^{-1} is a trigger logic with a nominal

Category	Selection criteria
trigger	`HLT_xe70`
data quality	GRL
vertex	≥ 1 vertex with $N_{\text{trk}} \geq 2$
pile-up suppression	JVT > 0.64 $(20 < p_{\text{T}} < 50$ GeV$, \lvert\eta\rvert < 2.4)$
jet cleaning	*loose*, $p_{\text{T}} > 30$ GeV$, \lvert\eta\rvert < 2.8$
leading jet	*tight*, $p_{\text{T}} > 250$ GeV, $\lvert\eta\rvert < 2.4$
electron veto	*loose*, $E_{\text{T}} > 20$ GeV, $\lvert\eta\rvert < 2.47$
muon veto	*medium*, $p_{\text{T}} > 10$ GeV, $\lvert\eta\rvert < 2.5$
jet multiplicity	$N_{\text{jet}} \leq 4$ $(p_{\text{T}} > 30$ GeV$, \lvert\eta\rvert < 2.8)$
multi-jet suppression	$\Delta\phi(\text{jet}, E_{\text{T}}^{\text{miss}}) > 0.4$
$E_{\text{T}}^{\text{miss}}$	> 250 GeV

Table 7.1. Summary of the cuts applied to define the SR.

threshold set to $E_{\text{T}}^{\text{miss}} > 70$ GeV. It relies on a calorimeter-based calculation without considering the muon system, thus the trigger can also fire on events with a high p_{T} muon balanced by another physics object.

Of course the threshold does not correspond one to one to the $E_{\text{T}}^{\text{miss}}$ value reconstructed offline as the online calculation does not make use of the final object calibrations. The trigger efficiency has been evaluated using a semi-data-driven technique consisting in two main steps:

- the pure MC efficiency of the $E_{\text{T}}^{\text{miss}}$ trigger has been measured in the SR and in a muon enriched region defined as the SR but inverting the muon veto and thus requiring a good muon in the final state. In order to increase the statistics for this study the leading jet p_{T} cut is moved to 150 GeV. The $E_{\text{T}}^{\text{miss}}$ cut is not applied and the trigger efficiency is evaluated as a function of $E_{\text{T}}^{\text{miss}}$ using background samples as the ratio between the number of selected and total events in each region;

- the same is repeated using data, by selecting single muon events with a single muon trigger requirement orthogonal to the $E_{\text{T}}^{\text{miss}}$ one, with a nominal cut on the muon $p_{\text{T}} > 26$ GeV;

In Figure 7.2 the results of this study for the different samples and regions are summarized using three unprescaled $E_{\text{T}}^{\text{miss}}$ triggers with different thresholds: `HLT_xe70`, `HLT_xe80` and `HLT_xe100`. These results prove that the trigger selection reaches the plateau and is fully efficient in the mono-jet SR.

7.4 Background Estimation

In this section the analysis strategy to estimate the background contributions in the SR is outlined. The dominant sources of background are given by the processes in which a vector boson W or Z is produced in association with jets, defined as electroweak background. As mentioned before, the irreducible background coming from the $Z(\nu\nu)$+jets process yields the major contribution since its topology is the same of the searched signals. In order to evaluate the electroweak background a

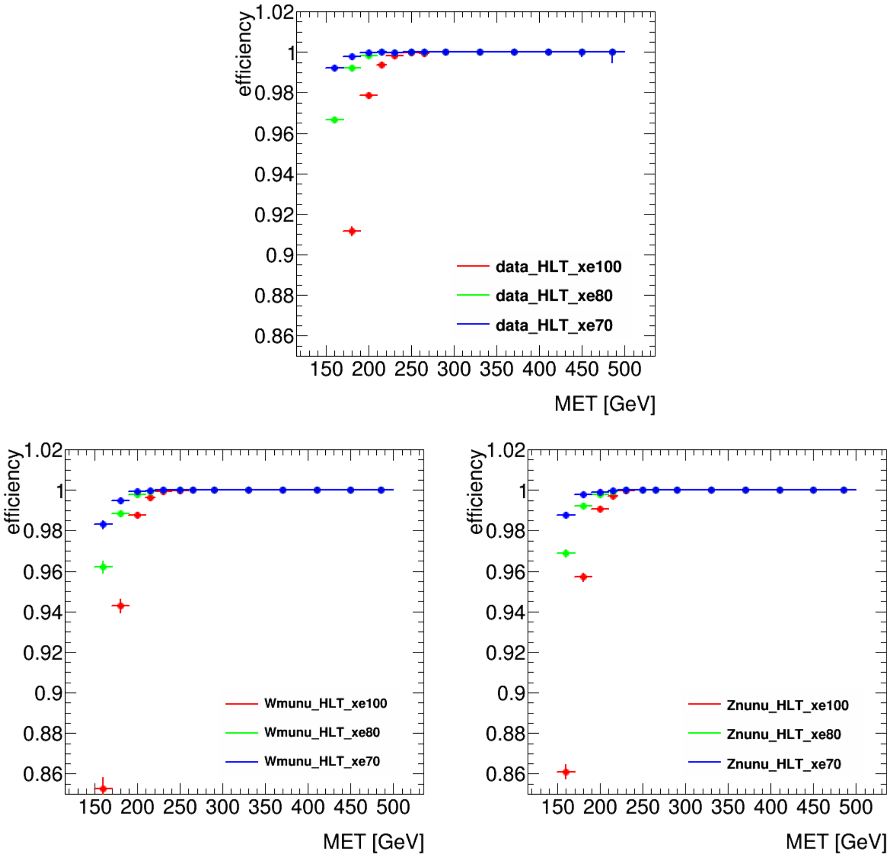

Figure 7.2. Comparison between the efficiencies of three $E_{\mathrm{T}}^{\mathrm{miss}}$ triggers with different thresholds `HLT_xe70` (blue), `HLT_xe80` (green) and `HLT_xe100` (red) in the muon enriched region using data (top) and $W(\mu\nu)$ MC samples (bottom left) and in the SR using $Z(\nu\nu)$ MC samples (bottom right). The data are selected applying a single muon trigger and a cut on jet leading p_{T} at 150 GeV is applied in all the plots.

semi-data-driven technique is adopted, getting a set of normalization factors from a final simultaneous fit that scales the several contributions using the information of background-enriched control regions. The estimation of the other subdominant processes is instead based on MC simulations, or data-driven methods. A schematic list of the estimation method for each background is shown in Table 7.2.

7.4.1 Electroweak Background

In order to reduce the total uncertainty resulting from the estimation of the dominant backgrounds using the MC simulations, a semi-data-driven method based on the introduction of control regions (CRs) is performed. These are populated mainly by a particular source of background and are used to extrapolate the normalization of one or more physics process through normalization factors that are estimated by a simultaneous fit. The contribution of a background process BG_i in a signal region SR_k can be extracted from a control region CR_j dominated by the background BG_j

Background	Estimation Method
$Z(\nu\nu)$+jets	simultaneous fit
$W(l\nu)$+jets	simultaneous fit
$Z(\mu\mu)$+jets	simultaneous fit
$Z(\tau\tau)$+jets	simultaneous fit
$Z(ee)$+jets	from MC
diboson	from MC
$t\bar{t}$ and single-top	from MC
multi-jet	jet smearing
NCB	tagger

Table 7.2. List of the several sources of background in the mono-jet analysis and corresponding estimation methods.

by[2]

$$N^{\mathrm{SR}_k}_{\mathrm{BG}_i} = \left(N^{\mathrm{CR}_j}_{\mathrm{data}} - N^{\mathrm{CR}_j}_{\text{non-BG}_j,\ \mathrm{MC}}\right) \cdot \frac{N^{\mathrm{SR}_k}_{\mathrm{BG}_i,\ \mathrm{MC}}}{N^{\mathrm{CR}_j}_{\mathrm{BG}_j,\ \mathrm{MC}}} = \frac{\left(N^{\mathrm{CR}_j}_{\mathrm{data}} - N^{\mathrm{CR}_j}_{\text{non-BG}_j,\ \mathrm{MC}}\right)}{N^{\mathrm{CR}_j}_{\mathrm{BG}_j,\ \mathrm{MC}}} \cdot N^{\mathrm{SR}_k}_{\mathrm{BG}_i,\ \mathrm{MC}} \,. \tag{7.5}$$

Thus the other subdominant background contributions based on MC ($N^{\mathrm{CR}_j}_{\text{non-BG}_j,\ \mathrm{MC}}$) are subtracted to the number of events counted in the CR_j ($N^{\mathrm{CR}_j}_{\mathrm{data}}$) to extrapolate the number of the pure BG_i which is then scaled via a transfer factor based on MC:

$$TF^{\mathrm{CR}_j \to \mathrm{SR}_k}_{\mathrm{BG}_i} \equiv \frac{N^{\mathrm{SR}_k}_{\mathrm{BG}_i,\ \mathrm{MC}}}{N^{\mathrm{CR}_j}_{\mathrm{BG}_j,\ \mathrm{MC}}} \,. \tag{7.6}$$

From Eq. (7.5) the normalization factors that are used as scaling parameters of the expected contribution BG_i in SR_k from the CR_j can be extracted and defined as:

$$\kappa_{ij} \equiv \frac{\left(N^{\mathrm{CR}_j}_{\mathrm{data}} - N^{\mathrm{CR}_j}_{\text{non-BG}_j,\ \mathrm{MC}}\right)}{N^{\mathrm{CR}_j}_{\mathrm{BG}_j,\ \mathrm{MC}}} \,. \tag{7.7}$$

Since the transfer factor is a ratio of MC predictions, most of the systematic uncertainties cancel out or are significantly reduced. To avoid larger uncertainties from the extrapolation from one kinematic region to another, the kinematic selections in the CRs should be as close as possible to the SRs. For this reason the CRs have been defined using the same selection of the SR adding or inverting some of the cuts to make them orthogonal and hence not overlapped to the SR.

As a given background process can contribute to several CRs, the normalization factors depend on each other and give a contribution to the term $N^{\mathrm{CR}_j}_{\text{non-BG}_j,\ \mathrm{MC}}$ that is small if the CRs are chosen as pure as possible.

To evaluate the normalization factors keeping into account all the correlations between the parameters properly, a simultaneous fit to all the CRs and the SR is performed.

[2] In Eq. (7.5) the source of background BG_j is assumed to have a contribution in CR_j much greater than the one in SR_k ($N^{\mathrm{CR}_j}_{\mathrm{BG}_j} \gg N^{\mathrm{SR}_k}_{\mathrm{BG}_j}$) and in the eventual other regions.

Three different lepton CRs are defined to constrain the electroweak backgrounds in the SR. In order to maintain a kinematic selection as close as possible to the SR, the same SR selection is kept replacing the lepton vetoes with dedicated lepton requirements. Furthermore, the missing transverse momentum is modified in some cases in order to treat the reconstructed leptons as invisible objects emulating the same processes that affect the SR.

The first CR is labelled as CR1μ and is defined requiring only one muon in the final state in order to populate the region with events coming from $W(\mu\nu)$+jets processes. The selected muon is not used in the $E_{\mathrm{T}}^{\mathrm{miss}}$ calculation and it is treated as an invisible particle so that the missing transverse momentum acts as a proxy for the vector boson p_{T}. In this way, the W boson decay emulates a Z boson decaying in two neutrinos as illustrated in the scheme in Figure 7.3.

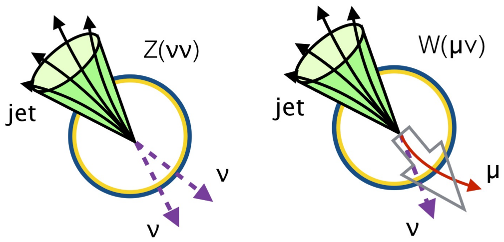

Figure 7.3. Scheme of the $Z(\nu\nu)$+jets and of the $W(\mu\nu)$+jets processes that shows how considering the muon as invisible particles the two processes are kinematically very similar.

This CR is crucial to evaluate the irreducible background given by the $Z(\nu\nu)$+jets process acquiring a major role in the analysis, and by construction it is also used to estimate the $W(\mu\nu)$+jets contribution that has a non-negligible impact in the SR. In fact, the events coming from this process can pass the SR selection if the muon crosses a region outside the detector acceptance, or if it is identified as another object or if does not fulfill some of the muon quality requirements. In order to increase the purity of the CR, an additional cut on the transverse mass of the system, composed by the muon and the neutrino coming from the W boson, is required. It is defined as

$$m_{\mathrm{T}} = \sqrt{2p_{\mathrm{T},\mu}p_{\mathrm{T},\nu}(1-\cos(\phi_\mu - \phi_\nu))}\,, \tag{7.8}$$

and only the events selected in the transverse mass range 30 GeV $< m_{\mathrm{T}} <$ 100 GeV are kept, in order to suppress the contribution from the $W\tau\nu$+jets process in this CR.

The other CR, labelled as CR1e, requires the presence of only one electron in the final state that passes the LooseTrackOnly electron isolation working point while the muon veto is applied. The CR is dominated by $W(e\nu)$+jets by construction and, differently from CR1μ, the selected electron is considered in the $E_{\mathrm{T}}^{\mathrm{miss}}$ calculation. In this case the missing transverse momentum describes mainly the neutrino E_{T}. Therefore the choice of using the same calorimeter based $E_{\mathrm{T}}^{\mathrm{miss}}$ definition in the two CRs leads to select events with different W boson p_{T} spectra with respect to CR1μ. Figure 7.4 shows the distribution of the W boson p_{T} at the truth level in CR1μ (in red), CR1e (in blue) and in a version of CR1e in which the electron is considered as invisible particle (in black). This proves that the W boson p_{T} is significantly harder in CR1e than in CR1μ and that, by subtracting the electron contribution from the $E_{\mathrm{T}}^{\mathrm{miss}}$ calculation in CR1e, the same distribution of CR1μ is obtained. The reason of using the calorimeter based $E_{\mathrm{T}}^{\mathrm{miss}}$ definition in CR1e is

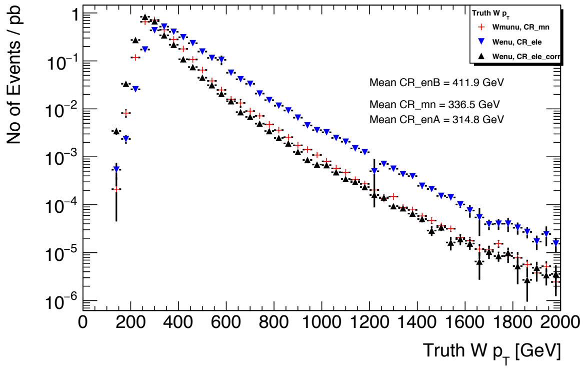

Figure 7.4. True W boson p_{T} in simulation after CR1e (blue downward triangles) and CR1μ (crosses) selections with $E_{\mathrm{T}}^{\mathrm{miss}} > 250$ GeV. The black upward triangles show the W momentum for a different electron CR, where the electron momentum is subtracted from the missing transverse energy.

to constrain the $W(\tau\nu)$+jets process that constitutes the second dominant source of background in the SR. Designing a CR ad-hoc for this process with similar jet topology and electroweak boson p_{T} as in the SR is really hard. In fact, τ leptons decay hadronically with a branching ratio of about 70% and thus the $W(\tau\nu)$+jets process can lead to mono-jet final states without emitting any jet from the initial state making it different from the other V+jets backgrounds.

A di-muon CR is defined to select $Z(\mu\mu)$+jets events requiring only two muons in the final state and treating the muons as invisible particles in the $E_{\mathrm{T}}^{\mathrm{miss}}$ calculation. A very high purity is then reached by applying a cut on the di-muon invariant mass compatible with the Z vector boson mass, 66 GeV $< m_{\mu\mu} <$ 116 GeV. This CR could be more naturally used to constrain the dominant $Z(\nu\nu)$+jets background than CR1μ because $Z(\mu\mu)$+jets has a more similar kinematic to the irreducible background than the $W(\mu\nu)$+jets process. However, because of its limited statistics it brings to a higher total uncertainty on the evaluation of the main background (the performance of alternative fitting strategies will be illustrated in details in Section 9.2.1). CR2μ is hence used to to constrain the marginal $Z(\mu\mu)$+jets background and, although its usage is not really necessary to improve the final results, it is useful to test the compatibility of the normalization factors obtained by both the muon-based CRs.

The selection criteria for all the lepton CRs defined above are summarized in Table 7.3, listing only the cuts that are different with respect to the SR. The missing transverse momentum distribution in the three CRs is shown in Figure 7.5 and an overall good agreement between data and SM predictions is observed.

Finally, since the $Z(ee)$+jets background contribution is tiny in the SR, it is evaluated directly from MC simulation.

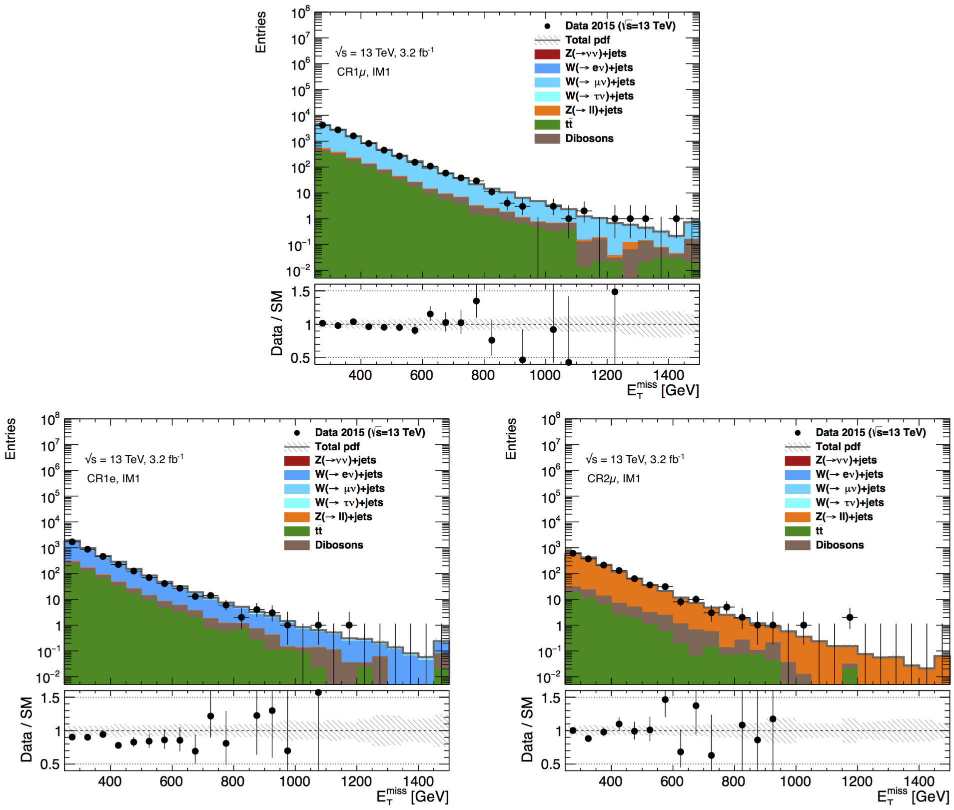

Figure 7.5. Data/MC comparison plots of the $E_{\mathrm{T}}^{\mathrm{miss}}$ distribution in CR1μ, CR1e and CR2μ, for the IM1 selection, using 3.2 fb^{-1} of data. MC expectations are scaled to the corresponding integrated luminosity. The error bands in the ratios include only the statistical uncertainties..

CR1μ	CR1e	CR2μ
1 good muon	1 good electron	2 good muons
electron veto	muon veto	electron veto
30 GeV $< m_{\mathrm{T}} <$ 100 GeV	electron LooseTrackOnly isolation	66 GeV $< m_{\mu\mu} <$ 116 GeV

Table 7.3. Lepton control region selection. Only the cuts that are different or in addition compared to the SR selection are listed treating the muons as invisible particles in the missing transverse momentum calculation in the muon CRs.

7.4.2 Diboson and Top Backgrounds

The production of two vector bosons is a background process that allows a wide range of different final states ranging from the completely leptonic to the completely hadronic one and including also the invisible final state with four neutrinos. For this reason it affects not only the SR but also all the CRs defined in the analysis. A multileptonic CR defined to evaluate such contribution could suffer too much of low statistic with the available integrated luminosity, because of the low cross-section of these physics processes. For this reason, the diboson background is evaluated using MC simulations of the different final states.

The top production processes, characterized by high cross-sections, are suppressed in particular by the high $E_{\mathrm{T}}^{\mathrm{miss}}$ and jet multiplicity cuts and the lepton veto applied in the selection. Nevertheless it remains a non negligible contribution in all the regions. A region defined as the SR but requiring one muon, treated as invisible particle in $E_{\mathrm{T}}^{\mathrm{miss}}$, and one electron in the final state is mainly populated by top-induced events but it is not used in the analysis as CR because of its low statistics. It is instead used as a validation region to cross-check the prediction from MC simulation, which is used to evaluate the contribution from $t\bar{t}$ and single-top processes in the analysis.

7.4.3 Multi-jet Background

The multi-jet background that affects the SR mainly originates from the misreconstruction of the jet energy in the calorimeter and from the presence of neutrinos in the jet cone. This source of background is strongly suppressed by the requirement of a limited jet multiplicity in the final state and by the cut on the minimum angular distance between the missing transverse momentum and the reconstructed jets. However its contribution is not negligible in the SR because of the high cross-section of the QCD processes. Due to the low accuracy of the modeling and limited statistics of the MC samples this process cannot be evaluated simply with simulation: a data-driven technique is applied to obtain the multi-jet distribution: the *jet smearing method* [147]. It consists in the four steps listed below.

1. Measure the jet response function for b-jets and non-b-tagged jets to estimate the fluctuation in the measured jet transverse momenta from PYTHIA multi-jet MC samples. This is done by comparing the truth level jet p_{T} to the reconstructed jet p_{T} and defining the jet p_{T} response:

$$R = \frac{p_{\mathrm{T}}^{\mathrm{reco}}}{p_{\mathrm{T}}^{\mathrm{truth}}} \, . \tag{7.9}$$

   The distribution of this observable can be broad because of jet p_{T} fluctuations due to several effects such as the energy resolution of the calorimeter, the presence of neutrinos coming from heavy flavor decays or if some parts of the jets are not contained in the cone defined for the reconstruction or fall outside the calorimeter. The resulting distribution of R as a function of the truth jet p_{T} for b-jets and b-vetoed jets is shown in Figure 7.6.

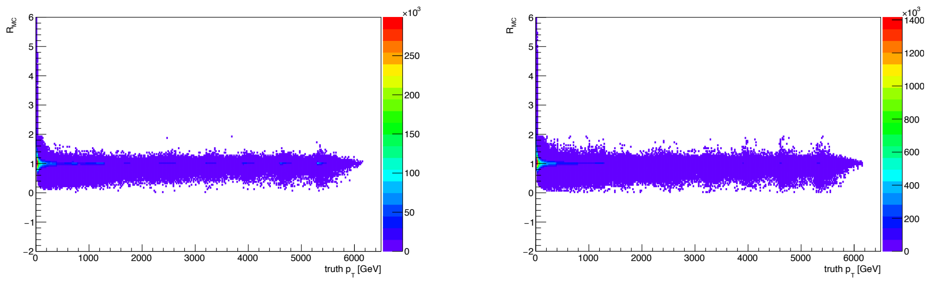

Figure 7.6. Jet p_{T} response estimated from MC simulations for b-jets (left) and non-b-tagged jets (right) as a function of the truth jet p_{T}.

2. A data sample is formed selecting events with low $E_{\mathrm{T}}^{\mathrm{miss}}$ ('seed events'). These events are required to fire at least one of the single jet triggers listed in Table 7.4. If more than one trigger is fired, then the trigger with highest p_{T} threshold is chosen if the p_{T} of the jet selected lies on the efficiency plateau. The presence of a primary vertex with the same criteria mentioned in Section 7.2 is also requested in each event. The *loose* jet cleaning requirements are applied for each jet reconstructed in the final state for which the p_{T} is greater than 100 GeV for the leading one and greater than 20 GeV for the others. Then each seed event is weighted by the trigger prescale factor f_{ps}. Finally an additional

Name	f_{ps}
HLT_j60	37353.9
HLT_j100	5918.7
HLT_j110	3993.6
HLT_j150	1080.0
HLT_j175	540.0
HLT_j200	292.0
HLT_j260	83.7
HLT_j300	42.0
HLT_j320	30.1
HLT_j360	1.0

Table 7.4. Single jet trigger used to select seed events where the number refers to the p_{T} threshold. The last column shows the average trigger prescale over the full data, though actual value is extracted run by run.

cut is applied on the $E_{\mathrm{T}}^{\mathrm{miss}}$ significance defined below to select events with well-measured jets:

$$S = \frac{E_{\mathrm{T}}^{\mathrm{miss}} - 8\ \mathrm{GeV}}{\sqrt{\sum E_{\mathrm{T}}}} < 0.70\sqrt{\mathrm{GeV}}\,. \tag{7.10}$$

The additional term in the numerator is summed to correct $E_{\mathrm{T}}^{\mathrm{miss}}$ resolution due to the TST.

3. The initial MC-based jet response functions are modified so that the generated pseudo-data agrees with data in special control regions sensitive to the jet response:

   - the di-jets enriched region, which constrains the 'Gaussian core' of the jet response, comparing the p_{T} asymmetry

     $$A(p_{\mathrm{T}}^1, p_{\mathrm{T}}^2) = \frac{p_{\mathrm{T}}^1 - p_{\mathrm{T}}^2}{p_{\mathrm{T}}^1 + p_{\mathrm{T}}^2} \tag{7.11}$$

     of dijet events in data to pseudo-data generated with the initial MC jet response.

   - a region enriched in events with more than three jets, which constrains the non-Gaussian response tail of a signal jet. The selection applied in this region ensures that one jet is associated in ϕ with $E_{\mathrm{T}}^{\mathrm{miss}}$ in the event and the variable R_2 is introduced to be sensitive to the tail of the response function based on MC simulations. R_2 is defined as:

$$R_2 = \frac{\boldsymbol{p}_{\mathrm{T}}^{\mathrm{jet}} \cdot (\boldsymbol{p}_{\mathrm{T}}^{\mathrm{jet}} + \boldsymbol{p}_{\mathrm{T}}^{\mathrm{miss}})}{|\boldsymbol{p}_{\mathrm{T}}^{\mathrm{jet}} + \boldsymbol{p}_{\mathrm{T}}^{\mathrm{miss}}|^2} \tag{7.12}$$

where $\boldsymbol{p}_{\mathrm{T}}^{\mathrm{jet}}$ is the transverse momentum of the jet closest to the missing transverse momentum $\boldsymbol{p}_{\mathrm{T}}^{\mathrm{miss}}$. If the jet p_{T} is over-measured, $\boldsymbol{p}_{\mathrm{T}}^{\mathrm{miss}}$ lies antiparallel to $\boldsymbol{p}_{\mathrm{T}}^{\mathrm{jet}}$ and $R_2 > 1$, while if it is under-measured $\boldsymbol{p}_{\mathrm{T}}^{\mathrm{miss}}$ is parallel and $R_2 < 1$.

4. Using the data-constrained jet response function obtained, each seed event is smeared generating 10^3 pseudo-events in order to increase the final multi-jet samples to be included in the signal and control region of the mono-jet analysis. The choice of considering in this study the jets with $p_{\mathrm{T}} > 20$ GeV, instead of 30 GeV as in the analysis selection, allows to take into account the migration effects due to the energy smearing. The resulting smeared events are plotted as a function of the leading jet p_{T} in Figure 7.7. A comparison with the seed events before and after the cut on the $E_{\mathrm{T}}^{\mathrm{miss}}$-significance is also shown, and proves that no bias is introduced by the method.

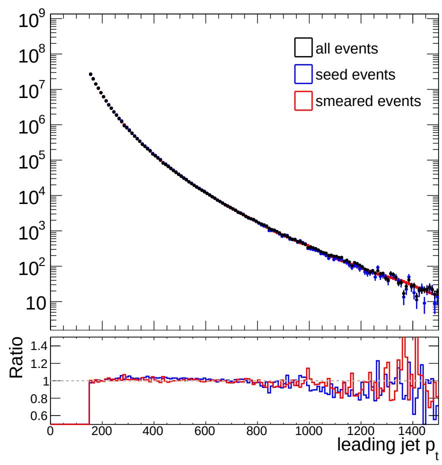

Figure 7.7. Comparison of the leading jet p_{T} distributions for seed events before (in black) and after (in blue) the $E_{\mathrm{T}}^{\mathrm{miss}}$-significance cut and the resulting smeared events as a function of the leading jet p_{T}.

The normalization of the smeared events sample, obtained by the jet smearing method, is evaluated on a multi-jet enriched CR defined by inverting the $\Delta\phi_{\mathrm{min}}(E_{\mathrm{T}}^{\mathrm{miss}}, \mathrm{jet})$ applied in the SR. Contributions from other backgrounds are subtracted using their respective MC expected yields in this region. The resulting $E_{\mathrm{T}}^{\mathrm{miss}}$ distribution in the multi-jet enriched CR is shown in Figure 7.8. The contribution of this background in the SR is hence evaluated and listed in several $E_{\mathrm{T}}^{\mathrm{miss}}$ ranges in Table 7.5.

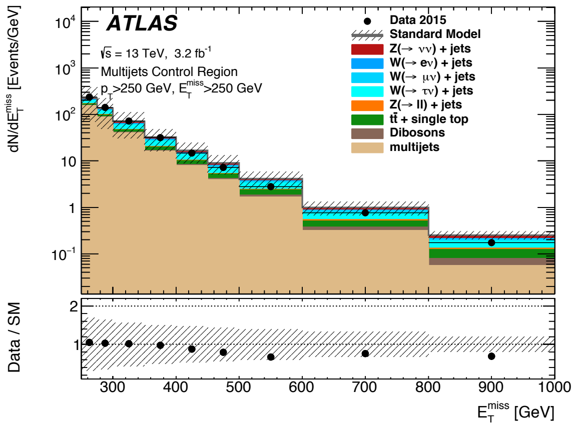

Figure 7.8. $E_{\mathrm{T}}^{\mathrm{miss}}$ distribution in the multi-jet enriched CR used to scale the multi-jet background evaluated by the jet smearing method [116].

$E_{\mathrm{T}}^{\mathrm{miss}}$ range [GeV]			[150, 250]		>250		
Yields			1167		50.7		
$E_{\mathrm{T}}^{\mathrm{miss}}$ range [GeV]	[250, 300]	[300, 350]	[350, 400]	[400, 500]	[500, 600]	[600, 700]	> 700
Yields	22.1	13.9	5.8	7.7	0.64	0.16	0.42

Table 7.5. Multi-jet yields in several $E_{\mathrm{T}}^{\mathrm{miss}}$ ranges of the SR.

7.4.4 Non-Collision Background

In the mono-jet analysis the NCB events would yield a huge contribution in the SR due to the topology and the nature of these events already described in Section 6.4. Nevertheless the *tight* jet cleaning criteria guarantee a suppression power of about 10^2 that allows to reduce this type of background to a sub-percent level. Figure 7.9 shows the leading jet p_{T} and ϕ distributions in the SR using the entire data sample and the MC expectation of all the SM processes without applying the *tight* jet cleaning to the leading jet. It is evident that the NCB would dominate without such cleaning requirements. The peculiar azimuthal jet shape is given by the main source of residual NCB produced by beam-induced muons. Those are originated in the particle cascades due to the interaction of beam halo protons with the LHC collimators. The geometry of the magnets hence draws the muons in the forward and backward directions of the beam.

However the contribution of the remaining NCB in the SR after all the applied selection is not completely negligible. It is estimated using a method that identifies beam-induced muons, using the spatial matching of calorimeter clusters in the LAr or Tile barrels with $E_{\mathrm{T}} > 10$ GeV to muon track segments reconstructed in CSC or MDT and pointing in a direction nearly parallel to the beam pipe [148].

In order to evaluate the NCB yields in the SR, the BIB tagging method defined as *two-sided no-time* method is used. It consists in the matching (in terms of the azimuthal angular distance and of the relative radial distance between cluster and segment) between a calorimeter cluster and a muon segment on both the detector sides, from which the beams income without applying any requirement on jet timing.

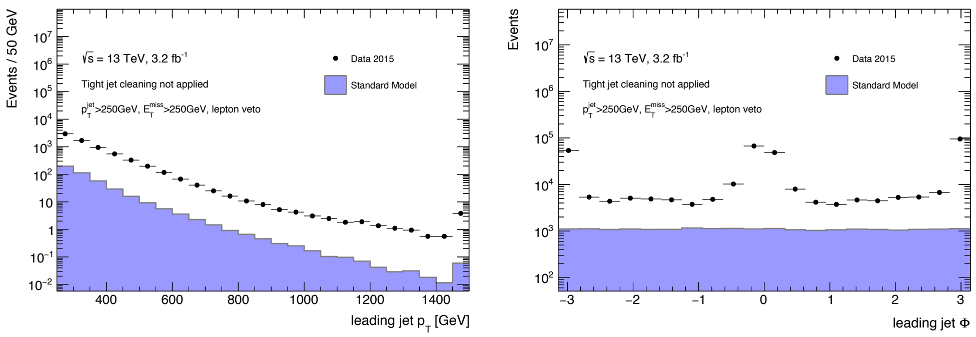

Figure 7.9. Leading jet p_{T} and ϕ distributions in the SR using the MC expectation of all the SM processes and the data collected corresponding to 3.2 fb^{-1} at $\sqrt{s} = 13$ TeV without applying the *tight* jet cleaning to the leading jet.

A sample enriched in BIB events is constructed by looking at events in the SR in which the leading jet fails the tight cleaning criteria. Then the BIB tagging efficiency can be evaluated as the ratio between the number of events tagged as BIB and the overall number of events in this BIB-enriched region:

$$\varepsilon_{\text{BIB tag}} = \frac{N_{\text{BIB tag}}^{\text{NCB region}}}{N^{\text{NCB region}}} . \tag{7.13}$$

The NCB yields in the SR is thus estimated as the ratio between the number of SR events which are tagged as BIB and the BIB tagging efficiency:

$$N_{\text{NCB}}^{\text{SR}} = \frac{N_{\text{BIB tag}}^{\text{SR}}}{\varepsilon_{\text{BIB tag}}} . \tag{7.14}$$

The BIB mistag rate is evaluated by the ratio of SR events which are flagged as BIB by the tagger but that pass the tight cleaning criteria:

$$r_{\text{mistag}} = \frac{N_{\text{BIB tag}}^{\text{SR}}}{N_{\text{BIB tag}}^{\text{SR without tight}}} . \tag{7.15}$$

Since the BIB tagger information was active only in part of the data taking corresponding to 2.7 fb^{-1} (the efficiency, mistag rate and number of events in SR and in the NCB region are listed in Table 7.6), a rescale to the entire dataset of 3.2 fb^{-1} is needed in order to extrapolate the total amount of NCB in the SR.
To do that, the amount of fake jets in runs in which the BIB tagger was not available has to be determined. The total number of events in the BIB-enriched region for the entire dataset is $N^{\text{NCB region}} = 324460$ for $E_{\mathrm{T}}^{\text{miss}} > 250$ GeV and $N^{\text{NCB region}} = 13113$ in the low $E_{\mathrm{T}}^{\text{miss}}$ region 150 GeV $< E_{\mathrm{T}}^{\text{miss}} <$ 250 GeV.

Assuming that the BIB tagging efficiency remains constant during all the data collection period, $N_{\text{BIB tag}}$ can be easily determined by rescaling $N_{\text{BIB tag}}^{\text{SR}}$ to evaluate the fake jet rate for the entire dataset. Therefore, the total amount of non-collision background in the SR can be calculated as:

$$N_{\text{NCB}}^{\text{SR}} = \left(\frac{N_{3.2\ \text{fb}^{-1}}^{\text{NCB region}}}{N_{2.7\ \text{fb}^{-1}}^{\text{NCB region}}} \right) \frac{N_{\text{BIB tag}}^{\text{SR}}}{\varepsilon_{\text{BIB tag}}} \tag{7.16}$$

	$E_{\mathrm{T}}^{\mathrm{miss}} > 250$ GeV	$E_{\mathrm{T}}^{\mathrm{miss}} \epsilon [150, 250]$ GeV
$N_{\text{BIB tag}}^{\text{SR}}$	24	22
$N_{\text{BIB tag}}^{\text{NCB region}}$	69653	2746
$N^{\text{NCB region}}$	275816	11209
$\varepsilon_{\text{BIB tag}}$	$25.0 \pm 0.2\%$	$24.0 \pm 1.0\%$
r_{mistag}	$0.0 \pm 0.4\%$	$0.8 \pm 2.0\%$

Table 7.6. Evaluation of the BIB tagger efficiency and mistag rate in the last 2.7 fb^{-1} of data collected in 2015. Errors shown are statistical uncertainties.

The resulting NCB contribution is shown in Table 7.7 in different $E_{\mathrm{T}}^{\mathrm{miss}}$-ranges.

$E_{\mathrm{T}}^{\mathrm{miss}}$ [GeV]		$[150, 250]$		>250	
Yields		105 ± 22		112 ± 23	
$E_{\mathrm{T}}^{\mathrm{miss}}$ [GeV]	$[250, 300]$	$[300, 350]$	$[350, 400]$	$[400, 500]$	>500
Yields	61 ± 17	23 ± 10	19 ± 9	9 ± 7	0

Table 7.7. Total amount of NCB in the specified $E_{\mathrm{T}}^{\mathrm{miss}}$-ranges with the corresponding statistical uncertainty associated.

7.5 Fit Strategy

Once all the signal and control regions have been defined, a global simultaneous fit based on the profile likelihood method [149] is performed in order to normalize on the basis of the observations in the control region the expectations in the signal regions. From the comparison of the estimated number of events in the SR with data the possible presence of an excess generated by the signal is assessed. All the systematics uncertainties are also included in the fit as functions that constrain some nuisance parameters defined for each systematic variation (details on the systematic uncertainties are given in Section 7.6).

In the Run-1 analysis a standard cut-and-count approach has been used to estimate the analysis sensitivity and to set limits on new physics processes, since no excesses in data have been observed. Although this approach is simple and computationally fast, it does not exploit fully the final state information. As mentioned and shown in Section 4.7 one of the most discriminating variables in the DM search in the mono-jet final state is the $E_{\mathrm{T}}^{\mathrm{miss}}$ distribution. In fact depending on the model, signals are expected to contribute to the low $E_{\mathrm{T}}^{\mathrm{miss}}$ region, for the pseudo-scalar DM model, and to the high $E_{\mathrm{T}}^{\mathrm{miss}}$ tail in the case of the simplified model with axial-vector mediators. The $E_{\mathrm{T}}^{\mathrm{miss}}$ distribution provides a good discriminating power also in the case of the ADD and compressed SUSY scenarios examined in this thesis. In order to increase the discovery potential in Run-2, the shape information of the missing transverse momentum distribution has been exploited, providing a better discrimination between signal and background processes.

The fit strategy implemented is based on a binned simultaneous shape fit in which each signal or control region has been divided in $E_{\mathrm{T}}^{\mathrm{miss}}$ exclusive bins and, for each bin, a counting experiment is performed. The shape information is taken into account, as the fit is performed simultaneously in all the bins, and the systematic uncertainties are assumed to be fully correlated between the bins. It avoids that statistical fluctuations, which in particular affect the high $E_{\mathrm{T}}^{\mathrm{miss}}$ bins, lead to dramatic changes in the nuisance parameters, that would happen if they were treated independently. The electroweak background contribution in each bin of the SR is evaluated by the corresponding bins of the CRs using a specific normalization factor. Hence the total number of normalization factors is $N_{\mathrm{NF}} = N_{\mathrm{CR}} \cdot N_{\mathrm{bin}}$ where N_{CR} denotes the number of CRs and N_{bin} the number of bins for each region. The choice of the number of bins is a compromise between the maximal gain obtainable by exploiting the shape information and the minimal decrease of the analysis sensitivity due to the low statistics in each bin.

The likelihood built and used in the analysis to perform the simultaneous global fit can be written as:

$$\mathcal{L}(\mu, \vec{\kappa}, \vec{\theta}) = \prod_{j=1}^{N_{\mathrm{reg}}} \prod_{b=1}^{N_{\mathrm{bin}}} \mathcal{P}(N_{j,b}^{\mathrm{obs}} | \mu N_{j,b}^{\mathrm{sig}}(\vec{\theta}) + \kappa_{j,b} N_{j,b}^{\mathrm{bkg}}(\vec{\theta})) \prod_{p=1}^{N_{\theta}} f_{p,j,b}(\theta_{p,j,b}) \,, \tag{7.17}$$

where $N_{j,b}^{X}$ denotes the number of observed (X = obs), expected signal (X = sig) or background (X = bkg) yields in each region for each bin, N_{reg} the number of regions and N_{θ} the number of nuisance parameters $\theta_{p,j,b}$ constrained by a function $f_{p,j,b}(\theta_{p,j,b})$. The probability density function $\mathcal{P}$ describes the Poissonian processes in each region and it depends on the signal strength μ and the array $\vec{\kappa}$ which contains all the normalization factors assigned to the different backgrounds in each bin.

In order to choose the optimal binning for the shape fit, different tests have been performed varying the number of bins. In this study the bin width has been kept constant in the full $E_{\mathrm{T}}^{\mathrm{miss}}$-range 250 GeV $< E_{\mathrm{T}}^{\mathrm{miss}} <$ 1 TeV except for the last inclusive bin with $E_{\mathrm{T}}^{\mathrm{miss}} >$ 1 TeV. Figure 7.10 shows, for a DM model with m_{χ} = 400 GeV and a vector mediator with $\mathrm{M}_{\mathrm{med}}$ = 5 TeV and $g_q = g_{\chi} = 1$, the limit on the signal strength in a background-only fit. The plot proves that the sensitivity improves reaching a sort of plateau with increasing the number of bins.

The gain in sensitivity obtained by using the shape fit has to be evaluated comparing its performance with the cut-and-count analysis looking at two main aspects: the improvement of the total uncertainty on the background expectation in the SR (that will be explained in the Section 7.6) and the gain in sensitivity reached for the several signals considered in the analysis. For this purpose, a first comparison between the results obtained using different inclusive regions moving the $E_{\mathrm{T}}^{\mathrm{miss}}$ threshold is performed to find the best cut-and-count analysis for a particular signal. These results are then compared with the one obtained with the same conditions performing the shape fit over the entire spectrum with $E_{\mathrm{T}}^{\mathrm{miss}} >$ 250 GeV.

Figure 7.11 shows a comparison between the upper limits at 95% CL on the signal strength between the shape fit and best counting analysis with $E_{\mathrm{T}}^{\mathrm{miss}} >$ 600 GeV, for the DM model with m_{χ} = 50 GeV and different values of the vector mediator fixing the couplings at $g_q = g_{\chi} = 1$. The sensitivity improvement in term of the signal strength evaluated in several signal models ranges between a few percent to about 25%.

For the analysis reported in this chapter, the seven exclusive $E_{\mathrm{T}}^{\mathrm{miss}}$ bins with a

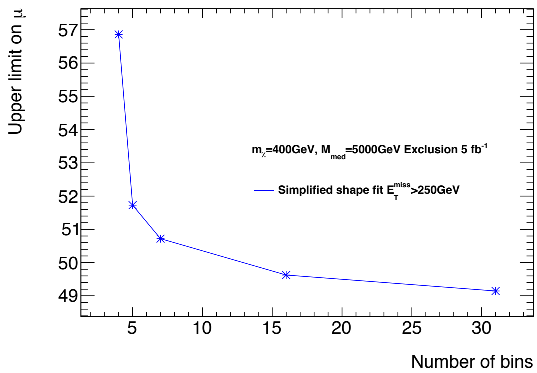

Figure 7.10. Upper limits at 95% CL on the signal strength μ for the simplified model with $\mathrm{m}_\chi = 400$ GeV and a vector mediator with $\mathrm{M}_{\mathrm{med}} = 5$ TeV and $g_q = g_\chi = 1$, as a function of the number of $E_{\mathrm{T}}^{\mathrm{miss}}$ bins with same bin width (the last bin includes the overflow). The MC expectations are normalized to an integrated luminosity of 5 fb^{-1}.

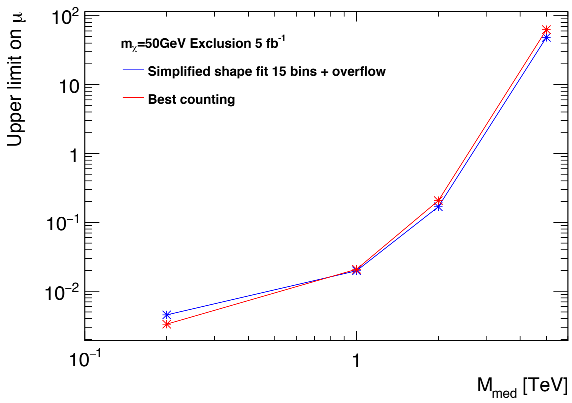

Figure 7.11. Upper limits at 95% CL on the signal strength μ: comparison between the shape fit, with 15 bins plus the inclusive bin $E_{\mathrm{T}}^{\mathrm{miss}} > 1$ TeV, and the best counting experiment with $E_{\mathrm{T}}^{\mathrm{miss}} > 600$ GeV, for the simplified model with $\mathrm{m}_\chi = 50$ GeV for different values of the vectorial mediator mass fixing the couplings at $g_q = g_\chi = 1$. The plot is performed normalizing the MC expectations to an integrated luminosity of 5 fb^{-1}.

variable bin width listed in Table 7.8 are chosen in the simultaneous shape fit, as well as the inclusive bins with a fixed low $E_{\mathrm{T}}^{\mathrm{miss}}$ threshold to maintain a consistent number of events in the last bins of each of the defined signal and control regions.

Inclusive SR $E_{\mathrm{T}}^{\mathrm{miss}}$[GeV]	IM1 > 250	IM2 > 300	IM3 > 350	IM4 > 400	IM5 > 500	IM6 > 600	IM7 > 700
Exclusive SR $E_{\mathrm{T}}^{\mathrm{miss}}$[GeV]	EM1 [250–300]	EM2 [300–350]	EM3 [350–400]	EM4 [400–500]	EM5 [500–600]	EM6 [600–700]	

Table 7.8. $E_{\mathrm{T}}^{\mathrm{miss}}$ bins used in the simultaneous shape fit.

Since the mono-jet analysis is performed to be a generic new physics search, the fitting strategy should not be set ad-hoc for a single BSM physics process. The shape fit has been compared with the best cut-and-count strategy chosen for the other processes considered in this thesis.

In the ADD scenario for $n = 2, ..., 6$ the maximal sensitivity is reached with the asymmetric cut of $E_{\mathrm{T}}^{\mathrm{miss}} > 700$ GeV and $p_{\mathrm{T}} > 300$ GeV for an integrated luminosity of 3.2 fb^{-1}. The expected limits on the reduced Planck scale M_D, as a function of the number of extra-dimensions n, based on the best cut-and-count strategy and the shape binned fit are shown in Figure 7.12 with 3.2 fb^{-1} of data. The shape fit procedure improve the limits on M_D by about 300 GeV for $n = 2$ and about 200 GeV for $n = 3, 4$. For higher dimensions the improvement is of the order of 100 GeV.

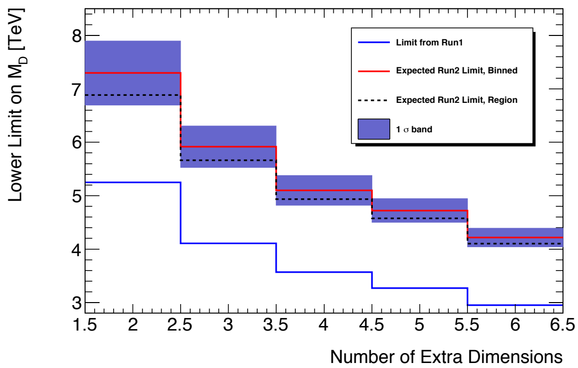

Figure 7.12. Comparison of the lower limits at 95% CL on the reduced Planck scale M_D as a function of the extra-dimensions n between the shape fit, with the binning proposed in Table 7.8, and the best counting experiment with $E_{\mathrm{T}}^{\mathrm{miss}} > 700$ GeV and $p_{\mathrm{T}} > 300$ GeV. The plot is performed normalizing the MC expectations to an integrated luminosity of 3.2 fb^{-1}.

Finally for the SUSY models considered, the SR defined by $E_{\mathrm{T}}^{\mathrm{miss}} > 700$ GeV and leading jet $p_{\mathrm{T}} > 300$ GeV has also been found to be the region that provides the best performance in terms of exclusion limits. A comparison between this and the shape fit method is shown in Figure 7.13 with 3.2 fb^{-1} of integrated luminosity in the compressed scenario in which a squark decays in a neutralino $\tilde{q} \to q + \tilde{\chi}_0$ $(q = u, d, c, s)$. Also in this case the shape fit method improves the expected limits, especially for the largest mass gaps considered.

In conclusion, the shape fit strategy leads to a sensitivity improvement in all the new physics scenarios probed by the analysis.

7.6 Systematic Uncertainties

In order to take into account the biases and the uncertainties coming from experimental measurements and from theoretical predictions, a set of systematic uncertainties are applied. The constraints on the several nuisance parameters are parametrized with gaussian probability density functions that multiply the likelihood described in the previous section and formulated in Eq. (7.17). The mean of the gaussian is

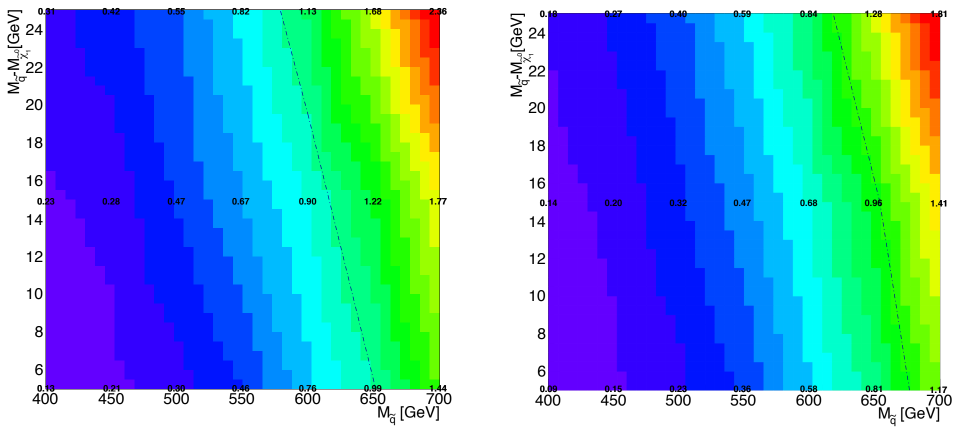

Figure 7.13. Comparison of the signal strength limits at 95% CL on the 2D plane with the squark mass versus the mass splitting between the NLSP and the LSP, between the shape fit, with the binning proposed in Table 7.8, and the best counting experiment with $E_{\mathrm{T}}^{\mathrm{miss}} > 700$ GeV and leading jet $p_{\mathrm{T}} > 300$ GeV. The upper limits on the signal strength are reported in the plots. The MC expectations are normalized to an integrated luminosity of 3.2 fb^{-1}.

set to zero, the variance is defined by the 68% of uncertainty of the measurements described or by the theoretical calculation of a determined process and the gaussian variable constitutes the so-called nuisance parameter. The systematic uncertainties implemented in the likelihood are fully correlated between all the bins. The global simultaneous fit affects the normalization of all the background and signal contributions on which it is applied.

Another kind of systematic applied and taken into account in the analysis arises from limited MC statistics in the samples used. When the relative statistical uncertainty of a MC sample in a given $E_{\mathrm{T}}^{\mathrm{miss}}$ bin is higher than the 5%, a systematic variation is applied to the likelihood model in form of a poissonian probability density function with mean set to one.

An overview of the systematic uncertainties applied in the mono-jet analysis is given in this section for the signals and for the backgrounds separately, while details on the impact of the several systematics in the SR before and after the global fit will be described in Section 7.7.

7.6.1 Background Systematics

In this section the methods to estimate the size of systematic uncertainties associated to the several sources of background are outlined. The considered systematics include the experimental uncertainties that come from physics measurements, like efficiencies or energy scale and resolution extrapolations. Along with the theoretical uncertainties, to take into account the corrections at higher perturbative orders that are not considered in the MC samples used in the analysis.

Luminosity

In order to account the uncertainty on the integrated luminosity measurement, a 5% uncertainty has been applied to all the background contributions except for the NCB and multi-jet backgrounds being these completely data-driven. It is derived following a methodology similar to that detailed in Run-1 [150], from a calibration of the luminosity scale using x-y beam-separation scans performed in August 2015.

Jet Energy Scale and Resolution

The systematic uncertainties given by the estimation of JES and JER affect all the physics processes in the mono-jet analysis and are evaluated by in-situ studies measuring the Z/γ+jets and multi-jet balance. The systematic variations are applied to all the background contributions that are not completely data-driven as a function of the $E_{\mathrm{T}}^{\mathrm{miss}}$ bins. These variations are evaluated by running the selection shifting one parameter at a time by a standard deviation from its nominal value and extracting the difference between the resulting $E_{\mathrm{T}}^{\mathrm{miss}}$ distribution and the nominal one.

The data-driven estimation procedure and the kinematic closeness of the W+jets and Z+jets events in the CRs and SR reduces strongly the impact of these systematics. Also in this case the transfer factors defined in Eq. (7.6) largely cancel the final effects of this source of uncertainty for the main electroweak background (more details will be introduced in Section 7.7.1).

Lepton ID and Energy/Momentum Scale

The lepton related systematics account the uncertainties relative to the identification and reconstruction scale factor efficiencies as well as to the energy or momentum scale and resolution. The requirement of the electron and muon veto in the SR makes the lepton systematics not negligible. In order to take into account the effect of the event migration between signal and controls region, due to the lepton systematic variations, the anti-SF calculation is redone using the SF obtained after the variation of each of the parameters relative to several source of systematic uncertainties. The systematic variations are hence applied to all the MC samples in the several $E_{\mathrm{T}}^{\mathrm{miss}}$ bins following the same procedure used for the JES and JER systematics.

E_T^{miss} Scale and Resolution

The $E_{\mathrm{T}}^{\mathrm{miss}}$ related uncertainties quantify the resolution and scale of the TST measurement obtained by the study of the balance between hard and soft contributions in $Z \to \mu\mu$ events, as described in detail in Reference [115]. The same procedure followed also to extract the jet and lepton related uncertainties has been applied to get the $E_{\mathrm{T}}^{\mathrm{miss}}$ related systematic variations in the different $E_{\mathrm{T}}^{\mathrm{miss}}$ bins used in the global fit.

Trigger

The differences in efficiency between the MC-based efficiency profiles in the SR and in CR1μ, and the ones in CR1μ obtained using data and MC, have been used to estimate the trigger efficiency systematic. Since the efficiency plateau for the `HLT_xe70` trigger is reached at a value below 250 GeV, no uncertainty is considered in the SR.

Top Background

As mentioned in Section 7.1.2, the top background normalization is based on MC simulation. For this reason, a systematic uncertainty related to the modeling of top backgrounds is taken into account. In order to evaluate the size of the top systematic uncertainty in the signal and control regions, the variation between the event yields predicted using different MC simulations is assigned as a systematic uncertainty. In particular a different ME (aMC@NLOHerwig++) and PS (PowhegHerwig++) generators are considered, in addition to PS models with different choices of the factorization and renormalization scales and another MC tuning (`A14`) with respect to PowhegPythia6 used in the analysis. More details on the systematic variations of the top backgrounds can be found in Ref. [152]. The study has been based on $t\bar{t}$ samples, since they provide the leading contribution.

To avoid to be sensitive to statistical fluctuations in the systematic estimation due to the limited size of the corresponding MC samples, the SR and all the CRs are merged in a inclusive region since similar shapes in the $E_{\mathrm{T}}^{\mathrm{miss}}$ distributions were observed. A linear fit for each variation is then performed to evaluate the systematic uncertainty applied to top quark backgrounds for each bin used in the shape fit. The variations evaluated by the fit are all symmetrized and added in quadrature except for the ones relative to the additional lower and higher radiation configurations of which the semi-difference is considered. The several contributions of systematic uncertainty are shown in Figure 7.14.

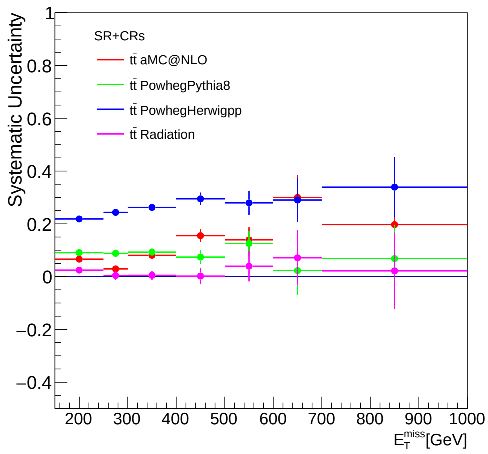

Figure 7.14. Systematic variations between the nominal $t\bar{t}$ model used in the analysis and the model with a different ME generator (in red), MC tuning (in green), parton shower (in blue) and radiation parameters (in pink) as a function of $E_{\mathrm{T}}^{\mathrm{miss}}$. The last bin includes the overflow. A linear fit for each contribution is performed to evaluate the total top systematic.

The final top background systematic uncertainty values for each $E_{\mathrm{T}}^{\mathrm{miss}}$ bin, used in the simultaneous fit, are listed in Table 7.9 and are applied to the $t\bar{t}$ and single-top production processes.

$E_{\mathrm{T}}^{\mathrm{miss}}$ bins	EM1	EM2	EM3	EM4	EM5	EM6	IM7
top BG systematic (%)	30	30	30	35	35	40	40

Table 7.9. Total relative systematic uncertainty (in %) on the top background in the different $E_{\mathrm{T}}^{\mathrm{miss}}$ bins in the signal and control regions.

Diboson Background

Similarly to the top background case, the MC-based diboson backgrounds are affected by a theoretical systematic uncertainty deriving by the specific simulation chosen for the analysis. The difference between the diboson $E_{\mathrm{T}}^{\mathrm{miss}}$ distributions based on SHERPA-2.1.1, used in the analysis, and the samples describing the WW, WZ and ZZ processes based on the POWHEG-BOX v2 generator interfaced to PYTHIA-8.186, is considered in each of the defined region.

Theoretical uncertainties on the NLO WW, WZ and ZZ inclusive cross-sections used in the normalization of these samples are also taken into account. These arise from PDF and scale uncertainties and are estimated in detail in Ref. [153]. They are of the order of 6% and are added in quadrature with half of the relative difference in the yields predicted in the signal and control region, comparing the $E_{\mathrm{T}}^{\mathrm{miss}}$ distributions obtained using the two different MC generators. The 6% absolute normalization systematic is kept the same for all the $E_{\mathrm{T}}^{\mathrm{miss}}$ bins since it affects only the inclusive cross-section. The values used in the analysis are summarized in Table 7.10 and range between 6% and 20% in the SR and CRs increasing with $E_{\mathrm{T}}^{\mathrm{miss}}$.

$E_{\mathrm{T}}^{\mathrm{miss}}$ bins	$[150, 250]$ GeV	EM1	EM2	EM3	EM4	EM5	EM6	IM7
SR	6.1	6.7	6.3	8.5	7.2	12.5	15.2	12.5
CR1e	6.7	6.0	7.8	6.3	6.1	6.0	6.1	6.1
CR1μ	6.3	6.1	6.3	7.2	7.2	10.8	9.2	16.2
CR2μ	8.5	9.2	6.7	7.8	6.3	13.4	19.9	19.9

Table 7.10. Total relative systematic uncertainty (in %) on the diboson background as function of the $E_{\mathrm{T}}^{\mathrm{miss}}$ bins in the SR and CRs. An additional low $E_{\mathrm{T}}^{\mathrm{miss}}$ bin is also added in the list to be used in the validation region (see Section 7.8).

NCB and Multi-jet Backgrounds

The estimation of NCB background is obtained as described in Section 7.4.4 by using the efficiency of the BIB tagger to rescale the events tagged as BIB in the SR. However, several methods exist to construct a BIB-enriched sample that can lead to different tagging efficiency values. The systematic uncertainty on the NCB yield is hence determined by evaluating the tagger efficiency starting from three separate BIB-enriched selections:

1. the technique used in the analysis is based on a BadTight jet sample consisting of events in the SR in which the leading jet fails the tight cleaning criteria that lead to an efficiency of $\varepsilon_{\mathrm{BIB\ tag}} = 25 \pm 0.2\%$ and to a total amount of NCB in the IM1 SR of 112 events.

2. building a sample with events in which the jets in the SR are selected without applying the tight cleaning criteria and in which the leading jet is out-of-time[3] with $t > 5$ ns, the tagger efficiency results to be $\varepsilon_{\mathrm{BIB\ tag}} = 45 \pm 0.7\%$, corresponding to an estimation of 63 NCB events in the IM1 SR.

3. selecting events in the SR without applying the tight jet cleaning criteria and requiring that the leading jet is out-of-time with $t < -5$ ns, the tagger efficiency measured is $\varepsilon_{\mathrm{BIB\ tag}} = 22 \pm 0.4\%$ and corresponding to an estimation of 128 in the IM1 SR.

Figure 7.15 shows the BIB-tagger efficiencies as a function of the jet timing for the three different BIB-enriched selections described above.

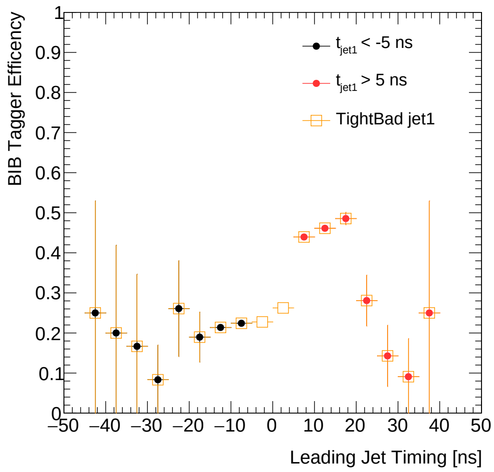

Figure 7.15. The BIB tagger efficiency as a function of the timing of the leading jet for the three different BIB-enriched selections on the NCB yield.

As the early and late jet selections produce NCB estimations significantly different with respect to the nominal one, a conservative 100% systematic uncertainty is applied on the NCB yield.

A conservative 100% systematic uncertainty is also assigned to the multi-jet contribution in each $E_{\mathrm{T}}^{\mathrm{miss}}$ bin.

Theoretical Transfer Factor Systematics

The evaluation of the dominant $Z(\nu\nu)$+jets background from the $W(\mu\nu)$+jets process suffers from systematic uncertainties due to the difference between the W and Z

[3]Out-of-time jets refers to jets occurring before or after the triggered collision event.

processes. In order to take into account such effects, a study based on the truth MC samples is performed comparing the distributions of the $Z(\nu\nu)$+jets processes in the SR and the $W(\mu\nu)$+jets ones in CR1μ, where its contribution is dominant. In this study the requirement on the transverse mass in this CR is not applied in order to increase the kinematical compatibility with the SR.

The shapes of the $E_{\mathrm{T}}^{\mathrm{miss}}$ distributions of the two sources of background are shown in Figure 7.16. The disagreement resulting from the envelope of differences observed in several distributions amounts to a difference of the order of 2-3% and it is assigned as a systematic uncertainty.

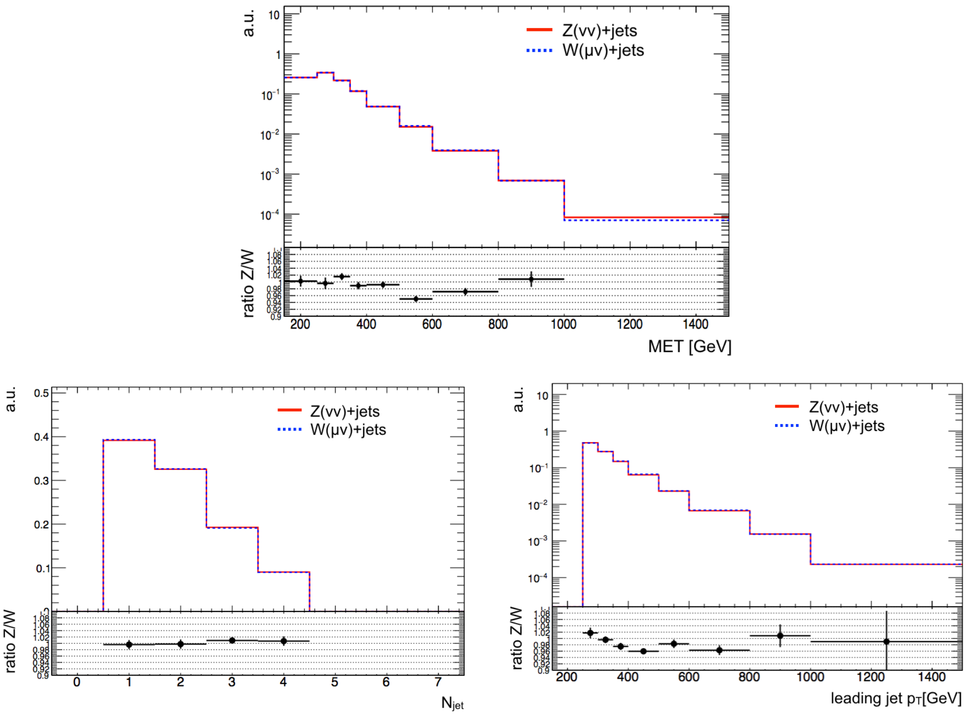

Figure 7.16. Comparison of the truth level $E_{\mathrm{T}}^{\mathrm{miss}}$, jet multiplicity and leading jet p_{T} distributions in the W and Z MC samples in CR1μ without the transverse mass cut and in the SR respectively.

In addition to this uncertainty, possible biases from electroweak corrections to the production of W-bosons with respect to the production of Z-bosons, expected in particular at large p_{T}, were also considered. The effects have been estimated ad-hoc for this analysis as a function of the vector bosons p_{T} updating the study discussed in Ref. [154]. This study consists in the estimation of the electroweak radiative corrections in the W-boson production in pp collisions in association with additional jets, that at the energy reached by LHC are strongly enhanced and can become crucial [155]. Their effect can be observed in Figure 7.17 that shows the distribution of the ratio between the W and Z production cross-sections as a function of the boson p_{T}.

Full electroweak corrections to the W+jets production processes, including virtual and real photons contributions, are hence evaluated. These variations for both the

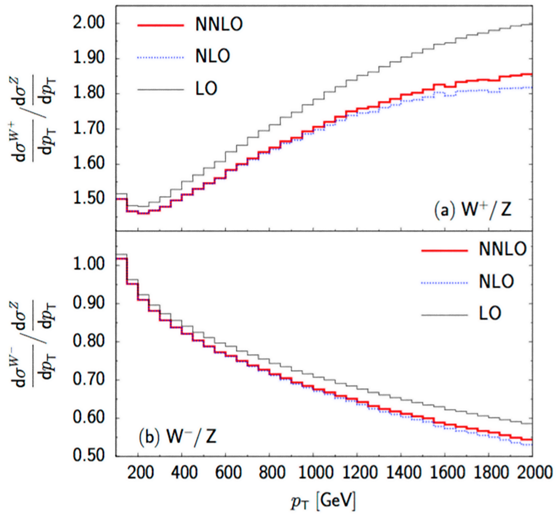

Figure 7.17. Ratio of the boson p_T distributions for the processes that produce W^+j and Zj on the top and W^-j and Zj on the bottom at $\sqrt{s} = 14$ TeV. The LO, NLO, NNLO predictions are plotted with a thin solid, dotted, thick solid lines respectively [154].

inclusive and exclusive E_T^{miss} bin selections are quoted in Table 7.11 and increase at large boson p_T. They suffer from large uncertainties, mainly due to the limited knowledge of the photon PDFs inside the proton. Therefore since the uncertainties on the corrections are actually as large as the correction themselves, a conservative approach has been followed to take into account these sources of uncertainty taking the central absolute value and adding linearly the largest uncertainty in each case.

The final "$W \to Z$ transfer factor" uncertainty used for the $Z(\nu\nu)$ prediction in the SR corresponds to the sum in quadrature of the 3% from MC modeling and the corresponding uncertainty from electroweak corrections. The values used are given in Table 7.12.

EWK correction by theoretical calculations						
EM1	EM2	EM3	EM4	EM5	EM6	
$\left(-0.4^{+1.6}_{-0.8}\right)$	$\left(0.1^{+1.6}_{-1.0}\right)$	$\left(-0.7^{+1.8}_{-1.2}\right)$	$\left(0.2^{+1.8}_{-1.4}\right)$	$\left(0.4^{+2.1}_{-1.9}\right)$	$\left(1.5^{+2.5}_{-2.3}\right)$	
IM1	IM2	IM3	IM4	IM5	IM6	IM7
$\left(-0.3^{+1.6}_{-1.0}\right)$	$\left(-0.1^{+1.7}_{-1.3}\right)$	$\left(-0.1^{+2.2}_{-1.5}\right)$	$\left(0.4^{+2.1}_{-1.7}\right)$	$\left(0.8^{+2.4}_{-2.2}\right)$	$\left(1.6^{+2.3}_{-2.8}\right)$	$\left(1.7^{+2.4}_{-3.5}\right)$

Table 7.11. NLO Z/W electroweak corrections (in %), as given by theoretical calculations. The large uncertainties on these estimations are mostly coming from errors in the photon PDFs.

V+jets Modeling Systematics

Theoretical systematic uncertainties on the SHERPA V+jets production used as nominal MC samples are evaluated varying the choice of the parameters set fixed

Total $W \to Z$ transfer factor uncertainties						
EM1	EM2	EM3	EM4	EM5	EM6	
±3.5	±3.5	±4.0	±4.0	±4.0	±5.0	
IM1	IM2	IM3	IM4	IM5	IM6	IM7
±3.5	±3.5	±4.0	±4.0	±4.5	±5.0	±6.0

Table 7.12. Final $W \to Z$ transfer factor uncertainties (in %), combining contributions from the MC modeling and the EWK corrections differences in the W+jets and Z+jets production.

in the generation. These parameters are the ME matching scale (CKKW) which is varied from the nominal value of 20 GeV to 30 and 15 GeV and the renormalization μ_R[4], factorization μ_F[5] and resummation μ_{QSF}[6] scales that are varied by a factor 2 and 1/2 with respect to their nominal value.

For this study a 2D parameterization is performed, binning the boson p_{T} (i) and the jet multiplicity (j) variables. For each sample (sliced in boson p_{T} and flavor filter as described in Section 7.1.2) a weight is calculated as the ratio of the number of events in a specific region of the nominal sample and the number of events in the variated sample, treating the up and down variations separately:

$$w_{i,j} = \frac{N_{i,j}^{syst}}{N_{i,j}^{nom}} \,. \tag{7.18}$$

This parametrization allows to assign weights to the nominal samples based on the number of truth jets ($p_{\mathrm{T}} > 20$ GeV and $|\eta| < 2.8$) for each of the different systematic variations considered above.

In order to extract the uncertainties based on this method, the effect of the variations on the transfer factor, defined for a given V+jets sample (Eq. (7.5)), has been evaluated based on the resulting distributions obtained applying the weight defined above. The CR used for each electroweak background is the one in which the sample is constrained: in the case of $Z(\nu\nu)$+jets and $W(\mu\nu)$+jets it is CR1μ, for $W(e\nu)$+jets and $W(\tau\nu)$+jets it is CR1e and for the $Z(\mu\mu)$+jets samples it is CR2μ (for all the processes with the Z boson decaying into charged leptons the same uncertainty extracted for $Z(\mu\mu)$+jets is used). The relative differences of each of the systematic variations (up and down) on the transfer factors for the electroweak backgrounds in each $E_{\mathrm{T}}^{\mathrm{miss}}$ bin are shown in Figure 7.18.

These variations are used for the final uncertainty by taking for each $E_{\mathrm{T}}^{\mathrm{miss}}$ bin the largest deviation from zero (from either up or down variation). The resulting uncertainties applied to the SR yields of the corresponding samples for each $E_{\mathrm{T}}^{\mathrm{miss}}$ bin are listed in Table 7.13.

A summary of all uncertainties applied to the backgrounds in the analysis is given in Table 7.14, along with the shorthand name of the systematic used throughout the

[4] μ_R varies the scale for the running strong coupling constant for the underlying hard process.
[5] μ_F varies the scale used for the PDFs.
[6] μ_{QSF} varies the scale used for the resummation of soft gluon emission.

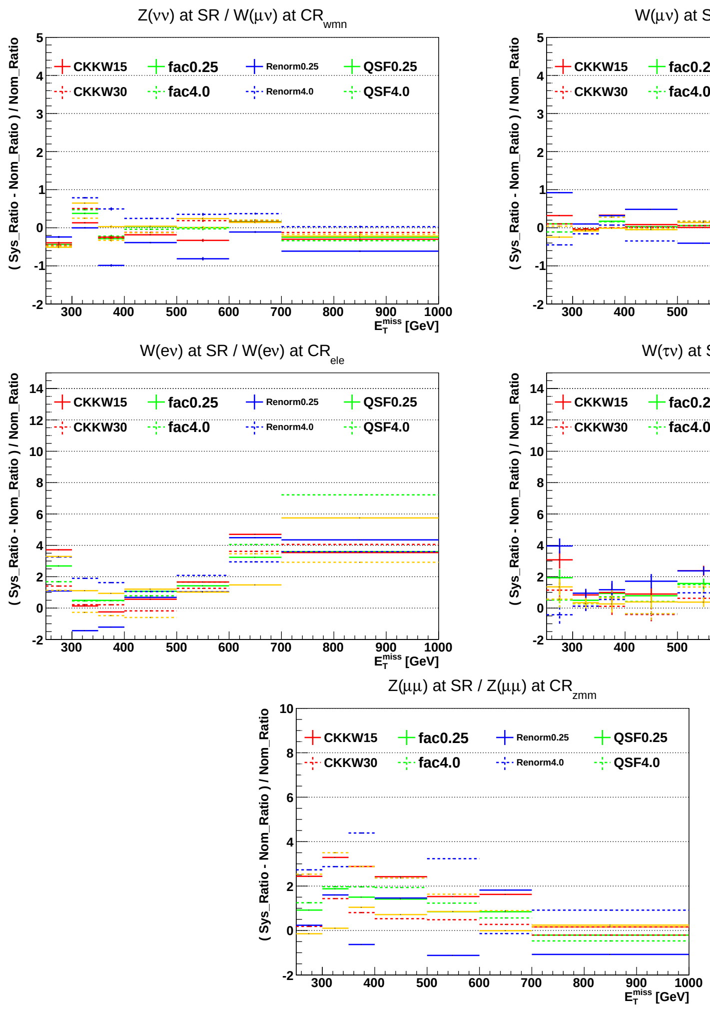

Figure 7.18. Relative difference of the transfer factor for the different systematic variations as a function of E_T^{miss} for V+jets backgrounds in their corresponding regions.

Background	[150, 250] GeV	EM1	EM2	EM3	EM4	EM5	EM6	IM7
$Z(\nu\nu)$+jets	0.2	0.51	0.8	1.0	0.4	0.8	0.4	0.6
$Z(\ell^+\ell^-)$+jets	7.1	2.7	3.5	4.4	2.4	3.2	1.8	1.1
$W(e\nu)$+jets	6.6	3.7	1.9	1.6	1.2	2.1	4.7	7.2
$W(\mu\nu)$+jets	1.1	0.9	0.2	0.3	0.5	0.4	0.3	1.3
$W(\tau\nu)$+jets	7.7	4.0	1.0	1.2	1.7	2.4	4.5	3.9

Table 7.13. Final V+jets systematic uncertainties (in %) for the different Sherpa samples, for each E_T^{miss} bin. An additional low E_T^{miss} bin is also added in the list to be used in the validation region study (see Section 7.8).

analysis, which is useful in the examination of spectra throughout this section.

Systematic uncertainty	Short description
	Electrons
EL_EFF_Reco	reconstruction efficiency uncertainty
EL_EFF_ID	ID efficiency uncertainty
EL_EFF_Iso	isolation efficiency uncertainty
EG_SCALE_ALL	energy scale uncertainty
EG_RESO_ALL	energy resolution uncertainty
	Muons
MUON_EFF_STAT	statistical component of the reconstruction and ID efficiency uncertainty
MUON_EFF_SYS	systematic component of the reconstruction and ID efficiency uncertainty
MUONS_SCALE	energy scale uncertainty
MUONS_ID	energy resolution uncertainty from inner detector
MUONS_MS	energy resolution uncertainty from muon system
	Jets
JET_GroupedNP	energy scale uncertainty split into 3 components
JET_JER_SINGLE_NP	energy resolution uncertainty
	$E_{\mathbf{T}}^{\mathbf{miss}}$
MET_SoftTrk_ResoPerp	track-based soft term related to transversal resolution uncertainty
MET_SoftTrk_ResoPara	track-based soft term related to longitudinal resolution uncertainty
MET_SoftTrk_Scale	track-based soft term related to longitudinal scale uncertainty
	Other sources
lumi	uncertainty on the total integrated luminosity
top	theoretical uncertainty on the top processes
NCB	uncertainty on the non-collision background
multi-jet	uncertainty on the multi-jet background
diboson	theoretical uncertainty on the diboson processes
VJets	theoretical uncertainty on the V+jets processes due to the MC modeling
WZ	theoretical uncertainty on the $W \to Z$ transfer factor

Table 7.14. Qualitative summary of the background systematic uncertainties considered in the analysis.

7.6.2 Signal Systematics

In this section the theoretical systematics evaluated for the signal processes and considered in this thesis are described. The uncertainty relative to the scale choice, PDFs and to the initial and final state radiation (ISR and FSR) are taken into account and studied in detail for each process.

DM Simplified Models

The theoretical uncertainties have been evaluated only for the axial-vector mediator samples because the analysis is not sensitive to the chosen generated samples with pseudo-scalar mediators with the first 3.2 fb^{-1} of data, as it will be shown in Section 7.9.3.

The PDF uncertainties are evaluated following the recommendations in Ref. [156] where the final uncertainty is derived as the envelope of the variations of the cross-section (given by the variation of the total number of signal events) and acceptance (defined by the ratio of number of signal events in a particular bin of the signal region). This is then divided by the total number of signal events, due to choosing different

PDF sets and their error sets. As just mentioned in Section 7.1.2 the nominal PDF set used is NNPDF30_nlo_as_0118 while the sets chosen to evaluate the variations are MMHT2014nlo68cl and CT10nlo. The resulting systematics associated to the DM samples amounts to 10% on the acceptance for DM masses between 100 GeV and 1 TeV and 20% otherwise, and 10% on the cross-sections.

The systematic uncertainty associated to the renormalization and factorization scales (μ_F and μ_R) is evaluated using six different variations: $(\mu_F, \mu_R) = [(1.0, 1.0)$, $(0.5, 0.5)$, $(0.5, 1)$, $(0.5, 2.0)$, $(2, 0.5)$, $(0.5, 1.0)$, $(2.0, 2.0)]$. The differences in the cross-sections and acceptances from all six variations with respect to their nominal values are summed up in quadrature and amount to 5% on the cross-sections and 3% on the acceptances.

Finally, the ISR/FSR modeling uncertainty has been evaluated following the recommendations in Ref. [136] via the VAR3a, VAR3b and VAR3c hessian variations of the A14 tune for PS in Pythia. The impact of these tune variations on the acceptance is estimated to be of 20% and negligible on the cross-sections.

ADD Model

As done for the DM simplified models, the systematic uncertainties due to the PDF choice for the ADD MC samples are evaluated comparing the impacts of using `CT10` and MMHT2014 [157] PDF sets with the nominal NNPDF23 via the LHCPDF re-weighting technique [158]. The final PDF uncertainty corresponds to the envelope that contains the error bands from the three PDF sets. The resulting uncertainty from PDF applied to the signal ADD samples ranges between 16% and 42% on the cross-sections increasing the number of dimension from $n = 2$ to $n = 6$ and from few percents up to 20% on the acceptance in the different $E_{\mathrm{T}}^{\mathrm{miss}}$ bins.

The renormalization and factorization scales are varied simultaneously by a factor 2 and 0.5 in truth-level MC samples. The final uncertainty has been evaluated as the average between the up and down variations. The scale variation affects mainly the cross-sections, and varies between 23% and 36% with the increase of the number of dimensions n.

A set of five MC generation tune parameters are varied in order to cover uncertainties from PS effects. For each number of extra-dimensions ten systematic samples are produced at the truth level and the resulting effect on the acceptances is between 7% and 11% decreasing with the $E_{\mathrm{T}}^{\mathrm{miss}}$ rise.

SUSY Scenarios

The PDF uncertainties are obtained also in this case by computing re-weight of the signal samples to NNPDF23LO, CT10LO and MMHT2014 PDF sets and by varying each PDF set by its own uncertainties. The resulting uncertainty on the cross-section and the acceptance is between 5% and 17%, increasing at higher squark mass.

Following the same procedure adopted for the ADD signal samples the factorization and normalization scale uncertainties have been estimated to vary between 4% and 13% in the signal yields.

The MC generation tune parameters are varied in order to cover the uncertainties coming from PS. The effect on the acceptance for all the considered signal samples is estimated to be between 7% and 27%.

7.7 Background-Only Fit

A background-only fit on the CRs is performed in order to evaluate the agreement between the data and MC and to assess the different background contributions in each region. It is also used to evaluate the impact of the several sources of systematic uncertainties in the SR.

The results of the fit in the CRs are shown in detail in Table 7.15 for the IM1 selection using the entire data sample of 3.2 fb^{-1}. All the background processes are listed for each of the three CRs with their associated uncertainties including both the statistic and systematic components. The yields are shown before and after the fit where the normalization factors change slightly the normalization, since good agreement is observed already in the pre-fit data-MC comparison.

IM1 control regions	CR1e	CR1μ	CR2μ
Observed events (3.2 fb^{-1})	3559	10481	1488
SM prediction (post-fit)	3559 ± 60	10480 ± 100	1488 ± 39
Fitted $W(e\nu)$	2410 ± 140	0.4 ± 0.1	–
Fitted $W(\mu\nu)$	2.4 ± 0.3	8550 ± 330	1.8 ± 0.3
Fitted $W(\tau\nu)$	462 ± 27	435 ± 28	0.14 ± 0.02
Fitted $Z(ee)$	0.5 ± 0.1	–	–
Fitted $Z(\mu\mu)$	0.02 ± 0.02	143 ± 10	1395 ± 41
Fitted $Z(\tau\tau)$	30 ± 2	22 ± 4	0.5 ± 0.1
Fitted $Z(\nu\nu)$	1.8 ± 0.1	2.3 ± 0.2	–
Expected $t\bar{t}$, single top	500 ± 150	1060 ± 330	42 ± 13
Expected diboson	150 ± 13	260 ± 25	48 ± 5
SM prediction (pre-fit)	3990 ± 320	10500 ± 710	1520 ± 98
Fit input $W(e\nu)$	2770 ± 210	0.4 ± 0.1	–
Fit input $W(\mu\nu)$	2.4 ± 0.3	8500 ± 520	1.8 ± 0.2
Fit input $W(\tau\nu)$	531 ± 39	500 ± 34	0.16 ± 0.03
Fit input $Z(ee)$	0.5 ± 0.1	–	–
Fit input $Z(\mu\mu)$	0.02 ± 0.02	146 ± 13	1427 ± 92
Fit input $Z(\tau\tau)$	34 ± 3	25 ± 4	0.6 ± 0.1
Fit input $Z(\nu\nu)$	1.8 ± 0.1	2.2 ± 0.1	–
Fit input $t\bar{t}$, single top	500 ± 160	1060 ± 340	42 ± 13
Fit input diboson	150 ± 13	260 ± 25	48 ± 5

Table 7.15. Data and background predictions in the CRs before (bottom) and after (top) the fit is performed for the IM1 selection using 3.2 fb^{-1} of data. The background predictions include both statistical and systematic uncertainties. The contributions from multi-jet and NCB are negligible in the CRs and are not included in the table [116].

A background-only fit in the CRs has been performed and the fitted values of the normalization factors are shown in Figure 7.19. A good agreement with unity is observed for all of them with values that range between 0.8 and 1.2 in all the $E_{\mathrm{T}}^{\mathrm{miss}}$ bins in all the regions. Although the normalization factors of CR1e are close

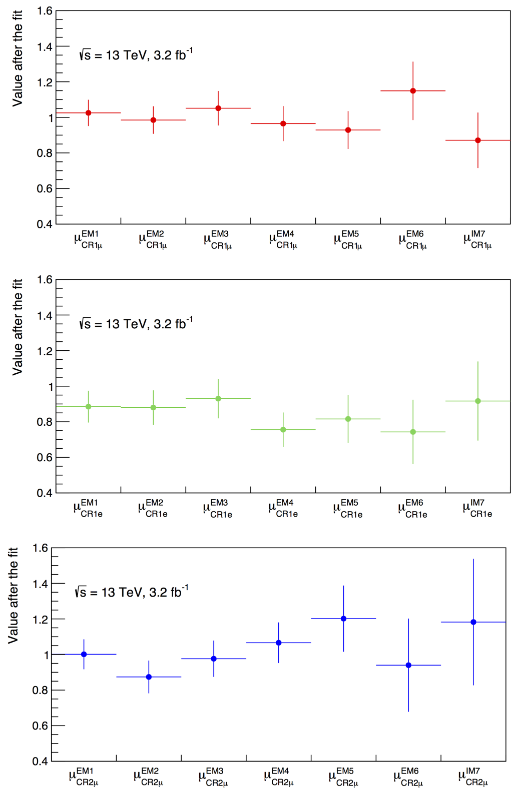

Figure 7.19. Normalization factors fitted by the background-only fit in the CRs in each exclusive bin. An overall good agreement with unity is observed.

to unity within uncertainties, the mean value is smaller than one, which shows how the high boson p_{T} regime is not perfectly modelled by the MC simulation.

All the other fitted nuisance parameters, introduced to take into account the systematic uncertainties, are in agreement with the nominal values and are not particularly constrained by the fit. A detailed description of the impacts of each systematic uncertainty on the several signal and control region yields is addressed in the next section.

In Tables 7.16–7.18 the results for the total background predictions are shown in each of the CRs for the inclusive and exclusive $E_{\mathrm{T}}^{\mathrm{miss}}$ selections. The distributions of the most relevant variables of the three CRs are shown in Figures 7.20–7.22 where the MC predictions include normalization factors extracted from the simultaneous shape fit. The MC simulations and the data-driven approach used provides a good description of the shape of the several distributions in the different CRs.

The fully correlation treatment of all the systematic uncertainties over all the $E_{\mathrm{T}}^{\mathrm{miss}}$ spectrum leads to a correlation between the normalization factors. This allows to take into account the subleading effect of the event migration among the neighbors $E_{\mathrm{T}}^{\mathrm{miss}}$ bins. It can be observed looking at the correlation matrices shown in Figure 7.23 when the systematics are turned off (top plot), where the normalization factors are strongly uncorrelated, and when they are normally applied (bottom plot).

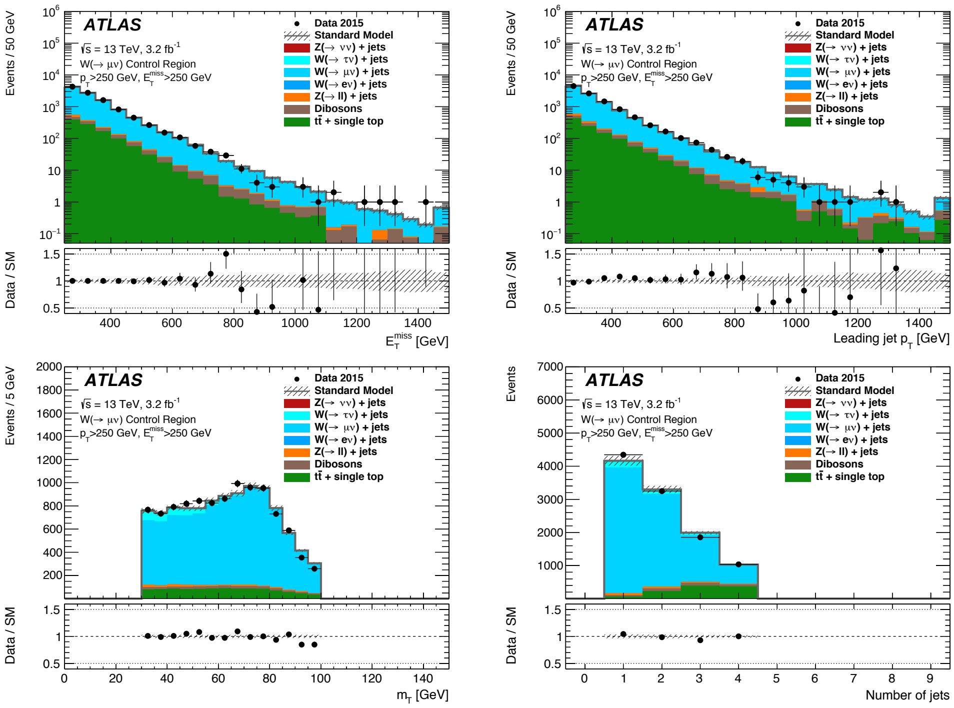

Figure 7.20. Data/MC comparison plots of the $E_{\mathrm{T}}^{\mathrm{miss}}$, leading-jet p_{T}, transverse mass and jet multiplicity distributions in CR1μ, for the IM1 selection, using 3.2 fb^{-1} of data. The MC expectations include the global normalization factors extracted from the background-only fit in the CRs performed in exclusive $E_{\mathrm{T}}^{\mathrm{miss}}$ bins. The error bands in the ratios include the statistical and experimental uncertainties obtained from the same fit [116].

Inclusive bins	IM1	IM2	IM3	
Observed events	10481	6279	3538	
SM prediction (post-fit)	10480 ± 100	6279 ± 79	3538 ± 60	
SM prediction (pre-fit)	10500 ± 710	6350 ± 460	3560 ± 280	
Exclusive bins	EM1	EM2	EM3	
Observed events	4202	2741	1599	
SM prediction (post-fit)	4202 ± 65	2741 ± 52	1599 ± 40	
SM prediction (pre-fit)	4140 ± 260	2800 ± 190	1540 ± 120	
Inclusive bins	IM4	IM5	IM6	IM7
Observed events	1939	677	261	95
SM prediction (post-fit)	1939 ± 44	677 ± 26	261 ± 16	95 ± 10
SM prediction (pre-fit)	2010 ± 160	700 ± 57	256 ± 23	106 ± 9
Exclusive bins	EM4	EM5	EM6	
Observed events	1262	416	166	
SM prediction (post-fit)	1262 ± 36	416 ± 20	166 ± 13	
SM prediction (pre-fit)	1310 ± 100	444 ± 35	150 ± 14	

Table 7.16. Data and SM background prediction, before and after the fit, in CR1μ for the exclusive and inclusive $E_{\mathrm{T}}^{\mathrm{miss}}$ bins using 3.2 fb^{-1} of data. For the SM predictions both the statistical and systematic uncertainties are included [116].

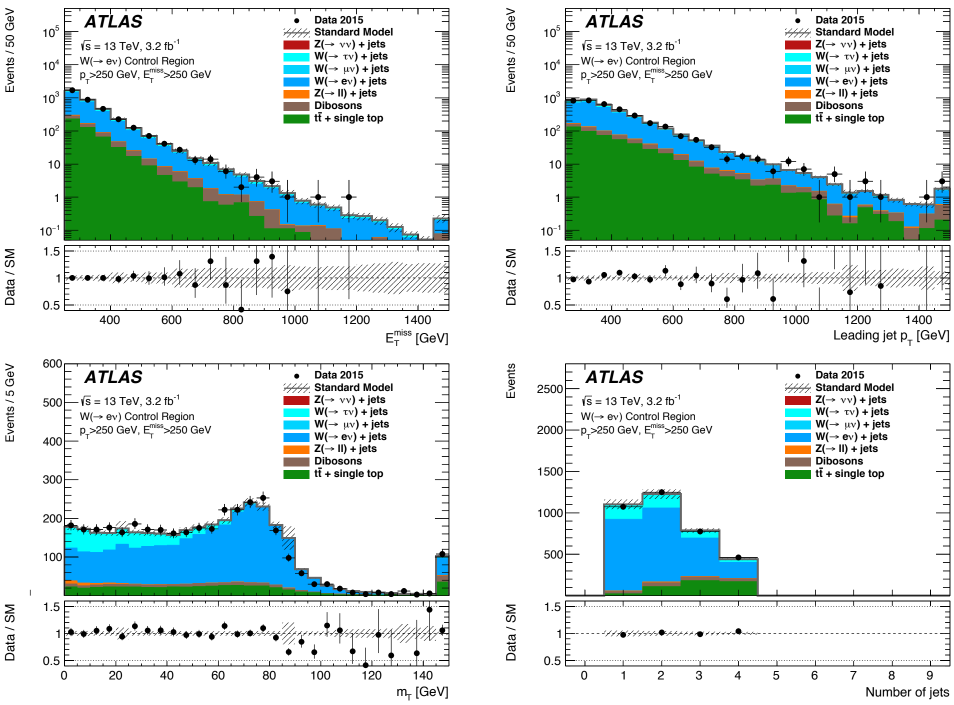

Figure 7.21. Data/MC comparison plots of the E_T^{miss}, leading-jet p_T, transverse mass and jet multiplicity distributions in CR1e, for the IM1 selection, using 3.2 fb^{-1} of data. The MC expectations include the global normalization factors extracted from the background-only fit in the CRs performed in exclusive E_T^{miss} bins. The error bands in the ratios include the statistical and experimental uncertainties obtained from the same fit [116].

Inclusive bins	IM1	IM2	IM3	
Observed events	3559	1866	992	
SM prediction (post-fit)	3559 ± 60	1866 ± 43	992 ± 32	
SM prediction (pre-fit)	3990 ± 320	2110 ± 170	1142 ± 94	
Exclusive bins	EM1	EM2	EM3	
Observed events	1693	874	460	
SM prediction (post-fit)	1693 ± 41	874 ± 30	460 ± 21	
SM prediction (pre-fit)	1880 ± 150	971 ± 79	488 ± 40	
Inclusive bins	IM4	IM5	IM6	IM7
Observed events	532	183	72	32
SM prediction (post-fit)	532 ± 23	183 ± 14	72 ± 8	32 ± 6
SM prediction (pre-fit)	654 ± 54	216 ± 19	85 ± 8	34 ± 3
Exclusive bins	EM4	EM5	EM6	
Observed events	349	111	40	
SM prediction (post-fit)	349 ± 19	111 ± 11	40 ± 6	
SM prediction (pre-fit)	439 ± 36	131 ± 12	50 ± 5	

Table 7.17. Data and SM background prediction, before and after the fit, in CR1e for the exclusive and inclusive E_T^{miss} bins using 3.2 fb^{-1} of data. For the SM predictions both the statistical and systematic uncertainties are included [116].

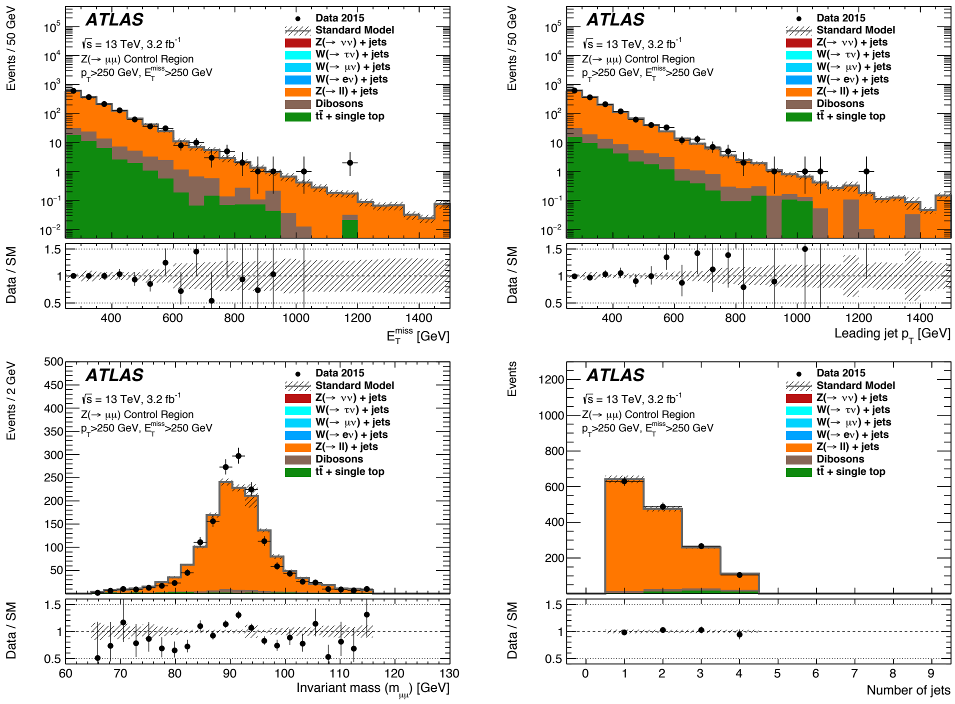

Figure 7.22. Data/MC comparison plots of the $E_{\mathrm{T}}^{\mathrm{miss}}$, leading-jet p_{T}, transverse mass and jet multiplicity distributions in CR2μ, for the IM1 selection, using 3.2 fb^{-1} of data. The MC expectations include the global normalization factors extracted from the background-only fit in the CRs performed in exclusive $E_{\mathrm{T}}^{\mathrm{miss}}$ bins. The error bands in the ratios include the statistical and experimental uncertainties obtained from the same fit [116].

Inclusive bins	IM1	IM2	IM3	
Observed events	1488	877	505	
SM prediction (post-fit)	1488 ± 39	877 ± 30	505 ± 22	
SM prediction (pre-fit)	1520 ± 98	910 ± 59	487 ± 34	
Exclusive bins	EM1	EM2	EM3	
Observed events	611	372	212	
SM prediction (post-fit)	611 ± 25	372 ± 19	212 ± 15	
SM prediction (pre-fit)	610 ± 42	422 ± 36	217 ± 15	
Inclusive bins	IM4	IM5	IM6	IM7
Observed events	293	100	33	15
SM prediction (post-fit)	293 ± 17	100 ± 10	33 ± 6	15 ± 4
SM prediction (pre-fit)	271 ± 19	89 ± 7	32 ± 3	13 ± 1
Exclusive bins	EM4	EM5	EM6	
Observed events	193	67	18	
SM prediction (post-fit)	193 ± 14	67 ± 8	18 ± 4	
SM prediction (pre-fit)	182 ± 13	57 ± 4	19 ± 2	

Table 7.18. Data and SM background prediction, before and after the fit, in CR2μ for the exclusive and inclusive $E_{\mathrm{T}}^{\mathrm{miss}}$ bins using 3.2 fb^{-1} of data. For the SM predictions both the statistical and systematic uncertainties are included [116].

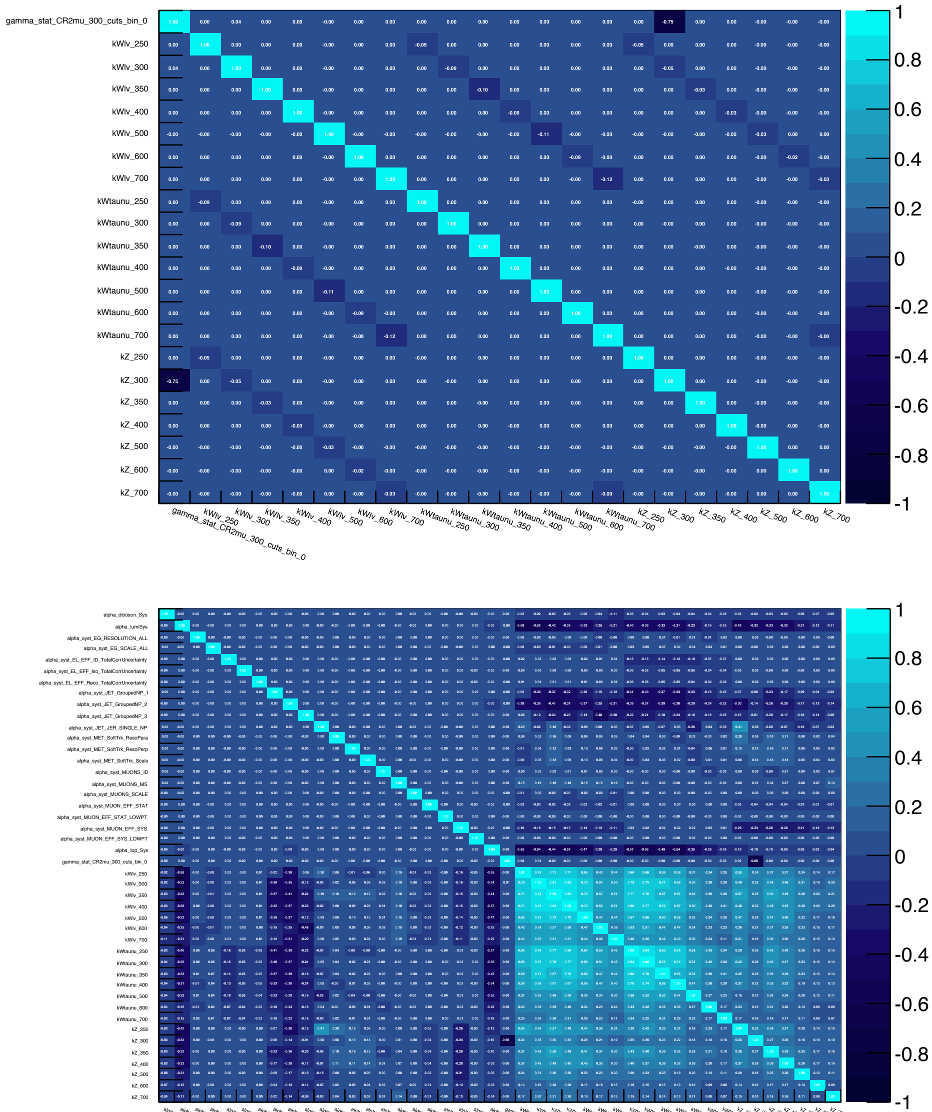

Figure 7.23. Correlation matrix for the fit parameters turning off (on) the systematics on the top (bottom). On the axes there are the parameters of the fit, that include all the nuisance parameters related to the systematic uncertainties and the normalization factors.

7.7.1 Impact of Systematic Uncertainties

All the systematic uncertainties applied to each background process lead to an impact in the SR in terms of variations of the expected yields of the several background and signal contributions. In Table 7.19 the pre-fit impacts, in percent, of each of the nuisance parameter included in the fit that produces a not negligible effect is listed in each of the CRs and in the SR. The values are calculated as the variation of the fitted event yield in a given region obtained by shifting up and down by a standard deviation each of the parameters at a time. If the parameter variation leads to a decrease of the final yields in the region a negative impact is listed and vice versa. The α_i parameters correspond to all the nuisance parameters included in the fit constrained by a gaussian probability density function, while the γ one is constrained by a Poissonian and represents the statistical uncertainty due to the low statistics of the $W(\mu\nu), W(\tau\nu), Z(\tau\tau)$ background MC samples in CR2μ.

The biggest pre-fit impacts come from the luminosity systematic applied to all the MC samples, the jet energy scale and resolution systematics that are all described with four de-correlated nuisance parameters with an effect of 2-3% in all regions and to the top systematic that affects all regions. Since it is associated to the main background in the region, the $W \to Z$ transfer systematic provides one of the larger uncertainties in the SR. Systematics related to muons and electrons mainly affect the CRs that require the presence of leptons in the final state, anyway a minor effect in the other regions is also present due to the lepton veto.

In order to evaluate the impact of each systematic uncertainty in the SR after the fit, a background-only fit in the CRs is performed by shifting up or down by one standard deviation and fixing each nuisance parameter at a time. Then the impact on the total fitted event yields in the SR is estimated. The statistical uncertainty is also evaluated by fixing all the nuisance parameters to their initial values and performing the fit, while the total uncertainties are obtained by leaving all the nuisance parameters free and performing the background-only fit as performed to get Table 7.15. In the last column of Table 7.20 the post-fit impacts of the systematic uncertainties in the IM1 are listed in percent, while in the other columns the impact in the different bins are quoted. The systematic uncertainties that are applied only to the samples in the SR ($W \to Z$, V+jets modeling, multi-jet) are separated from the others since the relative nuisance parameters does not take part to the fit on the CRs and their effects are not included in the value in the bottom of Table 7.20.

The impact of luminosity and jet-related uncertainties is reduced after the simultaneous fit. This can be explained by the fact that the impact on the numerator and on the denominator of the transfer factor mostly canceled out by the ratio. On the other hand, the systematics that affect only the SR maintain their pre-fit impact almost unchanged after the fit. Among these the $W \to Z$ transfer systematic is the most important, as it is applied to the main SR background, and amounts to more than 2%. Theoretical uncertainties on the top-quark background prediction, which is obtained from MC, have an impact of more than 2% on the background normalization. Muon systematic uncertainties also have an impact after the fit of the order of 2% (increasing with $E_{\mathrm{T}}^{\mathrm{miss}}$), due to the fact that they do not cancel out in the ratio between the $Z(\nu\nu)$+jets and $W(\mu\nu)$+jets prediction in the transfer factor.

Systematic	SR	CR1μ	CR2μ	CR1e
α_{NCB}	$(-0.50, 0.50)$	$(0.00, 0.00)$	$(0.00, 0.00)$	$(0.00, 0.00)$
α_{VJets}	$(-1.18, 1.18)$	$(0.00, 0.00)$	$(0.00, 0.00)$	$(0.00, 0.00)$
α_{WZ}	$(-2.05, 2.05)$	$(0.00, 0.00)$	$(0.00, 0.00)$	$(0.00, 0.00)$
$\alpha_{\mathrm{multi\text{-}jet}}$	$(-0.22, 0.23)$	$(0.00, 0.00)$	$(0.00, 0.00)$	$(0.00, 0.00)$
$\alpha_{\mathrm{diboson}}$	$(-0.18, 0.18)$	$(-0.18, 0.18)$	$(-0.28, 0.28)$	$(-0.25, 0.25)$
α_{lumi}	$(-4.96, 4.96)$	$(-5.00, 5.00)$	$(-5.00, 5.00)$	$(-5.00, 5.00)$
$\alpha_{\mathrm{EG\ RESO\ ALL}}$	$(0.00, 0.00)$	$(0.00, 0.00)$	$(0.00, 0.00)$	$(-0.01, -0.03)$
$\alpha_{\mathrm{EG\ SCALE\ ALL}}$	$(0.02, -0.02)$	$(0.00, 0.00)$	$(0.00, 0.00)$	$(0.44, -0.39)$
$\alpha_{\mathrm{EL\ EFF\ ID}}$	$(0.31, -0.31)$	$(0.06, -0.06)$	$(0.02, -0.02)$	$(-1.21, 1.21)$
$\alpha_{\mathrm{EL\ EFF\ Iso}}$	$(0.00, 0.00)$	$(0.00, 0.00)$	$(0.00, 0.00)$	$(-0.44, 0.44)$
$\alpha_{\mathrm{EL\ EFF\ Reco}}$	$(0.11, -0.11)$	$(0.02, -0.02)$	$(0.01, -0.01)$	$(-0.46, 0.46)$
$\alpha_{\mathrm{JET\ GroupedNP\ 1}}$	$(-1.52, 1.31)$	$(-1.44, 1.35)$	$(-1.18, 0.62)$	$(-3.08, 3.17)$
$\alpha_{\mathrm{JET\ GroupedNP\ 2}}$	$(-2.21, 2.06)$	$(-2.21, 2.42)$	$(-2.31, 1.63)$	$(-2.89, 3.15)$
$\alpha_{\mathrm{JET\ GroupedNP\ 3}}$	$(-0.79, 0.83)$	$(-0.95, 0.56)$	$(-1.14, 0.81)$	$(-1.61, 1.87)$
$\alpha_{\mathrm{JET\ JER\ SINGLE\ NP}}$	$(-0.37, 0.37)$	$(0.42, -0.42)$	$(1.05, -1.05)$	$(-0.28, 0.28)$
$\alpha_{\mathrm{MET\ SoftTrk\ ResoPara}}$	$(0.11, -0.11)$	$(0.47, -0.47)$	$(1.23, -1.23)$	$(0.24, -0.24)$
$\alpha_{\mathrm{MET\ SoftTrk\ ResoPerp}}$	$(0.16, -0.16)$	$(0.33, -0.33)$	$(1.11, -1.11)$	$(0.05, -0.05)$
$\alpha_{\mathrm{MET\ SoftTrk\ Scale}}$	$(0.11, -0.10)$	$(0.23, -0.24)$	$(0.55, -1.14)$	$(0.06, -0.12)$
$\alpha_{\mathrm{MUONS\ ID}}$	$(0.00, 0.00)$	$(0.15, 0.03)$	$(0.10, 0.04)$	$(0.00, 0.00)$
$\alpha_{\mathrm{MUONS\ MS}}$	$(-0.02, 0.01)$	$(1.35, -0.59)$	$(0.43, -0.11)$	$(0.00, 0.00)$
$\alpha_{\mathrm{MUONS\ SCALE}}$	$(0.00, 0.00)$	$(0.00, 0.02)$	$(0.01, -0.03)$	$(0.00, 0.00)$
$\alpha_{\mathrm{MUON\ EFF\ STAT}}$	$(0.13, -0.13)$	$(-0.16, 0.16)$	$(-0.33, 0.33)$	$(0.03, -0.03)$
$\alpha_{\mathrm{MUON\ EFF\ SYS}}$	$(0.83, -0.83)$	$(-0.88, 0.89)$	$(-2.11, 2.13)$	$(0.15, -0.15)$
α_{top}	$(-1.06, 1.06)$	$(-3.15, 3.15)$	$(-0.85, 0.85)$	$(-3.85, 3.85)$

Table 7.19. Pre-fit impact of the various systematic uncertainties on the overall background prediction in the signal and control regions, in %. The impacts after shifting up and down the different systematic uncertainties are reported between the parentheses.

Systematic	EM1	EM2	EM3	EM4	EM5	EM6	IM7	IM1
α_{NCB}	(−0.65, 0.65)	(−0.39, 0.40)	(−0.59, 0.59)	(−0.39, 0.40)	(0.00, 0.00)	(0.00, 0.00)	(0.00, 0.00)	(−0.51, 0.52)
α_{VJets}	(−1.52, 1.52)	(−0.81, 0.81)	(−0.96, 0.96)	(−0.61, 0.61)	(−1.04, 1.04)	(−0.94, 0.94)	(−1.29, 1.29)	(−1.13, 1.13)
α_{WZ}	(−1.89, 1.89)	(−2.03, 2.03)	(−2.42, 2.42)	(−2.59, 2.59)	(−2.57, 2.57)	(−3.56, 3.56)	(−3.90, 3.90)	(−2.14, 2.14)
$\alpha_{\mathrm{multi\text{-}jet}}$	(−0.23, 0.24)	(−0.24, 0.24)	(−0.18, 0.18)	(−0.34, 0.34)	(−0.09, 0.09)	(−0.06, 0.06)	(−0.25, 0.25)	(−0.23, 0.23)
$\alpha_{\mathrm{diboson}}$	(−0.02, 0.02)	(−0.07, 0.06)	(−0.02, 0.02)	(−0.06, 0.05)	(0.10, −0.09)	(0.27, −0.29)	(−0.42, 0.43)	(−0.03, 0.03)
α_{lumi}	(−0.44, 0.40)	(−0.52, 0.46)	(−0.52, 0.48)	(−0.61, 0.53)	(−0.57, 0.53)	(−0.54, 0.34)	(−0.60, 0.47)	(−0.50, 0.44)
$\alpha_{\mathrm{EG\ RESO\ ALL}}$	(0.03, 0.01)	(0.01, 0.01)	(0.01, −0.04)	(−0.02, 0.03)	(0.02, −0.01)	(−0.10, 0.07)	(0.11, −0.03)	(0.01, 0.01)
$\alpha_{\mathrm{EG\ SCALE\ ALL}}$	(0.08, −0.11)	(0.12, −0.08)	(0.13, −0.16)	(0.06, −0.07)	(0.13, −0.07)	(−0.02, −0.15)	(0.09, 0.07)	(0.10, −0.10)
$\alpha_{\mathrm{EL\ EFF\ ID}}$	(−0.58, 0.59)	(−0.59, 0.60)	(−0.54, 0.55)	(−0.44, 0.45)	(−0.68, 0.68)	(−0.51, 0.52)	(−0.61, 0.62)	(−0.56, 0.57)
$\alpha_{\mathrm{EL\ EFF\ Iso}}$	(−0.12, 0.12)	(−0.12, 0.13)	(−0.11, 0.11)	(−0.10, 0.10)	(−0.12, 0.09)	(−0.09, 0.11)	(−0.10, 0.07)	(−0.12, 0.12)
$\alpha_{\mathrm{EL\ EFF\ Reco}}$	(−0.22, 0.22)	(−0.22, 0.22)	(−0.20, 0.20)	(−0.16, 0.17)	(−0.25, 0.24)	(−0.21, 0.22)	(−0.31, 0.29)	(−0.21, 0.21)
$\alpha_{\mathrm{JET\ GroupedNP\ 1}}$	(−0.98, 1.13)	(−0.86, −0.22)	(0.23, 0.46)	(0.39, 0.08)	(−0.12, 1.02)	(−0.76, −0.89)	(1.02, 1.12)	(−0.58, 0.53)
$\alpha_{\mathrm{JET\ GroupedNP\ 2}}$	(−0.99, 0.45)	(−0.80, −0.33)	(−0.12, 1.26)	(−0.55, 0.13)	(−0.89, 1.36)	(−0.62, 0.44)	(−0.36, 1.95)	(−0.75, 0.37)
$\alpha_{\mathrm{JET\ GroupedNP\ 3}}$	(−0.05, 0.56)	(−0.41, −0.35)	(0.32, 0.92)	(0.27, 0.69)	(1.22, 0.70)	(−5.43, 1.06)	(−0.72, 0.91)	(−0.09, 0.40)
$\alpha_{\mathrm{JET\ JER\ single\ NP}}$	(0.78, −0.80)	(0.37, −0.38)	(0.91, −0.90)	(0.44, −0.45)	(−0.48, 0.54)	(0.15, −0.15)	(0.08, −0.03)	(0.60, −0.61)
$\alpha_{\mathrm{MET\ SoftTrk\ ResoPara}}$	(0.51, −0.50)	(−0.31, 0.31)	(0.83, −0.81)	(0.40, −0.39)	(0.80, −0.76)	(0.42, −0.48)	(0.64, −0.62)	(0.34, −0.33)
$\alpha_{\mathrm{MET\ SoftTrk\ ResoPerp}}$	(−0.16, 0.18)	(0.06, −0.07)	(0.59, −0.56)	(0.49, −0.48)	(0.58, −0.54)	(1.08, −1.12)	(0.39, −0.40)	(0.12, −0.11)
$\alpha_{\mathrm{MET\ SoftTrk\ Scale}}$	(−0.26, 0.43)	(0.26, −0.28)	(0.53, −0.58)	(0.40, −0.62)	(0.73, −0.60)	(0.80, −0.44)	(0.43, −0.50)	(0.11, −0.07)
$\alpha_{\mathrm{MUONS\ ID}}$	(−0.12, −0.13)	(−0.02, −0.15)	(0.11, −0.10)	(0.10, −0.03)	(0.10, −0.09)	(0.26, −0.17)	(0.12, −0.01)	(−0.02, −0.12)
$\alpha_{\mathrm{MUONS\ MS}}$	(0.38, −0.73)	(0.52, −1.10)	(0.53, −1.29)	(0.63, −1.68)	(0.59, −1.74)	(0.93, −2.28)	(1.49, −3.43)	(0.49, −1.08)
$\alpha_{\mathrm{MUONS\ SCALE}}$	(−0.04, 0.00)	(−0.00, −0.00)	(0.00, 0.00)	(−0.01, 0.01)	(0.04, 0.00)	(0.03, −0.01)	(−0.10, 0.10)	(−0.02, 0.00)
$\alpha_{\mathrm{MUON\ EFF\ STAT}}$	(−0.24, 0.23)	(−0.26, 0.25)	(−0.26, 0.26)	(−0.28, 0.28)	(−0.30, 0.31)	(−0.33, 0.32)	(−0.35, 0.34)	(−0.25, 0.25)
$\alpha_{\mathrm{MUON\ EFF\ SYS}}$	(−1.21, 1.23)	(−1.54, 1.55)	(−1.65, 1.68)	(−1.89, 1.92)	(−2.36, 2.45)	(−2.69, 2.71)	(−3.05, 3.16)	(−1.50, 1.52)
α_{top}	(−2.31, 2.30)	(−2.64, 2.63)	(−2.68, 2.69)	(−3.62, 3.61)	(−3.49, 3.53)	(−3.23, 3.14)	(−3.44, 3.43)	(−2.64, 2.64)
$\gamma_{\mathrm{CR2mu\_300}}$	(−0.01, 0.00)	(0.04, −0.04)	(−0.01, −0.00)	(−0.01, 0.00)	(0.00, 0.01)	(−0.01, −0.02)	(0.02, −0.04)	(0.01, −0.01)
Stat. unc.	1.41	1.83	2.42	2.78	4.84	7.68	10.17	0.93
Total unc.	3.56	3.85	4.51	5.30	6.90	9.69	11.64	3.62

Table 7.20. Total impact of systematic uncertainties, in %, on the SM background prediction in each $E_{\mathrm{T}}^{\mathrm{miss}}$ bin of the SR, and on the total SR in the last column, obtained after performing the simultaneous fit.

7.8 Validation of the Background Estimation Technique

In order to to verify and validate the knowledge of the various background processes in the SR and the background estimation strategy, a validation region (VR) has been introduced. The VR has been defined in a way to satisfy two main criteria:

- kinematically similar to the SR;
- negligible signal contamination with respect to the SR.

Following this prescriptions the VR has been defined by applying the same selection as the SR but in a lower $E_{\mathrm{T}}^{\mathrm{miss}}$ range, 150 GeV $< E_{\mathrm{T}}^{\mathrm{miss}} <$ 250 GeV, covering naturally the first point of the list above.

The signal contamination has been evaluated at the truth level using all the DM signals considered in the analysis and calculating for each of them the sensitivity ratio $N_{\mathrm{sig}}/\sqrt{N_{\mathrm{sig}} + N_{\mathrm{bkg}}}$, where N_{sig} and N_{bkg} are the number of expected signal and background events, respectively. The second requirement has been verified since the sensitivity ratio defined in the VR is found out to be smaller than the one calculated in the inclusive SR (IM1) for all signals.

A new set of low $E_{\mathrm{T}}^{\mathrm{miss}}$ leptonic CRs has been also defined as done in the analysis in order to test the fit machinery in the low-$E_{\mathrm{T}}^{\mathrm{miss}}$ regime. The same set of systematics defined in the previous sections are applied; a conservative 2% uncertainty is additionally applied to MC event yields to take into account the observed difference between the trigger efficiency profiles in data and MC in the VR (see Figure 7.2).

The background-only fit in the CRs is hence performed using only one bin in the low $E_{\mathrm{T}}^{\mathrm{miss}}$ region. The MC predictions before and after the fit and the observed events in the CRs and in the VR are summarized in Table 7.21. The data/MC comparison plots are shown in Figure 7.24 for the distributions of the missing transverse momentum, leading jet p_{T}, minimal angular distance between jets and $E_{\mathrm{T}}^{\mathrm{miss}}$ in the transverse plane and the jet multiplicity variables, scaling each background source with the normalization factors evaluated by the fit. A good agreement within uncertainties is observed between SM predictions and data and therefore the background estimation technique is considered to be validated. This confirms also the good knowledge of the multi-jet background evaluated with the *jet smearing method*, which provides a sizable contribution to the VR, in particular in the low $E_{\mathrm{T}}^{\mathrm{miss}}$ region.

$E_{\mathrm{T}}^{\mathrm{miss}} \in [150, 250]$ GeV	VR	CR1e	CR1μ	CR2μ
Observed events (3.2 fb^{-1})	15782	6011	6031	701
SM prediction (post-fit)	17358.13 ± 1299.82	6010.88 ± 77.69	6030.92 ± 77.88	700.99 ± 26.47
Fitted $W(e\nu)$	1953.47 ± 148.97	4263.67 ± 245.23	1.41 ± 0.14	0.00 ± 0.00
Fitted $W(\mu\nu)$	1704.92 ± 122.28	2.91 ± 0.40	4666.19 ± 270.46	1.13 ± 0.18
Fitted $W(\tau\nu)$	4174.29 ± 267.67	642.56 ± 37.90	216.10 ± 14.17	0.19 ± 0.03
Fitted $Z(ee)$	0.15 ± 0.07	2.68 ± 0.19	$-0.00^{+0.01}_{--0.00}$	0.00 ± 0.00
Fitted $Z(\mu\mu)$	50.72 ± 11.97	1.68 ± 0.44	110.08 ± 12.23	637.63 ± 29.04
Fitted $Z(\tau\tau)$	105.32 ± 9.12	64.71 ± 12.49	15.30 ± 14.13	0.45 ± 0.07
Fitted $Z(\nu\nu)$	6549.94 ± 493.90	1.55 ± 0.11	$4.53^{+7.60}_{-4.53}$	0.00 ± 0.00
Expected $t\bar{t}$, single top	1226.81 ± 372.28	891.10 ± 268.65	888.23 ± 267.82	37.49 ± 11.29
Expected diboson	320.82 ± 27.57	139.99 ± 12.12	129.08 ± 13.11	24.10 ± 2.51
Multijet	1166.69 ± 1160.86	0.00 ± 0.00	0.00 ± 0.00	0.00 ± 0.00
NCB	105.00 ± 104.47	0.00 ± 0.00	0.00 ± 0.00	0.00 ± 0.00
MC exp. SM events	16154.78 ± 1493.84	5993.23 ± 421.52	5369.65 ± 415.15	769.06 ± 57.50
Fit input $W(e\nu)$	1946.92 ± 133.46	4249.40 ± 235.94	1.40 ± 0.12	0.00 ± 0.00
Fit input $W(\mu\nu)$	1459.72 ± 105.20	2.49 ± 0.38	3995.10 ± 253.55	0.96 ± 0.14
Fit input $W(\tau\nu)$	4160.32 ± 252.77	640.42 ± 36.63	215.38 ± 13.59	0.19 ± 0.02
Fit input $Z(ee)$	0.15 ± 0.07	2.68 ± 0.19	$-0.00^{+0.01}_{--0.00}$	0.00 ± 0.00
Fit input $Z(\mu\mu)$	56.15 ± 12.89	1.86 ± 0.46	121.87 ± 10.47	705.89 ± 54.44
Fit input $Z(\tau\tau)$	104.97 ± 8.61	64.49 ± 12.42	15.25 ± 14.09	0.45 ± 0.07
Fit input $Z(\nu\nu)$	5607.97 ± 401.18	1.33 ± 0.07	$3.88^{+6.65}_{-3.88}$	0.00 ± 0.00
Fit input $t\bar{t}$, single top	1226.09 ± 376.67	890.57 ± 271.83	887.70 ± 270.99	37.47 ± 11.43
Fit input diboson	320.80 ± 27.76	139.99 ± 12.20	129.07 ± 13.20	24.09 ± 2.53
Multijet	1166.69 ± 1160.86	0.00 ± 0.00	0.00 ± 0.00	0.00 ± 0.00
Fit input NCB	105.00 ± 104.47	0.00 ± 0.00	0.00 ± 0.00	0.00 ± 0.00

Table 7.21. Data and background predictions in the VR and the relative CRs before and after the fit performed for the region with $E_{\mathrm{T}}^{\mathrm{miss}} \epsilon [150, 250]$ GeV. The background predictions include both the statistical and systematic uncertainties.

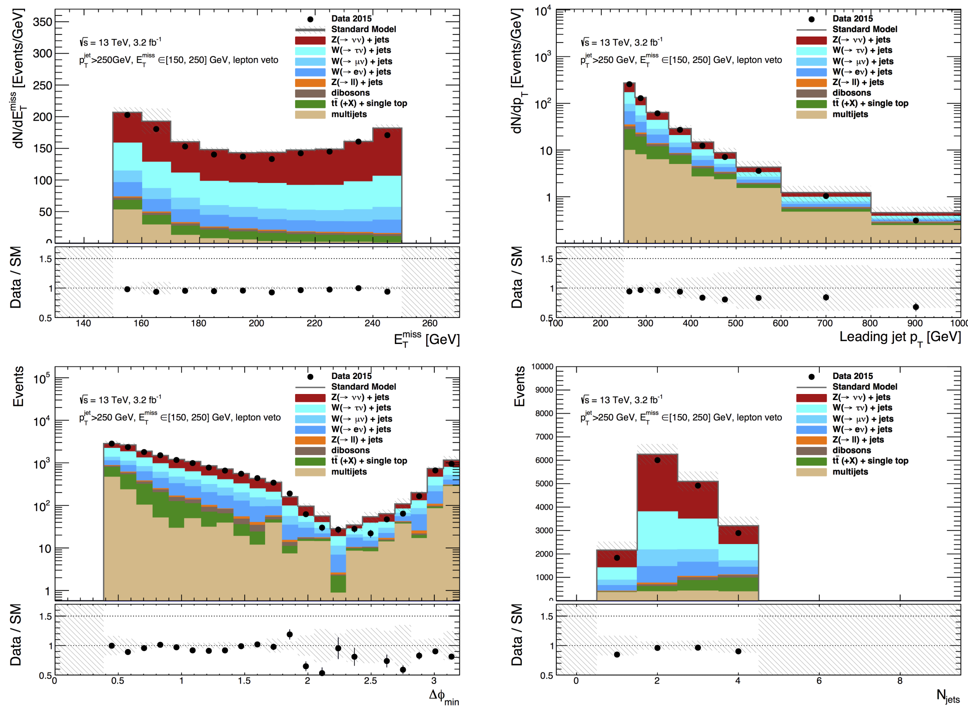

Figure 7.24. Data/MC comparison plots of the $E_{\mathrm{T}}^{\mathrm{miss}}$, leading jet p_{T}, jet multiplicity, minimal angular distance between the jets and the $E_{\mathrm{T}}^{\mathrm{miss}}$ distributions in the VR using 3.2 fb^{-1} of data. The MC expectations include the global normalization factors extracted from the background-only fit in the CRs performed in exclusive $E_{\mathrm{T}}^{\mathrm{miss}}$ bins. The error bands in the ratios include the statistical and experimental uncertainties obtained from the same fit.

7.9 Results and Interpretations

Once the fitting strategy has been tested and validated, the SR has been unblinded. The comparison between the data and the SM predictions, with the related uncertainties, obtained after the simultaneous shape fit is shown in Figure 7.25. The distributions of the most relevant variables are shown scaling the MC simulations with the fitted values of the normalization factors in each $E_{\mathrm{T}}^{\mathrm{miss}}$ bin. The signal predictions of a DM simplified model with a DM mass $m_\chi = 150$ GeV and an axial-vector mediator with mass $m_A = 1$ TeV, a ADD model with a number of extra-dimensions $n = 3$ and a gravity scale $M_D = 5.6$ TeV and a compressed scenario with a sbottom ($\tilde{b}$) decaying in a neutralino ($\tilde{\chi}_0$) with $\Delta m = m_{\tilde{b}} - m_{\tilde{\chi}_0} = 5$ GeV are also superimposed in the plots. The results for all the different inclusive and exclusive selections are summarized in Table 7.22 and are reported in detail in Appendix B. The SM predictions, determined with a total uncertainty on each $E_{\mathrm{T}}^{\mathrm{miss}}$ bin between 4% and 12% which increases with $E_{\mathrm{T}}^{\mathrm{miss}}$, are in good agreement with the observation in all the $E_{\mathrm{T}}^{\mathrm{miss}}$ regions. The number of observed events and the yields of the different SM backgrounds before and after the fit are listed in Table 7.23 for the inclusive region with $E_{\mathrm{T}}^{\mathrm{miss}} > 250$ GeV and summarized in the plot in Figure 7.26.

Inclusive bins	IM1	IM2	IM3	
Observed events	21447	11975	6433	
SM prediction (post-fit)	21730 ± 940	12340 ± 570	6570 ± 340	
SM prediction (pre-fit)	22500 ± 1400	12870 ± 870	6820 ± 490	
Exclusive bins	EM1	EM2	EM3	
Observed events	9472	5542	2939	
SM prediction (post-fit)	9400 ± 410	5770 ± 260	3210 ± 170	
SM prediction (pre-fit)	9620 ± 580	6050 ± 390	3160 ± 220	
Inclusive bins	IM4	IM5	IM6	IM7
Observed events	3494	1170	423	185
SM prediction (post-fit)	3390 ± 200	1125 ± 77	441 ± 39	167 ± 20
SM prediction (pre-fit)	3660 ± 270	1197 ± 87	443 ± 34	186 ± 15
Exclusive bins	EM4	EM5	EM6	
Observed events	2324	747	238	
SM prediction (post-fit)	2260 ± 140	686 ± 50	271 ± 28	
SM prediction (pre-fit)	2470 ± 180	754 ± 53	257 ± 19	

Table 7.22. Data and SM background predictions in the SR for the different inclusive and exclusive selections. For the SM predictions both the statistical and systematic uncertainties are included.

Since no excess of data over the background expectations is observed, the results can be translated into upper limits on the presence of new physics phenomena. The model-independent 95% confidence level (CL) upper limits on the visible cross-section, defined as the production cross-section times acceptance times efficiency $\sigma \times A \times \epsilon$, is obtained using the CL_s modified frequentist approach [159]. The inclusive $E_{\mathrm{T}}^{\mathrm{miss}}$ bins are used with the global fit performed with single normalization factors over the full $E_{\mathrm{T}}^{\mathrm{miss}}$ range considered. The results are shown in Table 7.24 and indicate that the values of $\sigma \times A \times \epsilon$ above 553 fb (for IM1) and above 19 fb (for

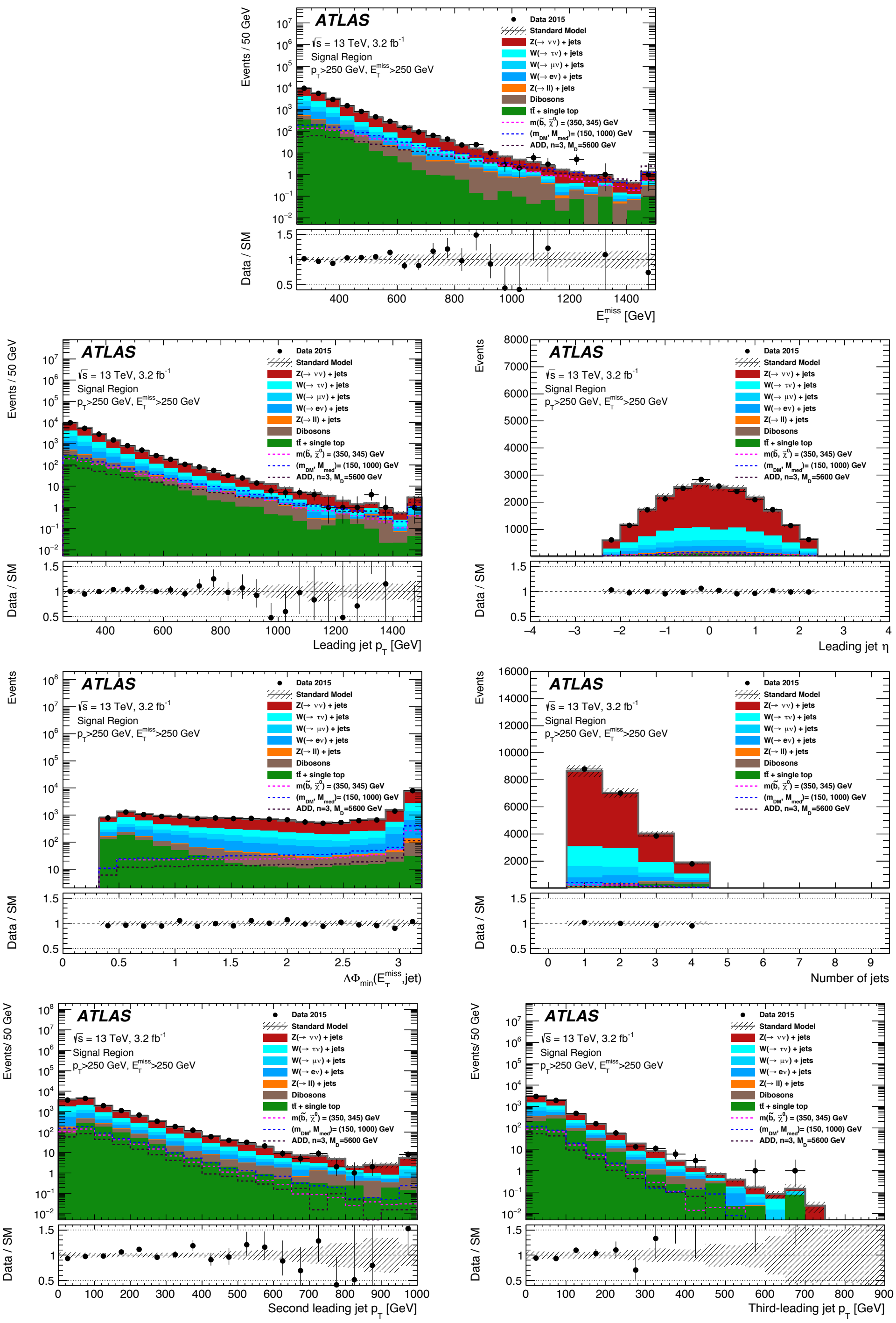

Figure 7.25. Data/MC comparison plots of the $E_{\mathrm{T}}^{\mathrm{miss}}$, leading jet p_{T} and η, jet multiplicity, minimal angular distance between the jets and the $E_{\mathrm{T}}^{\mathrm{miss}}$, second and third leading jet distributions in the SR, for the IM1 selection, using 3.2 fb^{-1} of data. The MC expectations include the global normalization factors extracted from the background-only fit in the CRs performed in exclusive $E_{\mathrm{T}}^{\mathrm{miss}}$ bins. The error bands in the ratios include the statistical and experimental uncertainties obtained from the same fit. The signal predictions of a WIMP, ADD and a SUSY scenario are also superimposed [116].

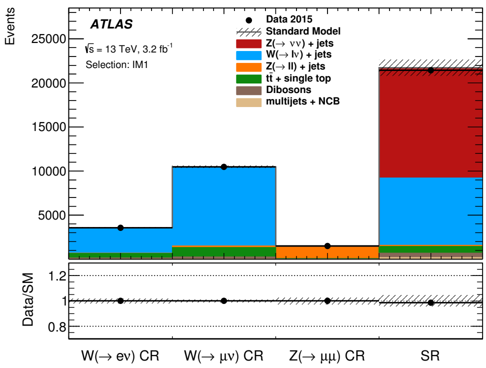

Figure 7.26. Summary plots showing the agreement of data and the SM predictions post-fit in the region IM1 and the relative CRs labelled with their dominant background process [116].

IM1	SR	CR1e	CR1μ	CR2μ
Observed events (3.2 fb^{-1})	21447	3559	10481	1488
SM prediction (post-fit)	21730 ± 940	3559 ± 60	10480 ± 100	1488 ± 39
Fitted $W(e\nu)$	1710 ± 170	2410 ± 140	0.4 ± 0.1	–
Fitted $W(\mu\nu)$	1950 ± 170	2.4 ± 0.3	8550 ± 330	1.8 ± 0.3
Fitted $W(\tau\nu)$	3980 ± 310	462 ± 27	435 ± 28	0.14 ± 0.02
Fitted $Z(ee)$	0.01 ± 0.01	0.5 ± 0.1	–	–
Fitted $Z(\mu\mu)$	76 ± 30	0.02 ± 0.02	143 ± 10	1395 ± 41
Fitted $Z(\tau\tau)$	48 ± 7	30 ± 2	22 ± 4	0.5 ± 0.1
Fitted $Z(\nu\nu)$	12520 ± 700	1.8 ± 0.1	2.3 ± 0.2	–
Expected $t\bar{t}$, single top	780 ± 240	500 ± 150	1060 ± 330	42 ± 13
Expected diboson	506 ± 48	150 ± 13	260 ± 25	48 ± 5
Multijet	51 ± 50	–	–	–
NCB	110 ± 110	–	–	–
MC exp. SM events	22500 ± 1400	3990 ± 320	10500 ± 710	1520 ± 98
Fit input $W(e\nu)$	1960 ± 160	2770 ± 210	0.4 ± 0.1	–
Fit input $W(\mu\nu)$	1930 ± 170	2.4 ± 0.3	8500 ± 520	1.8 ± 0.2
Fit input $W(\tau\nu)$	4570 ± 300	531 ± 39	500 ± 34	0.16 ± 0.03
Fit input $Z(ee)$	0.01 ± 0.01	0.5 ± 0.1	–	–
Fit input $Z(\mu\mu)$	78 ± 29	0.02 ± 0.02	146 ± 13	1427 ± 92
Fit input $Z(\tau\tau)$	55 ± 6	34 ± 3	25 ± 4	0.6 ± 0.1
Fit input $Z(\nu\nu)$	12440 ± 850	1.8 ± 0.1	2.2 ± 0.1	–
Fit input $t\bar{t}$, single top	780 ± 240	500 ± 160	1060 ± 340	42 ± 13
Fit input diboson	506 ± 48	150 ± 13	260 ± 25	48 ± 5
Multijet	51 ± 50	–	–	–
NCB	110 ± 110	–	–	–

Table 7.23. Data and background predictions in the signal and control regions before and after the fit performed for the IM1 selection. The background predictions include both the statistical and systematic uncertainties. The individual uncertainties are correlated and do not necessarily add in quadrature to the total background uncertainty [116].

SR	$\langle\sigma\rangle^{95}_{\rm obs}$ [fb]	$S^{95}_{\rm obs}$	$S^{95}_{\rm exp}$
IM1	553	1773	1864^{+829}_{-548}
IM2	308	988	1178^{+541}_{-348}
IM3	196	630	694^{+308}_{-204}
IM4	153	491	401^{+168}_{-113}
IM5	61	196	164^{+63}_{-45}
IM6	23	75	84^{+32}_{-23}
IM7	19	61	48^{+18}_{-13}

Table 7.24. Observed and expected 95% CL upper limits on the number of signal events, $S^{95}_{\rm obs}$ and $S^{95}_{\rm exp}$, and on the visible cross-section, defined as the product of cross-section, acceptance and efficiency, $\langle\sigma\rangle^{95}_{\rm obs}$, for the IM1–IM7 selections [116].

IM7) are excluded at 95% CL.

7.9.1 ADD Limits

The level of agreement between data and SM predictions can be interpreted into limits on the parameters of the ADD model. The regions at low $E_{\rm T}^{\rm miss}$ are not included in the fit because the SM predictions there are too large with respect to the signals, hence the simultaneous shape binned fit has been performed only in the $E_{\rm T}^{\rm miss}$ range with $E_{\rm T}^{\rm miss} > 400$ GeV where the shape difference between signal and the SM background becomes evident.

The acceptance times efficiency after the several selection criteria for a typical signal sample with $n = 3$ and $M_D = 4.1$ TeV is shown in Table 7.25. In general the values of $A \times \epsilon$ vary with the number of extra dimensions n between 5.5% and 6.6% for IM4 and between 2.9% and 4.2% for IM7. The number of expected events in the SR are shown in Appendix C in Table C.1.

The observed and expected 95% CL exclusion limits have been set on the fundamental Planck scale in $4 + n$ dimensions, M_D, as a function of the number of extra-dimensions n using the CL_s approach and exploiting the proportionality:

$$\sigma \propto \frac{C_n}{M^{M_D^{n+2}}} , \tag{7.19}$$

where C_n is a constant for a given n at a given center-of-mass energy. All the uncertainties on the signal acceptance times efficiency, the background predictions, and the luminosity are considered in the fit, and the correlations between systematic uncertainties in signal and background predictions are also taken into account.

The results are shown in Figure 7.27 and Table 7.26 improving sensitively the previous exclusions limits obtained using 8 TeV data of 5.3 and 3.1 TeV at $n = 2$ and $n = 6$ respectively [71].

The limits at 95% CL on the observed and expected signal strength are listed in Appendix D in Table D.1.

Since the analysis probes a phase space in which the EFT loses its validity, being the scale of the interaction of the same order or above the scale of the theory M_D as discussed in Refs. [71, 160], a truncation scheme is also applied.

This scheme consists in weighting down signal events for which the effective center-of-mass energy $\hat{s}$ is higher than M_D with a weight $w = M_D^4/\hat{s}^2$. The truncation

SR	Cut	ADD	
	Total Events	5722	100%
	Trigger	5593	98%
	Event cleaning	5555	97%
	Lepton veto	5551	97%
	$N_{\text{jets}} \leq 4$	5263	92%
	$\Delta\phi(\text{jet}, E_{\text{T}}^{\text{miss}}) > 0.4$	4879	85%
	Leading jet tight cleaning	4769	83%
	Leading jet $p_{\text{T}} > 250$ GeV, $\lvert\eta\rvert < 2.4$	1859	32%
	$E_{\text{T}}^{\text{miss}} > 250$ GeV	1720	30%
EM1	250 GeV $< E_{\text{T}}^{\text{miss}} <$ 300 GeV	271	5%
EM2	300 GeV $< E_{\text{T}}^{\text{miss}} <$ 350 GeV	297	5%
EM3	350 GeV $< E_{\text{T}}^{\text{miss}} <$ 400 GeV	245	4%
EM4	400 GeV $< E_{\text{T}}^{\text{miss}} <$ 500 GeV	355	6%
EM5	500 GeV $< E_{\text{T}}^{\text{miss}} <$ 600 GeV	217	4%
EM6	600 GeV $< E_{\text{T}}^{\text{miss}} <$ 700 GeV	123	2%
IM7	$E_{\text{T}}^{\text{miss}} > 700$ GeV	213	4%

Table 7.25. Number of accepted events and acceptance times efficiency after the application of each step of the mono-jet selection criteria for an ADD signal with $n = 3$, $M_D =$ 4.1 TeV. The event cleaning requirement includes the primary vertex condition and that all the jets that pass the overlap removal fulfill the baseline quality conditions. The number of signal events corresponds to the expectations for a total integrated luminosity of 3.2 fb^{-1}. The values are provided after the application of a filter of the leading jet $p_{\text{T}} > 100$ GeV at the truth level.

95% CL lower limits on M_D [TeV]				
n extra	95% CL observed limit		95% CL expected limit	
dimensions	Nominal (Nominal after damping)	$\pm$ 1σ (theory)	Nominal	$\pm$ 1σ (expected)
2	6.58 (6.58)	$^{+0.52}_{-0.42}$	6.88	$^{+0.65}_{-0.64}$
3	5.46 (5.44)	$^{+0.45}_{-0.34}$	5.67	$^{+0.41}_{-0.41}$
4	4.81 (4.74)	$^{+0.41}_{-0.29}$	4.96	$^{+0.29}_{-0.29}$
5	4.48 (4.34)	$^{+0.41}_{-0.26}$	4.60	$^{+0.23}_{-0.23}$
6	4.31 (4.10)	$^{+0.41}_{-0.24}$	4.38	$^{+0.19}_{-0.19}$

Table 7.26. 95% CL observed and expected lower limits, using an integrated luminosity of 3.2 fb^{-1} at $\sqrt{s} = 13$ TeV, on the fundamental Planck scale in $4 + n$ dimensions, M_D, as a function of the number of extra dimensions n, considering nominal LO signal cross-sections. The impact of the $\pm 1\sigma$ theoretical uncertainty on the observed limits and the expected $\pm 1\sigma$ range of limits in the absence of a signal are also provided. Finally, the 95% CL observed limits after damping of the signal cross-section for $\hat{s} > M_D^2$ (more details in the text) are quoted in parentheses [116].

is effectively a reduction of the number of signal events in the SR that yields a yet weaker limit on M_D. The $\hat{s}$ distribution follows the graviton mass distribution which becomes harder with larger number of extra-dimensions: the models with higher

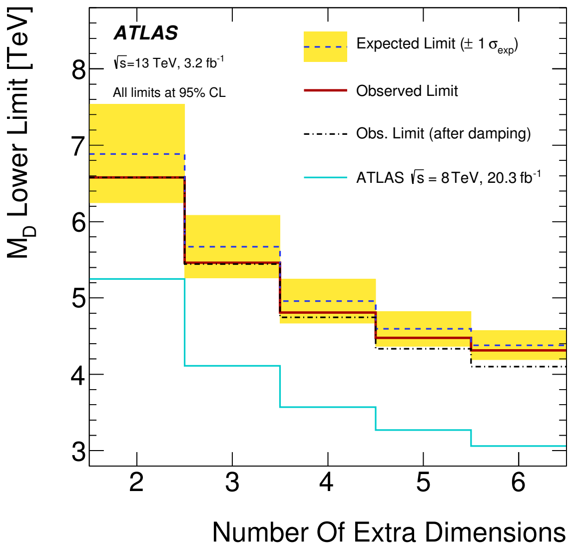

Figure 7.27. Observed and expected 95% CL lower limits on the fundamental Planck scale in $4 + n$ dimensions, M_D, as a function of the number of extra dimensions. The shaded area around the expected limit indicates the expected $\pm 1\sigma$ range of limits in the absence of a signal. Finally, the thin dashed line shows the 95% CL observed limits after the truncation scheme is applied, as described in the text. The results from this analysis are also compared to the previous limits from the ATLAS Collaboration based on the data collected at $\sqrt{s} = 8$ TeV [116].

number of extra-dimensions are therefore more affected by the truncation. Due to different distributions of $\hat{s}$ in each signal region $E_{\mathrm{T}}^{\mathrm{miss}}$ bin, the truncation factor is derived specifically for each of them. The observed 95% CL lower limit on M_D is found to have a negligible impact for the model with $n = 2$, while it has an amount of about 5% for $n = 6$. The observed limits results to be less stringent than expected, due to the fact that more data than the SM predictions are observed in the high $E_{\mathrm{T}}^{\mathrm{miss}}$ regions, which provide most of the discriminating power between signal and background.

7.9.2 SUSY Limits

Results are also interpreted in the SUSY compressed scenarios in which a stop, sbottom or squark pair is produced decaying in neutralinos as $\tilde{t}_1 \to c+\tilde{\chi}_1^0$, $\tilde{b}_1 \to b+\tilde{\chi}_0$, or $\tilde{q} \to q + \tilde{\chi}_0$ $(q = u, d, c, s)$ respectively, for different mass splittings between the NLSP and the LSP neutralino. The effects of each step of the mono-jet selection on the acceptance times efficiency in the various SUSY scenarios is quoted in Table 7.27 for three characteristic signal samples.

The typical $A \times \epsilon$ of the selection criteria varies, with increasing stop and neutralino masses, between 0.7% and 1.4% for IM1 and between 0.06% and 0.8% for IM7. The number of expected events in the SR are shown in Appendix C in Tables C.2–C.4.

In Figure 7.28 the 95% CL excluded regions are shown in the case of the

SR	Cut	$\tilde{q} \to q + \tilde{\chi}_1^0$		$\tilde{b} \to b + \tilde{\chi}_1^0$		$\tilde{t} \to c + \tilde{\chi}_1^0$	
	Total Events	1917	100%	4245	100%	3930	100%
	Trigger	1604	84%	3450	81%	3162	80%
	Event cleaning	1592	83%	3421	81%	3140	80%
	Lepton veto	1591	83%	3418	81%	3138	80%
	$N_{\text{jets}} \leq 4$	1492	78%	3180	75%	2926	74%
	$\Delta\phi(\text{jet}, E_{\text{T}}^{\text{miss}}) > 0.4$	1409	73%	3015	71%	2776	71%
	Leading jet tight cleaning	1343	70%	2842	67%	2618	67%
	Leading jet $p_{\text{T}} > 250$ GeV, $\lvert\eta\rvert < 2.4$	435	23%	761	18%	698	18%
	$E_{\text{T}}^{\text{miss}} > 250$ GeV	404	21%	693	16%	636	16%
EM1	250 GeV $< E_{\text{T}}^{\text{miss}} <$ 300 GeV	58	3%	134	3%	124	3%
EM2	300 GeV $< E_{\text{T}}^{\text{miss}} <$ 350 GeV	65	3%	139	3%	130	3%
EM3	350 GeV $< E_{\text{T}}^{\text{miss}} <$ 400 GeV	59	3%	111	3%	104	3%
EM4	400 GeV $< E_{\text{T}}^{\text{miss}} <$ 500 GeV	85	4%	145	3%	129	3%
EM5	500 GeV $< E_{\text{T}}^{\text{miss}} <$ 600 GeV	53	3%	78	2%	74	2%
EM6	600 GeV $< E_{\text{T}}^{\text{miss}} <$ 700 GeV	34	2%	41	1%	35	1%
IM7	$E_{\text{T}}^{\text{miss}} > 700$ GeV	49	3%	46	1%	40	1%

Table 7.27. Number of accepted events and acceptance times efficiency after the application of each step of the mono-jet selection criteria for different SUSY signals. Three different SUSY scenarios for squark pair production are presented: $\tilde{q} \to q + \tilde{\chi}_1^0$ ($m_{\tilde{q}} = 650$ GeV, $m_{\tilde{\chi}_1^0} = 645$ GeV), $\tilde{b} \to b + \tilde{\chi}_1^0$ ($m_{\tilde{b}} = 350$ GeV, $m_{\tilde{\chi}_1^0} = 345$ GeV), $\tilde{t} \to c + \tilde{\chi}_1^0$ ($m_{\tilde{t}} = 350$ GeV, $m_{\tilde{\chi}_1^0} = 345$ GeV). The event cleaning requirement includes the primary vertex condition and that all the jets that pass the overlap removal fulfill the baseline quality conditions. The number of signal events corresponds to the expectations for a total integrated luminosity of 3.2 fb^{-1}. The values are provided after the application of a filter requiring a leading jet $p_{\text{T}} > 100$ GeV at the truth level.

$\tilde{t}_1 \to c + \tilde{\chi}_1^0$ signal after performing the shape binned fit on the SR and CRs as done in the ADD case. The previous Run-1 results [161] are also shown. In the compressed scenario in which the stop and the neutralino are nearly degenerate in mass, the exclusion extends up to stop masses of 323 GeV. The region with $\Delta m < 5$ GeV is not considered in the exclusion since in this regime the stop could become long-lived.

The observed and expected 95% CL exclusion limits in the 2D plane of the sbottom mass and the sbottom–neutralino mass difference for the $\tilde{b}_1 \to b + \tilde{\chi}_1^0$ decay channel is presented on the left in Figure 7.29. On the right of Fig. 7.29 are instead plotted the observed and expected 95% CL exclusion limits of the process $\tilde{q} \to q + \tilde{\chi}_0$ ($q = u, d, c, s$) as a function of the squark mass and the squark–neutralino mass difference. In the scenario with $\Delta m = m_{\tilde{b}_1} - m_{\tilde{\chi}_0} \sim m_b$ the exclusion limit reaches the sbottom mass of 323 GeV while in models with $\tilde{q} \to q + \tilde{\chi}_1^0$ squark masses below 608 GeV are excluded at 95% CL.

These results significantly extend previous exclusion limits [161, 162, 163]. All the limits at 95% CL obtained on the observed and expected signal strength for the SUSY signal samples considered are listed in Appendix D in Tables D.2–D.4.

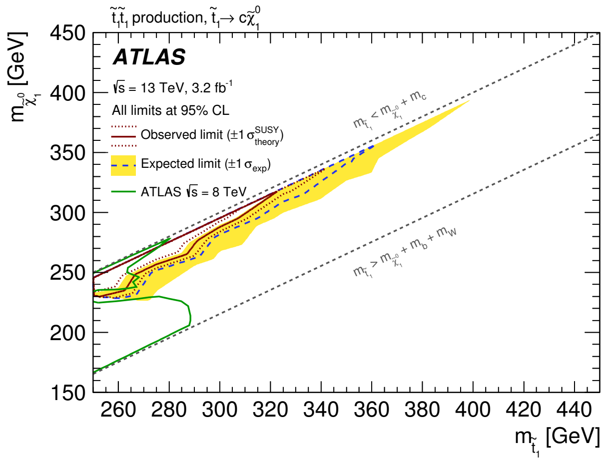

Figure 7.28. Excluded region at the 95% CL in the $(\tilde{t}_1, \tilde{\chi}_1^0)$ mass plane for the decay channel $\tilde{t}_1 \to c + \tilde{\chi}_1^0$ (BR = 100%). The dotted lines around the observed limit indicate the range of observed limits corresponding to $\pm1\sigma$ variations of the NLO SUSY cross-section predictions. The shaded area around the expected limit indicates the expected $\pm1\sigma$ limits in the absence of a signal. The results from this analysis are compared to previous results from the ATLAS Collaboration at $\sqrt{s} = 8$ TeV [116].

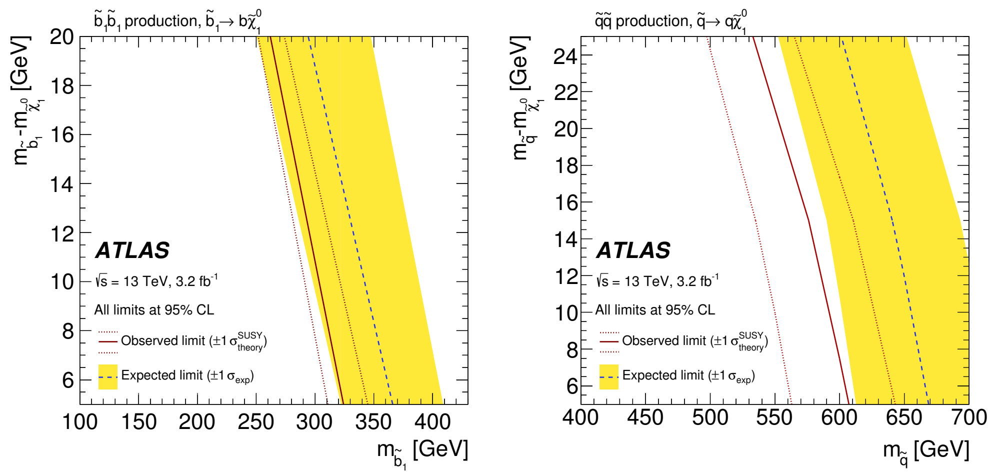

Figure 7.29. Exclusion region at 95% CL as a function of squark mass and the squark–neutralino mass difference for (left) the decay channel $\tilde{b}_1 \to b + \tilde{\chi}_1^0$ and (right) $\tilde{q} \to q + \tilde{\chi}_1^0$ $(q = u, d, c, s)$. The dotted lines around the observed limit indicate the range of observed limits corresponding to $\pm1\sigma$ variations of the NLO SUSY cross-section predictions. The shaded area around the expected limit indicates the expected $\pm1\sigma$ limits in the absence of a signal [116].

7.9.3 Dark Matter Limits

The results are finally translated into exclusion limits in the DM context. The WIMP pair-production processes, as discussed in Section 4.7, are evaluated in two different mediator spin hypotheses: the axial-vector and pseudo-scalar cases. The $E_{\mathrm{T}}^{\mathrm{miss}}$ spectra may differ substantially in the two kind of processes but also in the on-shell and off-shell regimes. In general the pseudo-scalar signals populate the low $E_{\mathrm{T}}^{\mathrm{miss}}$ region with event yields which decrease rapidly with the higher $E_{\mathrm{T}}^{\mathrm{miss}}$, while the axial-vector processes produce spectra with a slower decrease as a function of the momentum of the WIMP-pair system, in particular in the case with heavy mediators.

In Table 7.28 the acceptance times efficiency of two examples of on-shell WIMP pair-production via axial-vector and pseudo-scalar mediators are shown. The two processes have similar cross-sections but the expected yield for the pseudo-scalar sample is deeply suppressed by the leading jet p_{T} and $E_{\mathrm{T}}^{\mathrm{miss}}$ cut. The number of expected events in the SR of all the signals used in this thesis are shown in Appendix C in Tables C.5–C.9.

SR	Cut	Axial-vector		Pseudo-scalar	
	Total Events	4135	100%	4975	100%
	Trigger	3788	92%	4653	94%
	Event cleaning	3755	91%	4585	92%
	Lepton veto	3750	91%	4584	92%
	$N_{\mathrm{jets}} \leq 4$	3617	87%	4478	90%
	$\Delta\phi(\mathrm{jet}, E_{\mathrm{T}}^{\mathrm{miss}}) > 0.4$	3416	83%	4249	85%
	Leading jet tight cleaning	3358	81%	4064	82%
	Leading jet $p_{\mathrm{T}} > 250$ GeV, $\lvert\eta\rvert < 2.4$	1112	27%	572	11%
	$E_{\mathrm{T}}^{\mathrm{miss}} > 250$ GeV	1016	26%	472	9.5%
EM1	250 GeV $< E_{\mathrm{T}}^{\mathrm{miss}} <$ 300 GeV	190	4.6%	164	3.3%
EM2	300 GeV $< E_{\mathrm{T}}^{\mathrm{miss}} <$ 350 GeV	202	4.9%	130	2.6%
EM3	350 GeV $< E_{\mathrm{T}}^{\mathrm{miss}} <$ 400 GeV	167	4.0%	80	1.6%
EM4	400 GeV $< E_{\mathrm{T}}^{\mathrm{miss}} <$ 500 GeV	212	5.1%	68	1.4%
EM5	500 GeV $< E_{\mathrm{T}}^{\mathrm{miss}} <$ 600 GeV	114	2.8%	21	0.4%
EM6	600 GeV $< E_{\mathrm{T}}^{\mathrm{miss}} <$ 700 GeV	59	1.4%	7	0.14%
IM7	$E_{\mathrm{T}}^{\mathrm{miss}} > 700$ GeV	72	1.8%	4	0.08%

Table 7.28. Number of accepted events and acceptance times efficiency after the application of each step of the mono-jet selection criteria for a couple of representative WIMP signals in the case of a axial-vector and of a pseudo-scalar mediator in which $m_\chi = 1$ GeV, $m_A = 1$ TeV and $m_\chi = 10$ GeV, $m_P = 100$ GeV respectively are shown. The event cleaning requirement includes the primary vertex condition and that all the jets that pass the overlap removal fulfill the baseline quality conditions. The number of signal events corresponds to the expectation for a total integrated luminosity of 3.2 fb^{-1}. All the values in the table except the ones in the first row are obtained after the application of a filter cut of $p_T > 100$ GeV applied to the leading jet.

The observed and expected 95% exclusion limits are shown in the two dimensional plot with the WIMP mass m_χ versus the mediator mass with a fixed coupling choice.

In Figure 7.30 the results relative to the axial-vector mediator signals with the

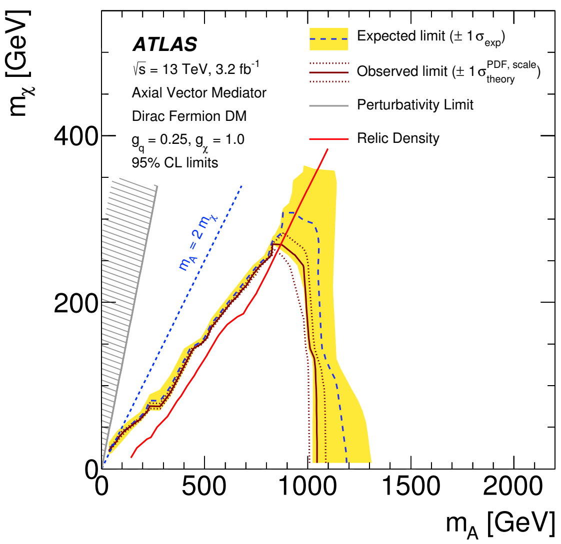

Figure 7.30. 95% CL exclusion contours in the m_χ versus m_A parameter plane in the axial-vector mediator hypothesis with coupling fixed at $g_\chi = 1$ and $g_q = 0.25$, using an integrated luminosity of 3.2 fb^{-1} at $\sqrt{s} = 13$ TeV. The solid curve shows the observed limit, the dashed contour line defines the expected limit, while the bands indicate the $\pm 1\sigma$ theory uncertainties in the observed limit and $\pm 1\sigma$ range of the expected limit in the absence of a signal.The red curve identifies the set of points for which $\Omega h^2 = 0.12$. The grey hatched area indicates the excluded are due to perturbative unitarity, defined by $m_\chi > \sqrt{\pi/2}\, m_A$ [116].

coupling $g_q = 0.25$ and $g_\chi = 1$ assuming the minimal mediator width condition are shown. The observed limits are shown with the contours that define $\pm 1\sigma$ theoretical uncertainties in the signal cross-sections.

Signals with mediator masses up to 1 TeV in the on-shell regime can be excluded at 95% CL. No sensitivity is achieved to processes in the off-shell region, where cross-sections are lower because the mediator decay into a pair of WIMPs is kinematically suppressed.

In the plot the relic density line (see Section 4.2) calculated with the MadDM numerical tool [164] is also illustrated. This line indicates where the processes predicted by the simplified model are by themselves sufficient to explain the observed DM abundance in the universe ($\Omega_\chi = 0.12$). The region towards high mediator masses and low DM masses corresponds to the overproduction regime, while on the opposite side of the curve other WIMP production mechanisms have to exist in order to explain the observed DM relic density. The exclusion contours can exclude a region in the plane which extends up to $m_A \sim 880$ GeV and $m_\chi \sim 270$ GeV in the absence of any interaction other than the one considered.

Couplings, as already said in Section 4.7, have been fixed to specific values which satisfy perturbative unitarity, which is in turn violated in the axial-vector model due to the DM Yukawa coupling becoming non-perturbative, if m_χ is significantly larger than m_A [165]. To ensure perturbative unitarity the condition $m_\chi^2 g_\chi^2/(\pi m_A^2) < 1/2$ must be satisfied. The line that delimits this region, $m_\chi = \sqrt{\pi/2}\, m_A$, is thus shown.

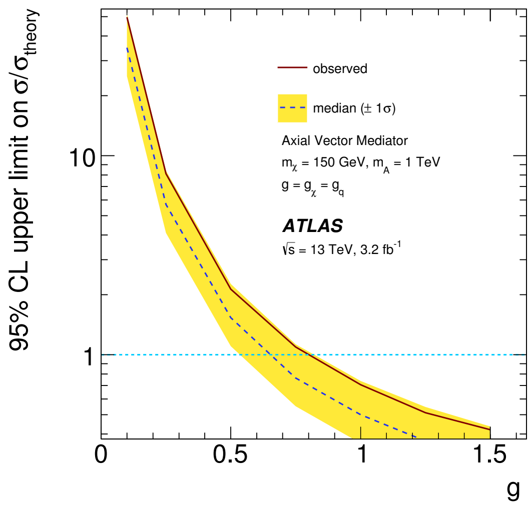

Figure 7.31. The ratios of the observed and expected 95% CL upper limits on cross-section to the predicted signal cross-section for the axial-vector simplified model $m_\chi = 150$ GeV, $m_A = 1$ TeV with different choices of the pseudo-scalar couplings $g = g_q = g_\chi$ where the minimal width of the mediator is assumed. The yellow band indicates the expected $\pm 1\sigma$ limits in the absence of a signal.

In the axial-vector hypothesis a scan of different couplings is performed keeping a fixed value of the mass of the WIMP $m_\chi = 150$ GeV and of the mediator $m_A = 1$ TeV. The results are shown in Figure 7.31 where the limits on the signal strength are plotted as a function of the coupling value $g = g_\chi = g_q$. With this choice of the masses the signals with coupling $g \gtrsim 0.65$ can be excluded at 95% CL.

The limits at 95% CL on the observed and expected signal strength for the DM simplified models with axial-vector mediators are listed in Appendix D in Tables D.5 and D.6.

The mono-jet analysis is in conclusion not sensitive to the pseudo-scalar simplified models with the coupling choice of $g = g_q = g_\chi = 1$ with the 3.2 fb^{-1} of data collected, due to the low acceptance after the mono-jet selection and to the low loop suppressed cross-sections. The 95% CL limits on the considered signal strength of all the signal samples are indeed $\gtrsim 3$ (see Table D.7 in Appendix D). Figure 7.32 shows the (m_χ,m_P) plot with the contour line on the 95% CL limit on signal strength at $\mu = 5$.

A scan of the couplings for the pseudo-scalar signal model with $m_\chi = 50$ GeV and $m_P = 300$ GeV, shown in Figure 7.33, proves that the analysis can exclude signals with $g \gtrsim 2$ basically due to the increase of the cross-section of the process (the limits at 95% CL on the observed and expected signal strength are listed in Table D.8 in Appendix D).

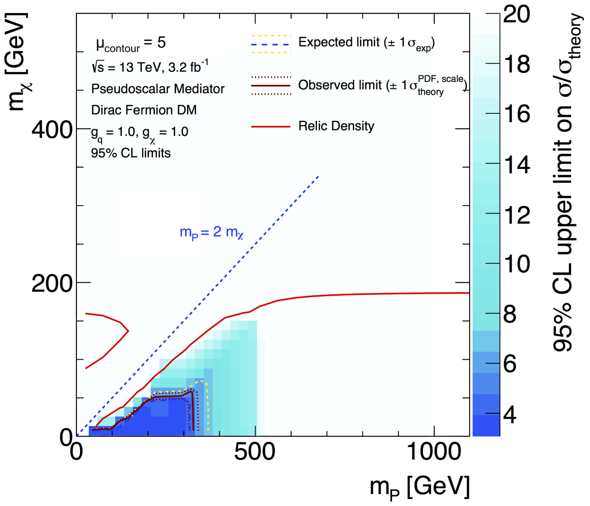

Figure 7.32. 95% CL contour limits fixed at $\mu = 5$ on the cross-section to the predicted signal cross-section in the m_χ versus m_P parameter plane in the pseudo-scalar mediator hypothesis with coupling fixed at $g = g_q = g_\chi = 1$, using an integrated luminosity of 3.2 fb^{-1} at $\sqrt{s} = 13$ TeV. The solid curve shows the observed limit, the dashed contour line defines the expected limit, while the yellow dashed lines indicate the $\pm 1\sigma$ theory uncertainties in the observed limit and $\pm 1\sigma$ range of the expected limit in the absence of a signal. The red curve identifies the set of points for which $\Omega h^2 = 0.12$.

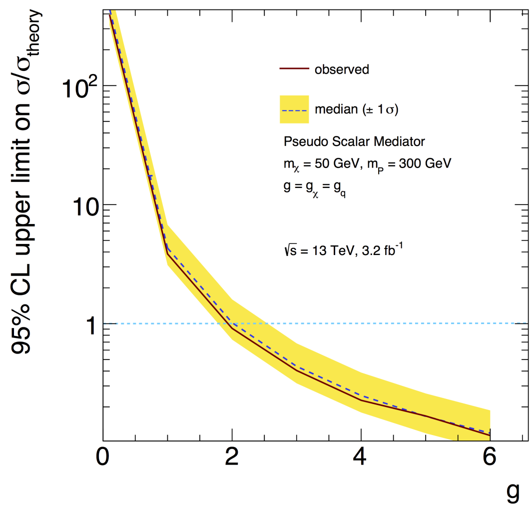

Figure 7.33. The ratios of the observed and expected 95% CL upper limits on cross-section to the predicted signal cross-section for the simplified model $m_\chi = 50$ GeV, $m_P = 300$ GeV with different choices of the pseudo-scalar couplings $g = g_q = g_\chi$ where the minimal width of the mediator is assumed. The yellow band indicates the expected $\pm 1\sigma$ limits in the absence of a signal.

Chapter 8

Mono-jet versus All

The DM interpretations of the mono-jet limits are relevant and give complementary results with respect to the other analyses performed at collider experiments, but also to results obtained by experiments based on direct and indirect detection of DM. In this chapter a comparison between the mono-jet and the other analyses and experiments results will be shown to illustrate the role of this analysis in the context of the DM search.

8.1 Mono-jet vs Direct Detection

As just mentioned in Section 4.5, the collider searches can be sensitive in the region of light WIMP mass where instead the experiments based on direct detection, that exploit the nuclei recoils after the collisions with the DM wind, are not.

The Run-2 mono-jet limits discussed in Section 7 can be translated onto the plane of the WIMP-nucleon scattering cross-section versus the WIMP mass parameter m_χ [166]. The reverse procedure of interpreting the non-collider results in the simplified models and in the (m_χ, m_A) plot is generally much more complicated, because it requires a detailed knowledge of the assumption on which they are based on. In fact, the relic density predicted by the simplified model changes in each point of the (m_χ, m_A) plot, while non-collider results are based on the assumption that the DM density saturates the cosmological density considering only one type of WIMP. Furthermore, the DM particles probed by non-collider experiments could constitute only a determined component of the DM density, so their results would have to be rescaled accordingly adding other assumptions on the results.

However, also in the translation of the simplified model results into the WIMP-nucleon cross-section limits generally used for the non-collider experiments, a few assumptions are needed. While the direct detection limits are valid for different DM models, the mono-jet limits are exclusively valid for the model chosen, i.e. for the property of the mediators and the strength of the couplings.

The contours obtained in the (m_χ, m_A) plane in the axial-vector mediator scenarios can be mapped in both the plots that show the cross-section of the interaction between the WIMP and a nucleon in the SD scenario, distinguishing protons and neutrons. This is usually done because the DM particles scatter with the spin of the isotope (see Section 4.5.1) which is approximately due to an unpaired neutron or unpaired proton. Thus the direct detection experiments have good sensitivity to one or the other interaction whereas the collider experiments do not distinguish the two cases and can set limits in both scenarios.

For the axial-vector mediator, the cross-section of the SD scattering process can be written as:

$$\sigma_{\mathrm{SD}} = \frac{3 f^2(g_q) g_\chi^2 \mu_{n\chi}^2}{\pi m_A^4} \,, \tag{8.1}$$

in which $\mu_{n\chi} = m_n m_\chi/(m_n + m_\chi)$ defines the WIMP-nucleon reduced mass, where $m_n \simeq 0.939$ GeV is the nucleon mass, and $f(g_q)$ the mediator-nucleon coupling that depends on the mediator-quark couplings. In general $f^{p,n}(g_q)$ can be defined for protons and neutrons as:

$$f^{p,n}(g_q) = \Delta_u^{(p,n)}\, g_u + \Delta_d^{(p,n)}\, g_d + \Delta_s^{(p,n)}\, g_s \,, \tag{8.2}$$

where $\Delta_u^{(p)} = \Delta_d^{(n)} = 0.84$, $\Delta_d^{(p)} = \Delta_u^{(n)} = -0.43$ and $\Delta_s = -0.09$ (these values are taken from Reference [31]). Then assuming the same coupling for all the quarks:

$$f(g_q) = 0.32 g_q \,, \tag{8.3}$$

the scattering cross-section with the nucleon can be obtained by:

$$\sigma^{\mathrm{SD}} \simeq 2.4 \times 10^{-42}\ \mathrm{cm}^2 \cdot \left(\frac{g_q g_\chi}{0.25}\right)^2 \left(\frac{1\,\mathrm{TeV}}{m_A}\right)^4 \left(\frac{\mu_{n\chi}}{1\,\mathrm{GeV}}\right)^2 . \tag{8.4}$$

The same result is valid for the SD DM-proton and DM-neutron scattering cross-sections, σ_{SD}^p and σ_{SD}^n. Using this equation it is therefore possible to map the mono-jet results on both the parameter planes with the best bounds obtained by direct detection experiments. The mono-jet limits in the two dimensional plots with WIMP-proton and WIMP-neutron scattering cross-section versus the WIMP mass m_χ are shown in Figure 8.1 with the XENON100 [58], LUX [62], and PICO [59, 60] bounds at 90%CL.

The analysis is able to exclude scattering cross-sections of the order of $\sigma_{\mathrm{SD}} \sim 10^{-42}\,\mathrm{cm}^2$ up to WIMP masses of about 300 GeV and, as expected, gives complementary results in the low DM mass region $m_\chi \lesssim 10$ GeV. In fact, in this region the energy exchanged during the collisions with the nuclei in the direct detection experiments is too small to be detected. In the models in which the WIMPS are produced by an off-shell mediator the analysis loses its sensitivity and the exclusion contour line turns back in the region of low WIMP masses crossing the direct detection exclusion contours at around $m_\chi = 80$ GeV. The turnover behavior of the mono-jet contours, that was not present in the Run-1 results based on the EFT approach (shown in Figure 4.14), is due to the finite mediator mass considered in the simplified models. In fact, since the mono-jet analysis is mostly able to exclude the on-shell region in the (m_χ, m_A) plane up to $m_A \sim 880$ GeV, the exclusion contour for each fixed value of m_χ passes through two values of m_A and, when the results are mapped in the m_χ versus σ_{SD} plane, they correspond to two values of σ_{SD}.

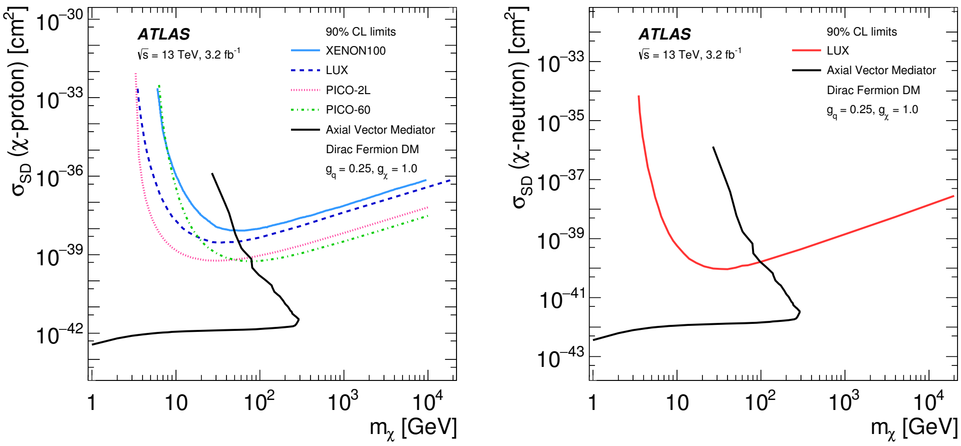

Figure 8.1. A comparison of the mono-jet limits to the constraints from direct detection experiments on the SD WIMP-proton (on the left) and WIMP-neutron (on the right) scattering cross-section in the context of the simplified models with the axial-vector couplings $g_q = 0.25$ and $g_\chi = 1$. The mono-jet limits are shown at 90% CL and exclude the region on the left of the contour. The results coming from the XENON100 [58], LUX [62], and PICO [59, 60] experiments are also shown to highlight the complementarity of the two approaches.

8.2 Mono-jet vs Di-jet Search

An alternative approach to investigate in a collider experiment the existence of DM is based on the analysis of di-jet final states, looking for processes in which the mediator particle is created on-shell in the pp collisions and decays back in two quarks [167]. An example of Feynman diagram that describes this kind of processes is illustrated in Figure 8.2.

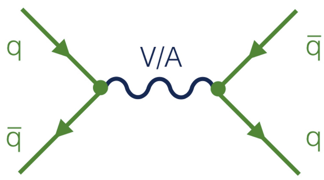

Figure 8.2. Di-jet diagram of the simplified model in which a vector or axial-vector mediator particle is produced in the s-channel and decays back in two quarks.

These searches can provide complementary results with respect to the mono-jet channel and are favoured in the models with higher values of the g_q couplings being the cross-section $\sigma \propto g_q^2$.

In this section several approaches followed by ATLAS analyses to probe this type of processes are outlined, and a comparison of these results to mono-jet results is illustrated.

8.2.1 Di-jet Analysis

The di-jet analysis is one of the most common searches for resonances at collider experiments [169]. It is based on the fact that a particle is produced resonantly from two partons in the *pp* collision and then the resonance can decay back in two quarks. This analysis is clearly dominated by the SM multi-jet background but, whereas the QCD processes provide a smoothly falling di-jet invariant mass m_{jj} distribution, new physics states decaying into two jets may introduce localized excesses in this distribution.

The SM multi-jet background is produced typically at small angles with respect to the beam pipe because *t*-channel scattering processes are dominant, while in many BSM theories particles are predicted to produce a large di-jet contribution at large polar angles. The rapidity variable $y = 1/2 \ln(E + p_z)/(E - p_z)$ is hence defined for each of the outgoing partons where E is its energy and p_z is the longitudinal component of its momentum. The rapidity semi-difference between the two outgoing partons $y^* = y_1 - y_2$ is invariant under Lorentz boosts and it is used in the di-jet analysis to suppress the multi-jet background.

The trigger applied in the analysis based on 15.7 fb^{-1} at $\sqrt{s} = 13$ TeV is the lowest unprescaled single jet trigger available with a p_{T} threshold of 380 GeV. In the final state at least two jets are required, reconstructed with the anti-k_t algorithm with radius parameter $R = 0.4$, with the leading (second leading) one with $p_{\mathrm{T}} > 440(60)$ GeV to ensure of lying on the full trigger efficiency. The m_{jj} distribution of events with $|y^*| < 0.6$ is analyzed in the search of BSM resonances in order to reduce the multi-jet background. With the rapidity and p_{T} requirements applied the di-jet selection is fully efficient for $m_{jj} > 1.1$ TeV.

In order to estimate the SM background the function

$$f(z) = p_1(1 - z)^{p_2} z^{p_3} , \tag{8.5}$$

where $z \equiv m_{jj}/\sqrt{s}$, is used to fit the p_i parameters to the m_{jj} distribution.

In Figure 8.3 is shown the observed m_{jj} distribution based on 15.7 fb^{-1} of data at $\sqrt{s} = 13$ TeV and the result of the fit. The BumpHunter algorithm [168] is used to quantify the statistical significance of any localized excess in the binned distributions considering contiguous mass intervals in all possible locations. The higher discrepancy between data and SM predictions is highlighted in the plot and corresponds to 5277-5487 GeV. However, without including systematic uncertainties, the probability that background fluctuations would produce an excess at least as significant as the one observed in the data, anywhere in the distribution, is of 67%. This means that no evidence of a localized contribution in the distribution due to BSM phenomena is observed.

The results can be then interpreted within the context of the same simplified model probed by the mono-jet analysis in which an axial-vector mediator is produced in the *s*-channel as it will be shown in Section 8.2.4.

In order to probe the existence of lighter mediators the di-jet results obtained in Run-1 with *pp* collisions at $\sqrt{s} = 8$ TeV are also considered [170]. The analysis that was performed is similar to the Run-2 one but because of the lower centre of mass energy of the *pp* collisions and of the lower luminosity, the available single jet trigger allowed to look at smaller di-jet invariant masses. In the Run-1 results also

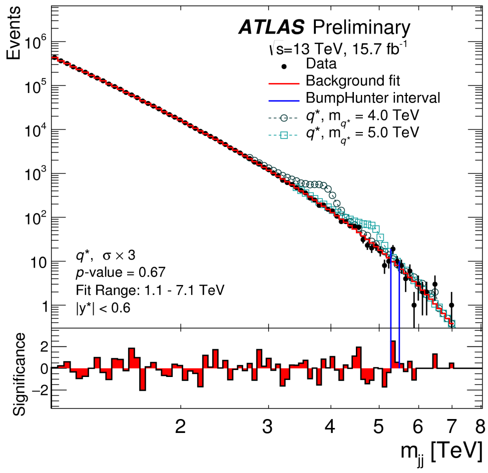

Figure 8.3. Di-jet mass distribution m_{jj} using 15.7 fb^{-1} of data at $\sqrt{s} = 13$ TeV and the results on the fit (more details in the text). The results of BumpHunter algorithm is shown on the bottom highlighting the largest discrepancy between data and SM predictions [169].

the prescaled single jet triggers were used maintaining a trigger efficiency greater than 99.5% for all considered values of the leading-jet p_{T}. The same rapidity cut $|y^*| < 0.6$ was applied and the invariant mass requirement of $m_{jj} > 250$ GeV was chosen such that the di-jet mass spectrum was unbiased by the kinematic selection on the jet transverse momenta. The SM prediction was finally estimated by the fit of the same function used in the 13 TeV results with the addition of a logarithmic term, whose impact was found to be negligible in the Run-2 analysis.

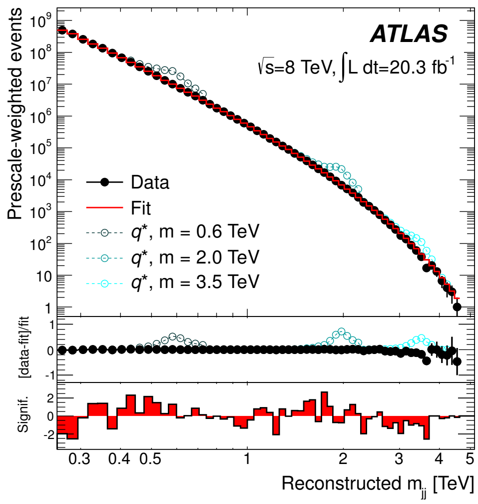

Figure 8.4. Di-jet mass distribution m_{jj} using 20.3 fb^{-1} of data at $\sqrt{s} = 8$ TeV and the results on the fit (more details in the text). The relative difference between data and SM predictions and results of BumpHunter algorithm are shown on the bottom [170].

The di-jet mass distribution, on which the BumpHunter algorithm was also applied, is shown in Figure 8.4 in which a good agreement between data and expectations is observed.

The limits on di-jet resonance production can be determined using a collection of hypothetical Gaussian signal shapes in the m_{jj} spectrum. Several simulated signal samples are generated for different mean values m_G and standard deviations σ_G, corresponding to the di-jet mass resolution estimated from MC simulation and ranging from 7% to 15% of the mean. These models can be used in the interpretations of generic BSM scenarios that foresee narrow resonances in the m_{jj} distribution. The limits on the cross-section times acceptance times branching ratio ($\sigma \times A \times BR$) are set at 95% CL and plotted in Figure 8.5.

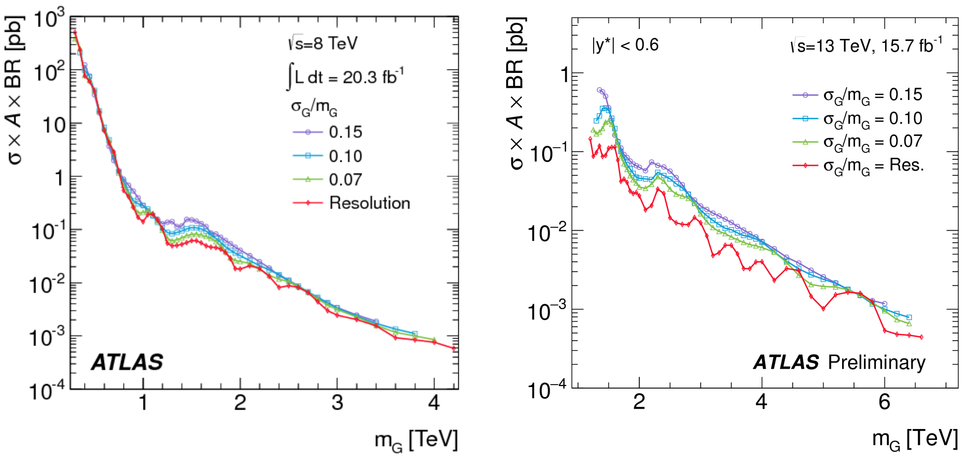

Figure 8.5. Upper limits on $\sigma \times A \times BR$ at 95% CL for a Gaussian resonance decaying into two jets as a function of the mean mass, m_G, for different values of σ_G/m_G, in the di-jet analysis performed using 20.3 fb^{-1} of data at $\sqrt{s} = 8$ TeV (left) and 15.7 fb^{-1} of data at $\sqrt{s} = 13$ TeV (right) [169, 170].

8.2.2 Trigger Level Di-jet Analysis

Since the main difficulty in probing the light di-jet resonances is due to the high p_{T} threshold of the single jet trigger, in Run-2 a trigger level di-jet analysis (TLA) is performed using trigger algorithms able to record only the subset of information in each event needed for such a search [171].

A first-level hardware (L1) based trigger has been implemented to record events at a rate of 100 kHz, identifying jet regions of interest (jet ROIs) from calorimeter segments using a sliding window algorithm. All events containing at least one L1 jet ROI with $E_{\mathrm{T}} > 75$ GeV at the electromagnetic scale, which correctly measures the energy deposited by particles produced in electromagnetic showers in the calorimeter, are stored.

Then the events selected are processed by a software-based high-level trigger that reconstructs the jets following a procedure similar to the one followed in the offline selection, based on the anti-k_t algorithm with radius $R = 0.4$. This second trigger level reduces the event rate by about a factor 100.

A set of dedicated data and MC based calibration procedures [172, 173], based on calorimeter information and pileup corrections [174], are applied to the partially built events in order to restore the jet energy scale equivalent to that of offline jets. To re-establish the agreement between data and simulations used to derive the MC calibration, the jet calibration constants obtained for offline jets from in situ techniques [175] are applied to the trigger jets.

In Figure 8.6 the di-jet invariant mass and p_{T} response of trigger jets with respect to offline jets are shown demonstrating the good quality of the reconstructed jets from the TLA events in the region $|y^{*}| < 0.6$. m_{jj} is defined for events passing at least one jet trigger with $E_{\mathrm{T}} > 110$ GeV while p_{T} uses jets that pass at least the jet trigger with $E_{\mathrm{T}} > 60$ GeV in order to avoid trigger biases. In both the distributions a cut on the transverse momentum of the leading jets is applied in order to guarantee a full trigger efficiency: leading jet $p_{\mathrm{T}} > 185$ GeV and 85 GeV for the m_{jj} and p_{T} plots respectively.

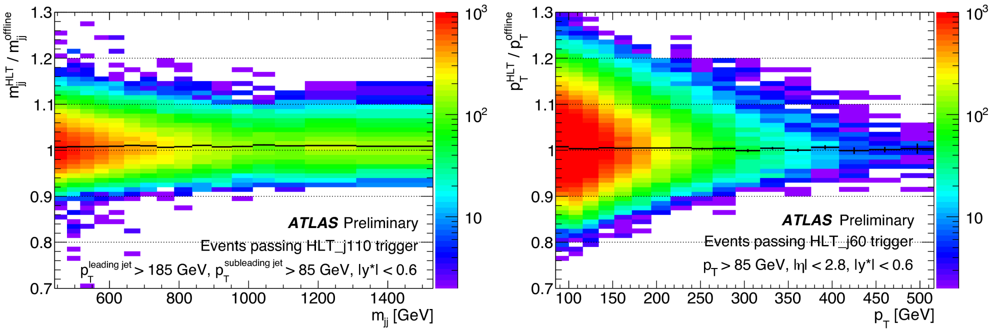

Figure 8.6. Ratio between the m_{jj} (left) and p_{T} (right) variables reconstructed from the HLT and offline jets. More details in the text [171].

The total jet energy scale uncertainty obtained for the TLA jets ranges from 3.5% in the central region ($|\eta| < 0.8$) to a maximum of 5% in the transition region between barrel and endcaps. The main difference between the offline and the trigger jet energy scale is due to the uncertainties on the flavor composition of the sample. Those are significantly reduced for offline jets by the application of corrections based on the inner detector, whose information is not recorded in the partially built TLA events.

The selection applied offline is similar to the one of the di-jet analysis described in the previous section. It requires at least two jets with $p_{\mathrm{T}} > 85$ GeV and $|\eta| < 2.8$ with the leading one with $p_{\mathrm{T}} > 185$ GeV. Two signal regions are defined: one with a cut of $|y^{*}| < 0.6$ and one with $|y^{*}| < 0.3$ which allows to reach values with $m_{jj} < 550$ GeV due to the fact it lowers the mass range affected by the turn-on of the L1 trigger efficiency for a given p_{T} cut.

The increase in statistics achieved by the TLA strategy with respect to using an OR logic of all the single jet triggers and reconstructing the jets offline is illustrated in Figure 8.7, where the m_{jj} distributions of events built with the two approaches are plotted. The fully reconstructed events containing jets with $p_{\mathrm{T}} < 360$ GeV are selected by prescaled triggers that reduce the available statistics, while in the high p_{T} region and $m_{jj} \gtrsim 900$ GeV the two distributions are equivalent. The ratio between the normalized distributions of offline jets selected by `HLT_j110` single-jet trigger and the TLA jets is also shown demonstrating that no biases are introduced using

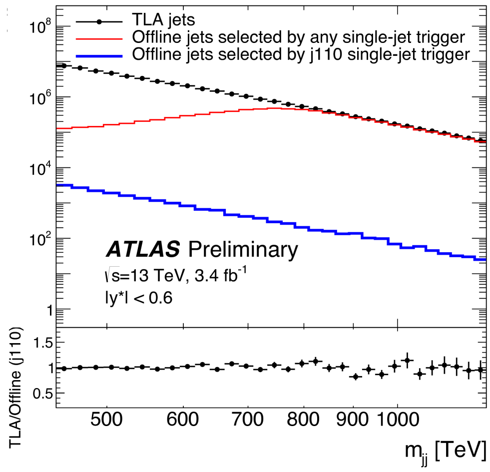

Figure 8.7. Di-jet mass distributions m_{jj} of the TLA jets and fully reconstructed jets using a logic OR of any single jet trigger. The ratio plot compares the shapes of the normalized di-jet mass distributions of TLA trigger jets and offline jets collected using the `HLT_j110` trigger [171].

the partially reconstructed events.

The di-jet mass resolution is finally derived from simulation of QCD di-jet processes and ranges from 6.5% for $m_{jj} \sim 400$ GeV to less than 5% for $m_{jj} \gtrsim 800$ GeV (see Figure 8.8).

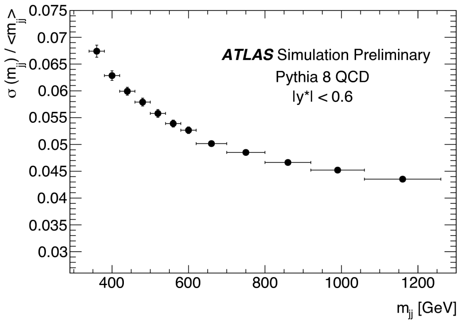

Figure 8.8. Distribution of the ratio of the di-jet mass resolution $\sigma_{m_{jj}}$ to average di-jet mass $\langle m_{jj} \rangle$ as a function of m_{jj} as determined in Pythia-8 simulation of QCD processes. [171].

The SM background is evaluated by fitting the function:

$$f(z) = \frac{p_1}{z^{p_2}} e^{-p_3 z - p_4 z^2} \,. \tag{8.6}$$

The statistical significance of any localized excess in the di-jet invariant mass spectrum is evaluated using the BumpHunter algorithm.

The mass distributions in the two SRs are shown in Figure 8.9 and no anomalous localized contribution is observed in data. The probability of observing a background fluctuation at least as significant as that highlighted by the BumpHunter algorithm is 44% and 19% in the spectrum with $|y^*| < 0.6$ and $|y^*| < 0.3$ respectively.

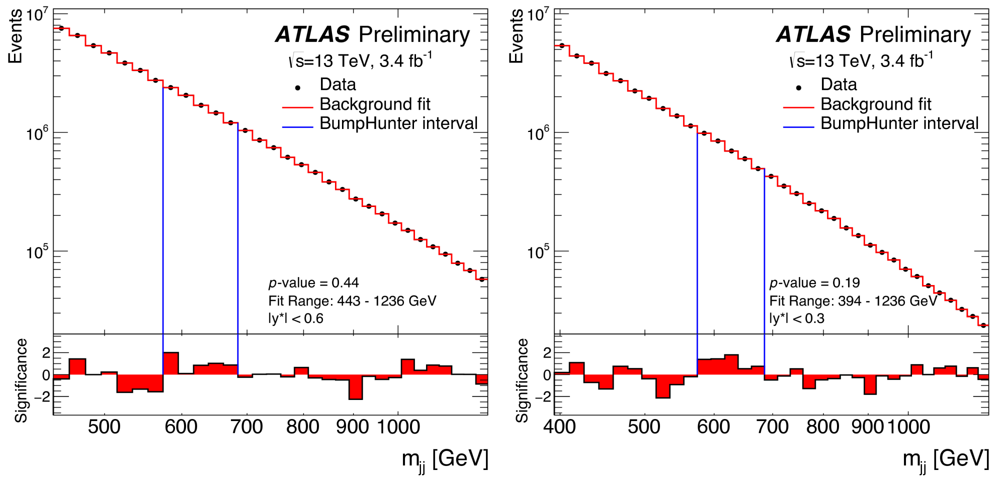

Figure 8.9. Di-jet mass distribution m_{jj} using 3.4 fb^{-1} of data at $\sqrt{s} = 13$ TeV in the signal regions with $|y^*| < 0.6$ (left) and $|y^*| < 0.3$ (right) and the results on the fit (more details in the text). The relative difference between data and SM predictions and results of BumpHunter algorithm are shown on the bottom [171].

The level of agreement is translated, also in this case, in limits on $\sigma \times A \times BR$ for a set of Gaussian signal models centered in m_G with a width of σ_G. The upper exclusion limits are shown in Figure 8.10 in the two signal regions.

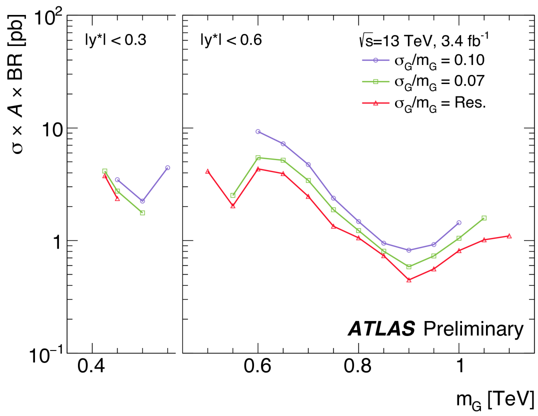

Figure 8.10. Upper limits on $\sigma \times A \times BR$ at 95% CL for a Gaussian resonance decaying into two jets as a function of the mean mass, m_G, for different values of σ_G/m_G, in the di-jet trigger level analysis using 3.4 fb^{-1} of data at $\sqrt{s} = 13$ TeV [171].

8.2.3 Di-jet plus ISR Analysis

In order to probe regions of smaller mediator masses, it is possible to exploit channels with pair jet production processes plus the request of a initial-state-radiation (ISR) of a photon or jet. In fact requiring a hard ISR object in the final state reduces the signal production rates, but allows to trigger with high efficiency a third high-momentum object selecting di-jet events with relative low invariant mass m_{jj}.

With the first 15.5 fb^{-1} of data collected at $\sqrt{s} = 13$ TeV, two signal regions with a ISR photon and jet are defined, tagging the events with a photon trigger with a transverse energy threshold of 140 GeV or a jet trigger with a threshold set to 380 GeV.

In the $X + \gamma$ search, the events are requested to have a tight isolated photon with $E_{\mathrm{T}} > 150$ GeV to ensure the photon trigger to be fully efficient and $|\eta| < 2.37$ excluding the region $1.37 < |\eta| < 1.52$. At least two jets with $p_{\mathrm{T}} > 25$ GeV and $|\eta| < 2.8$ have to be reconstructed in the final state using the anti-k_t algorithm with a radius parameter $R = 0.4$. In addition, half the difference in rapidity of the leading two jet is required to satisfy the requirement $|y^*_{1,2}| < 0.8$ in order to suppress the multi-jet background. To reduce the number of events in which jets emulate photons and pass the isolation criterion, and events with fragmentation photons where the photons are near or inside a jet, the triggered photon is required to be separated from the closest jet by $\Delta R > 0.85$.

Similarly the $X + j$ search uses a sample of events which contain at least one jet with $p_{\mathrm{T}} > 430$ GeV and at least two additional jets with $p_{\mathrm{T}} > 25$ GeV and $|\eta| < 2.8$. The second and third highest p_{T} jets are required to be separated by $|y^*| < 0.6$, to suppress the non-resonant di-jet QCD processes.

The invariant di-jet mass spectrum, where m_{jj} is formed by the two leading jets in the $X + \gamma$ and by the second and third leading jets in the $X + j$ searches, is estimated by a fit of the function:

$$f(z) = p_1(1 - z)^{p_2} z^{p_3 + p_4 \ln z}\,, \tag{8.7}$$

where p_4 is fixed at zero in the channel with the ISR jet. The function is fitted in the range $m_{jj}\,\epsilon\,[169, 1493]$ GeV for the $X + \gamma$ search, and $m_{jj}\,\epsilon\,[303, 611]$ GeV in the $X + j$ one. The results of the fit and the observed events in the two signal regions are shown in Figure 8.11. The BumpHunter algorithm has been also applied to search the highest discrepancies between data and SM expectations, that are identified in the interval between 861 GeV and 917 GeV for the $X + \gamma$ case and 482 GeV and 523 GeV for the $X + j$ one. However the probability that fluctuations of the background model would produce an excess at least as significant as the one observed in the data, anywhere in the distribution, is 67% for the $X + \gamma$ search and 60% for the $X + j$ one, thus, no evidence of a resonant contribution is observed.

The results are then interpreted in the search of BSM Gaussian resonances decaying in two jets with mass m_G and width σ_G. The limits on the $\sigma \times A \times BR$ at 95% CL in both the ISR channels considered are shown in Figure 8.12.

8.2.4 Comparison of Results

The level of agreement found in the m_{jj} spectra of the several di-jet analyses between data and the SM predictions can be translated in limits in the DM scenarios. In order to interpret the results in the (m_χ, m_A) plane with the mono-jet contours, a set of simulated signal samples are generated and the relative exclusion limits can be set following the criteria listed below in the narrow width approximation, and considering the resonances approximately Gaussian near the core [170]:

- generate a set of MC signal samples with MadGraph5_aMC@NLO (using the package DMSimp [178]) with a new axial-vector mediator with mass set to m_A;

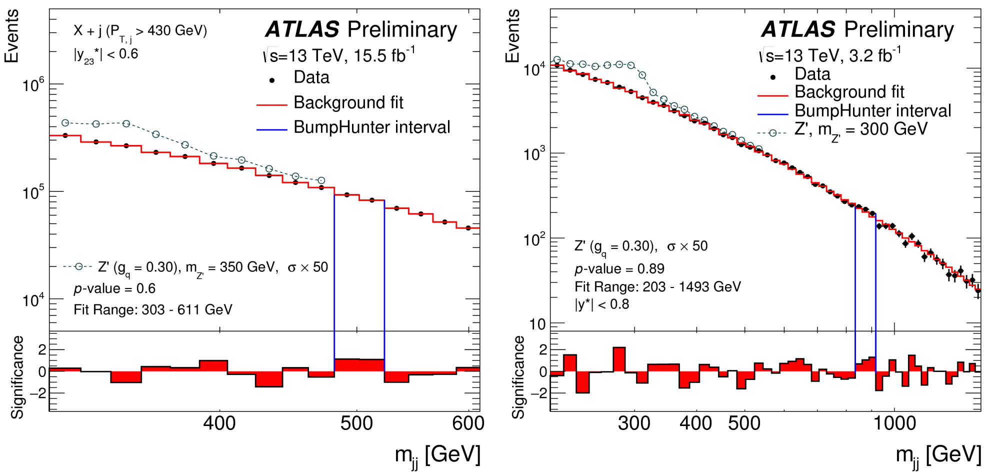

Figure 8.11. Di-jet mass distribution m_{jj} using 15.5 fb^{-1} of data at $\sqrt{s} = 13$ TeV in the signal regions with an additional ISR photon with $E_{\mathrm{T}} > 150$ GeV (left) and jet with $p_{\mathrm{T}} > 430$ GeV (right) and the results on the fit (more details in the text). The relative difference between data and SM predictions and results of BumpHunter algorithm are shown on the bottom [177].

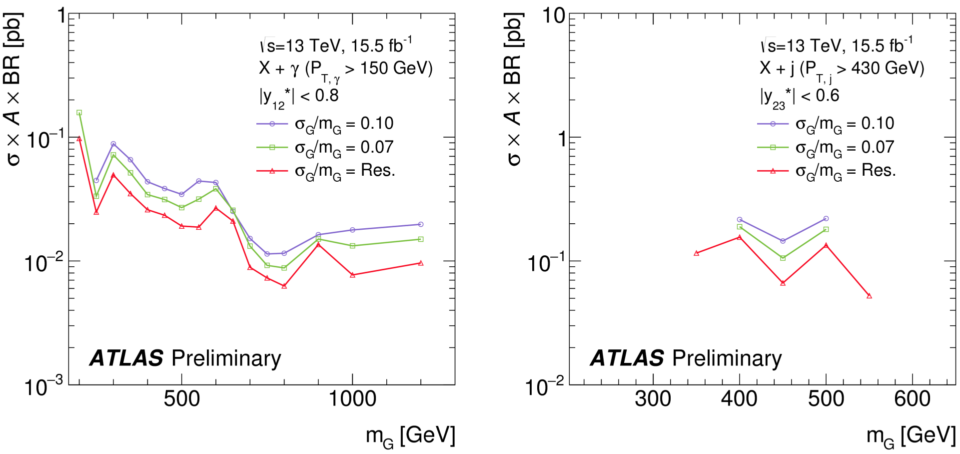

Figure 8.12. Upper limits on $\sigma \times A \times BR$ at 95% CL for a Gaussian resonance decaying into two jets as a function of the mean mass, m_G, for different values of σ_G/m_G, in the di-jet analysis with an ISR of a photon (left) and of a jet (right) performed using 3.2 fb^{-1} of data collected at $\sqrt{s} = 13$ TeV [177].

- apply the same kinematic selection on the parton η, p_{T}, and $|y^*|$ used in the considered di-jet analysis;
- smear the signal mass distribution to reflect the detector resolution using the smearing factors derived from multi-jet simulation as shown in Figure 8.8. This step is relevant for low-mass mediators with TLA jets for which the resolution is worse than the offline fully reconstructed di-jet events;
- assuming a Gaussian signal shape in determining the limits, the m_{jj} signal spectrum is fitted with a Crystal Ball function [179];

- the fitted parameters allow to calculate the Gaussian core efficiency, ,which is used as acceptance correction, counting the number of events in the m_{jj} distribution within $\pm 3\sigma$ around the mean $\bar{m}$ and dividing this value with the total number of events;

- select the gaussian signal with the value of m_G as close as possible to the mean $\bar{m}$ of the signal considered. If the exact value of $\bar{m}$ has not an exact corresponding Gaussian sample, consider the limit for the two values of m_G that are directly above and below $\bar{m}$, and use the larger of the two limits to be conservative;

- for this mass point, choose the value of σ_G/m_G such that the region within $\pm 2\sigma_G$ is contained in the (truncated) mass range;

- use the tabulated 95% CL upper limit on $\sigma \times A$ corresponding to the chosen Gaussian signal and multiply by the acceptance defined in the previous step and by the branching ratio into two jets.

The limits resulting from the procedure described above are plotted with the mono-jet and mono-photon [180] contours and shown in Figure 8.13.

The mono-photon process constitutes another important channel in the search for DM at ATLAS. The photon comes from ISR and therefore the search has a lower expected statistics with respect to the mono-jet final state ($\alpha_{EM} \ll \alpha_S$), but on the other hand it constitutes a cleaner process. The selection and analysis strategy is similar to the mono-jet one described in the previous chapter. It requires in the final state one isolated photon with high transverse energy $E_{\mathrm{T}} > 150$ GeV and considers an unique $E_{\mathrm{T}}^{\mathrm{miss}}$-bin. Four CRs are defined to constrain the main $Z/W+\gamma$ and γ+jets background contributions. A simultaneous fit is then performed to evaluate the SM predictions and the presence of signal contributions. The dominant uncertainty which affects the SR yields is due to the low statistics in the CRs, that amounts to 9% on the total of about 11%.

The resulting constraints are less stringent and constitute only a subset of the mono-jet ones.

The di-jet limits are almost independent on the WIMP mass and the slight dependence is due to the mediator width that changes when the DM production process becomes on-shell. The combination of the di-jet results is able to exclude a wide area of the parameter space in the (m_χ, m_A) plane starting from 200 GeV up to 2.5-2.8 TeV, depending on the value of the DM mass. The wiggles that appear along the di-jet contours are due to extrapolation and not to physics effects.

The plot shows the exclusion power of the di-jet searches in the case of a sizable coupling value between the mediator and the SM particles, while the mono-X searches provide complementary results only in the region with very low mediator masses. However, as will be shown in the next section, in the hypothesis of a lower value of g_q the di-jet searches lose drastically their sensitivity whereas mono-X ones still remains competitive.

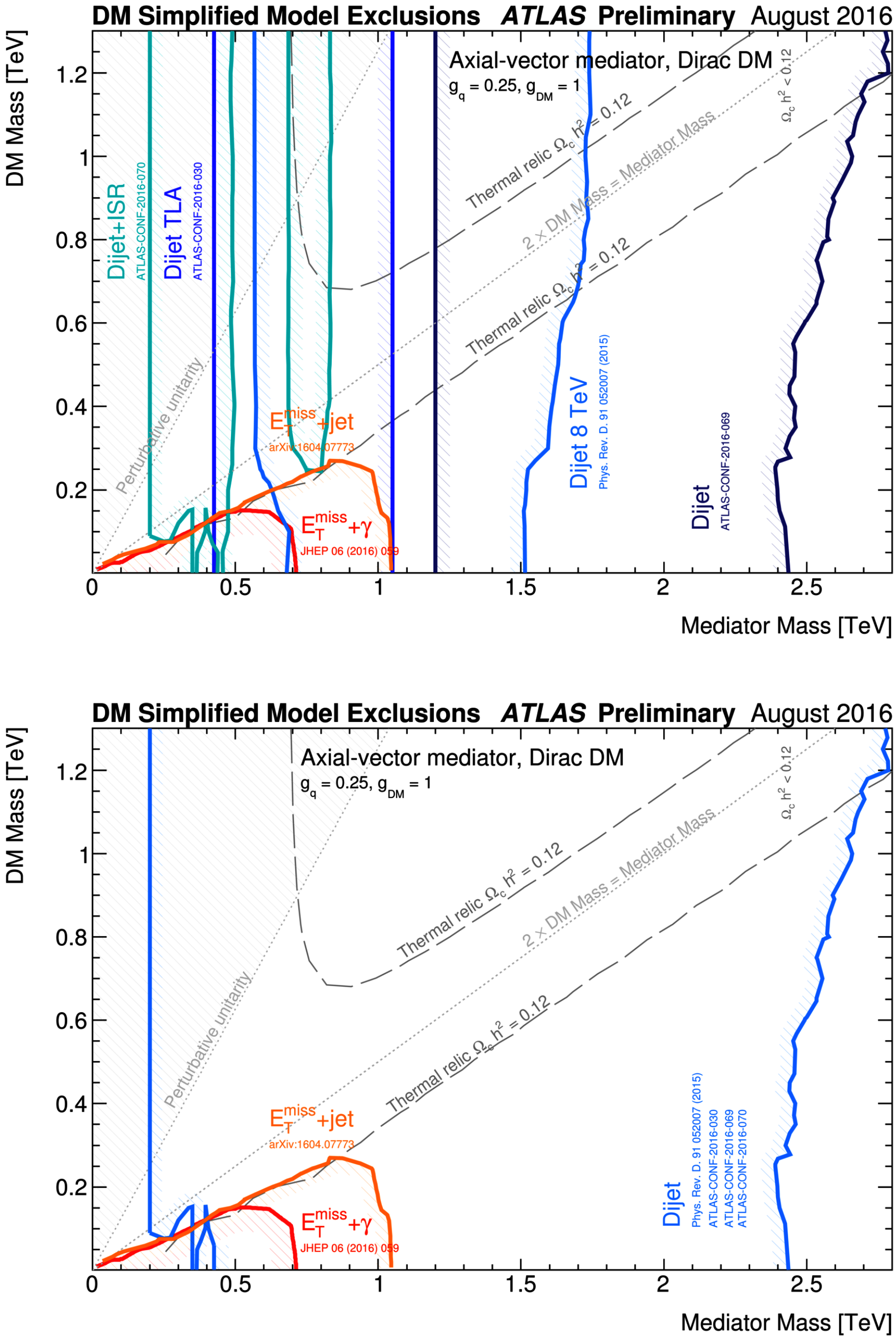

Figure 8.13. 95% CL observed exclusion contours in the m_χ versus m_A parameter plane in the axial-vector mediator hypothesis with the coupling fixed at $g_q = 0.25$ and $g_\chi = 1$. The orange and red curves correspond to the mono-jet and mono-photon results respectively while blue lines delimit the areas excluded by the several di-jet searches. On the bottom all the di-jet contours are combined. The grey curve corresponds to the expected relic density. The grey hatched area indicates the excluded are due to perturbative unitarity, defined by $m_\chi > \sqrt{\pi/2}\, m_A$ [181].

8.2.5 Coupling Rescaling

In order to set the limits in a different DM scenario a coupling rescaling is performed, choosing a lower mediator-SM coupling g_q and a higher mediator-DM coupling g_χ to give complementary results with respect to the di-jet searches. This method permits to avoid to generate another set of MC samples similar to the ones used to obtain the results shown above in the (m_χ, m_A) plane. In order to be applied, one needs to compare the acceptances between the signals with the two alternative coupling choices. They have to result compatible within the MC statistic uncertainties in all the bins used in the shape fit performed in the mono-jet analysis. A set of signal samples with the coupling values of $g_q = 0.1$ and $g_\chi = 1.5$ are generated at truth level to compare the distributions and acceptances with signals with $g_q = 0.25$ and $g_\chi = 1$. This new coupling setting has been chosen to get similar values of the cross-sections for mono-jet and di-jet processes.

The acceptances, defined as the ratio between the number of events passing the mono-jet selection at truth level and the total number of generated events, are calculated in each of the seven $E_{\mathrm{T}}^{\mathrm{miss}}$-bins. While the shapes of the distributions are compared using the Kolmogorov-Smirnov (KS) test. In Figure 8.14 the acceptances in the several $E_{\mathrm{T}}^{\mathrm{miss}}$-bins are shown for the signals with the couplings set at $g_q = 0.25$, $g_\chi = 1$ (closed circles) and $g_q = 0.1$, $g_\chi = 1.5$ (open circles) for different values of the WIMPs and mediator masses.

The resulting p-values, coming from the KS-tests that permits to determine if the two signals are compatible, are obtained and reported in the legend of the plot. All the p-values calculated for each sample are greater than 5%. This implies that the coupling rescaling can be performed and the new limits on the signal strengths can be simply obtained rescaling point-by-point the old ones by the ratio of the cross-sections $\sigma_{g_q=0.25, g_\chi=1}/\sigma_{g_q=0.1, g_\chi=1.5}$. The mono-jet limits in the (m_χ, m_A) plane, in the new coupling hypothesis, are shown in Figure 8.15. The interpolation in this case is not optimal since the set of generated points is exactly the same of the old coupling scenario. One can however see that the mono-jet channel is still sensitive to exclude a consistent region of the phase space.

Rescaling the mono-photon limits and plotting the contour limits with the di-jet ones obtained with the procedure described in the previous section, the summary plot for the new coupling scenario is shown in Figure 8.16. With this choice of couplings, the branching ratio to DM particles is enhanced; while the sensitivity of di-jet searches is reduced, due to the fact that mediator decays into quarks are suppressed. In this kind of scenario the mono-X searches remain the most important tool to probe the existence of WIMP pair production processes at colliders in the context of axial-vector simplified models.

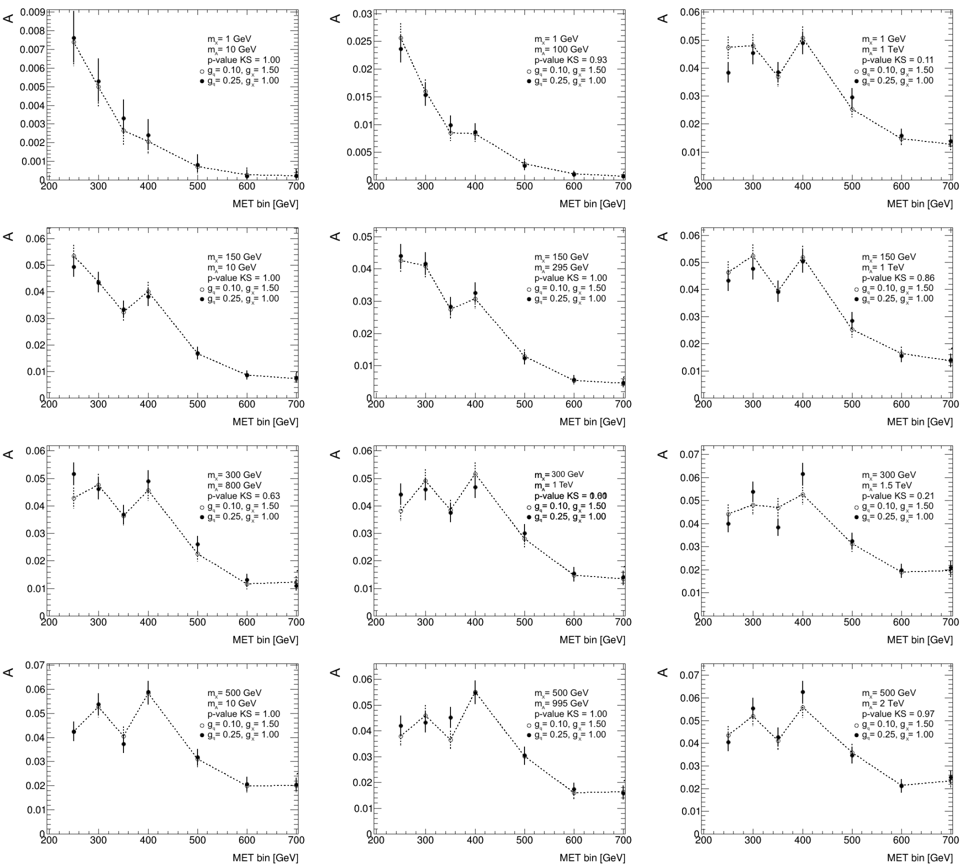

Figure 8.14. Acceptances as a function of the $E_{\mathrm{T}}^{\mathrm{miss}}$-bins for a subset of the total signal samples tested with an axial-vector mediator and the couplings fixed at $g_q = 0.25, g_\chi = 1$ (in closed circles) and $g_q = 0.1, g_\chi = 1.5$ (in opened circles). The results of the KS test based on the two distributions are expressed in terms of p-values reported in the legends.

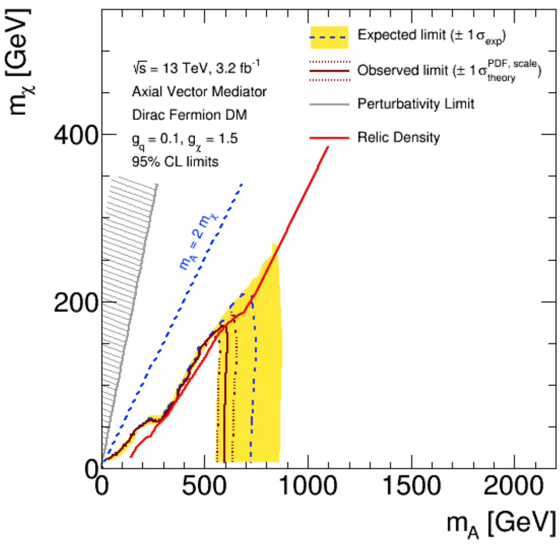

Figure 8.15. 95% CL exclusion contours in the m_χ versus m_A parameter plane in the axial-vector mediator hypothesis with couplings fixed at $g_q = 0.1, g_\chi = 1.5$. The solid curve shows the observed limit, the dashed contour line defines the expected limit, while the bands indicate the $\pm 1\sigma$ theory uncertainties in the observed limit and $\pm 1\sigma$ range of the expected limit in the absence of a signal one. The contours are obtained rescaling the limits relative to the simplified model with $g_q = 0.25, g_\chi = 1$ as described in the text. The grey dashed curve identifies the set of points for which $\Omega h^2 = 0.12$. The grey hatched area indicates the excluded are due to perturbative unitarity, defined by $m_\chi > \sqrt{\pi/2}\; m_A$.

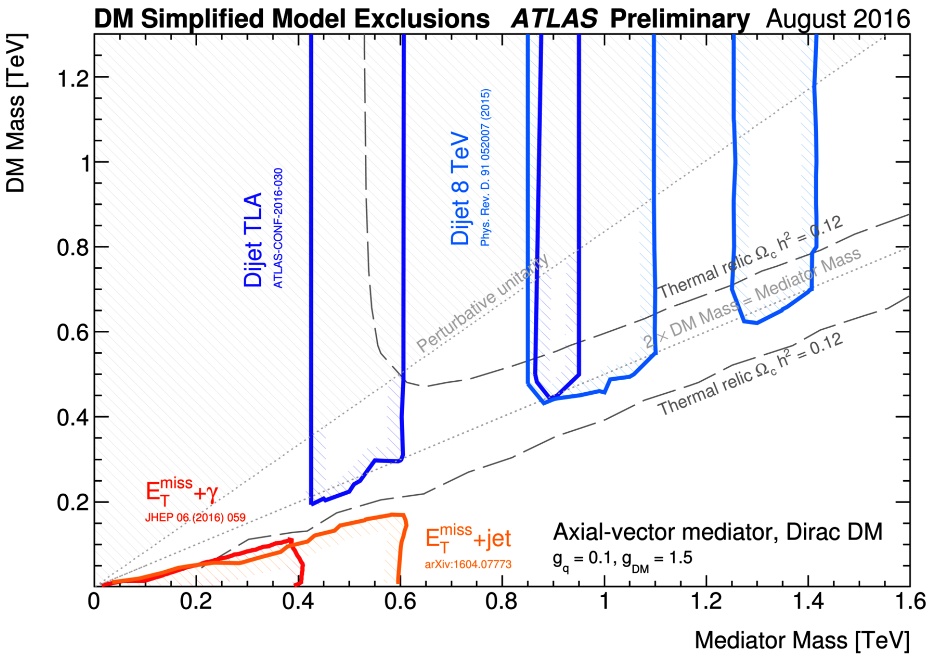

Figure 8.16. 95% CL observed exclusion contours in the m_χ versus m_A parameter plane in the axial-vector mediator hypothesis with the coupling fixed at $g_q = 0.1$ and $g_\chi = 1.5$. The orange and red curves correspond to the mono-jet and mono-photon channel respectively while blue lines delimit the areas excluded by the several di-jet searches. The grey dashed curve identifies the set of points for which $\Omega h^2 = 0.12$. The grey hatched area indicates the excluded are due to perturbative unitarity, defined by $m_\chi > \sqrt{\pi/2}\, m_A$ [181].

Chapter 9

Mono-jet Analysis Improvements

The mono-jet results based on the first 3.2 fb^{-1} of data collected in pp collisions at $\sqrt{s} = 13$ TeV at ATLAS have confirmed the contribution of this final state to the search for Dark Matter and new physics phenomena and its complementarity with respect to other analyses and experiments. In this chapter the improvements that can be applied in the mono-jet analysis in the future are discussed, taking into account the foreseen increase of the integrated luminosity.

9.1 Data Sample

Thanks to the great performance achieved by the LHC machine and the ATLAS detector, the total luminosity collected at the end of 2016 corresponds to an increase by more than a factor 10 with respect to 2015. This is a great opportunity to probe the tail of the high missing transverse momentum spectrum, which is expected to provide an important improvement of the signal to background discrimination power for most signals. Furthermore it will lead to a better knowledge of the background predictions evaluated by the CRs, reducing the statistical uncertainties coming from the semi-data-driven technique used to evaluate the main sources of background.

With the increase of the statistics, the high $E_{\mathrm{T}}^{\mathrm{miss}}$ tail can be probed splitting the last inclusive bin with $E_{\mathrm{T}}^{\mathrm{miss}} > 700$ GeV in Chapter 7 in multiple bins. The criterion applied to define the additional bins consists of maintaining in the new last inclusive bin a number of expected events in the signal and in the control regions close to the one obtained for the 2015 results. The new binning consequently includes the same $E_{\mathrm{T}}^{\mathrm{miss}}$-range used in the previous version of the analysis with the addition of three high $E_{\mathrm{T}}^{\mathrm{miss}}$ bins as shown in Table 9.1.

All the systematic uncertainties are re-evaluated for the entire $E_{\mathrm{T}}^{\mathrm{miss}}$ spectrum and in particular the theoretical one relative to the transfer factor is conservatively extrapolated in the additional bins reaching the value of 7.5% in IM10. The uncertainty of the luminosity systematic uncertainty has been reduced to 2.9% due to the better knowledge of integrated luminosity achieved during the data taking in 2016.

When performing a background-only fit in the CRs using an integrated luminosity

SR bins	EM1	EM2	EM3	EM4	EM5
$E_{\mathrm{T}}^{\mathrm{miss}}$[GeV]	[250–300]	[300–350]	[350–400]	[400–500]	[500–600]
SR bins	EM6	EM7	EM8	EM9	IM10
$E_{\mathrm{T}}^{\mathrm{miss}}$[GeV]	[600–700]	[700–800]	[800–900]	[900–1000]	> 1000

Table 9.1. $E_{\mathrm{T}}^{\mathrm{miss}}$ bins used in the simultaneous shape binned fit with the data sample collected during 2015 and 2016.

of 25 fb^{-1}, the total uncertainty on the background predictions, in terms of the variation of the yields in the SR, is reduced to $\sim 3.3\%$ of which only $\sim 0.3\%$ is the statistical component.

The projection results, for an integrated luminosity of 25 fb^{-1}, are produced for the simplified models with axial-vector mediators using a subset of the signal samples generated to obtained the results shown in Chapter 7. The 95% expected contour in the mass-mass plot is shown on the left of Figure 9.1. In the axial-vector hypothesis the contours can exclude a region in the plane which extends up to $m_A \sim 1420$ GeV and enlarge the excluded area in the region close to the on-shell line $m_A = 2m_\chi$. On the other hand, due to very low cross sections of the pseudo-scalar simplified models, the analysis is still not sensitive to exclude this scenario and the limits on the signal strength at 95% CL are $\mu_{\mathrm{excl}} \gtrsim 2$, for all the signal samples considered. The projection of the contour fixed at $\mu = 5$ on the simplified models with pseudo-scalar couplings is shown on the right of Figure 9.1.

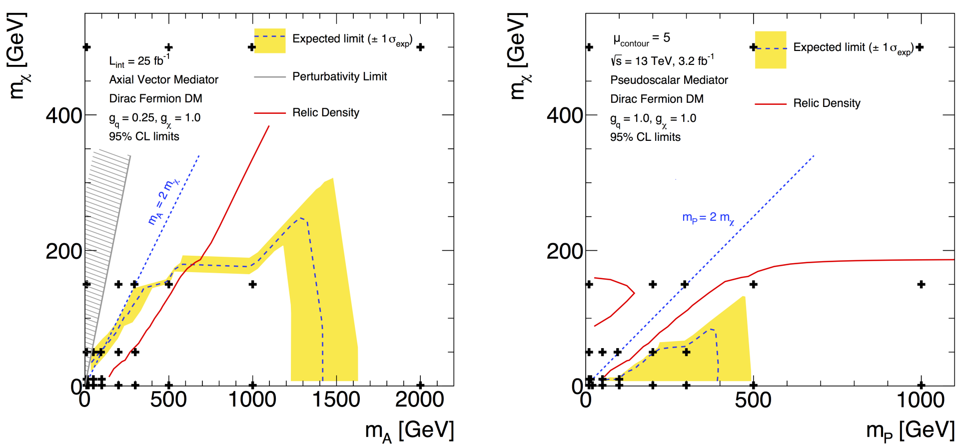

Figure 9.1. On the left: 95% CL expected exclusion contour in the m_χ versus m_A parameter plane in the axial-vector mediator hypothesis with coupling fixed at $g_\chi = 1$ and $g_q = 0.25$. On the right: 95% CL expected contour at $\mu = 5$ in the m_χ versus m_P parameter plane in the pseudo-scalar mediator hypothesis with coupling fixed at $g = g_q = g_\chi = 1$. The results are obtained using an integrated luminosity of 25 fb^{-1} at $\sqrt{s} = 13$ TeV with the new binning configuration.

9.2 Background Knowledge

Looking at the results of the background-only fit in the CRs shown in Section 7.7 and Appendix B, the main uncertainties that affect the analysis results, based on 3.2 fb^{-1} of data, are given by the low statistics in the high missing transverse momentum region of CR1μ and by the systematic uncertainties in the low missing energy region. A high number of events in CR1μ is crucial to reduce the total uncertainty and increase the analysis sensitivity, since this CR is dominated by the $W(\mu\nu)$+jets processes which constrain the irreducible $Z(\nu\nu)$+jets background in the SR. On the other hand the total background uncertainty in the low $E_{\mathrm{T}}^{\mathrm{miss}}$-region is dominated by the systematic uncertainties of which the largest contribution derives from the top background predictions. In this section the estimation and the strategies to reduce the total uncertainty related to the irreducible background and the $t\bar{t}$ processes are introduced.

9.2.1 $Z(\nu\nu)+$ jets Estimation

The evaluation of the irreducible background in the SR is the most critical question of the mono-jet analysis. In the first results based on 3.2 fb^{-1} of data, the most natural choice of estimating $Z(\nu\nu)$+jets from the $Z(\mu\mu)$+jets and $Z(ee)$+jets processes turned out to be not the optimal strategy because of the low statistics in the high $E_{\mathrm{T}}^{\mathrm{miss}}$-region in CR2$\ell$, in which this kind of processes largely dominates.

The $W(\mu\nu)$+jets process, used to evaluate the irreducible background, has turned out to be the best approach in the previous mono-jet analysis. In fact the number of process yields expected in CR1μ is more than 5 times higher with respect to the $Z(\mu\mu)$+jets in CR2μ. This allows to reduce the total uncertainty in the tails of the high $E_{\mathrm{T}}^{\mathrm{miss}}$ distribution, increasing the sensitivity to the signals which populate this part of the spectrum. On the other hand, as discussed in Section 7.6.1, this estimation strategy leads to an uncertainty due to the different EWK and QCD corrections between the W and the Z in the transfer factor, that increases the total uncertainty of the SM predictions in the SR in the low $E_{\mathrm{T}}^{\mathrm{miss}}$ regime.

A possible reduction of the statistical uncertainties in the high $E_{\mathrm{T}}^{\mathrm{miss}}$-region of the irreducible background can be obtained by evaluating these kind of processes from the γ+jets ones. The cross section of these latter is actually much higher than $W(\mu\nu)$+jets, so a new CR (CR1γ) close to the SR can be defined applying the same criteria selection of the SR with the addition of the requirement of a high energetic isolated photon with $E_{\mathrm{T}} > 250$ GeV. Then, similarly to CR1μ, the photon is treated as an invisible particle in the missing transverse momentum calculation so that the $E_{\mathrm{T}}^{\mathrm{miss}}$ distribution acts as a proxy for the boson p_{T} spectrum. The $E_{\mathrm{T}}^{\mathrm{miss}}$ distribution in the new CR1γ is shown in Figure 9.2 and the number of expected events is estimated to increase by a factor ~ 2.5 with respect to CR1μ. The photons, that were not reconstructed and considered as jets in the previous analysis, are vetoed in the other regions reducing the total background in the SR by 3.6% and the signals by ∼1-2%.

In order to test and quantify the benefit that can be achieved with the introduction of the new CR, a background-only fit in the CRs is performed evaluating the invisible decay of the Z in the SR from the γ introducing in the fit CR1γ. Also in this case

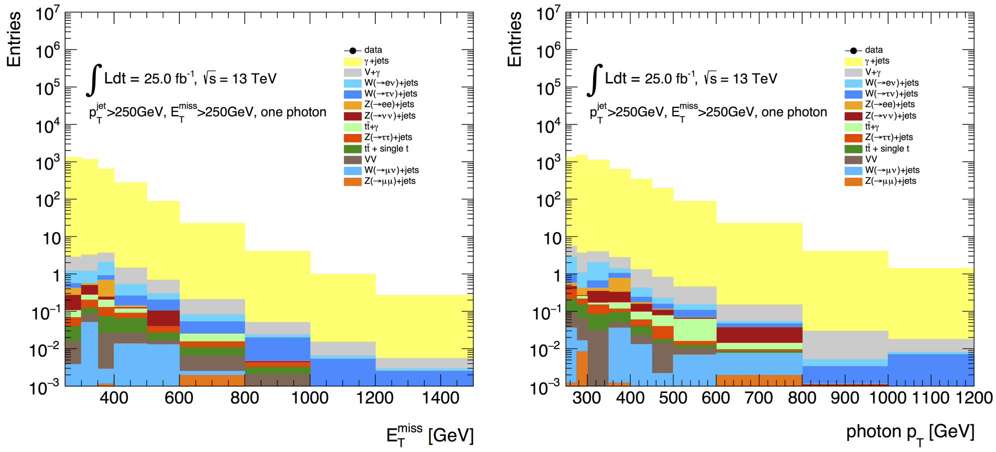

Figure 9.2. SM expectations corresponding to an integrated luminosity of 25 fb^{-1} in the missing transverse momentum and the photon p_{T} spectrum considering the photon considered as invisible particle in the $E_{\mathrm{T}}^{\mathrm{miss}}$ calculation.

a theoretical systematic on the $\gamma \rightarrow Z$ transfer factor has to be assigned to the $Z(\nu\nu)$+jets predictions to take into account the uncertainty on the different EWK and QCD higher-order corrections applied to the vector boson and the photon in the differential cross section $\mathrm{d}\sigma/\mathrm{d}p_{\mathrm{T}}$.

Since an updated calculation of the transfer factor systematic is not available for the analysis, it is estimated by the calculation in Reference [182]. The distribution of the ratio between the differential cross sections of the Z+jets and γ+jets processes is shown in Figure 9.3 based on calculations at LO, NLO and NNLO. The values of

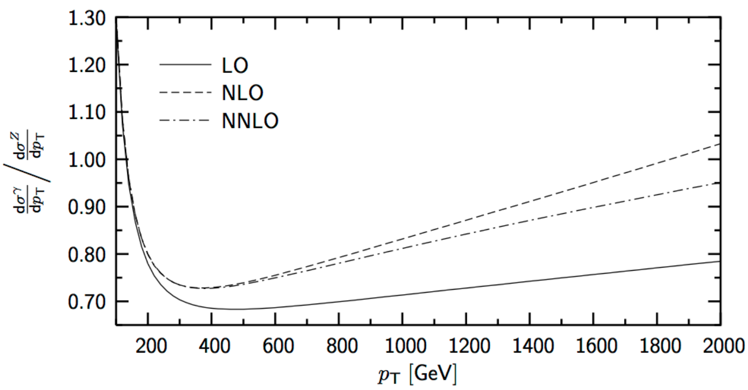

Figure 9.3. Ratio of the γ+jets and Z+jets differential cross sections as a function of the boson p_{T} at LO, NLO, NNLO [182].

the transfer factor systematic uncertainties to apply in the different $E_{\mathrm{T}}^{\mathrm{miss}}$ bins of the fit are evaluated from this plot taking the difference between the LO and NNLO predictions in the corresponding boson p_{T}. These values are conservatively chosen to range between 3.5% (EM1) and 13% (IM10) in the entire spectrum, thus the systematic uncertainty applied in this case are larger than the ones considered for the strategy based on the evaluation of the Z from a W boson in all the $E_{\mathrm{T}}^{\mathrm{miss}}$ bins of the SR.

Using the new binning configuration introduced in the previous section, a background-only fit in the CRs is performed and the relative uncertainties on the total SM prediction in each bin are shown in Figure 9.4. This fitting strategy reduces the relative uncertainty in the high $E_{\mathrm{T}}^{\mathrm{miss}}$ bins by $\sim 10\%$ and allows to consider also additional bins to enhance the analysis sensitivity to most of the signal considered.

The results are compared also with the strategy that exploits the $Z(\mu\mu)$+jets and $Z(ee)$+jets processes to evaluate the irreducible background. In this case a new CR with two electrons in the final state (CR2e) is introduced with the same definition of CR2μ to double the statistics of the effective new CR2ℓ, defined as the sum of the two di-leptonic CRs. The new CR2e is defined inverting the electron veto with respect to the SR, treating the electrons as invisible particle in the missing transverse momentum calculation and applying the cut on the di-electron invariant mass between 66 GeV $< m_{ee} <$ 116 GeV. The lowest unprescaled single electron trigger is used to tag the events in this region. In the limit of very high integrated luminosity where the statistical uncertainty is strongly reduced, the estimation of the irreducible background by using uniquely the $Z(\mu\mu)$+jets and $Z(ee)$+jets processes is favoured being not needed a theoretical uncertainty on the transfer factors. However this fitting strategy does not improve the results with the integrated luminosity $L \leq 25$ fb^{-1} because of the low statistics in the CRs with two charged leptons. In fact using an integrated luminosity of 25 fb^{-1}, the relative uncertainty in the last inclusive bin increases by $\sim 30\%$ with respect to the standard strategy used to obtain the previous mono-jet results. On the other hand, in the low $E_{\mathrm{T}}^{\mathrm{miss}}$-region, where the transfer systematic uncertainties are not applied, the relative uncertainty is reduced by 5-10% in the first bins.

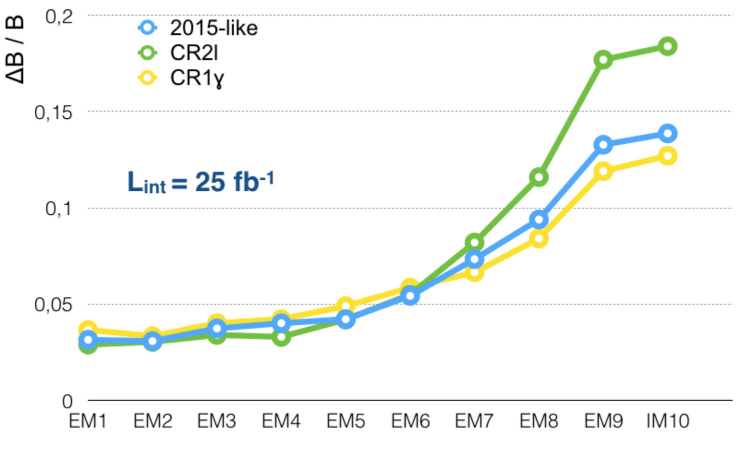

Figure 9.4. Relative uncertainties in the different $E_{\mathrm{T}}^{\mathrm{miss}}$ bins using the standard strategy fitting (blue), the new one with the introduction of CR1γ to evaluate the $Z(\nu\nu)$+jets background from the γ+jets processes and the strategy that uses the $Z(\ell\ell)$+jets contribution to evaluate the irreducible background with the introduction of CR2e. The fits are performed using the binning proposed in Table 9.1 and an integrated luminosity of 25 fb^{-1}.

Eventually a fitting strategy that includes the introduction of both CR2ℓ and CR1γ, to evaluate the $Z(\nu\nu)$+jets processes in the two $E_{\mathrm{T}}^{\mathrm{miss}}$ regimes in the SR, it would allow to reduce the final background uncertainty over all the spectrum considered with the integrated luminosity expected for the end of the year. It would also avoid to evaluate the kinematic of the Z+jets process from γ+jets in the low p_{T} part of the spectrum in which the effects due to the mass difference between the bosons considered could be not negligible.

9.2.2 Top Estimation

One of the main contributions of the total background uncertainty in the low $E_{\mathrm{T}}^{\mathrm{miss}}$-region comes from the top background prediction. It is mainly due to the large theoretical uncertainty that affects this kind of processes which is evaluated by MC simulations. With the increase of the integrated luminosity the data-driven technique based on the introduction of a new CR can be applied also for this source of background.

The b-tagging information is used for this purpose splitting CR1μ in a CR with at least one jet b-tagged (CR1μ+b-tag) and a CR in which the b-veto is applied (CR1μ+b-veto). CR1μ+b-tag is mostly populated by $t\bar{t}$ processes, which decay semi-leptonically since the contribution of the muons is subtracted in the $E_{\mathrm{T}}^{\mathrm{miss}}$ calculation. This kind of processes is kinematically close to the same ones in the SR in which the lepton is misidentified.

The expected events in CR1μ+b-tag are about 9% of CR1μ yields. The $E_{\mathrm{T}}^{\mathrm{miss}}$, leading jet p_{T}, jet and b-jet multiplicity distributions of the SM predictions are shown in Figure 9.5 normalized to an integrated luminosity of 25 fb^{-1}.

A background-only fit in the CRs is performed splitting CR1μ in the two CRs defined using the b-tagging information and using CR1μ+b-tag to constrain the top background in the SR by using an ad-hoc normalization factor. The fit is performed using the same binning introduced in Table 9.1 and an integrated luminosity of 25 fb^{-1}. The data-driven techniques applied to $t\bar{t}$ and single top production processes allows to reduce the impacts of the top theoretical systematics that is found to have an almost negligible effect on the total background in the SR.

The relative uncertainties in the several bins are evaluated by a background-only fit in the CRs and the results are shown in Figure 9.6. The introduction of the new CR reduces the total background uncertainty in the low $E_{\mathrm{T}}^{\mathrm{miss}}$-regions corresponding to an improvement in terms of the relative uncertainty of about 10-15% in the first bins. In the high $E_{\mathrm{T}}^{\mathrm{miss}}$-region the SM predictions are worse constrained because of the low statistics of CR1μ+b-tag, which leads to a higher uncertainty on the top background with respect to the standard evaluation based on the MC simulations.

The projections of the 95% CL exclusion limits on the simplified model with axial-vector mediators and the contour fixed at $\mu = 5$ on simplified models with pseudo-scalar couplings obtained for an integrated luminosity of 25 fb^{-1} are shown in Figure 9.7 in the mass-mass plots. They demonstrate how the reduction of the total uncertainty in the low $E_{\mathrm{T}}^{\mathrm{miss}}$-region leads to an improvement in sensitivity to the signals that populate this part of the spectrum: the contours of the spin-0 simplified models and of the spin-1 signals close to the resonance region are sensibly enlarged and the exclusion limits on the cross-sections improve by up to 35% with

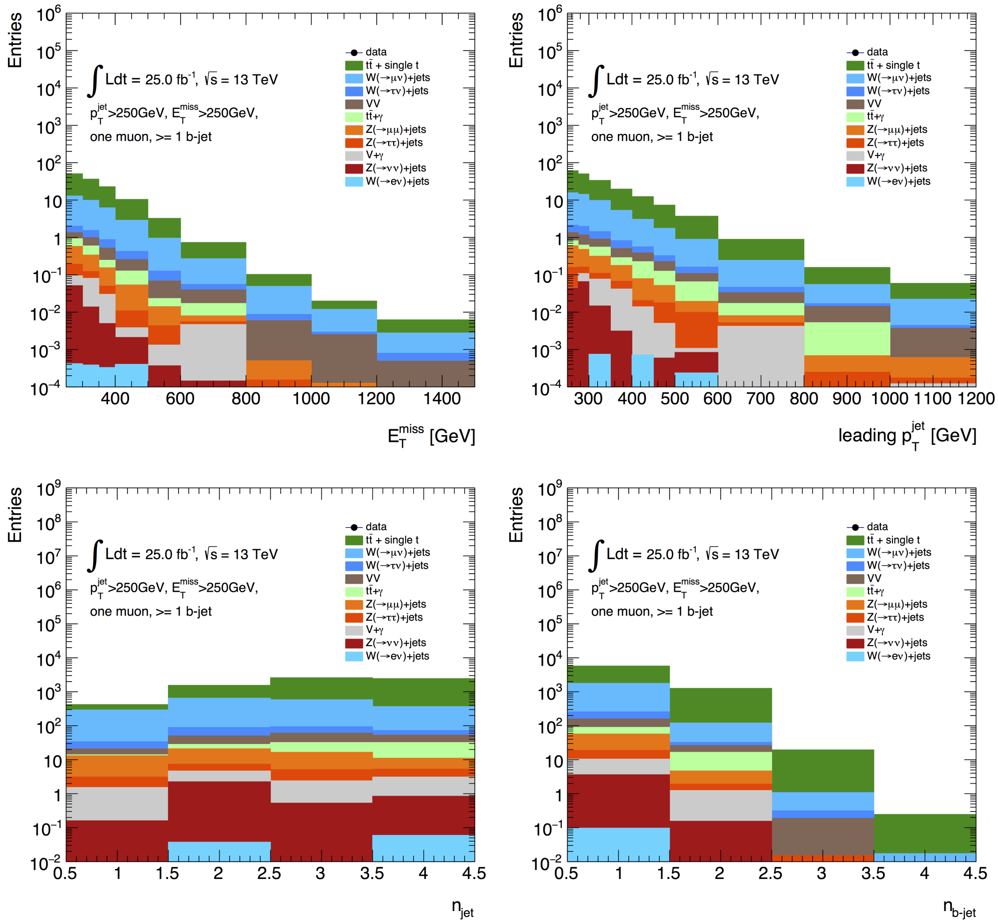

Figure 9.5. Distribution of the $E_{\mathrm{T}}^{\mathrm{miss}}$, leading jet p_{T}, jet and b-jet multiplicity variables in CR1μ+b-tag corresponding to an integrated luminosity of 25 fb^{-1}.

respect to the standard strategy.

Further studies can be performed to evaluate the best b-tagging working point in order to increase the statistics in CR1μ+b-tag and consequently improve the estimation of the top background.

A possible solution to reduce the uncertainty over all the $E_{\mathrm{T}}^{\mathrm{miss}}$ spectrum could be based on the combination of the evaluation strategies considered, by using the semi-data-driven technique in the low $E_{\mathrm{T}}^{\mathrm{miss}}$ regime where the statistics of CR1μ+b-tag is sufficient to decrease the total uncertainty and by preserving the standard strategy based on the top background estimation directly from MC simulation in the high $E_{\mathrm{T}}^{\mathrm{miss}}$ region.

9.3 Multi-dimensional Fitting Strategy

The increase of the integrated luminosity available can allow to exploit the information on the final state increasing the discrimination power between signals and background. Part of the information has been already used applying a fit binning the missing

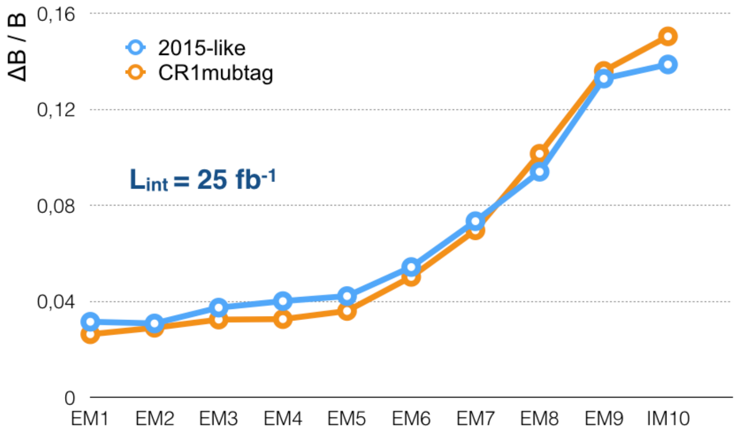

Figure 9.6. Relative uncertainties in the different $E_{\mathrm{T}}^{\mathrm{miss}}$ bins using the standard strategy fitting (blue) and the new one based on the introduction of CR1μ+b-tag in order to evaluate the $t\bar{t}$ and single top production processes in the SR. The fits are performed using the binning proposed in Table 9.1 and an integrated luminosity of 25 fb^{-1}.

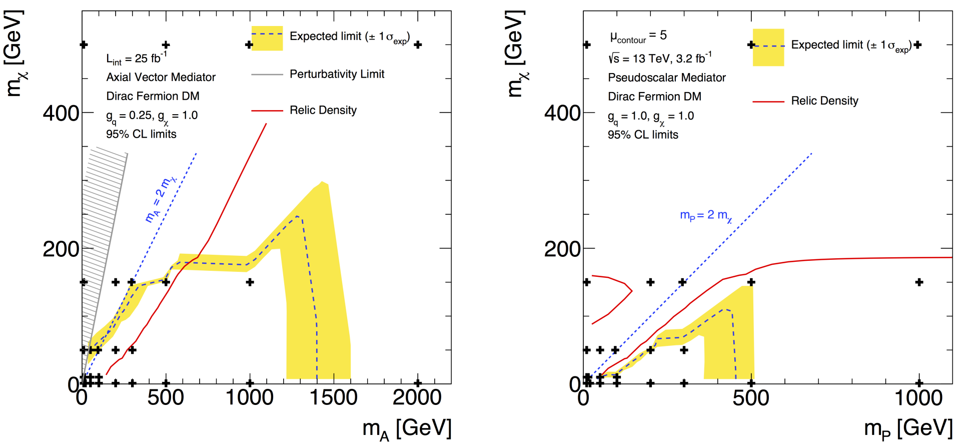

Figure 9.7. On the left: 95% CL expected exclusion contour in the m_χ versus m_A parameter plane in the axial-vector mediator hypothesis with coupling fixed at $g_\chi = 1$ and $g_q = 0.25$. On the right: 95% CL expected contour at $\mu = 5$ in the m_χ versus m_P parameter plane in the pseudo-scalar mediator hypothesis with coupling fixed at $g = g_q = g_\chi = 1$. The results are obtained using an integrated luminosity of 25 fb^{-1} at $\sqrt{s} = 13$ TeV using the binning proposed in Table 9.1 and evaluating the $t\bar{t}$ and single top background with CR1μ+b-tag.

transverse momentum distribution, but other variables could be useful for this purpose. In this section two alternative multi-dimensional fitting strategies are introduced with the relative improvements expressed in terms of exclusion limits at 95% CL with respect to the benchmark given by the results described in Chapter 7.

9.3.1 N_{jet} vs $E_{\text{T}}^{\text{miss}}$

The first simple procedure to add a useful information to the fit consists of adding a dimension to the fit with a discriminating variable: the jet multiplicity. This in fact can help to distinguish the signals from processes that foresee a higher jet multiplicity in the final states such as the events coming from the $t\bar{t}$ productions.

A two dimensional fit is hence performed in the plane $(N_{\text{jet}}, E_{\text{T}}^{\text{miss}})$ where for each of the seven $E_{\text{T}}^{\text{miss}}$ bins used in the previous mono-jet analysis, one defines correspondingly four bins with $N_{\text{jet}} = 1, 2, 3, 4$. For each of them the same $E_{\text{T}}^{\text{miss}}$-dependent normalization factors are assigned. The $E_{\text{T}}^{\text{miss}}$ distributions for each bin of jet multiplicity are shown in Figure 9.8.

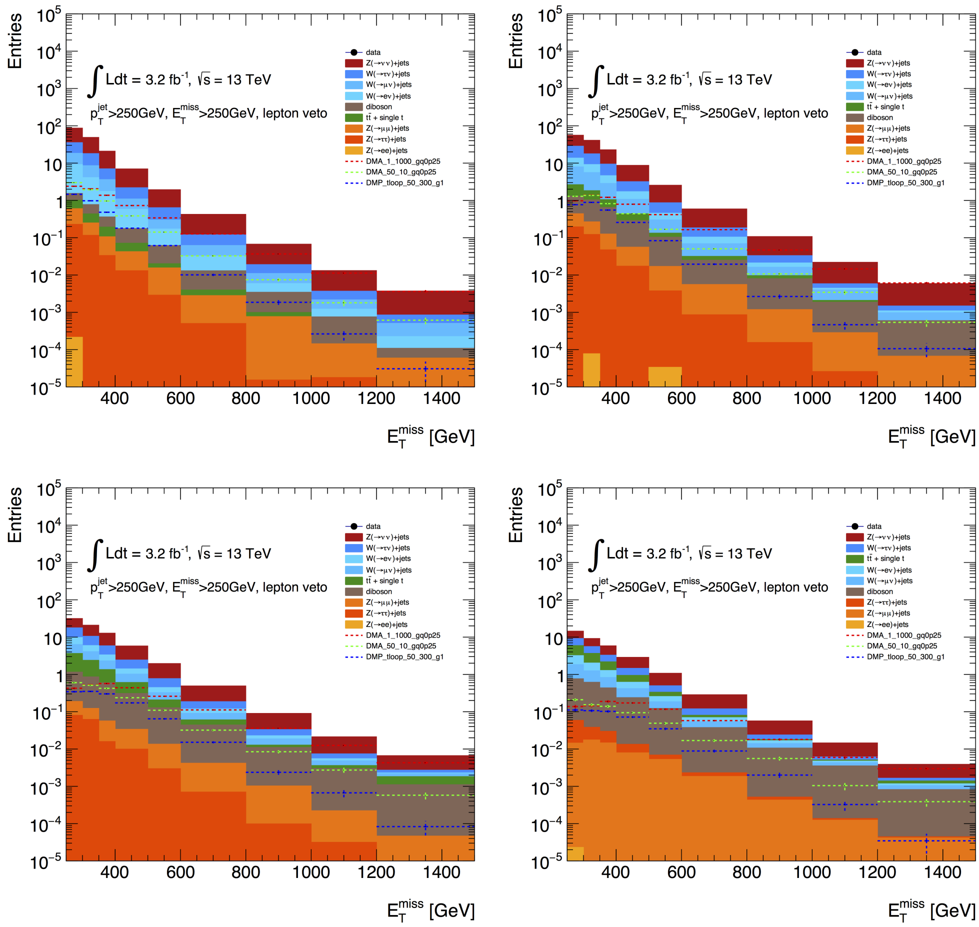

Figure 9.8. Distribution of the $E_{\text{T}}^{\text{miss}}$ variable in the SR requiring exactly one (top left), two (top right), three (bottom left), four (bottom right) jets. The data samples and the MC predictions correspond to an integrated luminosity of 3.2 fb^{-1} in the final state. The distributions of the simplified models with $m_\chi = 50, 1$ GeV and axial-vector mediator with $m_A = 10, 1000$ GeV with couplings $g_q = 0.25$ and $g_\chi = 1$ and $m_\chi = 50$ GeV and pseudo-scalar mediator with $m_P = 300$ GeV with couplings $g = g_1 = g_\chi = 1$ are also shown.

All the experimental systematics are re-evaluated and applied in each bin of the fit. The same is done for the top theoretical systematic following the same procedure described in Section 7.6.1, but considering four different $E_{\mathrm{T}}^{\mathrm{miss}}$ distributions, one for each jet-multiplicity-bin.

A background-only fit is performed without using the data sample to evaluate the expected SR yields of the different sources of background scaling the MC predictions scaling to an integrated luminosity of 3.2 fb^{-1}. The splitting of the $E_{\mathrm{T}}^{\mathrm{miss}}$ bins leads to a lower MC statistics in all the considered regions, but the impact of the systematics that take into account this among the bins is almost negligible. The study of the impact of systematic uncertainties, performed by using this new fitting strategy, demonstrates how the 2D fit reduces strongly the effect of the luminosity, jets experimental and theoretical top systematics with respect to the 1D fit. In particular the latter reduction is mainly due to the better estimation of the $t\bar{t}$ background that dominates the high jet-multiplicity-bins and corresponds to an impact on SR yields reduced to less than 1%.

The exclusion limits on the cross-sections at 95% CL of the simplified model with axial-vector couplings and the contour fixed at $\mu = 5$ at 95% CL on simplified models with pseudo-scalar mediators are shown in Figure 9.9[1]. The improvements in terms of 95% CL limits range between 20% and 35% for the DM simplified models considered. The 2D approach has been tested also on the SUSY samples obtaining an improvement on the 95% CL limits between 29-38%. These results should however be re-evaluated adding a CR on the $t\bar{t}$ processes introduced in the previous section, in order to test the complementarity of the two approaches.

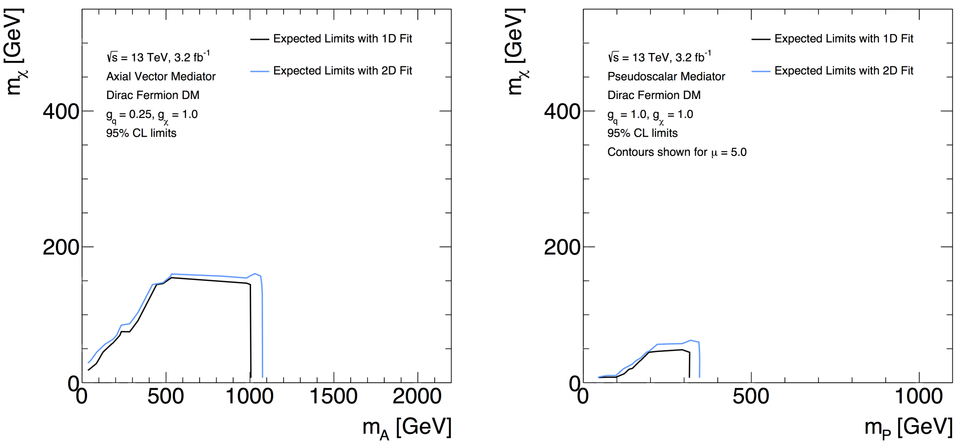

Figure 9.9. 95% CL expected contour limits on the cross section to the predicted signal cross section in the WIMP mass versus the mediator mass parameter plane in the axial-vector (left) and pseudo-scalar (right) couplings hypothesis fixed at $g_\chi = 1$ and $g_q = 0.25$ and $g = g_q = g_\chi = 1$ respectively. The 1D fit (black) and 2D fit (blue) contours are shown using a subset of the signal samples used to get the final mono-jet results and an integrated luminosity of 3.2 fb^{-1} at $\sqrt{s} = 13$ TeV.

[1]The minor diboson, multi-jet and NCB contributions of the total background have not been considered in this study.

9.3.2 Boosted-decision-tree vs $E_{\mathbf{T}}^{\mathbf{miss}}$

In order to exploit in a complete way the mono-jet final state, additional information can be included in a multivariate analysis based on the TMVA package [183]. The approach used to perform this study is based on a 2D fit in which a dimension exploits the missing transverse momentum distribution, as done in the standard strategy and a dimension in which additional kinematic observables are used to train a boosted decision tree (BDT) discriminant.

The BDT is a classifier defined in a binary tree structure that splits an input sample in many subsamples classified as signal- or background-like contribution. The splitting is performed in "nodes" of the tree in which each decision is taken by the most discriminating variable, choosing the best cut for the specific sample on which the BDT training is performed with the Gini index separation criterion (based on the purity of the sample). The iterative procedure in the tree is stopped when the statistics of the subset obtained by the selection applied in each node is smaller than 2.5% of the total events that compose the input sample or if the number of nodes in the three is greater than 20. In these studies the `AdaBoost` algorithm has been used, where after a decision tree a weight α is assigned to each bad classified event and the resulting weighted sample is then further used in a new decision tree. The weight applied is defined as

$$\alpha = \frac{1}{2} \ln \left(\frac{1-\epsilon}{\epsilon} \right) , \tag{9.1}$$

where ϵ is the probability that a signal event is actually classified as signal:

$$\epsilon = \int_{-\infty}^{y_t} p(y|s) dy \, , \tag{9.2}$$

in which y is the array that contains the used variables and y_t the hyper-surface defined by the requirements applied in the tree nodes in the entire phase space.

A total of 850 trees are used to train the BDT choosing as discriminating variables the pseudo-rapidity of the leading, second leading and third leading jets, the minimal angular distance in the transverse plane between the jets and the missing transverse momentum, the maximal angular distance in the same plane between the jets and the angular distance between the leading and the second leading jets. The jet multiplicity information is not directly used as input variable but it is used in the BDT training process. Indeed a BDT is trained in three different jet multiplicity range ($N_{\text{jets}} = 1, 2, > 2$) and then the outputs of these are merged to obtain a unique final discriminant.

The input variables used in each N_{jets} bin are illustrated in Figure 9.10 for a DM signal with $m_\chi = 150$ GeV and $m_A = 1$ TeV and axial-vector couplings with $g_q = 0.25$ and $g_\chi = 1$ and the total SM prediction[2], while the discrimination power of each of them is also listed in Table 9.2. The BDT classifiers obtained for each N_{jets} bin are shown in Figure 9.11.

For each of the signal samples a BDT discriminant has been trained, while for the background the BDT is trained on a unique sample including all the SM predictions. Each input sample is divided in two parts, one of the two is used to train the BDT

[2]The data-driven NCB and multi-jet background are not considered in the study.

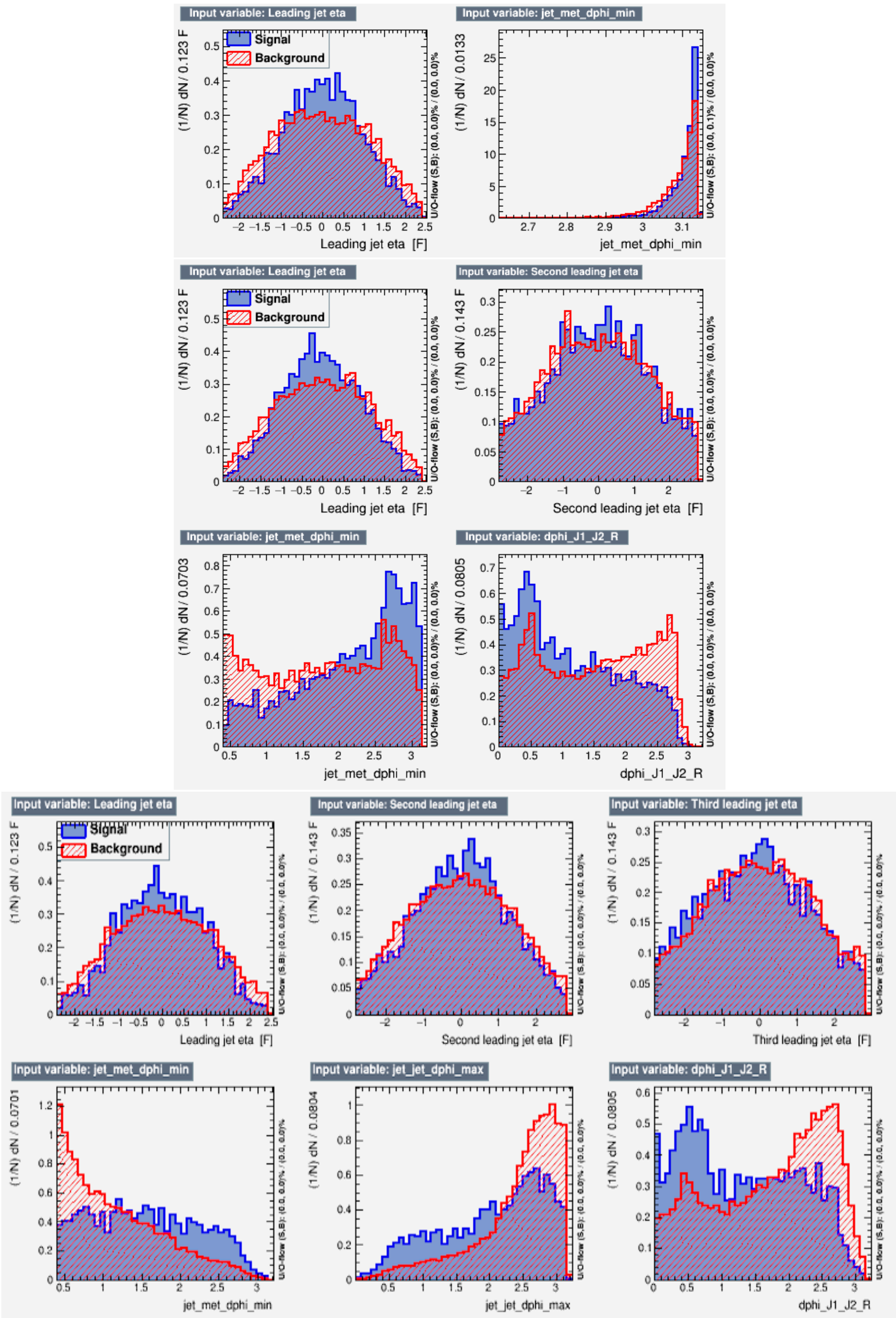

Figure 9.10. Shape comparison of the discrimination variables used as inputs in TMVA to build the classifiers relative to the $N_{\text{jets}} = 1$ (top), $N_{\text{jets}} = 2$ (middle), $N_{\text{jets}} > 2$ (bottom). In red are plotted the distributions relative to a signal with $m_\chi = 150$ GeV and $m_A = 1$ TeV and axial-vector couplings with $g_q = 0.25$ and $g_\chi = 1$ and in blue to the sum of the background predictions.

	Rank	Variable	Separation power
BDT $N_{\text{jet}} = 1$	1	leading jet η	0.29
	2	$\lvert\Delta\phi(\text{jets}, E_{\text{T}}^{\text{miss}})\rvert$	0.22
BDT $N_{\text{jet}} = 2$	1	$\min(\lvert\Delta\phi(\text{jets}, E_{\text{T}}^{\text{miss}})\rvert)$	0.52
	2	$\lvert\Delta\phi(\text{jet}_1, \text{jet}_2)\rvert$	0.50
	3	leading jet η	0.21
	4	2^{nd} leading jet η	0.05
BDT $N_{\text{jet}} > 2$	1	$\min(\lvert\Delta\phi(\text{jets}, E_{\text{T}}^{\text{miss}})\rvert)$	0.73
	2	$\max(\lvert\Delta\phi(\text{jet}_i, \text{jet}_j)\rvert)$	0.68
	3	$\lvert\Delta\phi(\text{jet}_1, \text{jet}_2)\rvert$	0.64
	4	leading jet η	0.21
	5	2^{nd} leading jet η	0.10
	6	3^{rd} leading jet η	0.06

Table 9.2. Input variables in each of the N_{jets} bin with the relative separation power between the SM predictions and the DM simplified model with $m_\chi = 150$ GeV and $m_A = 1$ TeV and axial-vector couplings with $g_q = 0.25$ and $g_\chi = 1$.

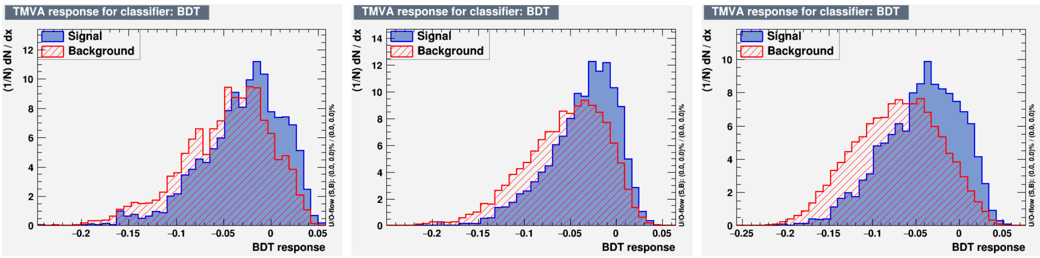

Figure 9.11. Shape comparison of the distributions of the BDT discriminants for $N_{\text{jets}} = 1$ (left), $N_{\text{jets}} = 2$ (middle) and $N_{\text{jets}} > 2$ (right). In red are plotted the distributions relative to a signal with $m_\chi = 150$ GeV and $m_A = 1$ TeV and axial-vector couplings with $g_q = 0.25$ and $g_\chi = 1$ and in blue to the sum of the background predictions.

while the other one is used to test the generality of the output proving that no overtraining is attained in the generation of the discriminants.

In the 2D fit strategy, the shape of the $E_{\text{T}}^{\text{miss}}$ distribution is exploited maintaining the same binning implemented for the standard strategy, while the BDT discriminant is divided in four bins in which the same $E_{\text{T}}^{\text{miss}}$-dependent normalization factor is applied. The criteria to choose the BDT binning are focused to apply an homogenous distribution of the expected yields between the bins, in all the SR and CRs, and at the same time to maximize the shape information of the BDT discriminant.

To achieve from the BDT discriminant an additional and complementary information with respect to the one obtained by the $E_{\text{T}}^{\text{miss}}$ shape, the leading jet p_{T} distribution is not included in the BDT training. This allows to have the two variables, on which the 2D fit is based, almost independent from each other as it can be observed in the plot in Figure 9.12 and to assign the $E_{\text{T}}^{\text{miss}}$-dependent systematics used to get the previous mono-jet results, keeping them fully correlated between the four BDT bins.

In order to achieve an improvement on the mono-jet results by using a fitting strategy as less-model-dependent as possible, the exclusion limits of the simplified

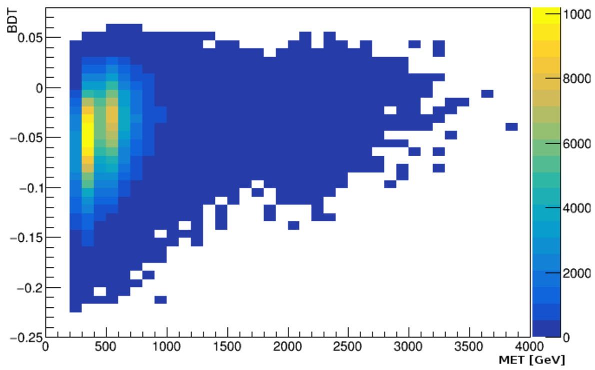

Figure 9.12. Correlation plot between the BDT discriminant and the missing transverse momentum for the SM prediction in the signal region.

models with axial-vector couplings are obtained training the signal BDT discriminant not only with the correspondent signal sample, but also with the signal samples with the same coupling hypothesis and different values of the masses m_χ and m_A.

The expected signal strength exclusion limits at 95% CL on the simplified models with axial-vector couplings are obtained using an integrated luminosity of 3.2 fb^{-1}, without using the observed number of events in the SR and CRs. The comparison with the standard 1D shape fit results shows improvements in terms of the signal strength limits between few percents up to $\sim$ 50% using the 2D fitting strategy. As expected the best improvements are achieved using the same signal sample in the training of the BDT variable. However the average gain of the signal strength limits, obtained using all the different BDT discriminants, range between 11% and 28% and prove an overall increase in sensitivity. The gain in terms of signal strength limits at 95% CL obtained for the signal samples are shown in Table 9.3.

This approach is by construction model dependent but the results obtained using different classifiers are promising. It would be interesting also repeat the same procedure with the pseudo-scalar samples and the non-DM signals and evaluate if, also with a completely different signal model, a sensitive improvement can be achieved. If it is not the case, a good solution suggested by the results introduced in this thesis is the possibility of applying this approach for a particular kind of process probed by the analysis, as the simplified model with a fixed choice of the axial-vector couplings or other BSM scenarios like SUSY and ADD models.

The use of angular correlations between jets and $E_{\mathrm{T}}^{\mathrm{miss}}$ and between the jets themselves can be an interesting tool to exploit fully the final state information in specific new physics scenarios. In simplified models with an axial-vector mediator the gain in sensitivity obtained from this variables is limited because the dominant SM contribution in the SR is due to the $Z(\nu\nu)$+jets processes where the main production mechanism is given by the same tree-level diagram of the signal. Therefore the angular correlations between the jets acts only in the discrimination of the other subdominant backgrounds with a different kinematic. However signals such as simplified models with a pseudo-scalar mediator receive a contribution in the production from distinct Feynman diagrams as shown in Section 4.7.2. The resulting kinematic distributions

m_χ [GeV]	m_A [GeV]	Mean gain [%]	m_χ [GeV]	m_A [GeV]	Mean gain [%]
1	10	13.96	50	200	27.83
1	20	20.95	50	300	22.20
1	50	23.32	50	10000	13.89
1	100	21.69	150	10	14.22
1	200	26.96	150	200	13.36
1	300	23.84	150	295	16.79
1	500	13.15	150	500	13.76
1	1000	10.83	150	1000	10.78
1	2000	13.06	150	10000	12.59
1	10000	14.12	500	10	12.90
10	10	30.34	500	500	12.49
10	15	26.85	500	995	11.67
10	50	21.75	500	2000	12.77
10	100	27.42	500	10000	14.00
10	10000	12.53	1000	10	15.68
50	10	25.97	1000	1000	14.63
50	50	24.19	1000	1995	13.61
50	95	27.33	1000	10000	16.07

Table 9.3. Average improvement in % in terms of the expected exclusion limit at 95% CL on the signal strength of several simplified models with axial-vector couplings fixed at $g_q = 0.25$ and $g_\chi = 1$ with respect to the ones obtained with the standard 1D shape binned fit using an integrated luminosity of 3.2 fb^{-1}.

can be different with respect to the SM predictions and can improve sensibly the background discrimination in the phase space with more than one jet (see for reference [184]). Certainly the best way to describe the angular correlations in these events is to generate simulations where the additional jets are defined by NLO calculations and not from PS from which the information is limited (see for example Ref. [185]). This kind of study can be a very interesting input for a second generation mono-jet analysis in which a multi-dimensional fit can be performed to exploit as much information as possible of the final state to increase the sensitivity to new physics processes.

Chapter 10

Conclusions

The mono-jet analysis is a relevant tool to search for scenarios beyond the Standard Model, a theory that at the moment is able to describe with high precision the particle physics phenomena up to the TeV scale.

Data collected at the impressive centre of mass energy of $\sqrt{s} = 13$ TeV at LHC, provide an unique occasion to probe the high boosted regime in which New Physics processes can leave a clear signature. Most of the beyond the Standard Model theories predict the production of particles with long lifetimes that do not interact with the detector material and can be investigated looking at the missing transverse momentum distribution. The requirement of a high transverse momentum jet in the final states allows to tag this kind of events. The mono-jet final state is particularly relevant in a hadronic machine such as LHC because it is statistically dominant with respect to the other channels that require an initial state radiated object in association with high missing transverse momentum in the final state.

In this thesis work, a full analysis based on the first 3.2 fb^{-1} of data at $\sqrt{s} = 13$ TeV has been presented. The innovative introduction of the shape information of the $E_{\mathrm{T}}^{\mathrm{miss}}$ distribution in a shape binned fit has improved the results in terms of cross section limits of about 20% with respect to a cut and count analysis.

Since no data excesses are observed in the signal region, the level of agreement between observed events and Standard Model predictions are translated in three different beyond the Standard Model scenarios.

In the ADD model, which foresees the existence of extra-spatial dimensions furnishing a possible explanation of the weakness of gravity relative to the other forces, the limits are set on the scale of gravity as a function of the n extra-dimensions. The analysis excludes values of M_D below 6.58 TeV at $n = 2$ and below 4.31 TeV at $n = 6$ at 95% CL, improving sensibly the previous mono-jet limits of 5.3 and 3.1 TeV at $n = 2$ and $n = 6$ respectively, based on 20.3 fb^{-1} of data at $\sqrt{s} = 8$ TeV.

In the context of Supersymmetry, which provides a solution to most of the anomalies and limitations of the Standard Model, three different compressed scenarios are considered, in the hypothesis of a very small mass difference Δm between the neutralino (considered as the lightest SUSY particle) and the next-to-lightest SUSY particle (stop, sbottom, or squark) which in turn are decoupled from the rest of the supersymmetric spectrum. In the decay channels in which $\tilde{b} \to b + \tilde{\chi}_1^0$ and $\tilde{t} \to t + \tilde{\chi}_1^0$ the exclusion limits at 95% CL reach the sbottom and stop mass of 323 GeV, while in the model in which $\tilde{q} \to q + \tilde{\chi}_1^0$ (with $q = u, d, c, s$) the squark masses below 608 GeV are excluded at 95% CL, significantly extending previous exclusion limits.

A large part of this thesis has been focused on the interpretation of the results in the Dark Matter scenario and in particular in the WIMP search. This latter consists in one of the most fascinating challenges of the particle physics nowadays. Actually, the WIMP observation would verify many cosmological and astrophysical measurements and would give a solid confirmation of the validity of the ΛCDM cosmological model used to quantify the actual amount of dark component of the matter in the universe. The limits are interpreted in the context of simplified models, in which a WIMP-pair is produced in the proton-proton collision through an axial-vector mediator fixing the couplings at $g_q = 0.25$ and $g_\chi = 1$. The excluded region in the Dark Matter versus mediator mass plane (m_χ, m_A), extends up to $m_A \sim 880$ GeV and $m_\chi \sim 270$ GeV in the absence of any interaction other than the one considered.

Then, the role of the mono-jet results in the context of the different existing Dark Matter searches, which are based on different analyses and detection techniques, has been highlighted. It demonstrates the relevance of the mono-jet results in particular in the region with $m_\chi \lesssim 10$ GeV and in the hypothesis of small coupling between the mediators and the Standard Model particles.

Finally, studies of different analysis improvements have been addressed in order to enhance the sensitivity of the future search in the mono-jet channel. The expected increase of data sample statistics of more than a factor ten with respect to the one used to get the results shown in the thesis, allows to enlarge the binning used to exploit the shape of the missing transverse momentum, enhancing the discovery potential and reducing the statistical uncertainty. The presented projection limits show that already with an integrated luminosity of 25 fb^{-1} it is possible to extend the exclusion contours up to $m_A \sim 1420$ GeV and in the region close to the on-shell line $m_A = 2m_\chi$.

The reduction of the total background uncertainty in the entire spectrum of the missing transverse momentum can be achieved by the introduction of new innovative control regions. A muon control region with at least a b-tagged jet allows to suppress the dominant systematic uncertainty that affects the top backgrounds in the low $E_{\mathrm{T}}^{\mathrm{miss}}$ regions and permits to reduce the relative uncertainty by 10-15%, improving the signal cross-section limits of the different simplified models up to 35%. The use of the γ+jets processes to evaluate the irreducible $Z(\nu\nu)$+jets contribution of background by introducing a new photon control region, reduces instead the statistical and dominant source of uncertainty in the high $E_{\mathrm{T}}^{\mathrm{miss}}$-regime by about 10%. In order to further decrease the uncertainty related to the dominant irreducible background, its estimation in the low $E_{\mathrm{T}}^{\mathrm{miss}}$-bins can be performed by $Z(\ell\ell)$+jets processes that would avoid to introduce the large systematic uncertainties applied on the transfer factor. It leads to reduce more the total background uncertainty in this region by 5-10%.

Preliminary studies on two different multidimensional fitting strategies are also discussed as a possible valid update for the future analysis. It allows to further improve the discrimination power between signals and background. Exploiting other information of the final state, a two dimensional shape binned fit can be performed by using the jet multiplicity or a multivariate discriminant distribution in addition to the missing transverse momentum. A sensitive improvement of the exclusion contours in the Dark Matter scenario has been quantified in terms of the signal cross-section limits, ranging between 20% and 35% and an average gain of 18% for the two strategies respectively.

In conclusion, the increase of the data sample statistics in addition to the implementation of improved fitting strategies will allow to increase sensibly the discovery potential and the analysis sensitivity. In the next future, the mono-jet channel will thus continue to constitute one of the most important tool to search for New Physics at ATLAS, maintaining its leading role in the context of search for Dark Matter and allowing to wide the spectrum of possible scenarios to investigate, which foresee elusive final states in a hadron collider and that could leave a mark in a region of the missing transverse momentum still unexplored.

Bibliography

[1] A. Purcell, "Go on a particle quest at the first CERN webfest. Le premier webfest du CERN se lance á la conquête des particules", BUL-NA-2012-269. 35/2012, Aug, 2012.

[2] F. Mandl and G. G. Shaw, "Quantum field theory", Wiley, New York, NY, 2010.

[3] A. Pich, "The Standard model of electroweak interactions", arXiv:0705.4264 [hep-ph].

[4] D. Hanneke, S. Fogwell and G. Gabrielse, "New Measurement of the Electron Magnetic Moment and the Fine Structure Constant", Phys. Rev. Lett. **100** (2008) 120801, [arXiv:0801.1134 [physics.atom-ph]].

[5] Taizo Muta, "Foundations of Quantum Chromodynamics", ISBN 9971-950-40-5.

[6] W. Greiner, S. Schramm, E. Stein, "Quantum Chromodynamics", ISBN-10 3-540-48534-1, Springer Berlin Heidelberg New York.

[7] E. Fermi, "Tentativo di una Teoria Dei Raggi β", Il Nuovo Cimento (1924-1942) **11** (1934) 1-19.

[8] S. Weinberg, "A Model of Leptons", Phys. Rev. Lett. **19** (Nov, 1967) 1264-1266.

[9] A. Salam and J. Ward, "Weak and electromagnetic interactions", Il Nuovo Cimento (1955-1965) **11** (1959) 568-577.

[10] P. W. Higgs, "Broken Symmetries and the Masses of Gauge Bosons", Phys. Rev. Lett. **13** (Oct, 1964) 508-509.

[11] F. Englert and R. Brout, "Broken Symmetry and the Mass of Gauge Vector Mesons", Phys. Rev. Lett. **13** (Aug, 1964) 321-323.

[12] P. Fayet, "Supersymmetry and Weak, Electromagnetic and Strong Interactions", Phys. Lett. B **64** (1976) 159.

[13] P. Fayet, "Spontaneously Broken Supersymmetric Theories of Weak, Electromagnetic and Strong Interactions", Phys. Lett. B **69** (1977) 489.

[14] R. Barbieri and G. F. Giudice, "Upper Bounds on Supersymmetric Particle Masses", Nucl. Phys. B **306** (1988) 63.

[15] A. Bilal, "Introduction to supersymmetry", hep-th/0101055.

[16] H. P. Nilles, “Supersymmetry, Supergravity and Particle Physics”, Phys. Rept. **110** (1984) 1.

[17] G. F. Giudice and R. Rattazzi, “Theories with gauge mediated supersymmetry breaking”, Phys. Rept. **322** (1999) 419.

[18] A. H. Chamseddine, R. L. Arnowitt and P. Nath, “Locally Supersymmetric Grand Unification”, Phys. Rev. Lett. **49** (1982) 970.

[19] P. Fayet, “Mixing Between Gravitational and Weak Interactions Through the Massive Gravitino”, Phys. Lett. B **70** (1977) 461.

[20] J. Edsjo, “Aspects of neutrino detection of neutralino dark matter”, hep-ph/9704384.

[21] W. Beenakker, R. Hopker, M. Spira and P. M. Zerwas, “Squark and gluino production at hadron colliders”, Nucl. Phys. B **492** (1997) 51.

[22] W. Beenakker, M. Kramer, T. Plehn, M. Spira and P. M. Zerwas, “Stop production at hadron colliders”, Nucl. Phys. B **515** (1998) 3.

[23] T. Kaluza, “On The Unification Problem In Physics”, In O’Raifeartaigh, L.: The dawning of gauge theory 53-58.

[24] O. Klein, “Quantum Theory and Five-Dimensional Theory of Relativity. (In German and English)”, Z. Phys. **37** (1926) 895 [Surveys High Energ. Phys. **5** (1986) 241].

[25] E. Witten, “String theory dynamics in various dimensions”, Nucl. Phys. B **443** (1995) 85

[26] N. Arkani-Hamed, S. Dimopoulos and G. R. Dvali, “The Hierarchy problem and new dimensions at a millimeter”, Phys. Lett. B **429** (1998) 263.

[27] G. F. Giudice, R. Rattazzi and J. D. Wells, “Quantum gravity and extra dimensions at high-energy colliders”, Nucl. Phys. B **544** (1999) 3.

[28] G. Bertone, D. Hooper and J. Silk, “Particle dark matter: Evidence, candidates and constraints”, Phys. Rept. **405** (2005) 279 [hep-ph/0404175].

[29] G. Lemaitre, “A Homogeneous Universe of Constant Mass and Growing Radius Accounting for the Radial Velocity of Extragalactic Nebulae”, Annales Soc. Sci. Brux. Ser. I Sci. Math. Astron. Phys. A **47** (1927) 49.

[30] E. Hubble, “A relation between distance and radial velocity among extra-galactic nebulae”, Proc. Nat. Acad. Sci. **15** (1929) 168.

[31] K.A. Olive *et al.* (Particle Data Group), “2015 Review of Particle Physics”, J Chin. Phys. C, **38**, 090001 (2014) and 2015 update.

[32] R. Adam *et al.* [Planck Collaboration], “Planck 2015 results. I. Overview of products and scientific results”, arXiv:1502.01582 [astro-ph.CO].

[33] L. Bergström, "Non-baryonic dark matter: Observational evidence and detection methods", Rept. Prog. Phys. **63** (2000) 793.

[34] Planck Collaboration, "Multimedia Gallery of Planck", url: `http://www.cosmos.esa.int/web/planck/picture-gallery`.

[35] D. Hooper, "Particle Dark Matter", arXiv:0901.4090 [hep-ph].

[36] K. Griest and D. Seckel, "Three exceptions in the calculation of relic abundances", Phys. Rev. D **43** (1991) 3191.

[37] G. Jungman, M. Kamionkowski and K. Griest, "Supersymmetric dark matter", Phys. Rept. **267** (1996) 195.

[38] P. Salati, "Quintessence and the relic density of neutralinos", Phys. Lett. B **571** (2003) 121.

[39] F. Zwicky, "Die Rotverschiebung von extragalaktischen Nebeln", Helv. Phys. Acta **6** (1933) 110.

[40] K. G. Begeman, A. H. Broeils and R. H. Sanders, "Extended rotation curves of spiral galaxies: Dark haloes and modified dynamics", Mon. Not. Roy. Astron. Soc. **249** (1991) 523.

[41] NASA, ESA, and D. Coe, "Detailed Dark Matter Map Yields Clues to Galaxy Cluster Growth", url: `http://www.nasa.gov/mission_pages/hubble/science/dark-matter-map.html`.

[42] NASA Chandra X-ray Observatory„ "NASA Finds Direct Proof of Dark Matter', url: `http://chandra.harvard.edu/press/06_releases/press_082106.html`.

[43] D. Clowe, M. Bradac, A. H. Gonzalez, M. Markevitch, S. W. Randall, C. Jones and D. Zaritsky, "A direct empirical proof of the existence of dark matter", Astrophys. J. **648** (2006) L109.

[44] N. Aghanim *et al.* [Planck Collaboration], "Planck 2015 results. XI. CMB power spectra, likelihoods, and robustness of parameters", arXiv:1507.02704 [astro-ph.CO]].

[45] J. Beringer *et al.* [Particle Data Group Collaboration], "Review of Particle Physics (RPP)", Phys. Rev. D **86** (2012) 010001.

[46] J. L. Feng, "Dark Matter Candidates from Particle Physics and Methods of Detection", Ann. Rev. Astron. Astrophys. **48** (2010) 495, arXiv:1003.0904 [astro-ph.CO].

[47] S. Dodelson and L. M. Widrow, "Sterile-neutrinos as dark matter", Phys. Rev. Lett. **72** (1994) 17.

[48] A. Kusenko, "Sterile neutrinos: The Dark side of the light fermions", Phys. Rept. **481** (2009) 1, [arXiv:0906.2968 [hep-ph]].

[49] K. N. Abazajian *et al.*, “Light Sterile Neutrinos: A White Paper”, arXiv:1204.5379 [hep-ph].

[50] R. D. Peccei and H. R. Quinn, Phys. Rev. Lett. **38** (1977) 1440. doi:10.1103/PhysRevLett.38.1440

[51] P. Sikivie, “Axion Cosmology”, Lect. Notes Phys. **741** (2008) 19, astro-ph/0610440.

[52] E. Di Valentino, E. Giusarma, M. Lattanzi, A. Melchiorri and O. Mena, “Axion cold dark matter: status after Planck and BICEP2”, Phys. Rev. D **90** (2014) no.4, 043534, arXiv:1405.1860 [astro-ph.CO].

[53] T. Marrodan Undagoitia and L. Rauch, “Dark matter direct-detection experiments”, J. Phys. G **43** (2016) no.1, 013001 arXiv:1509.08767 [physics.ins-det].

[54] R. Bernabei, P. Belli, F. Cappella, *et al.*, “Final model independent result of DAMA/LIBRA-phase1”, Eur. Phys. J. C **73** (2013) 12, 2648.

[55] C. E. Aalseth *et al.* [CoGeNT Collaboration], “CoGeNT: A Search for Low-Mass Dark Matter using p-type Point Contact Germanium Detectors”, Phys. Rev. D **88** (2013) 1, 012002.

[56] R. Agnese *et al.* [CDMS Collaboration], “Silicon Detector Dark Matter Results from the Final Exposure of CDMS II”, Phys. Rev. Lett. **111** (2013) 25, 251301.

[57] D. S. Akerib *et al.* [LUX Collaboration], “Results on the Spin-Dependent Scattering of Weakly Interacting Massive Particles on Nucleons from the Run 3 Data of the LUX Experiment”, Phys. Rev. Lett. **116** (2016) no.16, 161302, arXiv:1602.03489 [hep-ex].

[58] E. Aprile *et al.* [XENON100 Collaboration], “Limits on spin-dependent WIMP-nucleon cross sections from 225 live days of XENON100 data”, Phys. Rev. Lett. **111** (2013) no.2, 021301, arXiv:1301.6620 [astro-ph.CO].

[59] C. Amole *et al.* [PICO Collaboration], “Dark matter search results from the PICO-60 CF_3I bubble chamber”, Phys. Rev. D **93** (2016) no.5, 052014, arXiv:1510.07754 [hep-ex].

[60] C. Amole *et al.* [PICO Collaboration], “Improved dark matter search results from PICO-2L Run 2”, Phys. Rev. D **93** (2016) no.6, 061101, arXiv:1601.03729 [astro-ph.CO].

[61] M. Klasen, M. Pohl and G. Sigl, “Indirect and direct search for dark matter”, Prog. Part. Nucl. Phys. **85** (2015) 1 arXiv:1507.03800 [hep-ph].

[62] D. S. Akerib *et al.* [LUX Collaboration], “Results on the Spin-Dependent Scattering of Weakly Interacting Massive Particles on Nucleons from the Run 3 Data of the LUX Experiment”, Phys. Rev. Lett. **116** (2016) no.16, 161302, [arXiv:1602.03489 [hep-ex]].

[63] M. G. Aartsen *et al.* [IceCube Collaboration], "Search for dark matter annihilations in the Sun with the 79-string IceCube detector", Phys. Rev. Lett. **110** (2013) 13, 131302.

[64] T. Tanaka *et al.* [Super-Kamiokande Collaboration], "An Indirect Search for WIMPs in the Sun using 3109.6 days of upward-going muons in Super-Kamiokande", Astrophys. J. **742** (2011) 78, arXiv:1108.3384 [astro-ph.HE].

[65] M.Ackermann *et al.* [Fermi LAT Collaboration], "Searches for cosmic-ray electron anisotropies with the Fermi Large Area Telescope", Phys. Rev. D **82**, 092003 (2010).

[66] F. Calore, I. Cholis and C. Weniger, "Background model systematics for the Fermi GeV excess", JCAP **1503** (2015) 038, arXiv:1409.0042 [astro-ph.CO]].

[67] A. Abramowski *et al.* [H.E.S.S. Collaboration], "Search for dark matter annihilation signatures in H.E.S.S. observations of Dwarf Spheroidal Galaxies", Phys. Rev. D **90** (2014) 112012, [arXiv:1410.2589 [astro-ph.HE]].

[68] H. Abdallah *et al.* [HESS Collaboration], "Search for dark matter annihilations towards the inner Galactic halo from 10 years of observations with H.E.S.S", Phys. Rev. Lett. **117** (2016) no.11, 111301, [arXiv:1607.08142 [astro-ph.HE]].

[69] O. Adriani *et al.* [PAMELA Collaboration], Nature **458**, 607 (2009).

[70] M. Di Mauro, F. Donato, N. Fornengo, R. Lineros and A. Vittino, "Interpretation of AMS-02 electrons and positrons data", JCAP **1404** (2014) 006, arXiv:1402.0321 [astro-ph.HE].

[71] ATLAS Collaboration, "Search for new phenomena in final states with an energetic jet and large missing transverse momentum in pp collisions at $\sqrt{s} =$ 8 TeV with the ATLAS detector", Eur. Phys. J. C **75** (2015) 7, 299. Erratum: [Eur. Phys. J. C **75** (2015) no.9, 408] arXiv:1502.01518 [hep-ex].

[72] J. Goodman, M. Ibe, A. Rajaraman, W. Shepherd, T. M. P. Tait and H. B. Yu, "Constraints on Dark Matter from Colliders", Phys. Rev. D **82** (2010) 116010, arXiv:1008.1783 [hep-ph].

[73] G. Busoni, A. De Simone, E. Morgante and A. Riotto, "On the Validity of the Effective Field Theory for Dark Matter Searches at the LHC", Phys. Lett. B **728** (2014) 412, arXiv:1307.2253 [hep-ph].

[74] G. Busoni, A. De Simone, J. Gramling, E. Morgante and A. Riotto, "On the Validity of the Effective Field Theory for Dark Matter Searches at the LHC, Part II: Complete Analysis for the s-channel", JCAP **1406** (2014) 060, arXiv:1402.1275 [hep-ph].

[75] G. Busoni, A. De Simone, T. Jacques, E. Morgante and A. Riotto, "On the Validity of the Effective Field Theory for Dark Matter Searches at the LHC Part III: Analysis for the t-channel", JCAP **1409** (2014) 022, arXiv:1405.3101 [hep-ph].

[76] J. Abdallah *et al.*, “Simplified Models for Dark Matter Searches at the LHC”, Phys. Dark Univ. **9-10** (2015) 8, arXiv:1506.03116 [hep-ph].

[77] D. Abercrombie *et al.*, “Dark Matter Benchmark Models for Early LHC Run-2 Searches: Report of the ATLAS/CMS Dark Matter Forum”, arXiv:1507.00966 [hep-ex].

[78] G. Arcadi, Y. Mambrini, M. H. G. Tytgat and B. Zaldivar, “Invisible Z' and dark matter: LHC vs LUX constraints”, JHEP **1403** (2014) 134, arXiv:1401.0221 [hep-ph].

[79] O. Lebedev and Y. Mambrini, “Axial dark matter: The case for an invisible Z'”, Phys. Lett. B **734** (2014) 350, arXiv:1403.4837 [hep-ph].

[80] L. Evans and P. Bryant, “LHC Machine”, JINST **3**, S08001 (2008).

[81] M. Benedikt, P. Collier, V. Mertens, J. Poole and K. Schindl, “LHC Design Report. 3. The LHC injector chain”, CERN-2004-003-V-3, CERN-2004-003.

[82] C. Lefevre, “LHC: the guide”, CERN-Brochure-2008-001-Eng, Jan, 2008.

[83] G. Aad *et al.* ATLAS Collaboration, “The ATLAS Experiment at the CERN Large Hadron Collider”, JINST **3** (2008) S08003.

[84] K. Aamodt *et al.* [ALICE Collaboration], “The ALICE experiment at the CERN LHC”, JINST **3** (2008) S08002.

[85] S. Chatrchyan *et al.* [CMS Collaboration], “The CMS experiment at the CERN LHC”, JINST **3** (2008) S08004.

[86] A. A. Alves, Jr. *et al.* [LHCb Collaboration], “The LHCb Detector at the LHC”, JINST **3** (2008) S08005.

[87] The ATLAS Collaboration, “Luminosity Public Results Run-2”, url: `https://twiki.cern.ch/twiki/bin/view/AtlasPublic/LuminosityPublicResultsRun2`.

[88] ATLAS Collaboration, “ATLAS magnet system: Technical design report”, CERN-LHCC-97-18.

[89] ATLAS Collaboration, “ATLAS inner detector: Technical design report. Vol. 1”, CERN-LHCC-97-16, ATLAS-TDR-4.

[90] ATLAS Collaboration, “ATLAS inner detector: Technical design report. Vol. 2”, CERN-LHCC-97-17.

[91] ATLAS Collaboration, “ATLAS Insertable B-Layer Technical Design Report”, CERN- LHCC-2010-013.

[92] ATLAS Collaboration, “Track Reconstruction Performance of the ATLAS Inner Detector at $\sqrt{s} = 13$ TeV”, ATL-PHYS-PUB-2015-018.

[93] A. Airapetian *et al.* ATLAS Collaboration, “ATLAS calorimeter performance Technical Design Report”, CERN-LHCC-96-40.

[94] ATLAS Collaboration, “ATLAS liquid argon calorimeter: Technical design report”, CERN-LHCC-96-41.

[95] [ATLAS Collaboration], “ATLAS tile calorimeter: Technical design report”, CERN-LHCC-96-42.

[96] ATLAS Collaboration, “ATLAS muon spectrometer: Technical design report”, CERN-LHCC-97-22, ATLAS-TDR-10.

[97] G. Aad *et al.* [ATLAS Collaboration], “Commissioning of the ATLAS Muon Spectrometer with Cosmic Rays”, Eur. Phys. J. C **70** (2010) 875, [arXiv:1006.4384 [physics.ins-det]].

[98] ATLAS Collaboration, “2015 start-up trigger menu and initial performance assessment of the ATLAS trigger using Run-2 data”, ATL-DAQ-PUB-2016-001.

[99] M. Aaboud *et al.* [ATLAS Collaboration], “Performance of the ATLAS Trigger System in 2015,” Eur. Phys. J. C **77**, no. 5, 317 (2017), [arXiv:1611.09661 [hep-ex]].

[100] ATLAS Collaboration, “Electron efficiency measurements with the ATLAS detector using the 2015 LHC proton-proton collision data”, ATLAS-CONF-2016-024.

[101] ATLAS Collaboration, “Electron identification efficiency measured with $Z \to ee$ events using 2016 data”, url: `https://atlas.web.cern.ch/Atlas/GROUPS/PHYSICS/PLOTS/EGAM-2016-002/index.html`.

[102] W. Lampl *et al.*, “Calorimeter clustering algorithms: Description and performance”, ATL-LARG-PUB-2008-002, ATL-COM-LARG-2008-003.

[103] ATLAS Collaboration, “Photon identification in 2015 ATLAS data”, ATL-PHYS-PUB-2016-014.

[104] ATLAS Collaboration, “Photon Identification Efficiencies using 2016 Data with radiative Z boson decays”, url: `https://atlas.web.cern.ch/Atlas/GROUPS/PHYSICS/PLOTS/EGAM-2016-003/index.html`.

[105] ATLAS Collaboration, “Muon reconstruction performance of the ATLAS detector in proton-proton collision data at $\sqrt{s}$ =13 TeV”, Eur. Phys. J. C **76** (2016) no.5, 292, arXiv:1603.05598 [hep-ex].

[106] M. Cacciari, G. P. Salam and G. Soyez, “The Anti-k(t) jet clustering algorithm”, JHEP **0804** (2008) 063, arXiv:0802.1189 [hep-ph].

[107] ATLAS Collaboration, “Tagging and suppression of pileup jets”, ATLAS-CONF-2014-018.

[108] ATLAS Collaboration, “JVT Public Plots for ICHEP 2016”, url: `https://atlas.web.cern.ch/Atlas/GROUPS/PHYSICS/PLOTS/JETM-2016-011/`.

[109] ATLAS Collaboration, "Jet Calibration and Systematic Uncertainties for Jets Reconstructed in the ATLAS Detector at $\sqrt{s} = 13$ TeV", ATL-PHYS-PUB-2015-015.

[110] ATLAS Collaboration, "Jet energy scale uncertainties using full 13 TeV 2015 dataset", url: `http://atlas.web.cern.ch/Atlas/GROUPS/PHYSICS/PLOTS/JETM-2016-002/`.

[111] ATLAS Collaboration, "Selection of jets produced in 13 TeV proton-proton collisions with the ATLAS detector", ATLAS-CONF-2015-029.

[112] ATLAS Collaboration, "Optimisation of the ATLAS b-tagging performance for the 2016 LHC Run", ATL-PHYS-PUB-2016-012.

[113] ATLAS Collaboration, "Expected performance of the ATLAS b-tagging algorithms in Run-2", ATL-PHYS-PUB-2015-022.

[114] ATLAS Collaboration, "Missing transverse energy ($E_{\mathrm{T}}^{\mathrm{miss}}$) performance and systematic uncertainties using the full 2015 dataset", url: `http://atlas.web.cern.ch/Atlas/GROUPS/PHYSICS/PLOTS/JETM-2016-003/`.

[115] ATLAS Collaboration, "Expected performance of missing transverse momentum reconstruction for the ATLAS detector at $\sqrt{s} = 13$ TeV", ATL-PHYS-PUB-2015-023, url: `https://cds.cern.ch/record/2037700`.

[116] M. Aaboud *et al.* ATLAS Collaboration, "Search for new phenomena in final states with an energetic jet and large missing transverse momentum in pp collisions at $\sqrt{s} = 13$ TeV using the ATLAS detector", Phys. Rev. D **94** (2016) no.3, 032005 arXiv:1604.07773 [hep-ex].

[117] T. Gleisberg, S. Hoeche, F. Krauss, M. Schonherr, S. Schumann, F. Siegert and J. Winter, "Event generation with SHERPA 1.1", JHEP **0902** (2009) 007, arXiv:0811.4622 [hep-ph].

[118] url: `http://powhegbox.mib.infn.it`.

[119] S. Frixione, P. Nason and C. Oleari, "Matching NLO QCD computations with Parton Shower simulations: the POWHEG method", JHEP **0711** (2007) 070, arXiv:0709.2092 [hep-ph].

[120] J. Alwall *et al.*, "The automated computation of tree-level and next-to-leading order differential cross sections, and their matching to parton shower simulations", JHEP **1407** (2014) 079, arXiv:1405.0301 [hep-ph].

[121] H. L. Lai, M. Guzzi, J. Huston, Z. Li, P. M. Nadolsky, J. Pumplin and C.-P. Yuan, "New parton distributions for collider physics", Phys. Rev. D **82** (2010) 074024, arXiv:1007.2241 [hep-ph].

[122] T. Gleisberg and S. Hoeche, "Comix, a new matrix element generator", JHEP **0812** (2008) 039, arXiv:0808.3674 [hep-ph].

[123] F. Cascioli, P. Maierhofer and S. Pozzorini, "Scattering Amplitudes with Open Loops", Phys. Rev. Lett. **108** (2012) 111601, arXiv:1111.5206 [hep-ph].

[124] S. Schumann and F. Krauss, "A Parton shower algorithm based on Catani-Seymour dipole factorisation", JHEP **0803** (2008) 038, arXiv:0709.1027 [hep-ph].

[125] S. Hoeche, F. Krauss, M. Schonherr and F. Siegert, "QCD matrix elements + parton showers: The NLO case", JHEP **1304** (2013) 027, arXiv:1207.5030 [hep-ph].

[126] S. Catani, L. Cieri, G. Ferrera, D. de Florian and M. Grazzini, "Vector boson production at hadron colliders: a fully exclusive QCD calculation at NNLO", Phys. Rev. Lett. **103** (2009) 082001, arXiv:0903.2120 [hep-ph].

[127] S. Catani and M. Grazzini, "An NNLO subtraction formalism in hadron collisions and its application to Higgs boson production at the LHC", Phys. Rev. Lett. **98** (2007) 222002, hep-ph/0703012.

[128] A. D. Martin, W. J. Stirling, R. S. Thorne and G. Watt, "Parton distributions for the LHC", Eur. Phys. J. C **63** (2009) 189, arXiv:0901.0002 [hep-ph].

[129] S. Frixione, P. Nason and G. Ridolfi, "A Positive-weight next-to-leading-order Monte Carlo for heavy flavour hadroproduction", JHEP **0709** (2007) 126, arXiv:0707.3088 [hep-ph].

[130] T. Sjostrand, S. Mrenna and P. Z. Skands, "PYTHIA 6.4 Physics and Manual", JHEP **0605** (2006) 026, hep-ph/0603175.

Pumplin:2002vw

[131] J. Pumplin, D. R. Stump, J. Huston, H. L. Lai, P. M. Nadolsky and W. K. Tung, "New generation of parton distributions with uncertainties from global QCD analysis", JHEP **0207** (2002) 012, hep-ph/0201195.

[132] P. Z. Skands, "Tuning Monte Carlo Generators: The Perugia Tunes", Phys. Rev. D **82** (2010) 074018, arXiv:1005.3457 [hep-ph].

[133] D. J. Lange, "The EvtGen particle decay simulation package", Nucl. Instrum. Meth. A **462** (2001) 152.

[134] J. M. Campbell, R. K. Ellis and C. Williams, "Vector boson pair production at the LHC", JHEP **1107** (2011) 018, arXiv:1105.0020 [hep-ph].

[135] R. D. Ball *et al.*, "Parton distributions with LHC data", Nucl. Phys. B **867** (2013) 244, arXiv:1207.1303 [hep-ph].

[136] ATLAS Collaboration, "ATLAS Run 1 Pythia8 tunes", ATL-PHYS-PUB-2014-021, url: `http://cds.cern.ch/record/1966419`.

[137] L. Lonnblad and S. Prestel, "Matching Tree-Level Matrix Elements with Interleaved Showers", JHEP **1203** (2012) 019, arXiv:1109.4829 [hep-ph].

[138] W. Beenakker, S. Brensing, M. Kramer, A. Kulesza, E. Laenen and I. Niessen, "Supersymmetric top and bottom squark production at hadron colliders", JHEP **1008** (2010) 098, arXiv:1006.4771 [hep-ph].

[139] W. Beenakker, S. Brensing, M. n. Kramer, A. Kulesza, E. Laenen, L. Motyka and I. Niessen, "Squark and Gluino Hadroproduction", Int. J. Mod. Phys. A **26** (2011) 2637, arXiv:1105.1110 [hep-ph].

[140] C. Borschensky, M. Krämer, A. Kulesza, M. Mangano, S. Padhi, T. Plehn and X. Portell, "Squark and gluino production cross sections in pp collisions at $\sqrt{s}$ = 13, 14, 33 and 100 TeV", Eur. Phys. J. C **74** (2014) no.12, 3174, arXiv:1407.5066 [hep-ph].

[141] S. Alioli, P. Nason, C. Oleari and E. Re, "A general framework for implementing NLO calculations in shower Monte Carlo programs: the POWHEG BOX", JHEP **1006** (2010) 043, arXiv:1002.2581 [hep-ph].

[142] P. Nason, "A New method for combining NLO QCD with shower Monte Carlo algorithms", JHEP **0411** (2004) 040, [hep-ph/0409146].

[143] U. Haisch, F. Kahlhoefer and E. Re, "QCD effects in mono-jet searches for dark matter", JHEP **1312** (2013) 007, arXiv:1310.4491 [hep-ph].

[144] R. D. Ball *et al.* [NNPDF Collaboration], "Parton distributions for the LHC Run II", JHEP **1504** (2015) 040, arXiv:1410.8849 [hep-ph].

[145] G. Aad *et al.* ATLAS Collaboration, "The ATLAS Simulation Infrastructure", Eur. Phys. J. C **70** (2010) 823, arXiv:1005.4568 [physics.ins-det].

[146] S. Agostinelli *et al.* [GEANT4 Collaboration], "GEANT4: A Simulation toolkit", Nucl. Instrum. Meth. A **506** (2003) 250.

[147] G. Aad *et al.* ATLAS Collaboration, "Search for squarks and gluinos with the ATLAS detector in final states with jets and missing transverse momentum using 4.7 fb^{-1} of $\sqrt{s} = 7$ TeV proton-proton collision data", Phys. Rev. D **87** (2013) no.1, 012008, arXiv:1208.0949 [hep-ex].

[148] G. Aad *et al.* ATLAS Collaboration, "Characterisation and mitigation of beam-induced backgrounds observed in the ATLAS detector during the 2011 proton-proton run", JINST **8** (2013) P07004, arXiv:1303.0223 [hep-ex].

[149] G. Cowan, K. Cranmer, E. Gross and O. Vitells, "Asymptotic formulae for likelihood-based tests of new physics", Eur. Phys. J. C **71** (2011) 1554, Erratum: [Eur. Phys. J. C **73** (2013) 2501], arXiv:1007.1727 [physics.data-an]].

[150] G. Aad *et al.* ATLAS Collaboration, "Improved luminosity determination in pp collisions at $\sqrt{s} = 7$ TeV using the ATLAS detector at the LHC", Eur. Phys. J. C **73** (2013) no.8, 2518, arXiv:1302.4393 [hep-ex].

[151] M. Bahr *et al.*, "Herwig++ Physics and Manual", Eur. Phys. J. C **58** (2008) 639, [arXiv:0803.0883 [hep-ph]].

[152] ATLAS Collaboration, "Simulation of top quark production for the ATLAS experiment at $\sqrt{s} = 13$ TeV", ATL-PHYS-PUB-2016-004, url: `https://cds.cern.ch/record/2120417?ln=en`.

[153] ATLAS Collaboration, "Multi-Boson Simulation for 13 TeV ATLAS Analyses", ATL-PHYS-PUB-2016-002, url: `https://cds.cern.ch/record/2119986`.

[154] J. H. Kuhn, A. Kulesza, S. Pozzorini and M. Schulze, "Electroweak corrections to hadronic production of W bosons at large transverse momenta", Nucl. Phys. B **797** (2008) 27, arXiv:0708.0476 [hep-ph].

[155] M. Schönherr, S. Kallweit, J. M. Lindert, S. Pozzorini and P. Maierhöfer, "NLO QCD+EW for V+jets", arXiv:1609.01445 [hep-ph].

[156] M. Botje *et al.*, "The PDF4LHC Working Group Interim Recommendations", arXiv:1101.0538 [hep-ph].

[157] L. A. Harland-Lang, A. D. Martin, P. Motylinski and R. S. Thorne, "Parton distributions in the LHC era: MMHT 2014 PDFs", Eur. Phys. J. C **75** (2015) no.5, 204, arXiv:1412.3989 [hep-ph].

[158] A. Buckley, J. Ferrando, S. Lloyd, K. Nordström, B. Page, M. Rüfenacht, M. Schönherr and G. Watt, "LHAPDF6: parton density access in the LHC precision era", Eur. Phys. J. C **75** (2015) 132, arXiv:1412.7420 [hep-ph].

[159] A. L. Read, "Presentation of search results: The CL(s) technique", J. Phys. G **28** (2002) 2693.

[160] G. Aad *et al.* ATLAS Collaboration, "Search for dark matter candidates and large extra dimensions in events with a jet and missing transverse momentum with the ATLAS detector", JHEP **1304** (2013) 075, arXiv:1210.4491 [hep-ex].

[161] G. Aad *et al.* ATLAS Collaboration, "Search for pair-produced third-generation squarks decaying via charm quarks or in compressed supersymmetric scenarios in pp collisions at $\sqrt{s} = 8$ TeV with the ATLAS detector", Phys. Rev. D **90** (2014) no.5, 052008, arXiv:1407.0608 [hep-ex].

[162] T. Aaltonen *et al.* [CDF Collaboration], "Search for Scalar Top Quark Production in $p\bar{p}$ Collisions at $\sqrt{s} = 1.96$ TeV", JHEP **1210** (2012) 158, arXiv:1203.4171 [hep-ex].

[163] V. M. Abazov *et al.* [D0 Collaboration], "Search for scalar top quarks in the acoplanar charm jets and missing transverse energy final state in $p\bar{p}$ collisions at $\sqrt{s} = 1.96$-TeV", Phys. Lett. B **665** (2008) 1, arXiv:0803.2263 [hep-ex].

[164] M. Backovi?, A. Martini, O. Mattelaer, K. Kong and G. Mohlabeng, "Direct Detection of Dark Matter with MadDM v.2.0", Phys. Dark Univ. **9-10** 37, arXiv:1505.04190 [hep-ph].

[165] F. Kahlhoefer, K. Schmidt-Hoberg, T. Schwetz and S. Vogl, "Implications of unitarity and gauge invariance for simplified dark matter models", JHEP **1602** (2016) 016, arXiv:1510.02110 [hep-ph].

[166] A. Boveia *et al.*, "Recommendations on presenting LHC searches for missing transverse energy signals using simplified s-channel models of dark matter", arXiv:1603.04156 [hep-ex].

[167] M. Chala, F. Kahlhoefer, M. McCullough, G. Nardini and K. Schmidt-Hoberg, "Constraining Dark Sectors with Monojets and Dijets", JHEP **1507** (2015) 089, arXiv:1503.05916 [hep-ph].

[168] G. Choudalakis, "On hypothesis testing, trials factor, hypertests and the BumpHunter", arXiv:1101.0390 [physics.data-an].

[169] The ATLAS Collaboration, "Search for new phenomena in dijet mass and angular distributions from pp collisions at $\sqrt{s} = 13$ TeV with the ATLAS detector", Phys. Lett. B **754** (2016) 302, arXiv:1512.01530 [hep-ex].

[170] The ATLAS Collaboration, "Search for new phenomena in the dijet mass distribution using pp collision data at $\sqrt{s} = 8$ TeV with the ATLAS detector", Phys. Rev. D **91** (2015) no.5, 052007, arXiv:1407.1376 [hep-ex].

[171] The ATLAS Collaboration, "Search for light dijet resonances with the ATLAS detector using a Trigger-object Level Analysis in LHC pp collisions at $\sqrt{s} =$ 13 TeV", ATLAS-CONF-2016-030.

[172] The ATLAS Collaboration, "Pile-up subtraction and suppression for jets in ATLAS", ATLAS-CONF-2013-083.

[173] The ATLAS Collaboration, "Jet global sequential corrections with the ATLAS detector in proton-proton collisions at $\sqrt{s} = 8$ TeV", ATLAS-CONF-2015-002.

[174] The ATLAS Collaboration, "Performance of pile-up mitigation techniques for jets in pp collisions at $\sqrt{s} = 8$ TeV using the ATLAS detector", arXiv:1510.03823 [hep-ex].

[175] The ATLAS Collaboration, Data-driven determination of the energy scale and resolution of jets reconstructed in the ATLAS calorimeters using dijet and multijet events at $\sqrt{s} = 8$ TeV, ATLAS-CONF-2015-017.

[176] The ATLAS Collaboration, "Search for new light resonances decaying to jet pairs and produced in association with a photon in proton-proton collisions at $\sqrt{s} = 13$ TeV with the ATLAS detector", ATLAS-CONF-2016-029.

[177] The ATLAS Collaboration, "Search for new light resonances decaying to jet pairs and produced in association with a photon or a jet in proton-proton collisions at $\sqrt{s} = 13$ TeV with the ATLAS detector", ATLAS-CONF-2016-070.

[178] A. Martini, K. Mawatari, J. Wang, C. Zhang, "Simplified dark matter models". url: `http://feynrules.irmp.ucl.ac.be/wiki/DMsimp`.

[179] B. A. Dobrescu and F. Yu, "Coupling-mass mapping of dijet peak searches", Phys. Rev. D **88** (2013) no.3, 035021, Erratum: [Phys. Rev. D **90** (2014) no.7, 079901], arXiv:1306.2629 [hep-ph].

[180] The ATLAS Collaboration, "Search for new phenomena in events with a photon and missing transverse momentum in *pp* collisions at $\sqrt{s} = 13$ TeV with the ATLAS detector", JHEP **1606** (2016) 059, arXiv:1604.01306 [hep-ex].

[181] The ATLAS Collaboration, "Summary plots from the ATLAS Exotic physics group", url: `https://atlas.web.cern.ch/Atlas/GROUPS/PHYSICS/CombinedSummaryPlots/EXOTICS/index.html#ATLAS_DarkMatter_Summary`.

[182] J. H. Kuhn, A. Kulesza, S. Pozzorini and M. Schulze, "Electroweak corrections to hadronic photon production at large transverse momenta", JHEP **0603** (2006) 059, [hep-ph/0508253].

[183] A. Hocker *et al.*, "TMVA - Toolkit for Multivariate Data Analysis", PoS ACAT (2007) 040, physics/0703039 [PHYSICS].

[184] U. Haisch, A. Hibbs and E. Re, "Determining the structure of dark-matter couplings at the LHC", Phys. Rev. D **89** (2014) 034009, [arXiv:1311.7131 [hep-ph]].

[185] O. Mattelaer and E. Vryonidou, "Dark matter production through loop-induced processes at the LHC: the s-channel mediator case", Eur. Phys. J. C **75** (2015) no.9, 436, [arXiv:1508.00564 [hep-ph]].

Appendix A

Signal Cross-Sections

In the following pages the cross-sections of the signal samples used to interpret the results in the ADD model (Table A.1), SUSY compressed scenarios (Tables A.2–A.4) and the simplified models with axial-vector (Tables A.5 and A.6) and pseudo-scalar mediators (Tables A.7 and A.8).

n	m_D [GeV]	σ [pb]
2	5300	1.55
3	4100	1.82
4	3600	2.29
5	3200	4.20
6	3000	7.20

Table A.1. Cross-sections of the ADD signal model, for different M_D and number of extra-dimensions.

$m_{\tilde{b}_1}$ [GeV]	$m_{\tilde{\chi}_1^0}$ [GeV]	σ [pb]	$m_{\tilde{b}_1}$ [GeV]	$m_{\tilde{\chi}_1^0}$ [GeV]	σ [pb]
250	230	21.59	450	430	0.95
250	245	21.59	450	445	0.95
300	280	8.52	500	480	0.52
300	295	8.52	500	495	0.52
350	330	3.79	550	530	0.30
350	345	3.79	550	545	0.30
400	380	1.84	600	580	0.17
400	395	1.84	600	595	0.17

Table A.2. Cross-sections of the $\tilde{b}_1 \to b + \tilde{\chi}_1^0$ decay, for different $m_{\tilde{b}_1}$ and $m_{\tilde{\chi}_1^0}$.

$m_{\tilde{t}_1}$ [GeV]	$m_{\tilde{\chi}_1^0}$ [GeV]	σ [pb]	$m_{\tilde{t}_1}$ [GeV]	$m_{\tilde{\chi}_1^0}$ [GeV]	σ [pb]
250	230	20.45	375	295	2.40
275	195	12.53	375	315	2.39
275	225	12.53	375	345	2.40
275	250	12.53	375	370	2.40
275	270	12.53	400	320	1.68
300	220	7.95	400	330	1.68
300	260	7.96	400	370	1.68
300	280	7.96	400	395	1.68
300	295	7.96	450	370	0.86
325	245	5.20	450	395	0.86
325	260	5.20	450	425	0.86
325	295	5.20	450	445	0.86
325	320	5.20	500	420	0.47
350	270	3.49	500	445	0.47
350	295	3.49	500	485	0.47
350	305	3.49	500	495	0.47
350	345	3.49			

Table A.3. Cross-sections of the $\tilde{t}_1 \to c + \tilde{\chi}_1^0$ decay, for different $m_{\tilde{t}_1}$ and $m_{\tilde{\chi}_1^0}$.

$m_{\tilde{q}}$ [GeV]	$m_{\tilde{\chi}_1^0}$ [GeV]	σ [pb]	m_{χ} [GeV]	m_P [GeV]	σ [pb]
400	395	13.42	550	525	2.12
400	385	13.41	600	595	1.25
400	375	13.41	600	585	1.25
450	445	6.88	600	575	1.25
450	435	6.88	650	645	0.76
450	425	6.88	650	635	0.76
500	495	3.74	650	625	0.76
500	485	3.74	700	695	0.47
500	475	3.74	700	685	0.47
550	545	2.12	700	675	0.47
550	535	2.12			

Table A.4. Cross-sections of the $\tilde{q} \to q + \tilde{\chi}_1^0$ decay, for different $m_{\tilde{q}}$ and $m_{\tilde{\chi}_1^0}$.

m_χ [GeV]	m_A [GeV]	σ [pb]	m_χ [GeV]	m_A [GeV]	σ [pb]
1	10	1075.85	250	495	0.196964
1	20	680.6	250	800	1.65698
1	50	367.182	250	1000	0.972392
1	100	206.142	250	10000	5.7263e-06
1	200	83.5282	400	10	0.00628856
1	300	38.8329	400	795	0.0458389
1	500	10.9961	400	1000	0.430275
1	800	2.70628	400	1200	0.361954
1	1000	1.28846	400	10000	3.82701e-06
1	1200	0.66312	500	10	0.00249684
1	1500	0.2728	500	500	0.0032731
1	2000	0.0748208	500	800	0.00576859
1	10000	9.30699e-06	500	995	0.0204832
10	10	17.4106	500	1200	0.177898
10	15	20.3532	500	1500	0.147473
10	50	321.95	500	2000	0.0537762
10	100	201.066	500	10000	2.8939e-06
10	10000	9.34614e-06	600	10	0.00110966
50	10	2.02434	600	1000	0.0029445
50	50	2.33061	600	1195	0.0100926
50	95	4.90472	600	1500	0.0878726
50	200	66.3192	600	2000	0.0449219
50	300	35.4539	600	10000	2.18329e-06
50	10000	9.00024e-06	750	10	0.000359287
150	10	0.16404	750	1200	0.000913908
150	200	0.245473	750	1495	0.00383515
150	295	0.727244	750	2000	0.0294922
150	500	7.31968	750	10000	1.44175e-06
150	800	2.34511	1000	10	6.86926e-05
150	1000	1.15854	1000	1000	9.51969e-05
150	10000	7.4164e-06	1000	1500	0.000160234
250	10	0.0347474	1000	1995	0.000924116
250	300	0.0573318	1000	10000	7.09189e-07

Table A.5. Cross-sections of the DM signal models with axial-vector mediators and couplings $g_q = 0.25$, $g_\chi = 1$, for different m_χ and m_A.

g	σ [pb]
0.10	0.020536
0.50	0.48163
0.75	0.97893
1.00	1.5173
1.25	1.9866
1.50	2.3789

Table A.6. Cross-sections of the DM signal models with axial-vector mediators, with $m_\chi = 150$ GeV, $m_A = 1$ TeV and different values of the couplings $g_\chi = g_q = g$.

m_χ [GeV]	m_P [GeV]	σ [pb]	m_χ [GeV]	m_P [GeV]	σ [pb]
1	10	1.9437	50	200	1.1196
1	20	1.899	50	300	1.0145
1	50	1.782	50	10000	9.5051e-08
1	100	1.55	150	10	0.010043
1	200	1.1191	150	200	0.017939
1	300	1.0149	150	295	0.11594
1	500	0.21874	150	500	0.18976
1	1000	0.0077751	150	1000	0.0072619
1	10000	9.7192e-08	150	10000	7.5369e-08
10	10	0.11563	500	10	3.2141e-05
10	15	0.13388	500	500	4.7064e-05
10	50	1.7831	500	995	0.0010196
10	100	1.5505	500	10000	1.075e-08
10	10000	9.7169e-08	1000	10	2.2726e-07
50	10	0.040492	1000	1000	3.4606e-07
50	50	0.046404	1000	10000	9.2226e-10
50	95	0.11685			

Table A.7. Cross-sections of the DM signal models with pseudo-scalar mediators and couplings $g_q = g_\chi = 1$, for different m_χ and m_P.

g	σ [pb]
0.10	0.0099241
1.00	1.0145
2.00	4.213
3.00	9.3847
4.00	15.507
5.00	21.728
6.00	27.706

Table A.8. Cross-sections of the DM signal models, with $m_\chi = 50$ GeV, $m_P = 300$ TeV and different values of the couplings $g_\chi = g_q = g$.

Appendix B

Signal Region Results

In the following pages the results obtained using the data collected at $\sqrt{s} = 13$ TeV corresponding at an integrated luminosity of 3.2 fb^{-1} are shown.

In the Tables B.1–B.7 the observed events selected and the SM predictions obtained by the simultaneous shape binned fit in the CRs are listed for each of the $E_{\mathrm{T}}^{\mathrm{miss}}$ bins considered. In the bottom of the table are reported the MC expectation before performing the fit, while on the top there are the yields obtained after the fit.

Figures B.1–B.7 illustre the fit results in the SR and in the CRs for each of the bins with the relative uncertainties.

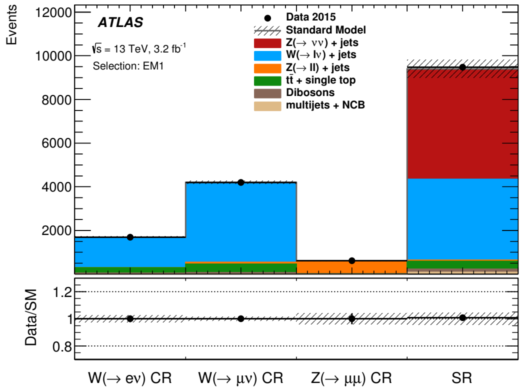

Figure B.1. Summary plot showing the agreement of data and the SM predictions post-fit in the region EM1 and the relative CRs labelled with their dominant background process [116].

EM1	SR	CR1e	CR1μ	CR2μ
Observed events (3.2 fb^{-1})	9472	1693	4202	611
SM prediction (post-fit)	9400 ± 410	1693 ± 41	4202 ± 65	611 ± 25
Fitted $W(e\nu)$	859 ± 86	1176 ± 70	0.3 ± 0.1	–
Fitted $W(\mu\nu)$	930 ± 66	1 ± 0.2	3480 ± 130	0.6 ± 0.1
Fitted $W(\tau\nu)$	1910 ± 170	210 ± 13	177 ± 12	0.06 ± 0.03
Fitted $Z(ee)$	0.01 ± 0.01	0.3 ± 0.1	–	–
Fitted $Z(\mu\mu)$	36 ± 12	$0.05^{+0.04}_{-0.05}$	74 ± 8	579 ± 25
Fitted $Z(\tau\tau)$	24 ± 5	16 ± 2	11 ± 4	0.06 ± 0.02
Fitted $Z(\nu\nu)$	5050 ± 270	0.8 ± 0.1	0.6 ± 0.1	–
Expected $t\bar{t}$, single top	350 ± 110	235 ± 70	390 ± 120	18 ± 5
Expected diboson	154 ± 13	54 ± 4	70 ± 7	13 ± 2
Multijet	22 ± 22	–	–	–
NCB	61 ± 61	–	–	–
MC exp. SM events	9620 ± 580	1880 ± 150	4140 ± 260	610 ± 42
Fit input $W(e\nu)$	971 ± 74	1329 ± 98	0.3 ± 0.1	–
Fit input $W(\mu\nu)$	908 ± 65	1 ± 0.2	3390 ± 190	0.6 ± 0.1
Fit input $W(\tau\nu)$	2160 ± 170	238 ± 18	200 ± 14	0.06 ± 0.03
Fit input $Z(ee)$	0.01 ± 0.01	0.3 ± 0.1	–	–
Fit input $Z(\mu\mu)$	35 ± 12	$0.05^{+0.04}_{-0.05}$	74 ± 9	579 ± 41
Fit input $Z(\tau\tau)$	27 ± 5	18 ± 2	13 ± 4	0.07 ± 0.02
Fit input $Z(\nu\nu)$	4930 ± 320	0.8 ± 0.1	0.6 ± 0.1	–
Fit input $t\bar{t}$, single top	350 ± 110	235 ± 72	390 ± 120	18 ± 5
Fit input diboson	154 ± 14	54 ± 5	70 ± 7	13 ± 2
Multijet	22 ± 22	–	–	–
NCB	61 ± 61	–	–	–

Table B.1. Data and background predictions in the signal and control regions before and after the fit performed for the EM1 selection. The background predictions include both the statistical and systematic uncertainties. The individual uncertainties are correlated and do not necessarily add in quadrature to the total background uncertainty [116].

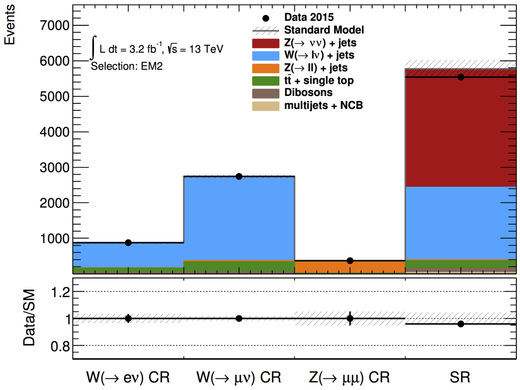

Figure B.2. Summary plot showing the agreement of data and the SM predictions post-fit in the region EM2 and the relative CRs labelled with their dominant background process.

EM2	SR	CR1e	CR1μ	CR2μ
Observed events (3.2 fb^{-1})	5542	874	2741	372
SM prediction (post-fit)	5770 ± 260	874 ± 30	2741 ± 52	372 ± 19
Fitted $W(e\nu)$	444 ± 48	584 ± 42	$0.03^{+0.03}_{-0.03}$	–
Fitted $W(\mu\nu)$	518 ± 50	0.7 ± 0.2	2248 ± 96	0.6 ± 0.1
Fitted $W(\tau\nu)$	1082 ± 90	118 ± 9	114 ± 9	0.03 ± 0.01
Fitted $Z(ee)$	$0.00^{+0.01}_{-0.00}$	0.1 ± 0.1	–	–
Fitted $Z(\mu\mu)$	15 ± 7	0.04 ± 0.03	33 ± 4	347 ± 20
Fitted $Z(\tau\tau)$	14 ± 2	7 ± 1	5 ± 1	0.17 ± 0.03
Fitted $Z(\nu\nu)$	3330 ± 200	0.3 ± 0.1	0.4 ± 0.1	–
Expected $t\bar{t}$, single top	209 ± 63	129 ± 39	280 ± 84	11 ± 4
Expected diboson	121 ± 10	36 ± 4	61 ± 5	13 ± 1
Multijet	14 ± 14	–	–	–
NCB	23 ± 23	–	–	–
MC exp. SM events	6050 ± 390	971 ± 79	2800 ± 190	422 ± 36
Fit input $W(e\nu)$	505 ± 45	664 ± 50	$0.03^{+0.04}_{-0.03}$	–
Fit input $W(\mu\nu)$	526 ± 53	0.7 ± 0.2	2280 ± 140	0.6 ± 0.1
Fit input $W(\tau\nu)$	1230 ± 68	134 ± 10	129 ± 8	0.03 ± 0.02
Fit input $Z(ee)$	$0.00^{+0.01}_{-0.00}$	0.1 ± 0.1	–	–
Fit input $Z(\mu\mu)$	17 ± 8	0.04 ± 0.03	38 ± 4	397 ± 34
Fit input $Z(\tau\tau)$	16 ± 2	8 ± 1	6 ± 1	0.19 ± 0.03
Fit input $Z(\nu\nu)$	3380 ± 240	0.3 ± 0.1	0.4 ± 0.1	–
Fit input $t\bar{t}$, single top	209 ± 64	129 ± 40	280 ± 86	11 ± 4
Fit input diboson	121 ± 10	36 ± 4	61 ± 5	13 ± 1
Multijet	14 ± 14	–	–	–
NCB	23 ± 23	–	–	–

Table B.2. Data and background predictions in the signal and control regions before and after the fit performed for the EM2 selection. The background predictions include both the statistical and systematic uncertainties. The individual uncertainties are correlated and do not necessarily add in quadrature to the total background uncertainty [116].

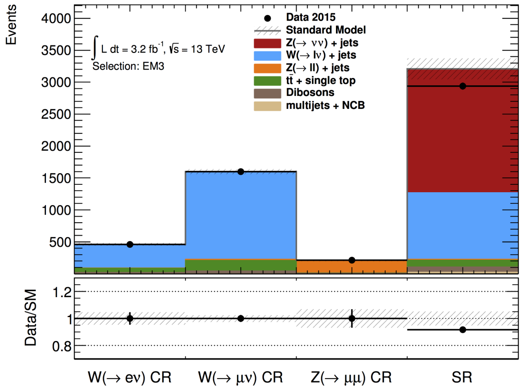

Figure B.3. Summary plot showing the agreement of data and the SM predictions post-fit in the region EM3 and the relative CRs labelled with their dominant background process.

EM3	SR	CR1e	CR1μ	CR2μ
Observed events (3.2 fb^{-1})	2939	460	1599	212
SM prediction (post-fit)	3210 ± 170	460 ± 21	1599 ± 40	212 ± 15
Fitted $W(e\nu)$	228 ± 26	306 ± 24	0.02 ± 0.01	–
Fitted $W(\mu\nu)$	263 ± 28	$0.08^{+0.12}_{-0.08}$	1300 ± 62	0.3 ± 0.1
Fitted $W(\tau\nu)$	551 ± 47	63 ± 5	69 ± 7	0.03 ± 0.02
Fitted $Z(ee)$	–	0.06 ± 0.01	–	–
Fitted $Z(\mu\mu)$	9 ± 5	0.02 ± 0.01	16 ± 2	198 ± 15
Fitted $Z(\tau\tau)$	5 ± 1	4 ± 1	3 ± 1	0.1 ± 0.1
Fitted $Z(\nu\nu)$	1940 ± 130	0.21 ± 0.04	1 ± 0.1	–
Expected $t\bar{t}$, single top	108 ± 32	66 ± 20	166 ± 50	6 ± 2
Expected diboson	82 ± 8	22 ± 3	44 ± 5	8 ± 1
Multijet	6 ± 6	–	–	–
NCB	19 ± 19	–	–	–
MC exp. SM events	3160 ± 220	488 ± 40	1540 ± 120	217 ± 15
Fit input $W(e\nu)$	245 ± 20	328 ± 25	0.02 ± 0.01	–
Fit input $W(\mu\nu)$	250 ± 28	$0.08^{+0.12}_{-0.08}$	1236 ± 89	0.28 ± 0.04
Fit input $W(\tau\nu)$	592 ± 38	68 ± 5	74 ± 5	0.03 ± 0.02
Fit input $Z(ee)$	–	0.06 ± 0.01	–	–
Fit input $Z(\mu\mu)$	10 ± 5	0.02 ± 0.01	16 ± 2	202 ± 14
Fit input $Z(\tau\tau)$	6 ± 1	4 ± 1	3 ± 1	0.1 ± 0.1
Fit input $Z(\nu\nu)$	1840 ± 150	0.2 ± 0.03	1 ± 0.1	–
Fit input $t\bar{t}$, single top	108 ± 33	66 ± 20	166 ± 51	6 ± 2
Fit input diboson	82 ± 8	22 ± 3	44 ± 5	8 ± 1
Multijet	6 ± 6	–	–	–
NCB	19 ± 19	–	–	–

Table B.3. Data and background predictions in the signal and control regions before and after the fit performed for the EM3 selection. The background predictions include both the statistical and systematic uncertainties. The individual uncertainties are correlated and do not necessarily add in quadrature to the total background uncertainty [116].

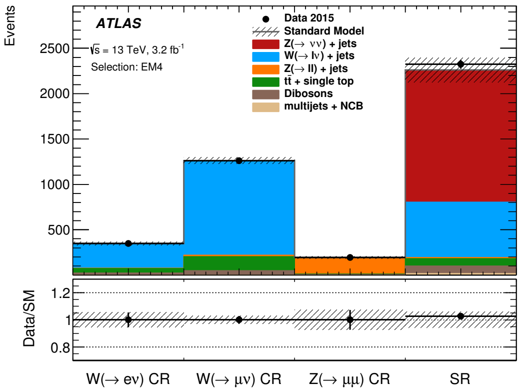

Figure B.4. Summary plot showing the agreement of data and the SM predictions post-fit in the region EM4 and the relative CRs labelled with their dominant background process [116].

EM4	SR	CR1e	CR1μ	CR2μ
Observed events (3.2 fb^{-1})	2324	349	1262	193
SM prediction (post-fit)	2260 ± 140	349 ± 19	1262 ± 36	193 ± 14
Fitted $W(e\nu)$	131 ± 16	228 ± 22	0.01 ± 0.01	–
Fitted $W(\mu\nu)$	167 ± 19	0.4 ± 0.1	998 ± 64	0.19 ± 0.04
Fitted $W(\tau\nu)$	310 ± 31	46 ± 4	46 ± 6	$0.01^{+0.02}_{-0.01}$
Fitted $Z(ee)$	–	0.03 ± 0.01	–	–
Fitted $Z(\mu\mu)$	10 ± 5	–	14 ± 1	180 ± 14
Fitted $Z(\tau\tau)$	3.4 ± 0.4	2.3 ± 0.2	1.8 ± 0.2	0.2 ± 0.1
Fitted $Z(\nu\nu)$	1460 ± 120	0.22 ± 0.04	0.2 ± 0.03	–
Expected $t\bar{t}$, single top	81 ± 28	50 ± 17	154 ± 54	5 ± 2
Expected diboson	84 ± 8	22 ± 3	48 ± 5	8 ± 1
Multijet	8 ± 8	–	–	–
NCB	9 ± 9	–	–	–
MC exp. SM events	2470 ± 180	439 ± 36	1310 ± 100	182 ± 13
Fit input $W(e\nu)$	173 ± 17	302 ± 23	0.01 ± 0.01	–
Fit input $W(\mu\nu)$	173 ± 20	0.4 ± 0.1	1035 ± 74	0.2 ± 0.03
Fit input $W(\tau\nu)$	410 ± 28	60 ± 4	61 ± 7	0.02 ± 0.02
Fit input $Z(ee)$	–	0.03 ± 0.01	–	–
Fit input $Z(\mu\mu)$	9 ± 4	–	13 ± 1	169 ± 12
Fit input $Z(\tau\tau)$	4.5 ± 0.4	3.1 ± 0.2	2.4 ± 0.2	0.2 ± 0.1
Fit input $Z(\nu\nu)$	1510 ± 120	0.22 ± 0.04	0.2 ± 0.02	–
Fit input $t\bar{t}$, single top	81 ± 29	50 ± 18	154 ± 55	5 ± 2
Fit input diboson	84 ± 8	22 ± 3	48 ± 5	8 ± 1
Multijet	8 ± 8	–	–	–
NCB	9 ± 9	–	–	–

Table B.4. Data and background predictions in the signal and control regions before and after the fit performed for the EM4 selection. The background predictions include both the statistical and systematic uncertainties. The individual uncertainties are correlated and do not necessarily add in quadrature to the total background uncertainty [116].

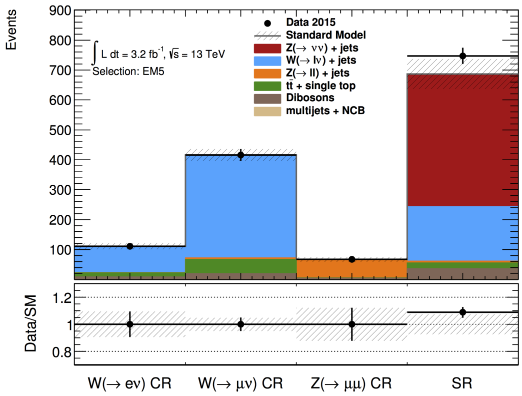

Figure B.5. Summary plot showing the agreement of data and the SM predictions post-fit in the region EM5 and the relative CRs labelled with their dominant background process.

EM5	SR	CR1e	CR1μ	CR2μ
Observed events (3.2 fb^{-1})	747	111	416	67
SM prediction (post-fit)	686 ± 50	111 ± 11	416 ± 20	67 ± 8
Fitted $W(e\nu)$	37 ± 7	72 ± 9	–	–
Fitted $W(\mu\nu)$	44 ± 8	0.13 ± 0.03	326 ± 26	0.09 ± 0.02
Fitted $W(\tau\nu)$	101 ± 15	16 ± 2	18 ± 3	0.01 ± 0
Fitted $Z(ee)$	–	0.02 ± 0	–	–
Fitted $Z(\mu\mu)$	5 ± 2	–	4 ± 1	61 ± 8
Fitted $Z(\tau\tau)$	0.9 ± 0.2	0.7 ± 0.1	0.6 ± 0.1	0.03 ± 0.02
Fitted $Z(\nu\nu)$	443 ± 42	0.1 ± 0.01	0.09 ± 0.01	–
Expected $t\bar{t}$, single top	19 ± 7	14 ± 5	48 ± 17	2 ± 1
Expected diboson	36 ± 5	9 ± 1	20 ± 2	4 ± 1
Multijet	1 ± 1	–	–	–
NCB	–	–	–	–
MC exp. SM events	754 ± 53	131 ± 12	444 ± 35	57 ± 4
Fit input $W(e\nu)$	46 ± 5	88 ± 9	–	–
Fit input $W(\mu\nu)$	47 ± 7	0.14 ± 0.03	350 ± 25	0.1 ± 0.01
Fit input $W(\tau\nu)$	124 ± 8	19 ± 2	22 ± 3	0.01 ± 0
Fit input $Z(ee)$	–	0.02 ± 0	–	–
Fit input $Z(\mu\mu)$	4 ± 1	–	3.4 ± 0.3	51 ± 4
Fit input $Z(\tau\tau)$	1.1 ± 0.1	0.8 ± 0.1	0.7 ± 0.1	0.03 ± 0.02
Fit input $Z(\nu\nu)$	476 ± 38	0.11 ± 0.01	0.1 ± 0.01	–
Fit input $t\bar{t}$, single top	19 ± 7	14 ± 5	48 ± 17	2 ± 1
Fit input diboson	36 ± 5	9 ± 1	20 ± 2	4 ± 1
Multijet	1 ± 1	–	–	–
NCB	–	–	–	–

Table B.5. Data and background predictions in the signal and control regions before and after the fit performed for the EM5 selection. The background predictions include both the statistical and systematic uncertainties. The individual uncertainties are correlated and do not necessarily add in quadrature to the total background uncertainty [116].

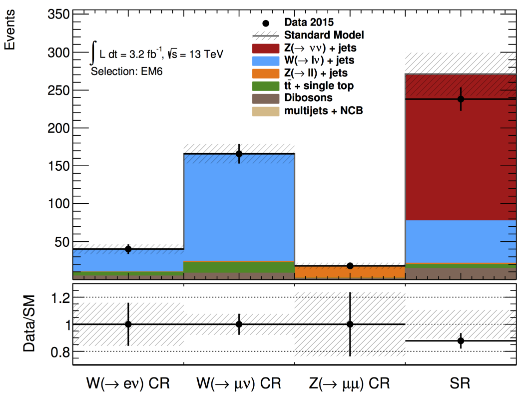

Figure B.6. Summary plot showing the agreement of data and the SM predictions post-fit in the region EM6 and the relative CRs labelled with their dominant background process.

EM6	SR	CR1e	CR1μ	CR2μ
Observed events (3.2 fb^{-1})	238	40	166	18
SM prediction (post-fit)	271 ± 28	40 ± 6	166 ± 13	18 ± 4
Fitted $W(e\nu)$	11 ± 3	25 ± 6	–	–
Fitted $W(\mu\nu)$	18 ± 4	0.07 ± 0.02	137 ± 14	0.03 ± 0.01
Fitted $W(\tau\nu)$	27 ± 7	5 ± 1	5 ± 1	–
Fitted $Z(ee)$	–	0.01 ± 0	–	–
Fitted $Z(\mu\mu)$	2 ± 1	–	1 ± 1	16 ± 4
Fitted $Z(\tau\tau)$	0.3 ± 0.1	0.2 ± 0.1	0.2 ± 0.1	0.01 ± 0
Fitted $Z(\nu\nu)$	193 ± 24	0.04 ± 0.01	0.01 ± 0	–
Expected $t\bar{t}$, single top	5 ± 2	5 ± 2	14 ± 6	0.3 ± 0.1
Expected diboson	15 ± 3	5 ± 1	8 ± 1	1.6 ± 0.4
Multijet	0.2 ± 0.2	–	–	–
NCB	–	–	–	–
MC exp. SM events	257 ± 19	50 ± 5	150 ± 14	19 ± 2
Fit input $W(e\nu)$	14 ± 2	34 ± 3	–	–
Fit input $W(\mu\nu)$	16 ± 3	0.06 ± 0.01	119 ± 11	0.03 ± 0.01
Fit input $W(\tau\nu)$	37 ± 3	6.8 ± 0.4	7 ± 1	–
Fit input $Z(ee)$	–	0.01 ± 0	–	–
Fit input $Z(\mu\mu)$	1.6 ± 0.4	–	1 ± 1	17 ± 1
Fit input $Z(\tau\tau)$	0.37 ± 0.03	0.28 ± 0.03	0.3 ± 0.1	0.01 ± 0
Fit input $Z(\nu\nu)$	168 ± 14	0.04 ± 0.01	0.01 ± 0	–
Fit input $t\bar{t}$, single top	5 ± 2	5 ± 2	14 ± 6	0.3 ± 0.1
Fit input diboson	15 ± 3	5 ± 1	8 ± 1	1.6 ± 0.4
Multijet	0.2 ± 0.2	–	–	–
NCB	–	–	–	–

Table B.6. Data and background predictions in the signal and control regions before and after the fit performed for the EM6 selection. The background predictions include both the statistical and systematic uncertainties. The individual uncertainties are correlated and do not necessarily add in quadrature to the total background uncertainty [116].

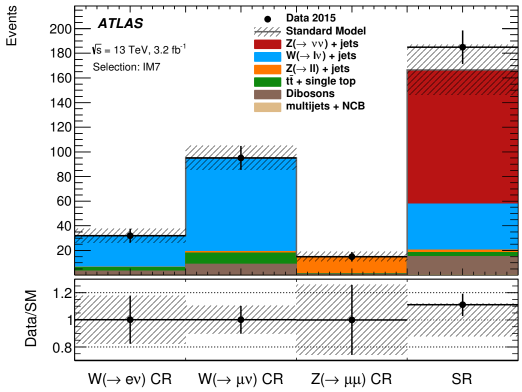

Figure B.7. Summary plot showing the agreement of data and the SM predictions post-fit in the region IM7 and the relative CRs labelled with their dominant background process [116].

IM7	SR	CR1e	CR1μ	CR2μ
Observed events (3.2 fb^{-1})	185	32	95	15
SM prediction (post-fit)	167 ± 20	32 ± 6	95 ± 10	15 ± 4
Fitted $W(e\nu)$	7 ± 2	21 ± 5	–	–
Fitted $W(\mu\nu)$	11 ± 2	0.05 ± 0.01	71 ± 11	0.01 ± 0
Fitted $W(\tau\nu)$	19 ± 4	5 ± 1	5 ± 1	0.01 ± 0
Fitted $Z(ee)$	–	–	–	–
Fitted $Z(\mu\mu)$	2 ± 1	–	1.1 ± 0.3	14 ± 4
Fitted $Z(\tau\tau)$	0.2 ± 0.1	0.16 ± 0.04	0.17 ± 0.04	0.02 ± 0.01
Fitted $Z(\nu\nu)$	109 ± 18	0.05 ± 0.01	0.01 ± 0	–
Expected $t\bar{t}$, single top	3 ± 1	3 ± 1	9 ± 4	0.4 ± 0.2
Expected diboson	15 ± 2	3.4 ± 0.3	9 ± 2	1 ± 0.3
Multijet	0.4 ± 0.4	–	–	–
NCB	–	–	–	–
MC exp. SM events	186 ± 15	34 ± 3	106 ± 9	13 ± 1
Fit input $W(e\nu)$	8 ± 1	23 ± 2	–	–
Fit input $W(\mu\nu)$	12 ± 2	0.06 ± 0.01	81 ± 7	0.01 ± 0
Fit input $W(\tau\nu)$	21 ± 2	5 ± 0.4	5 ± 1	0.01 ± 0
Fit input $Z(ee)$	–	–	–	–
Fit input $Z(\mu\mu)$	1.5 ± 0.4	–	0.9 ± 0.1	11 ± 1
Fit input $Z(\tau\tau)$	0.22 ± 0.03	0.18 ± 0.01	0.19 ± 0.02	0.02 ± 0
Fit input $Z(\nu\nu)$	125 ± 12	0.06 ± 0.01	0.01 ± 0	–
Fit input $t\bar{t}$, single top	3 ± 1	3 ± 1	9 ± 4	0.4 ± 0.2
Fit input diboson	15 ± 2	3.5 ± 0.3	9 ± 2	1 ± 0.3
multijet	0.4 ± 0.4	–	–	–
NCB	–	–	–	–

Table B.7. Data and background predictions in the signal and control regions before and after the fit performed for the IM7 selection. The background predictions include both the statistical and systematic uncertainties. The individual uncertainties are correlated and do not necessarily add in quadrature to the total background uncertainty [116].

Appendix C

Signal Expected Yields in the Signal Region

In the following pages the expected number of events of the ADD signal model (Table C.1), SUSY compressed scenarios (Tables C.2–C.4) and the simplified models with axial-vector (Tables C.5, C.6 and C.8) and pseudo-scalar mediators (Tables C.7 and C.9) in each of the $E_{\mathrm{T}}^{\mathrm{miss}}$-bins of the signal region used in the analysis are shown. The yields are scaled to the integrated luminosity of 3.2 fb^{-1} and the experimental systematic uncertainties are also quoted.

n [GeV]	m_D [GeV]	EM4	EM5	EM6	IM7
2	5300	$268.28^{+14.47}_{-15.00}$	$156.70^{+8.66}_{-8.56}$	$87.95^{+5.08}_{-4.75}$	$136.20^{+7.67}_{-8.35}$
3	4100	$355.39^{+18.86}_{-18.29}$	$17.80^{+11.11}_{-12.37}$	$123.37^{+6.52}_{-6.91}$	$213.17^{+11.65}_{-12.06}$
4	3600	$459.31^{+23.88}_{-24.46}$	$287.07^{+14.81}_{-14.96}$	$169.65^{+10.66}_{-9.74}$	$320.46^{+16.84}_{-17.63}$
5	3200	$870.11^{+44.47}_{-46.10}$	$520.53^{+29.24}_{-27.86}$	$316.56^{+16.48}_{-19.21}$	$593.20^{+31.48}_{-34.70}$
6	3000	$1393.27^{+76.39}_{-76.27}$	$872.38^{+47.88}_{-50.65}$	$648.93^{+33.29}_{-33.29}$	$936.79^{+54.39}_{-59.22}$

Table C.1. Expected number of events in 3.2 fb^{-1} and the experimental systematic uncertainties for each ADD signal samples. MC statistical uncertainty is not included.

$m_{\tilde{b}_1}$ [GeV]	$m_{\tilde{\chi}_1^0}$ [GeV]	EM1	EM2	EM3	EM4	EM5	EM6	IM7
250	230	$498.14^{+27.48}_{-26.59}$	$426.43^{+22.72}_{-22.28}$	$291.71^{+15.65}_{-15.20}$	$321.61^{+16.96}_{-17.47}$	$130.77^{+7.16}_{-7.08}$	$52.91^{+3.14}_{-2.94}$	$39.42^{+2.44}_{-2.60}$
250	245	$573.07^{+28.94}_{-29.77}$	$546.96^{+28.20}_{-29.65}$	$413.64^{+22.49}_{-21.98}$	$506.27^{+28.92}_{-27.85}$	$241.04^{+14.07}_{-15.03}$	$112.86^{+6.04}_{-6.52}$	$109.07^{+6.82}_{-7.27}$
300	280	$250.50^{+14.35}_{-14.53}$	$225.08^{+11.57}_{-11.41}$	$163.52^{+8.68}_{-10.15}$	$178.81^{+10.53}_{-9.65}$	$81.72^{+5.29}_{-5.20}$	$35.81^{+1.91}_{-1.95}$	$28.79^{+2.26}_{-2.37}$
300	295	$278.25^{+17.13}_{-15.83}$	$269.96^{+13.92}_{-13.93}$	$211.28^{+11.41}_{-11.53}$	$260.34^{+15.03}_{-13.56}$	$138.85^{+8.39}_{-8.60}$	$65.88^{+3.68}_{-4.03}$	$72.81^{+4.32}_{-4.33}$
350	330	$125.07^{+6.92}_{-6.60}$	$118.92^{+6.45}_{-6.41}$	$90.57^{+4.77}_{-4.74}$	$109.61^{+5.77}_{-5.65}$	$52.28^{+2.86}_{-2.88}$	$24.68^{+1.36}_{-1.35}$	$22.34^{+1.36}_{-1.34}$
350	345	$134.37^{+7.03}_{-7.01}$	$138.65^{+7.02}_{-7.12}$	$111.27^{+5.66}_{-5.72}$	$145.23^{+7.90}_{-7.63}$	$77.59^{+4.21}_{-4.19}$	$40.55^{+2.33}_{-2.31}$	$45.69^{+2.73}_{-2.78}$
400	380	$66.60^{+4.12}_{-4.23}$	$67.37^{+3.73}_{-3.56}$	$52.39^{+2.86}_{-3.51}$	$65.39^{+3.55}_{-3.41}$	$33.64^{+2.81}_{-2.11}$	$14.87^{+1.65}_{-1.69}$	$16.99^{+1.34}_{-1.30}$
400	395	$72.43^{+4.34}_{-4.46}$	$74.83^{+5.34}_{-4.23}$	$62.20^{+3.41}_{-3.72}$	$83.09^{+4.52}_{-4.37}$	$46.16^{+2.88}_{-3.14}$	$24.59^{+1.24}_{-1.35}$	$30.13^{+1.78}_{-1.78}$
450	430	$36.08^{+2.12}_{-2.24}$	$37.58^{+2.84}_{-2.95}$	$30.16^{+1.70}_{-2.45}$	$37.99^{+2.12}_{-2.43}$	$18.60^{+1.53}_{-1.29}$	$10.37^{+0.76}_{-0.98}$	$11.82^{+0.98}_{-0.85}$
450	445	$36.30^{+2.07}_{-2.03}$	$41.00^{+2.63}_{-2.59}$	$33.70^{+2.10}_{-1.90}$	$51.55^{+2.74}_{-3.42}$	$25.10^{+2.16}_{-1.76}$	$15.22^{+1.19}_{-1.22}$	$20.18^{+1.24}_{-1.29}$
500	480	$17.49^{+1.32}_{-1.55}$	$20.85^{+1.43}_{-1.67}$	$15.17^{+1.29}_{-1.61}$	$24.88^{+1.35}_{-2.47}$	$12.53^{+0.87}_{-1.37}$	$8.30^{+0.59}_{-0.79}$	$8.07^{+0.63}_{-0.53}$
500	495	$21.50^{+1.95}_{-1.50}$	$23.67^{+1.51}_{-1.56}$	$18.05^{+1.46}_{-1.15}$	$30.52^{+1.99}_{-1.96}$	$16.68^{+1.68}_{-1.83}$	$9.59^{+1.15}_{-0.79}$	$12.13^{+0.69}_{-0.66}$
550	530	$12.67^{+0.87}_{-1.12}$	$13.71^{+0.96}_{-0.90}$	$10.03^{+0.81}_{-1.02}$	$14.30^{+1.28}_{-0.97}$	$8.47^{+0.63}_{-0.51}$	$4.43^{+0.44}_{-0.37}$	$4.10^{+0.37}_{-0.33}$
550	545	$13.06^{+0.95}_{-0.83}$	$14.48^{+1.18}_{-1.10}$	$11.83^{+1.32}_{-0.94}$	$19.04^{+1.10}_{-1.08}$	$9.49^{+0.66}_{-1.12}$	$6.42^{+0.36}_{-0.58}$	$7.38^{+0.60}_{-0.64}$
600	580	$7.06^{+0.51}_{-0.59}$	$8.01^{+0.55}_{-0.71}$	$6.92^{+0.74}_{-0.47}$	$8.21^{+0.95}_{-0.60}$	$5.90^{+0.54}_{-0.46}$	$3.72^{+0.29}_{-0.28}$	$4.78^{+0.39}_{-0.36}$
600	595	$8.92^{+0.53}_{-0.57}$	$8.25^{+0.52}_{-0.67}$	$7.53^{+0.69}_{-0.67}$	$11.10^{+0.97}_{-0.95}$	$6.31^{+0.45}_{-0.49}$	$4.25^{+0.41}_{-0.42}$	$6.31^{+0.41}_{-0.55}$

Table C.2. Expected number of events in 3.2 fb^{-1} and the experimental systematic uncertainties for each $\tilde{b}_1 \to b + \tilde{\chi}_1^0$ signal samples. MC statistical uncertainty is not included.

$m_{\tilde{t}_1}$ [GeV]	$m_{\tilde{\chi}_1^0}$ [GeV]	EM1	EM2	EM3	EM4	EM5	EM6	IM7
250	230	$473.65^{+25.63}_{-25.15}$	$394.32^{+21.13}_{-21.05}$	$268.95^{+14.13}_{-14.30}$	$286.47^{+15.62}_{-15.24}$	$120.83^{+7.21}_{-7.19}$	$44.82^{+3.21}_{-3.53}$	$37.56^{+2.57}_{-2.34}$
275	195	$225.75^{+12.42}_{-12.76}$	$180.48^{+10.19}_{-9.78}$	$121.93^{+6.60}_{-6.49}$	$121.41^{+7.52}_{-8.65}$	$42.58^{+2.86}_{-2.39}$	$17.20^{+0.99}_{-1.21}$	$11.54^{+0.81}_{-0.75}$
275	225	$239.19^{+15.33}_{-14.72}$	$195.46^{+9.96}_{-10.02}$	$126.64^{+7.47}_{-6.89}$	$138.36^{+7.55}_{-8.17}$	$53.23^{+3.98}_{-3.41}$	$21.81^{+1.75}_{-1.85}$	$14.12^{+1.24}_{-1.00}$
275	250	$283.58^{+17.42}_{-17.59}$	$250.95^{+13.28}_{-13.57}$	$173.99^{+10.27}_{-10.41}$	$190.76^{+10.18}_{-10.54}$	$78.50^{+5.52}_{-5.30}$	$31.25^{+2.21}_{-2.60}$	$26.61^{+1.58}_{-1.88}$
275	270	$368.78^{+20.66}_{-20.29}$	$354.80^{+18.93}_{-19.39}$	$275.59^{+15.17}_{-15.64}$	$342.45^{+19.47}_{-21.12}$	$165.11^{+9.98}_{-8.57}$	$75.32^{+4.51}_{-4.50}$	$71.60^{+4.19}_{-4.19}$
300	220	$161.97^{+8.27}_{-8.30}$	$134.09^{+7.54}_{-7.48}$	$93.74^{+5.15}_{-4.90}$	$94.27^{+5.17}_{-5.04}$	$34.53^{+1.96}_{-2.39}$	$13.91^{+1.10}_{-0.99}$	$9.80^{+0.74}_{-0.66}$
300	260	$176.51^{+10.36}_{-11.18}$	$155.46^{+8.44}_{-8.69}$	$111.99^{+7.49}_{-6.17}$	$120.11^{+6.24}_{-6.77}$	$51.05^{+3.93}_{-3.01}$	$21.02^{+1.51}_{-1.55}$	$15.62^{+1.29}_{-1.07}$
300	280	$221.18^{+13.23}_{-12.90}$	$202.92^{+12.45}_{-12.21}$	$145.63^{+9.36}_{-8.77}$	$167.00^{+9.91}_{-9.32}$	$72.72^{+5.11}_{-4.95}$	$31.77^{+2.75}_{-1.75}$	$24.21^{+1.88}_{-1.79}$
300	295	$249.08^{+13.37}_{-13.23}$	$250.78^{+14.95}_{-14.89}$	$187.44^{+13.03}_{-12.85}$	$250.58^{+14.22}_{-14.23}$	$125.98^{+8.48}_{-8.32}$	$64.25^{+4.20}_{-4.90}$	$59.67^{+3.65}_{-3.50}$
325	245	$110.94^{+6.34}_{-6.69}$	$97.47^{+5.34}_{-5.50}$	$68.32^{+4.21}_{-3.87}$	$76.39^{+4.55}_{-4.39}$	$29.95^{+2.07}_{-2.07}$	$11.84^{+1.10}_{-1.48}$	$8.10^{+0.79}_{-0.72}$
325	260	$107.68^{+7.17}_{-6.99}$	$103.91^{+6.17}_{-5.66}$	$71.17^{+4.78}_{-4.22}$	$79.10^{+4.23}_{-4.10}$	$33.65^{+2.12}_{-2.12}$	$13.53^{+0.78}_{-0.92}$	$10.27^{+0.70}_{-0.68}$
325	295	$136.53^{+8.31}_{-8.83}$	$129.93^{+7.17}_{-7.22}$	$90.35^{+5.04}_{-4.74}$	$106.65^{+5.82}_{-5.69}$	$47.07^{+2.54}_{-3.20}$	$19.54^{+2.13}_{-1.89}$	$17.03^{+1.23}_{-1.25}$
325	320	$174.61^{+9.34}_{-10.70}$	$177.61^{+9.14}_{-9.53}$	$139.19^{+8.37}_{-9.04}$	$183.24^{+9.73}_{-9.38}$	$92.97^{+5.07}_{-6.35}$	$46.32^{+3.10}_{-2.42}$	$50.25^{+2.91}_{-2.95}$
350	270	$77.78^{+6.46}_{-4.59}$	$72.28^{+4.88}_{-4.98}$	$52.80^{+3.10}_{-2.97}$	$53.96^{+3.16}_{-3.13}$	$21.58^{+1.25}_{-1.27}$	$8.98^{+1.00}_{-0.81}$	$7.86^{+0.60}_{-0.52}$
350	295	$84.62^{+6.49}_{-6.13}$	$78.08^{+4.70}_{-4.37}$	$59.54^{+3.22}_{-3.28}$	$65.60^{+3.84}_{-3.79}$	$28.79^{+1.68}_{-1.65}$	$13.60^{+0.93}_{-1.34}$	$10.84^{+0.91}_{-0.74}$
350	305	$89.65^{+5.92}_{-4.91}$	$83.94^{+4.96}_{-5.56}$	$63.42^{+5.61}_{-4.61}$	$65.77^{+4.85}_{-3.84}$	$28.75^{+2.79}_{-2.77}$	$11.13^{+1.63}_{-1.66}$	$11.67^{+1.00}_{-0.90}$
350	345	$124.41^{+6.80}_{-6.75}$	$129.95^{+7.99}_{-7.64}$	$103.86^{+5.68}_{-5.40}$	$129.37^{+6.67}_{-8.20}$	$74.00^{+4.00}_{-3.87}$	$34.62^{+2.45}_{-2.63}$	$39.91^{+2.73}_{-2.47}$
375	295	$58.10^{+4.82}_{-4.84}$	$55.46^{+3.50}_{-3.52}$	$38.36^{+2.40}_{-2.72}$	$46.91^{+2.94}_{-2.86}$	$19.77^{+2.27}_{-1.72}$	$7.32^{+0.73}_{-0.82}$	$6.91^{+0.40}_{-0.63}$
375	315	$59.17^{+3.37}_{-4.32}$	$54.07^{+3.43}_{-3.33}$	$39.58^{+2.65}_{-2.10}$	$47.89^{+2.77}_{-2.57}$	$21.25^{+1.20}_{-1.43}$	$9.27^{+0.82}_{-0.66}$	$8.14^{+0.62}_{-0.54}$
375	345	$72.06^{+4.19}_{-5.03}$	$71.86^{+4.21}_{-4.02}$	$49.76^{+4.03}_{-4.02}$	$66.76^{+3.55}_{-3.82}$	$30.85^{+1.89}_{-1.86}$	$13.93^{+1.19}_{-0.83}$	$11.86^{+0.87}_{-1.13}$
375	370	$87.66^{+5.86}_{-5.28}$	$94.97^{+6.09}_{-5.07}$	$77.21^{+4.79}_{-4.68}$	$102.14^{+6.18}_{-5.57}$	$58.38^{+3.59}_{-4.11}$	$27.49^{+2.60}_{-1.75}$	$33.87^{+1.89}_{-2.16}$
400	320	$42.16^{+3.28}_{-3.26}$	$41.89^{+2.60}_{-2.87}$	$32.31^{+2.29}_{-2.29}$	$31.79^{+1.97}_{-2.00}$	$14.74^{+0.99}_{-0.93}$	$6.23^{+0.61}_{-1.02}$	$7.03^{+0.54}_{-0.41}$
400	330	$40.94^{+2.33}_{-2.78}$	$41.84^{+2.75}_{-3.07}$	$32.23^{+2.08}_{-2.13}$	$36.14^{+2.15}_{-2.12}$	$16.36^{+1.06}_{-0.99}$	$8.13^{+0.52}_{-0.77}$	$5.36^{+0.55}_{-0.46}$
400	370	$53.00^{+3.91}_{-3.44}$	$53.70^{+3.22}_{-3.00}$	$40.62^{+2.56}_{-2.19}$	$48.91^{+3.14}_{-2.95}$	$23.68^{+1.50}_{-1.47}$	$10.03^{+0.96}_{-1.28}$	$10.58^{+0.88}_{-0.84}$
400	395	$65.36^{+3.38}_{-3.50}$	$65.70^{+3.43}_{-3.50}$	$56.81^{+3.38}_{-3.45}$	$78.42^{+4.58}_{-4.75}$	$41.56^{+2.44}_{-3.32}$	$21.46^{+1.54}_{-1.11}$	$26.14^{+1.82}_{-1.56}$
450	370	$22.73^{+1.84}_{-1.64}$	$23.35^{+1.23}_{-1.35}$	$17.72^{+1.43}_{-1.23}$	$24.03^{+1.32}_{-1.32}$	$10.60^{+0.61}_{-0.64}$	$4.82^{+0.34}_{-0.40}$	$4.80^{+0.36}_{-0.32}$
450	395	$23.65^{+1.34}_{-1.34}$	$22.81^{+1.49}_{-1.62}$	$18.84^{+1.47}_{-2.05}$	$23.66^{+1.55}_{-1.42}$	$11.55^{+0.73}_{-0.83}$	$6.05^{+0.57}_{-0.38}$	$5.46^{+0.52}_{-0.41}$
450	425	$31.47^{+2.53}_{-2.05}$	$30.86^{+1.97}_{-1.81}$	$24.72^{+1.41}_{-1.57}$	$31.26^{+1.68}_{-1.80}$	$17.39^{+1.09}_{-1.03}$	$8.39^{+0.52}_{-0.52}$	$8.38^{+0.65}_{-0.57}$
450	445	$33.89^{+2.06}_{-2.08}$	$39.08^{+2.32}_{-2.74}$	$32.26^{+1.83}_{-1.77}$	$46.08^{+2.60}_{-2.41}$	$25.91^{+1.33}_{-1.77}$	$13.61^{+0.94}_{-0.79}$	$16.85^{+1.08}_{-1.15}$
500	420	$12.57^{+0.98}_{-0.93}$	$13.24^{+1.22}_{-0.91}$	$10.27^{+0.63}_{-0.73}$	$14.02^{+0.76}_{-0.77}$	$6.96^{+0.45}_{-0.48}$	$3.45^{+0.26}_{-0.25}$	$3.37^{+0.24}_{-0.18}$
500	445	$12.83^{+0.99}_{-0.81}$	$14.45^{+0.85}_{-0.84}$	$11.03^{+0.71}_{-0.65}$	$15.07^{+0.89}_{-0.95}$	$7.48^{+0.64}_{-0.61}$	$3.95^{+0.27}_{-0.28}$	$3.31^{+0.25}_{-0.22}$
500	485	$20.33^{+1.17}_{-1.63}$	$20.20^{+1.06}_{-1.06}$	$17.35^{+1.12}_{-1.11}$	$24.64^{+1.42}_{-1.35}$	$13.82^{+0.74}_{-0.74}$	$6.86^{+0.43}_{-0.50}$	$8.70^{+0.56}_{-0.54}$
500	495	$19.90^{+1.04}_{-1.40}$	$21.78^{+1.19}_{-1.16}$	$19.69^{+1.38}_{-1.49}$	$26.05^{+1.53}_{-1.35}$	$16.65^{+0.91}_{-1.00}$	$8.83^{+0.56}_{-0.57}$	$11.29^{+0.83}_{-0.71}$

Table C.3. Expected number of events in 3.2 fb^{-1} and the experimental systematic uncertainties for each $\tilde{t}_1 \rightarrow c + \tilde{\chi}_1^0$ signal samples. MC statistical uncertainty is not included.

$m_{\tilde{q}}$ [GeV]	$m_{\tilde{\chi}_1^0}$ [GeV]	EM1	EM2	EM3	EM4	EM5	EM6	IM7
400	395	$863.45^{+53.04}_{-53.04}$	$870.35^{+47.11}_{-46.05}$	$711.65^{+41.78}_{-36.38}$	$1060.61^{+55.27}_{-55.40}$	$565.74^{+34.58}_{-33.23}$	$301.81^{+17.74}_{-18.82}$	$378.39^{+20.56}_{-24.01}$
400	385	$889.22^{+46.96}_{-58.29}$	$819.47^{+47.19}_{-45.51}$	$677.38^{+36.14}_{-38.07}$	$921.73^{+51.32}_{-51.32}$	$440.96^{+25.43}_{-31.50}$	$190.77^{+16.46}_{-12.50}$	$222.71^{+15.18}_{-18.00}$
400	375	$757.02^{+42.63}_{-56.36}$	$680.87^{+48.00}_{-35.26}$	$555.98^{+31.29}_{-31.29}$	$708.98^{+44.68}_{-38.26}$	$319.24^{+17.38}_{-21.26}$	$146.45^{+8.14}_{-7.70}$	$165.31^{+10.70}_{-13.33}$
450	445	$462.29^{+24.13}_{-26.20}$	$488.90^{+25.59}_{-25.71}$	$422.16^{+25.11}_{-22.35}$	$606.22^{+32.81}_{-43.19}$	$309.94^{+16.77}_{-16.88}$	$188.38^{+10.70}_{-14.65}$	$231.80^{+13.40}_{-13.62}$
450	435	$449.42^{+26.80}_{-26.00}$	$472.81^{+27.80}_{-27.80}$	$365.34^{+20.84}_{-20.55}$	$517.17^{+28.17}_{-28.20}$	$265.58^{+14.11}_{-14.81}$	$147.92^{+8.77}_{-10.44}$	$167.61^{+10.95}_{-10.42}$
450	425	$379.80^{+28.51}_{-21.51}$	$393.27^{+22.48}_{-25.29}$	$331.38^{+18.28}_{-19.24}$	$437.01^{+24.89}_{-26.26}$	$207.24^{+11.21}_{-11.03}$	$109.28^{+6.44}_{-8.91}$	$110.88^{+8.38}_{-9.05}$
500	495	$256.71^{+18.39}_{-18.39}$	$265.68^{+15.04}_{-14.80}$	$232.82^{+13.50}_{-13.53}$	$344.98^{+18.94}_{-18.98}$	$198.23^{+10.22}_{-10.21}$	$114.18^{+7.20}_{-8.31}$	$169.93^{+10.92}_{-11.03}$
500	485	$270.04^{+15.55}_{-16.48}$	$283.39^{+15.35}_{-16.36}$	$235.71^{+14.62}_{-15.28}$	$308.59^{+17.70}_{-16.17}$	$173.82^{+11.58}_{-12.07}$	$92.54^{+5.83}_{-5.77}$	$107.41^{+7.16}_{-7.81}$
500	475	$224.52^{+16.83}_{-15.18}$	$229.32^{+12.75}_{-14.52}$	$187.01^{+10.35}_{-10.35}$	$273.37^{+14.43}_{-15.57}$	$135.40^{+9.49}_{-8.49}$	$67.47^{+3.99}_{-5.64}$	$83.37^{+6.18}_{-4.49}$
550	545	$152.19^{+7.92}_{-8.18}$	$171.54^{+9.18}_{-9.18}$	$143.21^{+7.98}_{-7.98}$	$230.16^{+12.75}_{-13.32}$	$135.64^{+7.66}_{-9.16}$	$70.75^{+4.27}_{-4.44}$	$104.83^{+6.11}_{-6.45}$
550	535	$153.60^{+8.84}_{-10.22}$	$157.54^{+8.45}_{-8.45}$	$135.70^{+7.28}_{-7.57}$	$207.48^{+11.26}_{-11.11}$	$117.58^{+6.66}_{-6.49}$	$65.30^{+4.30}_{-3.71}$	$75.26^{+4.16}_{-4.41}$
550	525	$126.49^{+10.04}_{-8.45}$	$137.65^{+7.40}_{-7.63}$	$114.46^{+7.07}_{-8.76}$	$178.85^{+9.50}_{-9.31}$	$92.66^{+4.69}_{-4.90}$	$45.33^{+3.01}_{-4.32}$	$59.00^{+3.28}_{-3.42}$
600	595	$90.23^{+5.92}_{-7.17}$	$105.61^{+5.55}_{-5.53}$	$98.58^{+5.14}_{-6.05}$	$144.28^{+7.45}_{-7.67}$	$82.31^{+5.06}_{-4.91}$	$54.10^{+3.73}_{-3.73}$	$64.10^{+4.11}_{-4.84}$
600	585	$91.69^{+5.23}_{-5.39}$	$98.76^{+5.15}_{-6.61}$	$85.57^{+4.31}_{-4.30}$	$130.13^{+6.92}_{-7.22}$	$74.99^{+4.27}_{-4.27}$	$42.73^{+2.26}_{-2.86}$	$55.93^{+3.35}_{-3.05}$
600	575	$85.11^{+5.19}_{-6.52}$	$88.36^{+4.97}_{-5.14}$	$72.13^{+4.33}_{-5.00}$	$107.30^{+5.81}_{-5.60}$	$63.13^{+3.53}_{-4.07}$	$32.83^{+2.57}_{-2.57}$	$39.10^{+2.74}_{-2.59}$
650	645	$57.54^{+2.90}_{-3.94}$	$66.05^{+3.37}_{-3.35}$	$58.87^{+3.46}_{-3.49}$	$86.53^{+4.78}_{-5.77}$	$52.70^{+2.69}_{-2.72}$	$34.19^{+1.95}_{-1.82}$	$49.72^{+3.03}_{-3.41}$
650	635	$62.22^{+3.52}_{-5.05}$	$62.59^{+3.94}_{-3.15}$	$56.75^{+3.50}_{-2.97}$	$83.99^{+4.45}_{-4.58}$	$47.39^{+2.43}_{-2.44}$	$30.10^{+1.83}_{-1.82}$	$38.62^{+2.14}_{-2.46}$
650	625	$53.19^{+3.15}_{-4.23}$	$53.94^{+4.13}_{-3.37}$	$45.56^{+2.36}_{-2.90}$	$69.64^{+4.16}_{-4.16}$	$40.72^{+2.75}_{-2.85}$	$22.19^{+1.42}_{-1.41}$	$28.60^{+1.64}_{-1.96}$
700	695	$37.71^{+2.43}_{-2.03}$	$42.97^{+2.31}_{-2.37}$	$36.56^{+2.25}_{-2.25}$	$57.20^{+3.10}_{-3.27}$	$37.98^{+2.01}_{-2.03}$	$23.80^{+1.44}_{-1.28}$	$34.12^{+2.25}_{-2.39}$
700	685	$36.72^{+2.02}_{-2.07}$	$42.25^{+2.19}_{-2.41}$	$34.78^{+1.84}_{-1.85}$	$55.24^{+2.93}_{-2.94}$	$31.51^{+1.69}_{-1.76}$	$19.66^{+1.19}_{-1.18}$	$28.67^{+1.65}_{-1.73}$
700	675	$32.44^{+2.49}_{-2.97}$	$35.88^{+2.18}_{-2.03}$	$29.87^{+1.58}_{-1.98}$	$44.31^{+2.36}_{-2.51}$	$27.84^{+1.60}_{-2.10}$	$16.97^{+0.90}_{-0.89}$	$20.23^{+1.26}_{-1.18}$

Table C.4. Expected number of events in 3.2 fb^{-1} and the experimental systematic uncertainties for each $\tilde{q} \to q + \tilde{\chi}_1^0$ signal samples. MC statistical uncertainty is not included.

m_χ [GeV]	m_A [GeV]	EM1	EM2	EM3	EM4	EM5	EM6	IM7
1.0	10.0	$2.79e+04^{1.7e+03}_{1.7e+03}$	$1.72e+04^{1.1e+03}_{9.5e+02}$	$8.96e+03^{5.9e+02}_{6.7e+02}$	$7.37e+03^{4.2e+02}_{5.7e+02}$	$2.31e+03^{2.6e+02}_{2.1e+02}$	$9.32e+02^{9.3e+01}_{1.3e+02}$	$5.97e+02^{8.0e+01}_{9.7e+01}$
1.0	20.0	$2.37e+04^{1.5e+03}_{1.4e+03}$	$1.52e+04^{9.9e+02}_{1.1e+03}$	$8.65e+03^{5.6e+02}_{6.3e+02}$	$6.44e+03^{4.6e+02}_{5.3e+02}$	$2.04e+03^{1.7e+02}_{1.9e+02}$	$7.35e+02^{1.1e+02}_{9.4e+01}$	$5.59e+02^{4.1e+01}_{4.4e+01}$
1.0	50.0	$2.16e+04^{1.3e+03}_{1.4e+03}$	$1.29e+04^{8.1e+02}_{6.9e+02}$	$7.49e+03^{4.6e+02}_{5.0e+02}$	$5.87e+03^{4.9e+02}_{5.3e+02}$	$1.98e+03^{1.4e+02}_{1.3e+02}$	$6.20e+02^{5.6e+01}_{4.9e+01}$	$5.11e+02^{2.7e+01}_{3.3e+01}$
1.0	100.0	$1.66e+04^{9.8e+02}_{9.2e+02}$	$1.17e+04^{7.2e+02}_{8.3e+02}$	$5.99e+03^{5.7e+02}_{4.1e+02}$	$5.38e+03^{3.0e+02}_{4.3e+02}$	$1.71e+03^{1.3e+02}_{1.2e+02}$	$6.50e+02^{7.6e+01}_{6.8e+01}$	$5.03e+02^{4.0e+01}_{5.0e+01}$
1.0	200.0	$1.02e+04^{5.7e+02}_{5.8e+02}$	$7.00e+03^{5.2e+02}_{4.5e+02}$	$4.17e+03^{2.6e+02}_{2.9e+02}$	$4.03e+03^{2.6e+02}_{2.5e+02}$	$1.41e+03^{1.1e+02}_{1.1e+02}$	$5.29e+02^{3.4e+01}_{4.8e+01}$	$3.95e+02^{4.8e+01}_{3.7e+01}$
1.0	300.0	$5.48e+03^{3.0e+02}_{3.0e+02}$	$4.40e+03^{2.4e+02}_{3.2e+02}$	$2.98e+03^{1.7e+02}_{1.7e+02}$	$2.74e+03^{2.0e+02}_{1.6e+02}$	$1.04e+03^{8.2e+01}_{6.1e+01}$	$4.31e+02^{4.0e+01}_{4.0e+01}$	$3.54e+02^{2.6e+01}_{2.1e+01}$
1.0	500.0	$1.74e+03^{9.8e+01}_{9.3e+01}$	$1.62e+03^{8.6e+01}_{9.4e+01}$	$1.11e+03^{7.7e+01}_{6.4e+01}$	$1.24e+03^{6.7e+01}_{7.1e+01}$	$5.71e+02^{3.6e+01}_{3.2e+01}$	$2.59e+02^{1.5e+01}_{1.9e+01}$	$2.38e+02^{1.8e+01}_{1.6e+01}$
1.0	800.0	$4.45e+02^{2.9e+01}_{3.6e+01}$	$4.30e+02^{2.4e+01}_{2.4e+01}$	$3.22e+02^{2.0e+01}_{1.7e+01}$	$4.05e+02^{2.1e+01}_{2.1e+01}$	$2.15e+02^{1.3e+01}_{1.4e+01}$	$1.05e+02^{8.0e+00}_{6.6e+00}$	$1.22e+02^{7.2e+00}_{7.0e+00}$
1.0	1000.0	$1.97e+02^{1.1e+01}_{1.0e+01}$	$2.06e+02^{1.1e+01}_{1.1e+01}$	$1.67e+02^{9.5e+00}_{9.5e+00}$	$2.13e+02^{1.1e+01}_{1.2e+01}$	$1.13e+02^{7.1e+00}_{6.1e+00}$	$6.05e+01^{3.3e+00}_{4.1e+00}$	$7.30e+01^{4.4e+00}_{4.2e+00}$
1.0	1200.0	$1.06e+02^{5.9e+00}_{5.7e+00}$	$1.11e+02^{6.5e+00}_{6.5e+00}$	$8.61e+01^{5.6e+00}_{5.6e+00}$	$1.19e+02^{6.6e+00}_{7.0e+00}$	$6.35e+01^{3.9e+00}_{3.9e+00}$	$3.39e+01^{1.8e+00}_{1.9e+00}$	$4.45e+01^{2.6e+00}_{2.5e+00}$
1.0	1500.0	$4.10e+01^{2.3e+00}_{2.3e+00}$	$4.54e+01^{2.7e+00}_{2.5e+00}$	$3.94e+01^{2.2e+00}_{2.6e+00}$	$4.95e+01^{2.6e+00}_{2.6e+00}$	$2.90e+01^{1.5e+00}_{1.6e+00}$	$1.63e+01^{8.9e-01}_{1.0e+00}$	$2.32e+01^{1.3e+00}_{1.3e+00}$
1.0	2000.0	$1.08e+01^{7.7e-01}_{6.7e-01}$	$1.25e+01^{6.6e-01}_{7.4e-01}$	$1.05e+01^{5.6e-01}_{5.6e-01}$	$1.51e+01^{8.0e-01}_{8.1e-01}$	$8.62e+00^{4.4e-01}_{4.7e-01}$	$5.07e+00^{3.0e-01}_{2.8e-01}$	$7.79e+00^{4.3e-01}_{4.3e-01}$
1.0	10000.0	$1.43e-03^{7.2e-05}_{7.3e-05}$	$1.43e-03^{7.5e-05}_{7.5e-05}$	$1.20e-03^{6.3e-05}_{6.9e-05}$	$1.55e-03^{8.3e-05}_{8.5e-05}$	$8.63e-04^{4.5e-05}_{4.6e-05}$	$5.02e-04^{3.1e-05}_{3.0e-05}$	$7.00e-04^{4.1e-05}_{3.9e-05}$
10.0	10.0	$1.18e+03^{8.1e+01}_{7.5e+01}$	$8.12e+02^{5.4e+01}_{4.7e+01}$	$4.75e+02^{2.7e+01}_{2.8e+01}$	$4.31e+02^{3.6e+01}_{3.0e+01}$	$1.39e+02^{9.1e+00}_{8.6e+00}$	$5.37e+01^{4.3e+00}_{5.0e+00}$	$4.40e+01^{2.9e+00}_{2.6e+00}$
10.0	15.0	$1.35e+03^{8.0e+01}_{8.7e+01}$	$8.79e+02^{6.1e+01}_{5.0e+01}$	$5.04e+02^{4.7e+01}_{3.7e+01}$	$4.46e+02^{2.8e+01}_{3.1e+01}$	$1.66e+02^{1.2e+01}_{1.1e+01}$	$5.73e+01^{3.5e+00}_{5.4e+00}$	$4.45e+01^{2.9e+00}_{2.7e+00}$
10.0	50.0	$1.85e+04^{1.1e+03}_{1.2e+03}$	$1.21e+04^{9.9e+02}_{9.1e+02}$	$6.46e+03^{4.1e+02}_{3.8e+02}$	$5.46e+03^{4.4e+02}_{4.8e+02}$	$1.75e+03^{1.6e+02}_{1.3e+02}$	$5.48e+02^{7.7e+01}_{7.6e+01}$	$5.40e+02^{4.4e+01}_{5.8e+01}$
10.0	100.0	$1.62e+04^{9.7e+02}_{9.1e+02}$	$1.11e+04^{6.0e+02}_{6.6e+02}$	$5.99e+03^{4.7e+02}_{5.7e+02}$	$5.27e+03^{4.1e+02}_{3.4e+02}$	$1.67e+03^{1.0e+02}_{1.3e+02}$	$5.70e+02^{7.1e+01}_{6.6e+01}$	$4.89e+02^{3.8e+01}_{3.2e+01}$
10.0	10000.0	$1.41e-03^{7.2e-05}_{7.2e-05}$	$1.51e-03^{8.0e-05}_{8.1e-05}$	$1.13e-03^{6.7e-05}_{6.5e-05}$	$1.55e-03^{8.3e-05}_{8.1e-05}$	$8.87e-04^{4.7e-05}_{5.6e-05}$	$4.74e-04^{2.6e-05}_{2.5e-05}$	$6.94e-04^{3.9e-05}_{3.9e-05}$
50.0	10.0	$2.55e+02^{1.3e+01}_{1.3e+01}$	$1.98e+02^{1.2e+01}_{1.3e+01}$	$1.17e+02^{7.0e+00}_{8.1e+00}$	$1.16e+02^{8.3e+00}_{6.4e+00}$	$4.68e+01^{2.7e+00}_{3.3e+00}$	$1.87e+01^{1.2e+00}_{1.6e+00}$	$1.66e+01^{1.1e+00}_{1.0e+00}$
50.0	50.0	$2.78e+02^{1.5e+01}_{1.6e+01}$	$2.19e+02^{1.3e+01}_{1.2e+01}$	$1.35e+02^{8.7e+00}_{9.3e+00}$	$1.38e+02^{8.3e+00}_{8.0e+00}$	$4.96e+01^{3.5e+00}_{3.5e+00}$	$2.06e+01^{1.5e+00}_{1.6e+00}$	$1.78e+01^{1.3e+00}_{1.1e+00}$
50.0	95.0	$5.28e+02^{2.8e+01}_{2.8e+01}$	$3.93e+02^{2.5e+01}_{2.5e+01}$	$2.37e+02^{1.3e+01}_{1.4e+01}$	$2.16e+02^{1.5e+01}_{1.4e+01}$	$7.81e+01^{5.6e+00}_{5.8e+00}$	$3.13e+01^{2.8e+00}_{2.6e+00}$	$2.73e+01^{2.0e+00}_{2.1e+00}$
50.0	200.0	$8.07e+03^{4.7e+02}_{4.3e+02}$	$5.95e+03^{3.2e+02}_{3.5e+02}$	$3.48e+03^{2.4e+02}_{2.5e+02}$	$3.20e+03^{1.9e+02}_{1.9e+02}$	$1.12e+03^{1.0e+02}_{7.5e+01}$	$4.05e+02^{2.8e+01}_{3.6e+01}$	$3.25e+02^{2.4e+01}_{2.0e+01}$
50.0	300.0	$5.15e+03^{2.9e+02}_{3.0e+02}$	$4.05e+03^{2.5e+02}_{2.2e+02}$	$2.57e+03^{1.8e+02}_{1.7e+02}$	$2.61e+03^{1.5e+02}_{1.6e+02}$	$1.04e+03^{7.3e+01}_{7.1e+01}$	$4.06e+02^{2.2e+01}_{2.5e+01}$	$3.38e+02^{2.4e+01}_{2.3e+01}$
50.0	10000.0	$1.37e-03^{9.3e-05}_{8.3e-05}$	$1.50e-03^{8.0e-05}_{8.4e-05}$	$1.18e-03^{6.0e-05}_{6.1e-05}$	$1.59e-03^{8.7e-05}_{8.8e-05}$	$8.29e-04^{4.4e-05}_{4.8e-05}$	$4.61e-04^{2.9e-05}_{2.5e-05}$	$6.87e-04^{3.7e-05}_{3.8e-05}$
150.0	10.0	$2.60e+01^{1.4e+00}_{1.5e+00}$	$2.51e+01^{1.5e+00}_{1.3e+00}$	$1.76e+01^{9.2e-01}_{9.3e-01}$	$2.01e+01^{1.2e+00}_{1.1e+00}$	$9.04e+00^{5.4e-01}_{5.9e-01}$	$4.48e+00^{2.7e-01}_{2.4e-01}$	$4.66e+00^{2.7e-01}_{2.9e-01}$
150.0	200.0	$3.86e+01^{2.0e+00}_{2.0e+00}$	$3.52e+01^{1.9e+00}_{1.8e+00}$	$2.48e+01^{1.6e+00}_{1.4e+00}$	$2.87e+01^{1.6e+00}_{1.9e+00}$	$1.33e+01^{7.1e-01}_{8.7e-01}$	$5.99e+00^{3.6e-01}_{3.8e-01}$	$6.15e+00^{3.6e-01}_{4.0e-01}$
150.0	295.0	$1.10e+02^{5.8e+00}_{5.8e+00}$	$9.66e+01^{5.4e+00}_{5.5e+00}$	$6.69e+01^{3.8e+00}_{3.7e+00}$	$7.21e+01^{4.5e+00}_{4.4e+00}$	$3.11e+01^{1.8e+00}_{2.0e+00}$	$1.30e+01^{9.7e-01}_{9.7e-01}$	$1.28e+01^{8.1e-01}_{8.1e-01}$
150.0	500.0	$1.16e+03^{6.0e+01}_{6.0e+01}$	$1.08e+03^{6.0e+01}_{6.0e+01}$	$7.71e+02^{5.6e+01}_{4.3e+01}$	$8.66e+02^{5.1e+01}_{4.8e+01}$	$3.96e+02^{2.1e+01}_{2.6e+01}$	$1.76e+02^{1.2e+01}_{1.1e+01}$	$1.63e+02^{9.8e+00}_{9.8e+00}$
150.0	800.0	$3.68e+02^{2.1e+01}_{2.0e+01}$	$3.79e+02^{2.2e+01}_{2.5e+01}$	$2.87e+02^{1.6e+01}_{1.6e+01}$	$3.64e+02^{2.0e+01}_{1.9e+01}$	$1.84e+02^{1.2e+01}_{1.1e+01}$	$9.07e+01^{5.9e+00}_{5.3e+00}$	$1.09e+02^{6.3e+00}_{7.3e+00}$
150.0	1000.0	$1.87e+02^{1.1e+01}_{1.0e+01}$	$1.94e+02^{1.1e+01}_{1.1e+01}$	$1.52e+02^{8.6e+00}_{8.5e+00}$	$1.96e+02^{1.1e+01}_{1.1e+01}$	$1.06e+02^{5.5e+00}_{5.8e+00}$	$5.35e+01^{3.4e+00}_{3.1e+00}$	$6.74e+01^{3.8e+00}_{3.7e+00}$
150.0	10000.0	$1.13e-03^{6.0e-05}_{6.1e-05}$	$1.22e-03^{6.1e-05}_{6.4e-05}$	$1.00e-03^{5.6e-05}_{5.4e-05}$	$1.35e-03^{7.3e-05}_{7.1e-05}$	$7.61e-04^{4.1e-05}_{4.5e-05}$	$4.13e-04^{2.3e-05}_{2.2e-05}$	$6.33e-04^{3.7e-05}_{3.6e-05}$
250.0	10.0	$5.71e+00^{3.4e-01}_{3.1e-01}$	$5.60e+00^{3.4e-01}_{4.1e-01}$	$4.30e+00^{2.9e-01}_{2.8e-01}$	$5.46e+00^{2.8e-01}_{3.8e-01}$	$2.76e+00^{1.6e-01}_{1.6e-01}$	$1.46e+00^{9.4e-02}_{1.0e-01}$	$1.66e+00^{1.1e-01}_{9.3e-02}$
250.0	300.0	$9.03e+00^{5.3e-01}_{5.4e-01}$	$9.21e+00^{5.4e-01}_{5.1e-01}$	$6.90e+00^{4.1e-01}_{3.9e-01}$	$8.79e+00^{4.6e-01}_{5.3e-01}$	$4.52e+00^{2.7e-01}_{2.5e-01}$	$2.29e+00^{1.5e-01}_{1.4e-01}$	$2.61e+00^{1.7e-01}_{1.6e-01}$
250.0	495.0	$3.15e+01^{1.7e+00}_{1.8e+00}$	$3.15e+01^{1.8e+00}_{1.7e+00}$	$2.21e+01^{1.4e+00}_{1.4e+00}$	$2.61e+01^{1.6e+00}_{1.5e+00}$	$1.26e+01^{7.4e-01}_{7.5e-01}$	$6.30e+00^{4.3e-01}_{4.2e-01}$	$6.74e+00^{4.4e-01}_{4.4e-01}$
250.0	800.0	$2.69e+02^{1.4e+01}_{1.4e+01}$	$2.67e+02^{1.4e+01}_{1.4e+01}$	$2.12e+02^{1.1e+01}_{1.2e+01}$	$2.70e+02^{1.5e+01}_{1.6e+01}$	$1.33e+02^{9.6e+00}_{8.1e+00}$	$6.60e+01^{3.9e+00}_{3.4e+00}$	$7.80e+01^{4.7e+00}_{5.7e+00}$
250.0	1000.0	$1.64e+02^{1.0e+01}_{9.6e+00}$	$1.53e+02^{8.3e+00}_{8.1e+00}$	$1.21e+02^{7.4e+00}_{6.7e+00}$	$1.63e+02^{9.1e+00}_{1.0e+01}$	$8.69e+01^{4.8e+00}_{4.6e+00}$	$4.70e+01^{2.8e+00}_{3.2e+00}$	$5.71e+01^{3.4e+00}_{3.5e+00}$
250.0	10000.0	$9.04e-04^{5.5e-05}_{5.4e-05}$	$9.58e-04^{5.8e-05}_{5.5e-05}$	$7.97e-04^{4.2e-05}_{4.2e-05}$	$1.09e-03^{5.6e-05}_{5.7e-05}$	$6.38e-04^{3.5e-05}_{3.6e-05}$	$3.60e-04^{2.0e-05}_{2.1e-05}$	$5.55e-04^{3.2e-05}_{3.4e-05}$

Table C.5. Expected number of events in 3.2 fb^{-1} and the experimental systematic uncertainties for each DM signal sample with axial-vector mediator and couplings $g_q = 0.25$, $g_\chi = 1.00$. MC statistical uncertainty is not included.

m_χ [GeV]	m_A [GeV]	EM1	EM2	EM3	EM4	EM5	EM6	IM7
400.0	10.0	$9.85e-01^{6.5e-02}_{5.2e-02}$	$1.04e+00^{5.5e-02}_{6.5e-02}$	$8.65e-01^{6.5e-02}_{5.8e-02}$	$1.13e+00^{6.3e-02}_{6.5e-02}$	$6.30e-01^{3.7e-02}_{4.0e-02}$	$3.45e-01^{1.9e-02}_{1.9e-02}$	$4.76e-01^{2.9e-02}_{2.8e-02}$
400.0	795.0	$7.07e+00^{3.7e-01}_{3.7e-01}$	$7.55e+00^{4.4e-01}_{4.5e-01}$	$6.11e+00^{3.8e-01}_{3.9e-01}$	$7.63e+00^{5.0e-01}_{4.1e-01}$	$4.02e+00^{2.1e-01}_{2.2e-01}$	$2.25e+00^{1.4e-01}_{1.3e-01}$	$2.66e+00^{1.6e-01}_{1.7e-01}$
400.0	1000.0	$6.79e+01^{3.8e+00}_{4.0e+00}$	$6.84e+01^{3.8e+00}_{3.7e+00}$	$5.62e+01^{3.2e+00}_{3.2e+00}$	$7.10e+01^{4.2e+00}_{4.1e+00}$	$3.84e+01^{2.0e+00}_{2.0e+00}$	$2.14e+01^{1.3e+00}_{1.3e+00}$	$2.59e+01^{1.6e+00}_{1.5e+00}$
400.0	1200.0	$5.50e+01^{3.0e+00}_{3.1e+00}$	$5.88e+01^{3.4e+00}_{3.2e+00}$	$4.68e+01^{2.6e+00}_{2.7e+00}$	$6.46e+01^{3.3e+00}_{3.6e+00}$	$3.59e+01^{2.3e+00}_{1.9e+00}$	$1.92e+01^{1.1e+00}_{1.0e+00}$	$2.60e+01^{1.4e+00}_{1.5e+00}$
400.0	10000.0	$5.90e-04^{3.5e-05}_{3.7e-05}$	$6.65e-04^{4.4e-05}_{4.4e-05}$	$5.11e-04^{3.0e-05}_{2.8e-05}$	$7.91e-04^{4.1e-05}_{4.1e-05}$	$4.58e-04^{2.4e-05}_{2.4e-05}$	$2.69e-04^{1.5e-05}_{1.5e-05}$	$4.20e-04^{2.3e-05}_{2.4e-05}$
500.0	10.0	$3.86e-01^{2.2e-02}_{2.2e-02}$	$4.16e-01^{2.2e-02}_{2.2e-02}$	$3.62e-01^{2.0e-02}_{2.0e-02}$	$4.82e-01^{2.7e-02}_{2.5e-02}$	$2.76e-01^{1.4e-02}_{1.5e-02}$	$1.50e-01^{9.1e-03}_{8.4e-03}$	$2.24e-01^{1.3e-02}_{1.2e-02}$
500.0	500.0	$4.91e-01^{2.8e-02}_{2.7e-02}$	$5.41e-01^{2.8e-02}_{2.7e-02}$	$4.49e-01^{2.3e-02}_{2.9e-02}$	$6.19e-01^{3.4e-02}_{3.2e-02}$	$3.48e-01^{1.8e-02}_{2.0e-02}$	$1.93e-01^{1.0e-02}_{1.2e-02}$	$2.82e-01^{1.6e-02}_{1.6e-02}$
500.0	800.0	$8.77e-01^{5.6e-02}_{5.5e-02}$	$1.01e+00^{5.5e-02}_{5.4e-02}$	$7.73e-01^{4.1e-02}_{4.3e-02}$	$1.03e+00^{6.4e-02}_{5.7e-02}$	$6.20e-01^{3.4e-02}_{3.5e-02}$	$3.41e-01^{2.0e-02}_{1.9e-02}$	$4.95e-01^{2.7e-02}_{3.0e-02}$
500.0	995.0	$3.20e+00^{1.8e-01}_{1.9e-01}$	$3.47e+00^{1.8e-01}_{1.8e-01}$	$2.86e+00^{1.5e-01}_{1.5e-01}$	$3.69e+00^{2.1e-01}_{2.0e-01}$	$2.01e+00^{1.1e-01}_{1.1e-01}$	$1.13e+00^{5.8e-02}_{6.0e-02}$	$1.54e+00^{9.4e-02}_{9.1e-02}$
500.0	1200.0	$2.79e+01^{1.7e+00}_{1.6e+00}$	$3.04e+01^{2.2e+00}_{2.3e+00}$	$2.44e+01^{1.7e+00}_{1.7e+00}$	$3.24e+01^{1.9e+00}_{1.7e+00}$	$1.76e+01^{9.8e-01}_{1.0e+00}$	$9.72e+00^{7.1e-01}_{5.9e-01}$	$1.26e+01^{7.7e-01}_{7.4e-01}$
500.0	1500.0	$2.39e+01^{1.6e+00}_{1.6e+00}$	$2.47e+01^{2.0e+00}_{2.0e+00}$	$2.02e+01^{1.3e+00}_{1.3e+00}$	$2.77e+01^{1.6e+00}_{1.7e+00}$	$1.59e+01^{9.0e-01}_{8.3e-01}$	$9.12e+00^{5.1e-01}_{6.2e-01}$	$1.30e+01^{7.4e-01}_{7.2e-01}$
500.0	2000.0	$8.03e+00^{4.3e-01}_{4.3e-01}$	$9.03e+00^{4.7e-01}_{4.7e-01}$	$7.82e+00^{4.1e-01}_{4.1e-01}$	$1.08e+01^{5.7e-01}_{5.6e-01}$	$6.32e+00^{3.9e-01}_{3.5e-01}$	$3.83e+00^{2.1e-01}_{2.4e-01}$	$5.85e+00^{3.3e-01}_{3.1e-01}$
500.0	10000.0	$4.26e-04^{2.6e-05}_{2.7e-05}$	$4.71e-04^{2.5e-05}_{2.5e-05}$	$4.06e-04^{2.5e-05}_{2.2e-05}$	$5.95e-04^{3.0e-05}_{3.0e-05}$	$3.49e-04^{2.0e-05}_{1.9e-05}$	$2.11e-04^{1.2e-05}_{1.1e-05}$	$3.42e-04^{1.8e-05}_{1.9e-05}$
600.0	10.0	$1.68e-01^{1.0e-02}_{1.1e-02}$	$1.87e-01^{1.1e-02}_{1.1e-02}$	$1.57e-01^{9.4e-03}_{8.5e-03}$	$2.04e-01^{1.1e-02}_{1.1e-02}$	$1.26e-01^{7.2e-03}_{7.4e-03}$	$7.37e-02^{4.6e-03}_{3.9e-03}$	$1.08e-01^{5.6e-03}_{6.0e-03}$
600.0	1000.0	$4.67e-01^{2.9e-02}_{3.0e-02}$	$4.82e-01^{2.6e-02}_{2.6e-02}$	$4.25e-01^{2.4e-02}_{2.4e-02}$	$5.69e-01^{3.3e-02}_{3.1e-02}$	$3.32e-01^{1.7e-02}_{1.8e-02}$	$1.88e-01^{1.1e-02}_{1.1e-02}$	$2.82e-01^{1.5e-02}_{1.7e-02}$
600.0	1195.0	$1.58e+00^{8.2e-02}_{8.3e-02}$	$1.79e+00^{9.5e-02}_{9.8e-02}$	$1.36e+00^{7.9e-02}_{7.8e-02}$	$1.88e+00^{1.1e-01}_{1.1e-01}$	$1.07e+00^{6.2e-02}_{6.2e-02}$	$6.10e-01^{3.2e-02}_{3.3e-02}$	$8.78e-01^{5.3e-02}_{5.1e-02}$
600.0	1500.0	$1.42e+01^{1.0e+00}_{1.0e+00}$	$1.34e+01^{9.2e-01}_{7.9e-01}$	$1.18e+01^{7.2e-01}_{7.2e-01}$	$1.69e+01^{9.0e-01}_{8.8e-01}$	$9.60e+00^{5.7e-01}_{5.5e-01}$	$5.40e+00^{3.4e-01}_{3.0e-01}$	$7.77e+00^{4.3e-01}_{4.3e-01}$
600.0	2000.0	$7.00e+00^{4.5e-01}_{4.7e-01}$	$7.73e+00^{4.7e-01}_{4.7e-01}$	$6.52e+00^{3.4e-01}_{3.4e-01}$	$9.07e+00^{4.7e-01}_{4.9e-01}$	$5.62e+00^{3.1e-01}_{3.3e-01}$	$3.31e+00^{2.5e-01}_{1.9e-01}$	$4.85e+00^{2.5e-01}_{2.7e-01}$
600.0	10000.0	$3.29e-04^{2.3e-05}_{2.3e-05}$	$3.81e-04^{1.9e-05}_{1.9e-05}$	$3.09e-04^{1.8e-05}_{1.7e-05}$	$4.53e-04^{2.3e-05}_{2.4e-05}$	$2.61e-04^{1.5e-05}_{1.6e-05}$	$1.65e-04^{8.4e-06}_{8.4e-06}$	$2.68e-04^{1.6e-05}_{1.5e-05}$
750.0	10.0	$5.34e-02^{3.2e-03}_{3.1e-03}$	$6.13e-02^{3.3e-03}_{3.3e-03}$	$5.02e-02^{2.8e-03}_{2.8e-03}$	$7.30e-02^{4.1e-03}_{4.3e-03}$	$4.32e-02^{2.3e-03}_{2.4e-03}$	$2.46e-02^{1.5e-03}_{1.3e-03}$	$4.23e-02^{2.3e-03}_{2.4e-03}$
750.0	1200.0	$1.42e-01^{8.2e-03}_{9.0e-03}$	$1.49e-01^{8.3e-03}_{9.7e-03}$	$1.24e-01^{7.0e-03}_{6.9e-03}$	$1.81e-01^{9.4e-03}_{9.5e-03}$	$1.08e-01^{6.2e-03}_{5.6e-03}$	$6.13e-02^{3.4e-03}_{3.6e-03}$	$1.03e-01^{5.4e-03}_{5.8e-03}$
750.0	1495.0	$6.26e-01^{3.5e-02}_{3.6e-02}$	$6.32e-01^{3.5e-02}_{3.6e-02}$	$5.50e-01^{2.9e-02}_{2.9e-02}$	$8.13e-01^{4.2e-02}_{4.4e-02}$	$4.44e-01^{2.4e-02}_{2.6e-02}$	$2.54e-01^{1.4e-02}_{1.3e-02}$	$3.76e-01^{2.0e-02}_{2.0e-02}$
750.0	2000.0	$4.42e+00^{3.0e-01}_{2.9e-01}$	$4.73e+00^{2.9e-01}_{2.9e-01}$	$4.39e+00^{2.6e-01}_{2.6e-01}$	$5.83e+00^{3.3e-01}_{3.0e-01}$	$3.44e+00^{1.8e-01}_{1.8e-01}$	$2.05e+00^{1.1e-01}_{1.2e-01}$	$3.23e+00^{1.9e-01}_{1.8e-01}$
750.0	10000.0	$2.05e-04^{1.5e-05}_{1.5e-05}$	$2.51e-04^{1.3e-05}_{1.4e-05}$	$2.09e-04^{1.4e-05}_{1.3e-05}$	$2.99e-04^{1.6e-05}_{1.7e-05}$	$1.82e-04^{1.0e-05}_{9.5e-06}$	$1.09e-04^{6.2e-06}_{7.1e-06}$	$1.89e-04^{1.0e-05}_{9.8e-06}$
1000.0	10.0	$9.89e-03^{6.1e-04}_{6.6e-04}$	$1.14e-02^{7.0e-04}_{6.8e-04}$	$1.00e-02^{5.5e-04}_{5.4e-04}$	$1.45e-02^{7.8e-04}_{7.8e-04}$	$8.55e-03^{4.4e-04}_{4.4e-04}$	$5.25e-03^{2.8e-04}_{2.6e-04}$	$9.23e-03^{5.0e-04}_{5.4e-04}$
1000.0	1000.0	$1.43e-02^{8.8e-04}_{9.1e-04}$	$1.55e-02^{8.9e-04}_{8.0e-04}$	$1.36e-02^{7.0e-04}_{7.0e-04}$	$1.93e-02^{1.0e-03}_{1.0e-03}$	$1.19e-02^{6.6e-04}_{6.0e-04}$	$7.10e-03^{3.7e-04}_{3.8e-04}$	$1.22e-02^{6.6e-04}_{6.8e-04}$
1000.0	1500.0	$2.42e-02^{1.7e-03}_{1.7e-03}$	$2.62e-02^{1.5e-03}_{1.5e-03}$	$2.26e-02^{1.2e-03}_{1.3e-03}$	$3.26e-02^{1.8e-03}_{1.8e-03}$	$1.99e-02^{1.1e-03}_{1.0e-03}$	$1.16e-02^{6.5e-04}_{6.7e-04}$	$2.01e-02^{1.1e-03}_{1.1e-03}$
1000.0	1995.0	$1.37e-01^{7.5e-03}_{7.3e-03}$	$1.58e-01^{8.2e-03}_{8.2e-03}$	$1.34e-01^{6.9e-03}_{7.0e-03}$	$1.90e-01^{1.0e-02}_{1.0e-02}$	$1.15e-01^{6.3e-03}_{6.2e-03}$	$6.76e-02^{3.6e-03}_{3.7e-03}$	$1.10e-01^{6.1e-03}_{6.1e-03}$
1000.0	10000.0	$1.02e-04^{6.5e-06}_{6.9e-06}$	$1.17e-04^{6.1e-06}_{6.1e-06}$	$1.05e-04^{6.0e-06}_{5.7e-06}$	$1.53e-04^{7.8e-06}_{7.8e-06}$	$9.34e-05^{5.5e-06}_{4.9e-06}$	$5.86e-05^{3.7e-06}_{3.7e-06}$	$1.03e-04^{5.7e-06}_{5.5e-06}$

Table C.6. Expected number of events in 3.2 fb^{-1} and the experimental systematic uncertainties for each DM signal sample with axial-vector mediator and couplings $g_q = 0.25$, $g_\chi = 1.00$. MC statistical uncertainty is not included.

m_χ [GeV]	m_P [GeV]	EM1	EM2	EM3	EM4	EM5	EM6	IM7
1.0	10.0	$2.11e+02^{1.2e+01}_{1.5e+01}$	$1.44e+02^{1.1e+01}_{8.4e+00}$	$8.07e+01^{6.0e+00}_{7.1e+00}$	$6.98e+01^{4.6e+00}_{5.0e+00}$	$2.15e+01^{1.5e+00}_{1.7e+00}$	$7.18e+00^{4.0e-01}_{4.7e-01}$	$4.68e+00^{5.8e-01}_{4.1e-01}$
1.0	20.0	$1.96e+02^{1.0e+01}_{1.1e+01}$	$1.44e+02^{1.0e+01}_{9.1e+00}$	$8.11e+01^{5.2e+00}_{4.9e+00}$	$6.85e+01^{5.2e+00}_{5.9e+00}$	$2.04e+01^{1.9e+00}_{1.5e+00}$	$6.52e+00^{7.0e-01}_{5.0e-01}$	$4.30e+00^{3.4e-01}_{3.5e-01}$
1.0	50.0	$1.89e+02^{1.0e+01}_{1.0e+01}$	$1.38e+02^{8.2e+00}_{8.4e+00}$	$7.84e+01^{7.7e+00}_{5.6e+00}$	$6.77e+01^{5.3e+00}_{6.7e+00}$	$2.05e+01^{1.4e+00}_{1.4e+00}$	$7.03e+00^{6.6e-01}_{6.3e-01}$	$4.35e+00^{2.8e-01}_{2.5e-01}$
1.0	100.0	$1.76e+02^{1.1e+01}_{1.0e+01}$	$1.26e+02^{7.3e+00}_{7.8e+00}$	$7.50e+01^{5.4e+00}_{5.1e+00}$	$6.44e+01^{5.3e+00}_{4.4e+00}$	$1.99e+01^{1.4e+00}_{1.5e+00}$	$7.32e+00^{5.8e-01}_{6.2e-01}$	$4.48e+00^{4.5e-01}_{5.4e-01}$
1.0	200.0	$1.36e+02^{7.8e+00}_{7.5e+00}$	$1.11e+02^{6.2e+00}_{6.4e+00}$	$7.07e+01^{4.5e+00}_{4.9e+00}$	$6.05e+01^{4.6e+00}_{4.1e+00}$	$1.94e+01^{1.7e+00}_{1.5e+00}$	$7.01e+00^{6.1e-01}_{7.3e-01}$	$4.32e+00^{4.3e-01}_{3.9e-01}$
1.0	300.0	$1.34e+02^{7.0e+00}_{7.2e+00}$	$1.14e+02^{6.7e+00}_{7.0e+00}$	$7.28e+01^{5.0e+00}_{4.4e+00}$	$6.85e+01^{4.2e+00}_{4.5e+00}$	$2.34e+01^{2.4e+00}_{2.2e+00}$	$8.30e+00^{6.5e-01}_{6.1e-01}$	$5.29e+00^{4.1e-01}_{4.5e-01}$
1.0	500.0	$3.04e+01^{1.7e+00}_{2.0e+00}$	$2.93e+01^{1.6e+00}_{1.6e+00}$	$2.08e+01^{1.3e+00}_{1.3e+00}$	$2.19e+01^{1.3e+00}_{1.3e+00}$	$8.55e+00^{5.8e-01}_{6.4e-01}$	$3.00e+00^{1.9e-01}_{1.9e-01}$	$2.31e+00^{1.8e-01}_{2.1e-01}$
1.0	1000.0	$1.14e+00^{6.9e-02}_{7.3e-02}$	$1.23e+00^{6.8e-02}_{6.7e-02}$	$9.83e-01^{5.6e-02}_{5.6e-02}$	$1.28e+00^{6.9e-02}_{7.4e-02}$	$6.35e-01^{4.2e-02}_{3.7e-02}$	$3.08e-01^{2.0e-02}_{2.0e-02}$	$3.07e-01^{1.8e-02}_{1.9e-02}$
1.0	10000.0	$1.39e-05^{7.4e-07}_{7.1e-07}$	$1.38e-05^{7.4e-07}_{7.4e-07}$	$1.08e-05^{6.3e-07}_{6.9e-07}$	$1.20e-05^{7.6e-07}_{6.4e-07}$	$5.71e-06^{3.2e-07}_{3.6e-07}$	$2.58e-06^{1.9e-07}_{1.4e-07}$	$2.63e-06^{1.5e-07}_{1.7e-07}$
10.0	10.0	$1.31e+01^{7.8e-01}_{7.2e-01}$	$1.01e+01^{6.4e-01}_{6.9e-01}$	$6.07e+00^{3.9e-01}_{3.4e-01}$	$5.68e+00^{4.4e-01}_{4.3e-01}$	$1.79e+00^{1.5e-01}_{1.5e-01}$	$6.32e-01^{4.2e-02}_{4.5e-02}$	$3.91e-01^{4.3e-02}_{3.0e-02}$
10.0	15.0	$1.50e+01^{9.7e-01}_{8.0e-01}$	$1.19e+01^{6.9e-01}_{7.6e-01}$	$6.91e+00^{4.5e-01}_{4.8e-01}$	$6.17e+00^{4.3e-01}_{4.2e-01}$	$2.01e+00^{1.2e-01}_{1.6e-01}$	$7.19e-01^{5.4e-02}_{4.7e-02}$	$4.66e-01^{4.3e-02}_{4.1e-02}$
10.0	50.0	$1.86e+02^{1.1e+01}_{1.0e+01}$	$1.41e+02^{7.9e+00}_{7.8e+00}$	$8.01e+01^{5.7e+00}_{6.3e+00}$	$6.53e+01^{5.9e+00}_{4.3e+00}$	$2.07e+01^{1.2e+00}_{2.3e+00}$	$7.10e+00^{4.5e-01}_{7.3e-01}$	$4.05e+00^{4.3e-01}_{3.6e-01}$
10.0	100.0	$1.70e+02^{9.8e+00}_{9.5e+00}$	$1.30e+02^{7.7e+00}_{8.1e+00}$	$7.78e+01^{5.4e+00}_{4.7e+00}$	$6.57e+01^{5.0e+00}_{4.9e+00}$	$2.06e+01^{1.4e+00}_{1.5e+00}$	$6.91e+00^{8.9e-01}_{5.8e-01}$	$3.91e+00^{2.5e-01}_{2.7e-01}$
10.0	10000.0	$1.39e-05^{8.5e-07}_{8.8e-07}$	$1.39e-05^{8.5e-07}_{8.4e-07}$	$1.05e-05^{5.9e-07}_{7.8e-07}$	$1.22e-05^{7.4e-07}_{6.5e-07}$	$5.62e-06^{3.2e-07}_{3.6e-07}$	$2.70e-06^{1.7e-07}_{1.5e-07}$	$2.59e-06^{1.8e-07}_{1.7e-07}$
50.0	10.0	$5.21e+00^{2.9e-01}_{2.9e-01}$	$4.35e+00^{2.7e-01}_{2.6e-01}$	$2.77e+00^{1.7e-01}_{2.1e-01}$	$2.62e+00^{1.4e-01}_{1.6e-01}$	$9.03e-01^{7.8e-02}_{5.9e-02}$	$3.27e-01^{1.8e-02}_{2.8e-02}$	$2.19e-01^{1.8e-02}_{1.5e-02}$
50.0	50.0	$5.89e+00^{3.3e-01}_{3.5e-01}$	$4.90e+00^{2.8e-01}_{2.9e-01}$	$3.01e+00^{2.1e-01}_{1.8e-01}$	$2.95e+00^{1.9e-01}_{1.9e-01}$	$9.94e-01^{8.1e-02}_{8.2e-02}$	$3.48e-01^{3.3e-02}_{3.2e-02}$	$2.41e-01^{1.7e-02}_{1.6e-02}$
50.0	95.0	$1.41e+01^{8.3e-01}_{8.3e-01}$	$1.08e+01^{6.5e-01}_{6.1e-01}$	$6.74e+00^{4.1e-01}_{5.4e-01}$	$6.24e+00^{4.3e-01}_{3.8e-01}$	$1.99e+00^{1.5e-01}_{1.5e-01}$	$6.56e-01^{5.6e-02}_{5.7e-02}$	$4.66e-01^{3.4e-02}_{4.6e-02}$
50.0	200.0	$1.44e+02^{7.8e+00}_{8.6e+00}$	$1.12e+02^{6.7e+00}_{7.1e+00}$	$6.76e+01^{4.4e+00}_{4.9e+00}$	$6.11e+01^{4.9e+00}_{4.4e+00}$	$2.03e+01^{1.6e+00}_{1.7e+00}$	$7.09e+00^{4.3e-01}_{7.0e-01}$	$4.46e+00^{4.2e-01}_{3.2e-01}$
50.0	300.0	$1.34e+02^{6.9e+00}_{7.1e+00}$	$1.16e+02^{7.0e+00}_{6.4e+00}$	$7.18e+01^{5.4e+00}_{4.8e+00}$	$6.81e+01^{4.6e+00}_{5.4e+00}$	$2.44e+01^{1.3e+00}_{1.7e+00}$	$7.66e+00^{9.1e-01}_{5.7e-01}$	$5.27e+00^{3.4e-01}_{4.7e-01}$
50.0	10000.0	$1.33e-05^{7.3e-07}_{7.4e-07}$	$1.41e-05^{7.8e-07}_{7.9e-07}$	$1.02e-05^{6.6e-07}_{6.5e-07}$	$1.20e-05^{6.6e-07}_{6.9e-07}$	$5.62e-06^{4.1e-07}_{3.4e-07}$	$2.64e-06^{1.6e-07}_{1.6e-07}$	$2.57e-06^{1.9e-07}_{1.6e-07}$
150.0	10.0	$1.36e+00^{7.4e-02}_{7.5e-02}$	$1.26e+00^{6.8e-02}_{7.8e-02}$	$8.81e-01^{6.5e-02}_{5.3e-02}$	$8.72e-01^{5.6e-02}_{5.8e-02}$	$3.38e-01^{2.1e-02}_{2.3e-02}$	$1.33e-01^{8.2e-03}_{1.2e-02}$	$8.75e-02^{8.4e-03}_{5.2e-03}$
150.0	200.0	$2.45e+00^{1.7e-01}_{1.7e-01}$	$2.13e+00^{1.5e-01}_{1.2e-01}$	$1.49e+00^{8.0e-02}_{1.1e-01}$	$1.51e+00^{9.7e-02}_{1.0e-01}$	$5.58e-01^{3.8e-02}_{3.3e-02}$	$1.97e-01^{2.1e-02}_{1.7e-02}$	$1.46e-01^{1.1e-02}_{1.3e-02}$
150.0	295.0	$1.55e+01^{8.5e-01}_{8.0e-01}$	$1.32e+01^{8.8e-01}_{8.2e-01}$	$8.88e+00^{5.0e-01}_{5.7e-01}$	$8.08e+00^{6.1e-01}_{6.2e-01}$	$2.91e+00^{1.8e-01}_{1.8e-01}$	$1.01e+00^{1.0e-01}_{6.8e-02}$	$6.92e-01^{4.5e-02}_{4.9e-02}$
150.0	500.0	$2.65e+01^{1.5e+00}_{1.4e+00}$	$2.53e+01^{1.3e+00}_{1.3e+00}$	$1.81e+01^{1.1e+00}_{1.1e+00}$	$1.93e+01^{1.2e+00}_{1.3e+00}$	$7.45e+00^{4.7e-01}_{5.1e-01}$	$2.84e+00^{1.8e-01}_{2.1e-01}$	$1.90e+00^{1.5e-01}_{1.5e-01}$
150.0	1000.0	$1.10e+00^{5.8e-02}_{6.2e-02}$	$1.11e+00^{6.3e-02}_{6.1e-02}$	$9.56e-01^{6.2e-02}_{6.7e-02}$	$1.24e+00^{6.9e-02}_{6.7e-02}$	$5.97e-01^{4.0e-02}_{3.6e-02}$	$2.92e-01^{1.8e-02}_{1.7e-02}$	$2.93e-01^{1.7e-02}_{2.0e-02}$
150.0	10000.0	$1.10e-05^{5.8e-07}_{5.8e-07}$	$1.10e-05^{5.9e-07}_{5.9e-07}$	$8.68e-06^{4.5e-07}_{5.4e-07}$	$1.08e-05^{6.6e-07}_{6.3e-07}$	$4.88e-06^{2.8e-07}_{3.1e-07}$	$2.31e-06^{1.5e-07}_{1.3e-07}$	$2.44e-06^{1.5e-07}_{1.6e-07}$
500.0	10.0	$4.64e-03^{2.9e-04}_{2.6e-04}$	$5.32e-03^{3.0e-04}_{3.2e-04}$	$4.49e-03^{2.4e-04}_{2.4e-04}$	$6.11e-03^{3.4e-04}_{3.2e-04}$	$3.35e-03^{1.9e-04}_{1.8e-04}$	$1.78e-03^{1.1e-04}_{1.1e-04}$	$2.08e-03^{1.2e-04}_{1.2e-04}$
500.0	500.0	$6.62e-03^{4.1e-04}_{3.4e-04}$	$7.72e-03^{4.8e-04}_{4.8e-04}$	$6.19e-03^{3.9e-04}_{3.8e-04}$	$9.02e-03^{4.9e-04}_{5.6e-04}$	$4.78e-03^{2.7e-04}_{2.6e-04}$	$2.59e-03^{1.4e-04}_{1.7e-04}$	$2.98e-03^{1.9e-04}_{1.7e-04}$
500.0	995.0	$1.50e-01^{9.2e-03}_{9.7e-03}$	$1.63e-01^{9.2e-03}_{9.2e-03}$	$1.39e-01^{8.9e-03}_{8.7e-03}$	$1.85e-01^{9.5e-03}_{9.9e-03}$	$9.72e-02^{5.2e-03}_{5.4e-03}$	$4.85e-02^{3.1e-03}_{2.8e-03}$	$5.23e-02^{3.2e-03}_{3.2e-03}$
500.0	10000.0	$1.53e-06^{9.0e-08}_{9.3e-08}$	$1.71e-06^{9.3e-08}_{9.1e-08}$	$1.57e-06^{8.8e-08}_{8.8e-08}$	$2.21e-06^{1.1e-07}_{1.2e-07}$	$1.26e-06^{7.0e-08}_{6.7e-08}$	$6.88e-07^{3.9e-08}_{3.7e-08}$	$9.34e-07^{5.3e-08}_{5.7e-08}$
1000.0	10.0	$3.03e-05^{1.8e-06}_{1.7e-06}$	$3.69e-05^{1.9e-06}_{2.2e-06}$	$3.45e-05^{1.9e-06}_{1.9e-06}$	$5.00e-05^{2.6e-06}_{2.6e-06}$	$3.10e-05^{1.6e-06}_{1.7e-06}$	$1.91e-05^{1.0e-06}_{1.0e-06}$	$3.02e-05^{1.6e-06}_{1.7e-06}$
1000.0	1000.0	$4.62e-05^{2.9e-06}_{3.0e-06}$	$5.59e-05^{2.9e-06}_{2.9e-06}$	$5.20e-05^{2.8e-06}_{2.8e-06}$	$7.67e-05^{3.9e-06}_{4.1e-06}$	$4.80e-05^{2.5e-06}_{2.7e-06}$	$2.85e-05^{1.5e-06}_{1.5e-06}$	$4.56e-05^{2.6e-06}_{2.5e-06}$
1000.0	10000.0	$1.28e-07^{6.9e-09}_{7.1e-09}$	$1.45e-07^{9.5e-09}_{9.5e-09}$	$1.38e-07^{7.6e-09}_{7.6e-09}$	$2.03e-07^{1.0e-08}_{1.1e-08}$	$1.27e-07^{7.5e-09}_{7.0e-09}$	$8.04e-08^{4.4e-09}_{4.1e-09}$	$1.35e-07^{7.1e-09}_{7.4e-09}$

Table C.7. Expected number of events in 3.2 fb^{-1} and the experimental systematic uncertainties for each Dark Matter signal samples with pseudo-scalar mediator and couplings $g = g_q = g_\chi = 1$. MC statistical uncertainty is not included.

$g = g_q = g_\chi$	EM1	EM2	EM3	EM4	EM5	EM6	IM7
0.1	$3.27e+00^{1.9e-01}_{1.9e-01}$	$3.21e+00^{1.7e-01}_{1.7e-01}$	$2.72e+00^{1.4e-01}_{1.6e-01}$	$3.50e+00^{1.8e-01}_{1.9e-01}$	$1.87e+00^{1.1e-01}_{1.1e-01}$	$9.48e-01^{5.1e-02}_{5.3e-02}$	$1.19e+00^{7.8e-02}_{6.7e-02}$
0.25	$2.09e+01^{1.1e+00}_{1.2e+00}$	$2.00e+01^{1.0e+00}_{1.1e+00}$	$1.65e+01^{8.3e-01}_{8.3e-01}$	$2.14e+01^{1.2e+00}_{1.2e+00}$	$1.14e+01^{6.0e-01}_{6.9e-01}$	$5.83e+00^{3.0e-01}_{3.0e-01}$	$7.37e+00^{4.5e-01}_{4.1e-01}$
0.5	$7.30e+01^{4.1e+00}_{4.1e+00}$	$7.99e+01^{4.2e+00}_{4.3e+00}$	$6.21e+01^{3.4e+00}_{3.8e+00}$	$8.05e+01^{4.2e+00}_{4.4e+00}$	$4.11e+01^{2.3e+00}_{2.3e+00}$	$2.23e+01^{1.3e+00}_{1.2e+00}$	$2.73e+01^{1.6e+00}_{1.5e+00}$
0.75	$1.51e+02^{7.9e+00}_{8.3e+00}$	$1.59e+02^{8.4e+00}_{8.2e+00}$	$1.23e+02^{7.0e+00}_{6.8e+00}$	$1.66e+02^{8.5e+00}_{9.0e+00}$	$8.48e+01^{4.7e+00}_{5.1e+00}$	$4.28e+01^{2.5e+00}_{2.2e+00}$	$5.51e+01^{3.4e+00}_{3.4e+00}$
1.0	$2.51e+02^{1.5e+01}_{1.5e+01}$	$2.51e+02^{1.4e+01}_{1.3e+01}$	$1.93e+02^{1.1e+01}_{1.1e+01}$	$2.44e+02^{1.4e+01}_{1.3e+01}$	$1.31e+02^{6.9e+00}_{8.6e+00}$	$6.58e+01^{4.2e+00}_{3.4e+00}$	$8.61e+01^{4.8e+00}_{5.2e+00}$
1.25	$3.16e+02^{1.7e+01}_{1.7e+01}$	$3.21e+02^{1.8e+01}_{1.8e+01}$	$2.56e+02^{1.4e+01}_{1.4e+01}$	$3.22e+02^{1.8e+01}_{1.7e+01}$	$1.67e+02^{9.6e+00}_{8.9e+00}$	$9.34e+01^{5.0e+00}_{5.3e+00}$	$1.14e+02^{7.1e+00}_{6.4e+00}$
1.5	$3.72e+02^{2.1e+01}_{2.0e+01}$	$3.87e+02^{2.0e+01}_{2.1e+01}$	$2.93e+02^{1.7e+01}_{1.5e+01}$	$3.94e+02^{2.0e+01}_{2.1e+01}$	$2.13e+02^{1.2e+01}_{1.2e+01}$	$1.12e+02^{7.3e+00}_{5.9e+00}$	$1.44e+02^{7.9e+00}_{8.7e+00}$

Table C.8. Expected number of events in 3.2 fb^{-1} and the experimental systematic uncertainties for each Dark Matter signal samples with a axial-vector mediator with $m_A = 1$ TeV and $m_\chi = 150$ GeV for different values of the couplings. MC statistical uncertainty is not included.

$g = g_q = g_\chi$	EM1	EM2	EM3	EM4	EM5	EM6	IM7
0.1	$1.297e+00^{6.8e-02}_{6.6e-02}$	$1.097e+00^{7.5e-02}_{6.6e-02}$	$7.038e-01^{4.0e-02}_{5.4e-02}$	$6.739e-01^{5.0e-02}_{4.3e-02}$	$2.238e-01^{1.7e-02}_{2.0e-02}$	$8.025e-02^{6.7e-03}_{5.6e-03}$	$5.508e-02^{4.1e-03}_{4.4e-03}$
1.0	$1.340e+02^{6.9e+00}_{7.1e+00}$	$1.161e+02^{7.0e+00}_{6.4e+00}$	$7.181e+01^{5.4e+00}_{4.8e+00}$	$6.810e+01^{4.6e+00}_{5.4e+00}$	$2.444e+01^{1.3e+00}_{1.7e+00}$	$7.658e+00^{9.1e-01}_{5.7e-01}$	$5.268e+00^{3.4e-01}_{4.7e-01}$
2.0	$5.621e+02^{3.1e+01}_{3.3e+01}$	$4.718e+02^{3.1e+01}_{2.8e+01}$	$3.070e+02^{2.1e+01}_{2.2e+01}$	$2.895e+02^{1.9e+01}_{2.1e+01}$	$1.031e+02^{7.9e+00}_{7.1e+00}$	$3.346e+01^{2.2e+00}_{2.8e+00}$	$2.193e+01^{1.8e+00}_{1.6e+00}$
3.0	$1.251e+03^{6.5e+01}_{6.7e+01}$	$1.059e+03^{6.3e+01}_{6.1e+01}$	$6.989e+02^{5.1e+01}_{4.9e+01}$	$6.725e+02^{4.2e+01}_{4.1e+01}$	$2.405e+02^{1.6e+01}_{1.8e+01}$	$8.147e+01^{8.6e+00}_{5.6e+00}$	$5.446e+01^{3.3e+00}_{4.7e+00}$
4.0	$2.084e+03^{1.1e+02}_{1.1e+02}$	$1.817e+03^{9.7e+01}_{1.2e+02}$	$1.199e+03^{9.3e+01}_{7.2e+01}$	$1.158e+03^{8.0e+01}_{7.1e+01}$	$4.181e+02^{2.3e+01}_{3.3e+01}$	$1.540e+02^{1.8e+01}_{1.4e+01}$	$9.671e+01^{6.2e+00}_{6.8e+00}$
5.0	$2.913e+03^{1.6e+02}_{1.5e+02}$	$2.593e+03^{1.5e+02}_{1.5e+02}$	$1.686e+03^{1.1e+02}_{9.7e+01}$	$1.716e+03^{1.2e+02}_{1.1e+02}$	$6.354e+02^{4.7e+01}_{5.6e+01}$	$2.204e+02^{1.5e+01}_{1.8e+01}$	$1.557e+02^{1.2e+01}_{1.1e+01}$
6.0	$3.730e+03^{2.0e+02}_{2.0e+02}$	$3.411e+03^{2.0e+02}_{1.8e+02}$	$2.324e+03^{1.3e+02}_{1.6e+02}$	$2.292e+03^{1.7e+02}_{1.5e+02}$	$8.521e+02^{5.4e+01}_{5.2e+01}$	$3.312e+02^{2.5e+01}_{2.6e+01}$	$2.207e+02^{2.3e+01}_{1.7e+01}$

Table C.9. Expected number of events in 3.2 fb^{-1} and the experimental systematic uncertainties for each Dark Matter signal samples with a pseudo-scalar mediator with $m_P = 300$ GeV and $m_\chi = 50$ GeV for different values of the couplings. MC statistical uncertainty is not included.

Appendix D

Signal Limits

In the following pages the limits at 95% CL on the observed and expected signal strength for the signal samples used to interpret the results in the ADD model (Table D.1), SUSY compressed scenarios (Tables D.2–D.4) and the simplified models with axial-vector (Tables D.5 and D.6) and pseudo-scalar mediators (Tables D.7 and D.8).

n	m_D [GeV]	obs. μ	exp. μ
2	5300	0.42	0.35
3	4100	0.27	0.23
4	3600	0.19	0.16
5	3200	0.12	0.10
6	3000	0.08	0.07

Table D.1. Observed and expected limits on the signal strength μ and $\mathrm{CL_s}$ for the ADD signal model, for different M_D and number of extra-dimensions.

$m_{\tilde{b}_1}$ [GeV]	$m_{\tilde{\chi}_1^0}$ [GeV]	obs. μ	exp. μ	$m_{\tilde{b}_1}$ [GeV]	$m_{\tilde{\chi}_1^0}$ [GeV]	obs. μ	exp. μ
250	230	0.84	0.68	450	430	4.55	3.23
250	245	0.43	0.31	450	445	2.92	1.98
300	280	1.33	1.03	500	480	6.35	4.38
300	295	0.72	0.50	500	495	4.94	3.19
350	330	1.98	1.44	550	530	11.63	8.08
350	345	1.16	0.81	550	545	7.42	5.18
400	380	3.05	2.11	600	580	11.99	8.38
400	395	1.86	1.28	600	595	10.11	6.71

Table D.2. Observed and expected limits on the signal strength μ and $\mathrm{CL_s}$ for the $\tilde{b}_1 \to b + \tilde{\chi}_1^0$ decay, for different $m_{\tilde{b}_1}$ and $m_{\tilde{\chi}_1^0}$.

$m_{\tilde{t}_1}$ [GeV]	$m_{\tilde{\chi}_1^0}$ [GeV]	obs. μ	exp. μ	$m_{\tilde{t}_1}$ [GeV]	$m_{\tilde{\chi}_1^0}$ [GeV]	obs. μ	exp. μ
250	230	0.95	0.76	375	295	6.31	4.29
275	195	2.16	2.09	375	315	5.39	3.80
275	225	2.01	1.72	375	345	3.57	2.50
275	250	1.36	1.10	375	370	1.62	1.10
275	270	0.63	0.45	400	320	6.66	5.21
300	220	2.70	2.58	400	330	5.95	4.86
300	260	2.10	1.72	400	370	4.47	3.20
300	280	1.46	1.15	400	395	2.12	1.44
300	295	0.79	0.56	450	370	9.66	6.75
325	245	3.65	2.95	450	395	8.52	5.97
325	260	3.27	2.61	450	425	5.82	3.98
325	295	2.34	1.76	450	445	3.33	2.25
325	320	1.02	0.71	500	420	14.03	9.79
350	270	4.35	3.81	500	445	12.82	9.30
350	295	3.50	2.76	500	485	6.56	4.33
350	305	3.73	2.89	500	495	5.10	3.41
350	345	1.33	0.92				

Table D.3. Observed and expected limits on the signal strength μ and $\mathrm{CL_s}$ for the $\tilde{t}_1 \to c + \tilde{\chi}_1^0$ decay, for different $m_{\tilde{t}_1}$ and $m_{\tilde{\chi}_1^0}$.

$m_{\tilde{q}}$ [GeV]	$m_{\tilde{\chi}_1^0}$ [GeV]	obs. μ	exp. μ	$m_{\tilde{q}}$ [GeV]	$m_{\tilde{\chi}_1^0}$ [GeV]	obs. μ	exp. μ
400	395	13.42	0.17	550	525	2.12	1.12
400	385	13.41	0.27	600	595	1.25	0.94
400	375	13.41	0.36	600	585	1.25	1.17
450	445	6.88	0.27	600	575	1.25	1.60
450	435	6.88	0.36	650	645	0.76	1.33
450	425	6.88	0.50	650	635	0.76	1.66
500	495	3.74	0.40	650	625	0.76	2.29
500	485	3.74	0.57	700	695	0.47	1.96
500	475	3.74	0.77	700	685	0.47	2.36
550	545	2.12	0.66	700	675	0.47	3.05
550	535	2.12	0.82				

Table D.4. Observed and expected limits on the signal strength μ and $\mathrm{CL_s}$ for the $\tilde{q} \to q + \tilde{\chi}_1^0$ decay, for different $m_{\tilde{q}}$ and $m_{\tilde{\chi}_1^0}$.

m_χ [GeV]	m_A [GeV]	obs. μ	exp. μ	m_χ [GeV]	m_A [GeV]	obs. μ	exp. μ
1	20	2.98e-02	3.78e-02	250	800	7.35e-01	5.27e-01
1	50	3.74e-02	4.27e-02	250	1000	1.04	7.35e-01
1	100	4.53e-02	5.11e-02	250	10000	1.18e+05	8.12e+04
1	200	8.30e-02	7.53e-02	400	10	1.29e+02	91.55
1	300	1.02e-01	9.98e-02	400	795	21.59	15.59
1	500	2.14e-01	1.64e-01	400	1000	2.22	1.62
1	800	5.00e-01	3.55e-01	400	1200	2.39	1.64
1	1000	8.61e-01	6.03e-01	400	10000	1.57e+05	1.07e+05
1	1200	1.46	1.01	500	10	2.83e+02	1.97e+02
1	1500	2.87	2.00	500	500	2.27e+02	1.56e+02
1	2000	8.84	6.09	500	800	1.27e+02	88.99
1	10000	9.51e+04	6.67e+04	500	995	39.47	28.19
10	10	6.56e-01	6.93e-01	500	1200	4.76	3.36
10	15	6.67e-01	6.30e-01	500	1500	4.87	3.39
10	50	4.48e-02	4.80e-02	500	2000	10.87	7.62
10	100	5.02e-02	5.31e-02	500	10000	1.92e+05	1.32e+05
10	10000	9.90e+04	6.77e+04	600	10	5.78e+02	4.10e+02
50	10	2.74	2.29	600	1000	2.28e+02	1.59e+02
50	50	2.32	2.05	600	1195	71.94	50.24
50	95	1.33	1.32	600	1500	8.20	5.59
50	200	9.15e-02	9.35e-02	600	2000	12.97	9.06
50	300	1.20e-01	1.04e-01	600	10000	2.42e+05	1.70e+05
50	10000	9.97e+04	6.91e+04	750	10	1.57e+03	1.08e+03
150	10	11.04	8.59	750	1200	6.52e+02	4.42e+02
150	200	8.20	6.33	750	1495	1.70e+02	1.17e+02
150	295	3.65	2.93	750	2000	19.97	13.95
150	500	2.83e-01	2.22e-01	750	10000	3.48e+05	2.41e+05
150	800	5.30e-01	3.79e-01	1000	10	7.19e+03	4.99e+03
150	1000	8.12	5.68	1000	1000	5.44e+03	3.75e+03
150	10000	1.01e+05	7.06e+04	1000	1995	5.96e+02	4.13e+02
250	10	34.03	24.63	1000	1500	3.32e+03	2.28e+03
250	300	21.77	15.56	1000	10000	6.47e+05	4.46e+05
250	495	7.97	5.96				

Table D.5. Observed and expected limits on the signal strength μ and CL_s for the DM signal models with axial-vector mediators and couplings $g_q = 0.25$, $g_\chi = 1$, for different m_χ and m_A.

g	obs. μ	exp. μ
0.10	49.70	34.86
0.50	2.13	1.53
0.75	1.09	7.64e-01
1.00	7.07e-01	4.99e-01
1.25	5.11e-01	3.69e-01
1.50	4.19e-01	2.95e-01

Table D.6. Observed and expected limits on the signal strength μ and CL_s for the DM signal modelss with axial-vector mediators, with $m_\chi = 150$ GeV, $m_A = 1$ TeV and different values of the couplings $g_\chi = g_q = g$.

m_χ [GeV]	m_P [GeV]	obs. μ	exp. μ	m_χ [GeV]	m_P [GeV]	obs. μ	exp. μ
1	10	3.34	3.99	50	200	4.08	4.89
1	20	3.09	4.03	50	300	3.85	4.31
1	50	3.29	4.18	50	10000	1.97e+07	1.51e+07
1	100	3.55	4.51	150	10	2.82e+02	2.87e+02
1	200	3.62	4.85	150	200	1.81e+02	1.75e+02
1	300	3.74	4.34	150	295	29.17	33.75
1	500	12.97	11.97	150	500	13.65	12.81
1	1000	1.74e+02	1.25e+02	150	1000	1.71e+02	1.23e+02
1	10000	1.94e+07	1.50e+07	150	10000	2.09e+07	1.54e+07
10	10	45.73	53.82	500	10	2.70e+04	1.91e+04
10	15	38.27	47.62	500	500	1.90e+04	1.32e+04
10	50	3.01	4.14	500	995	1.02e+03	7.22e+02
10	100	3.24	4.36	500	10000	6.50e+07	4.50e+07
10	10000	1.94e+07	1.50e+07	1000	10	2.11e+06	1.47e+06
50	10	1.00e+02	1.13e+02	1000	1000	1.41e+06	9.72e+05
50	50	94.43	1.03e+02	1000	10000	$<$ 1.00e-06	3.62e+20
50	95	42.59	49.23				

Table D.7. Observed and expected limits on the signal strength μ for the DM signal models with a scalar mediator and couplings fixed at $g = g_q = g_\chi = 1$, for different m_χ and m_P.

g	obs. μ	exp. μ
0.10	3.94e+02	4.46e+02
1.00	3.74	4.34
2.00	9.14e-01	1.02
3.00	4.04e-01	4.38e-01
4.00	2.27e-01	2.49e-01
5.00	1.68e-01	1.67e-01
6.00	1.15e-01	1.20e-01

Table D.8. Observed and expected limits on the signal strength μ for the DM signal models with a scalar mediator, with $m_\chi = 50$ GeV, $m_P = 300$ TeV and different values of the couplings $g_\chi = g_q = g$.